UNIVERSITY OF LIVERPOOL

Aqueous Polyoxometalates: Design and Analysis of Electrochemical Catalysts for the Indirect Reduction of Oxygen in PEM Fuel Cells

By

Ben M. Alston

Supervisors

Prof. Andrew I. Cooper

Prof. Richard J. Nichols

September 2013

Thesis submitted in accordance with the requirements of the University of Liverpool for the degree of Doctor in Philosophy.

Table of Contents

Chapter 2: Characterization Methods and Theory

Abstract

The applicability of aqueous, mixed addenda polyoxometalates with the general formula $[PMo_{12-x}V_xO_{40}]^{(3+x)-}$ as catalysts for FlowCath® technology has been demonstrated. These compounds were used as a platinum substitute in the PEM fuel cell cathode for the indirect reduction of oxygen. The effect of increased vanadium substitution within the Keggin structure upon the diffusion coefficient (D_o) and the standard rate constant for electron transfer (k_o) was investigated via simulation and electrochemical analysis. The apparent decrease in electrode kinetics linked with increased vanadium substitution is explained via simulation modelling, with the V_xPOMs systems demonstrating multiple redox processes. The effects of solvent and electrode material upon the voltammetry are also discussed.

Self supporting conditions analogous to the in fuel cell were employed to the V_xPOM catalysts and their behaviour compared to the $[Fe(CN)_6]^{4-/3-}$ redox couple via CV, simulation and RDE analysis. The resulting self-supported $[Fe(CN)_6]^{3-/4-}$ system demonstrated significantly increased currents, but less than theoretically expected due to increases in cell resistance. The self-supported V_xPOM system electrode processes are hindered due to the formation of a VO_2^0 driven blocking layer reducing the actual potential experienced by the redox active species at the electrode surface. The resulting blocking layer prevented the V_xPOM from approaching the electrode surface thus not experiencing the actual potential applied at the electrode surface. Tafel plots based upon the V_xPOM systems showed characteristics not resembling 'classical' Tafel analysis with curvature preventing extrapolation for exchange current density. An 'alternative' analysis method involving the interpolation of the raw rotating disc electrode data to determine the required overpotential to generate a desired current was developed. The regeneration of the V_4POM catalysts was investigated which demonstrated a possible change in speciation and a more ordered structure based upon single crystal X-ray analysis.

The effects of formulation development of the lead V_4POM catalyst upon its electrochemical and fuel cell performance were investigated. Substitution of Na^+ counter ions with H^+ (HV_4POM) showed a decrease in charge transfer resistance (R_c) as well increase in membrane resistance (R_s) and cathodic current. The affects of adding stoichiometric quantities of H_3PO_4, HBF_4 and $VOSO_4$ were investigated with RDE and fuel cell testing indicating improved performance for the HBF_4 formulation at fuel cell conditions. The effects of current developments in FlowCath® technology upon the H_3PO_4 formulation are also discussed.

Roman Symbols

Listed here are symbols and abbreviations that are used throughout this work to define or express various parameters and properties. The symbols used here, in most cases, follow the recommendations outline buy the IUPAC Commission on Electrochemistry.

Symbol	Meaning	Usual Units
a_j^i	Activity of substance j in phase i	none
C_d	Differential capacitance of the double layer	F cm^{-2}
C_j	Concentration of species j	mol cm^{-3}
C_j^*	Bulk concentration of species j	mol cm^{-3}
$C_\mathrm{j}(\mathrm{x})$	Concentration of species j at distance x	mol cm^{-3}
D_j	Diffusion coefficient of species j	cm^2 s^{-1}
E	Potential of an electrode versus a reference	V
E^o	Standard electrode potential of an electrode or couple	V
ΔE^o	Difference standard electrode potential of two couples	V
$E^{o'}$	Formal potential of an electrode or couple	V
E_A	Activation energy	kj mol^{-1}
E_eq	Equilibrium potential of an electrode	V
$\mathrm{E_F}$	Fermi level	eV
E_p	Peak potential	V
ΔE_p	Difference in peak potential for anodic and cathodic processes	V
E_p^a	Anodic peak potential	V
E_p^c	Cathodic peak potential	V
$E_{1/2}$	Measured or expected half wave potential	V
F	Faraday consatnt	C
f	F/RT	V^{-1}
G	Gibbs free energy	kj mol^{-1}
ΔG	Change in Gibbs free energy in a chemical process	kj mol^{-1}
G^o	Standard Gibbs energy	kj mol^{-1}
ΔG^o	Change in standard Gibbs free energy in a chemical process	kj mol^{-1}
$\Delta G^{\ddagger}$	Standard Gibbs energy of activation	kj mol^{-1}

I	Current	A
I_a	Anodic component current	A
I_c	Cathodic component current	A
I_p	Peak Current	A
I_p^a	Anodic peak current	A
I_p^c	Cathodic peak current	A
I_L	a) Limiting current or b) Levich current	A
I_o	Exchange current	A
J	Current density	A cm^{-2}
J_o	Exchange current density	A cm^{-2}
K	Equilibrium constant	none
k	Rate constant for a homogeneous reaction	Order Dependent
k^o	Standard heterogeneous rate constant	cm s^{-1}
N_A	Avagadros number	none
n	Stoichiometirc number of electrons involved in an electrode reaction	none
Q	Charge passed in electrolysis	C
R	Gas constant	J mol^{-1} K^{-1}
R_{ct}	Charge transfer resistance	Ω
R_s	Solution resistance	Ω
R_u	Uncompensated resistance	Ω
Re	Reynolds number	none
T	Absolute temperature	K
t	Time	s
V	Volume	cm^3
v	Linear potential scan rate	V s^{-1}
Z	Impedance	Ω
Z_{Im}	Imaginary part of impedance	Ω
Z_{Re}	Real part of impedance	Ω
Z_W	Warburg impedence	Ω

Greek Symbols

Symbol	Meaning	Usual Units
α	Transfer coefficent	none
β	1 - α	none
γ_j	Activity coefficient of species j	none
δ_j	Diffusion layer thickness of species j at an electrode surafce	cm
ε_j	Molar absorbtivity of species j	mol dm^{-3} cm^{-1}
η	Overpotential	V
λ	Reorganisation energy for electron transfer	eV
$\bar{\mu}_j^i$	Electrochemical potential of species j in phase i	kj mol^{-1}
μ_j^i	Chemical potential of species j in phase	kj mol^{-1}
ν	Kinematic viscosity	cm^2 s^{-1}
ϕ	Electrostatic potential	V
$\Delta\phi$	Electrostatic potential difference between two points or phases	V
ω	Angular frequency of rotation	s^{-1}

Standard Abbreviations

Symbol	Meaning
AFC	Alkaline fuel cell
BV	Butler - Volmer
CV	Cyclic voltammetry
EC	Heterogeneous electron transfer followed by homogeneous chemical reaction
EIS	Electrochemical impedance spectroscopy
HOPG	Highly oriented pyrolytic graphite
IHP	Innerr Helmholtz plane
LSV	Linear sweep voltammetry
MCFC	Molten carbonate fuel cell
NHE	Normal hydrogen electrode = SHE
OHP	Outer Helmholtz plane
PAFC	Phosporic acid fuel cell

PEM	Proton exchange membrane
POM	Polyoxometalate
RDE	Rotating disk electrode
RDS	Rate-determining step
SCE	Saturated calomel electrode
SHE	Standard hydrogen electrode = NHE
SOFC	Solid oxide fuel cell
V_xKegin	Specific Keggin species within the V_xPOM system
V_xPOM	Experimental formula of the synthesised system with x representing the number of vanadium's contained within the general formula; $Na_xH_3PMo_{12-x}V_xO_{40}$

Acknowledgements

Firstly I would like to express my deepest gratitude to my academic and industrial supervisors, Prof. Richard Nichols, Prof. Andrew Cooper and Dr. Hywel Davies for their help, guidance and support during the last four years. I would also like to thank Dr. Andrew Creeth and ACAL Energy Ltd for sponsorship and the opportunity to contribute to their world leading research.

The research highlighted in this thesis would not have been possible without the help and guidance of Dr. Trevor Davies to whom I will forever be indebted too. I would also like to express my gratitude to Dr. Dave Adams for his constant support and advice throughout the duration of this work.

The task of completing a PhD is not an easy one and without my family and I can confidently say, 'I would not be where I am today'. My parents, Ken and Maureen, have provided me with love and support that has never wavered even during the most testing days of this PhD. For this I will always be grateful. The help and support a brother can provide is not only unique but helpful in its own special way. Thank you to Steven, Andrew and Peter. I would also like to extend a special thanks to Neil and Helen for their continued support throughout my studies.

This thesis would not have been possible without one person in particular. She has been forever present in my life for the past seven years and provided me with love, friendship, support, encouragement and countless cups of tea. Hannah, you are irreplaceable.

I would like to finally thank my fellow members of the Cooper group for making my time within the group one to remember as well as my fellow PhD graduates; Liam, Ryan, Jamie, Rob, Mike, Paul, Dan, Aled, Jaclyn, Emily, Fiona, Tamara Emma and Gemma.

Chapter 1

Introduction

Table of Contents

1.1 Polyoxometalates

1.1.1 Overview

Polyoxometalates (POM) are a unique group of inorganic compounds which form a three dimensional discrete framework via the self-assembly of at least two simple oxoanions in acidic media (equation 1.1).[1-7] Under the right conditions (pH, temperature and concentration), the protonation of the oxoanion (e.g. MoO_4^{2-}) gives rise to polycondensation of the MoO_4^{2-} and formation of the more complex polyoxometalate structure.

$$12\,MoO_4^{2-} + HPO_4^{2-} + 23\,H^+ \longrightarrow [PMo_{12}O_{40}]^{3-} + 12\,H_2O \qquad (1.1)$$

The polyoxometalate group is generally split into two categories, isopoly anions and heteropoly anions, which are easily distinguished based upon their structure and composition. The general formula for the isopoly and heteropoly anions is $[M_mO_y]^{p-}$ and $[X_xM_mO_y]^{q-}$ respectively where x ≤ m in the case of the heteropoly anion.[1-7] M is the addenda atom and is commonly a group 5 or 6 transition metal in their high oxidation states typically with an electron configuration of d^1 or d^0.[1,2,8] Typically, the addenda atom is molybdenum(VI) or tungsten(VI) due to the favourable environment created by their ionic radius, charge and available (empty) d orbitals to form the required metal oxygen π bond.[1-7] Although molybdenum and tungsten are the ideal metal centres, the polyoxometalate structure is not limited to these addenda atoms, with vanadium(V), niobium(V) and tantalum(V) all having been successfully incorporated.[9-13]

1.1.2 Background

The history of polyoxometalates dates back to the times of the early Native Americans where the mysterious 'blue water' was observed in the Valley of the Ten Thousand Smokes, Katmai National Park in southern Alaska.[14] Despite this initial sighting, polyoxometalates only gathered scientific interest in the late eighteenth century. The yellow precipitate that formed upon the addition of ammonium molybdate to an excess of phosphoric acid, which is now commonly known as phosphomolybdic acid $\{(NH_4)_3[PMo_{12}O_{40}]\}$, was described by Berzelius in 1826.[15]

By the early 20th century over seven hundred heteropoly compounds had been reported with only the 12:1 composition of 12-tungstosilic acid revealed by Marignac in 1864,[16] but the true structure remained unresolved. In 1907, work began on determining the structure of polyoxometalates with the first attempt by Werner,[17] which was then developed further by Miolati and Pizzighelli[18] with later developments made by Roshenheim.[19] The work of Miolati and Roshenheim postulated that the polyoxometalate's building blocks were based upon six-coordinate units of MO_4^{2-} or $M_2O_7^{2-}$ (M being any of the possible addenda atoms). However, this leads to structures different to those obtained via modern chemistry methods. Pauling challenged this theory and argued that the building block units were of octahedral geometry based upon his measurements of element radii.[20] Pauling's theory was supported by Keggin who successfully solved the first crystal structure of the polyoxometalate series using X-ray diffraction, based on 12-tungstophosphoric acid, $(H_5O_2)_3[PW_{12}O_{40}]$.[21] During the 20th century, the polyoxometalate field came to fruition with the chemical and physical properties and some structures of many heteropoly anions being reported.[19] At this point, there was minimal knowledge on polyoxometalate reactions of formation, degradation and the inter conversion of species until work by Souchay studied the condensation reactions involved in polyoxometalate formation.[8] In the 1960's, Pope followed on from Souchay's work and used NMR to determine the polyoxometalate structure.[22,23] Pope's contribution to the field of polyoxometalate chemistry was immense resulting in hundreds of publications, establishing him as one of the key researchers in this field. He went onto to develop methods for the preparation and characterization of substituted heteropolyanions containing vanadium, niobium, tantalum as well as including their organic derivatives.[24-26] Pope laid the foundations for the further development of this field, with many researchers namely Kozhevnikov,[2,27-31] Hill,[6,32-35] Muller,[36-42] Neumann,[43-48] Tsigdinos,[9,49-52], Maksimov[53] and Odyakov and Mateev.[11,30,54-63]

1.1.3 Structure of Polyoxometalates

As mentioned in section 1.1.1, polyoxometalates can exist as isopolyanions or heteropolyanions depending upon the incorporation of a central hetero atom into the structure. The work in this thesis focuses upon the heteropolyanion structure and thus

the isopolyanion will not be considered, but a detailed analysis and description can be obtained elsewhere.[1] The heteropolyanions adopt the general formula $[X_xM_mO_y]^{q-}$ where M is the addenda atom and, as stated above, is usually a transition metal situated in group 5 or 6 in a high oxidation state with a d^0 or d^1 electron configuration.[1,2,8] The addenda atoms physical properties such as ionic radii, charge and vacant d orbital to form metal oxygen π bonds are key to determining their applicability to polyoxometalate chemistry.[1-7] Based on these criteria, the addenda atom is restricted to only a few elements. However, the hetero atom does not appear to have the same restrictions, with over sixty elements from across all groups in the periodic table (excluding noble gasses) having been successfully used.[1] Considering the possibility of numerous X/M ratios, hetero atoms and more than one type of addenda atom being used in a single structure, the number of different structures possible could be endless. The relative size of the polyoxometalate structure does not appear to be limited with the range of addenda atoms being between two and six,[1] the upper limit is ever increasing with numerous systems having in excess of 100 addenda atoms highlighted in Cronin's review,[64] with the 'lemon' cluster containing 368 molybdenum (addenda) centres.[65] Although there is a wide variation in the possible structures, there are two general principles (stated by Pope and Muller) which apply to the polyoxometalate structure:[1,41]

- Addenda atoms commonly adopt a somewhat distorted octahedron. In this instance the metal is not at the centre of the polyhedron but displace towards the terminal oxygen as a consequence of metal oxygen π bonding.
- Heteropolyanions which contain three or more terminal oxo-groups do not exist as a result of the strong 'trans effect' of the terminal M-O bond resulting in dissociation from the cluster.[66]

There are many variations to the polyoxometalate structure but essentially all derive from three parent structures as described by Pope and Muller.[41] The central polyhedron (XO_n) of the parent structures are a tetrahedron (n =4), octahedron (n = 6) and an icosahedrons (n = 12) and in each case the adopted symmetry of the parent structure is the same as that of the central polyhedron. The tetrahedron and icosahedrons centred structures, known as the Keggin and Dexter-Silverton structures respectively are well known in the field polyoxometalates. However the

octahedron centred structure has yet to be isolated, for reasons that are not truly understood, but believed to originate for electrostatic restrictions.[41] It should be noted that derivatives of this unidentified structure have been isolated namely the Anderson-Evans anion.

The polyoxometalate series is not limited to the already named structures, but can be expanded to much larger dimensions. Based upon the lacunary derivatives of the Keggin and Wells-Dawson, there is the 'sandwich' structure which consists of two trivacant A-type $\{XM_9\}$ (Keggin) or $\{X_2M_{15}\}$ (Wells-Dawson) units linked by transition metal cation linkers.[67] There are also reports of much larger structures such as the 'crown' or 'wheel' structure[68] and the closely related Preyssler $[NaP_5W_{30}O_{110}]^{14-}$ anion.[69] Finally, polyoxometalates have been used to successfully synthesis supramolecular structures containing 3d and 3f metallic centres.[70] The review by Cronin[71] gives an excellent insight into the building blocks of large polyoxometalate structures as well as synthetic strategies.

1.1.3.1 Keggin Structure

The Keggin structure is represented by the general formula $[XM_{12}O_{40}]^{x-8}$ where X is the heteroatom and x is the oxidation state of heteroatom in question.[2] As stated above, the addenda atom is commonly, but not limited to, either Mo^{6+} or W^{6+}. The Keggin structure was the first fully characterised polyoxometalate[21] and is probably the most well know of the parent structures.[2] The structure is classed as a quasi-spherical molecule with a diameter of approximately 1.2 nm with a tetrahedron, XO_4, at its centre surrounded by four M_3O_{13} groups (triads). Each triad is situated at the end of one of the corresponding XO_4 vertices and is formed by three edge sharing MO_6 octahedra each sharing a common oxygen with the central tetrahedron. The four triads are connected by corner sharing bridging oxygen's. The oxygen atoms present within the structure are divided in to four sub categories which consist of: twelve terminal M=O, twelve edge bridging M-O-M which form the M_3O_{13} triad, twelve corner bridging M-O-M which connect the four triads and four internal X-O-M connecting each of the four triads to the central hetero atom.

From a geometrical point there are five possible isomers proposed by Baker[72]. The α isomer is the most thermodynamically stable and is the dominant isomer[73] with an

overall T_d symmetry. The remaining isomers are a result of a 60° rotation of each M_3O_{13} triad about its three-fold axis leading to the β (C_{3v}) ,γ (C_{2v}), δ (T_d), and ε (C_{3v}) isomers (Figure 1.1). Substitution of one of the addenda atoms for a second type of metal centre e.g. vanadium, can lead to the existence of positional isomers increasing the number of possible polyoxometalate species. For example, in $[PV_2Mo_{10}O_{40}]^{5-}$, the α-structure has five positional isomers and the β structure has 14 positional isomers which increases with further substitution of the molybdenum centres. The existence of these positional isomers has been studied and confirmed by NMR and ESR spectroscopy.[74]

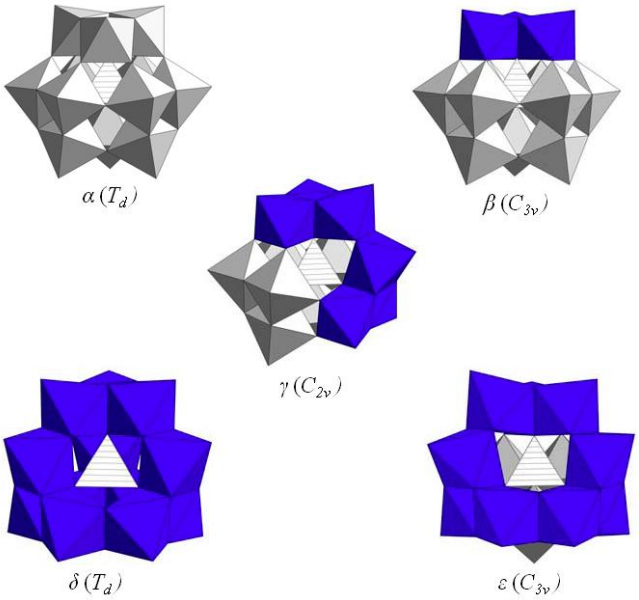

Figure 1.1: The structures of the five Baker-Figgis isomers of the parent Keggin anion $[XM_{12}O_{40}]^{x-8}$

It is possible to remove one, two or even three of the MO_6 octahedra from the Keggin structure, resulting in a 'defective' or lacuanry Keggin.[1,2] The removal of these octahedra can be achieved through controlled hydrolysis with the addition of a sufficient base under certain conditions (temperature, ionic strength, concentration). The Keggin structure is only stable at low pH ranges and, upon increasing the pH, a complex series of hydrolysis reactions occur. The lacuanry Keggin are typically only stable in specific pH ranges and increasing the pH results in the mono, bi, and tri vacant lacuanry species being formed. The mono and bivacant species can be used as precursors to form mixed Keggin materials, consisting of more than one type of addenda atom. The trivacant species can be formed by either the loss of corner

shared group of MO_6 octahedra termed A-type or by the removal of a complete M_3O_{13} triad termed B-type. The trivacant species can be used as the building blocks to larger polyoxometalates, either directly or by the incorporation of 'linkers'.

The work in this thesis solely focuses upon the applications of Keggin type polyoxometalates as potential catalyst for FlowCath® technology. However it should be noted that the polyoxometalate series is not just limited to Keggin motif. The other parent structures and derivatives are briefly highlighted below.

1.1.3.2 Wells-Dawson Structure

The Wells-Dawson anion is a derivative of the parent Keggin with the general formula $[X_2M_{18}O_{62}]^{2x-16}$ shown in Figure 1.2. The structure was first synthesised by Kehrmann[75] in 1892, but the crystal structure was only solved 60 years later by Dawson.[76] The structure is constructed from two A-type lacuanry Keggin species (green segments, Figure 1.2) directly linked across the lacunae (red segment, Figure 1.2). The Wells-Dawson structure does show some isomerism with a 60^o rotation of the M_3O_{13} triad resulting in the β isomers. The Wells-Dawson structures, like the Keggin, can be chemically manipulated to form defects with up to six MO_6 octahedra being removed. These defects can then be filled with by other coordinating elements (octahedral) to form substituted structures or, analogous to the trivacant Keggin, they can connect directly to form larger polyoxometatle structures.

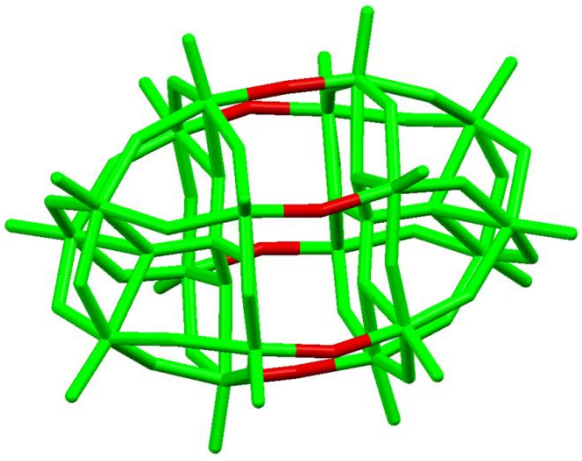

Figure 1.2: The structure of the Wells-Dawson anion $[X_2M_{18}O_{62}]^{2x-16}$. Green segments represent the two A-type $\{XM_9\}$ units with the direct link (red segment) across the lacunae

1.1.3.3 Anderson-Evans

The Anderson-Evans[77] structure is the derivative of the unresolved but theoretically possible $[XM_{12}O_{38}]$ anion. In this instance, the heteroatom adopts the octahedral geometry at the centre of the structure and is surrounded by six MO_6 octahedra in a ring like formation sharing edges. This particular derivative is not as well known as the Wells-Dawson or Keggin structures but is common in the molybdotellurate series, $[TeMo_6O_{24}]^{6-}$.[78]

1.1.3.4 Dexter-Silverton

The Dexter-Silverton Structure, $[XM_{12}O_{42}]^{x-12}$ where again x is the oxidation state of the of the central atom X, is a less common type of heteropoly anion containing twelve addenda atoms. At the centre of this particular structure is a polyhedron surrounded by twelve oxygen atoms forming an icosahedron. The central atom is typically a highly coordinating lanthanide or actinide namely, cerium(IV), uranium(IV) or thorium(IV).[79]

1.1.4 State and Stability in Solution

The solubility of heteropoly anions is commonly dictated by the solvation energy of the supporting cation due to low lattice and solvation energies.[2] The solubility of the heteropoly anions in aqueous solutions is extremely high with a reported weight percentage of 88, which remains high for other polar solvents such as ethyl acetate (86 wt%) and diethyl ether (85 wt%).[49] The salts of heteropolyanions which contain small cations (Li^+ or Na^+) remain highly soluble. However, when substituted for large cations ($K^{+,}$ Cs^+) or organic derivatives (tetrabutylammonium), the salts are insoluble.[2] Large cations are frequently used to isolate heteropolyanions from solution.[2]

Polyoxometalate chemistry has traditionally been studied in aqueous media with non-aqueous chemistry somewhat under developed in comparison. For the basis of the work in this thesis, only aqueous based polyoxometalates are considered, but we do not disregard the importance of the non-aqueous based chemistry for other applications.[19] The quasi-spherical Keggin anion which is shown to have an extremely low negative charge density upon the peripheral oxygens and the exterior

(bridging and terminal oxygens) only forms weak hydrogen bonds. This evidently leads to the heteropoly anions only being weakly solvated in solution.[1,2]

The speciation of a polyoxometalate when in solution is complex with multiple species existing in a dynamic equilibrium with the position of said equilibrium being strongly dependent upon the final pH.[8] Pettersson et al. studied the speciation of the hydrogen molybdate – phosphate system across an extended pH and concentration range via ^{31}P NMR.[80] The system was much more complicated than first thought and showed that solutions containing $[MoO_4]^{2-}$ and $[HPO_4]^{2-}$ in a 12:1 ratio contained more than a single specie at a given pH. At low pH (< 1.5), the 12:1 species dominates the solution, although there is a significant amount of the 9:1 specie present. Upon increasing the pH (1.5 < pH < 5), the monovacant lacunary species dominates, as a result of the Keggin being subject to hydrolysis. Above pH 5, the Keggin structure is completely hydrolysed and only the single oxoanion species exist. Pettersson and Grate expanded this work to a ternary Keggin system consisting of protons, molybdate, phosphate and vanadate anions.[80] The system explored contained $[MoO_4]^{2-}$, $[VO_4]^{2-}$ and $[HPO_4]^{2-}$ in a 9:3:1 ratio maintaining the 12:1 ration (with respect to total addenda atoms) for a Keggin structure. The analysis showed the system was dominated by the $\{PMo_9V_3\}$ anion with the most dominant isomers identified at low pH. The system also showed the presence of the $\{PMo_{10}V_2\}$ and $\{PMo_{11}V\}$ anions showing the increased complexity in speciation of the mixed addenda system. The ratio of the $\{PMo9V_3\}$, $\{PMo_{10}V_2\}$ and $\{PMo_{11}V\}$ species in equilibrium changes with pH with the evidence of the distribution of species changing as pH is increased. This evidently leads to the $\{PMo_9V_3\}$ species (and its isomers) no longer dominating the system at higher pH.

The stability of the Keggin heteropoly anions in aqueous solutions is strongly dependent upon the addenda atom(s) incorporated into the structure.[8,49] Considering the three main addend atom types, tungsten, molybdenum and vanadium the corresponding stability towards hydrolysis decreases in the order:

$$W^{(6+)} > Mo^{(6+)} > V^{(5+)}$$

The stability of the molybdenum based heteropoly anions is also dependent upon the heteroatom, decreasing in the order:

$$Si^{(4+)} > Ti^{(4+)} > Zr^{(4+)} > Ge^{(5+)} > P^{(4+)} > As^{(5+)}$$

Tsigdinos showed that12-Molybdophsphate is stable in solution at pH < 1.5 but is subject to alkaline hydrolysis as pH is increased.[49] At concentrations below 1 mM the hydrolysis occurs via the formation of the monovacant lacunary species (equation 1.2), which is then subject to further hydrolysis resulting in the much smaller molybdophosphate species (Strandberg structure).

$$[PMo_{12}O_{40}]^{3-} \rightleftharpoons [PMo_{11}O_{39}]^{7-} + MoO_4^{2-} \rightleftharpoons H[P_2Mo_5O_{23}]^{5-} + MoO_4^{2-} \quad (1.2)$$

The decompositon of the initial Keggin structure will continue as the pH increases untill the structure as been complety hydrolysed back to its simple oxoanions. The alkaline hydrolysis of the Keggin structure is also apparent at higher concetrations but proceeds via the formaiton of the Wells-Dawson derivative $[P_2Mo_{18}O_{62}]$ as an intermediate. Although the trivacant $\{PMo_9\}$ lacuanry species is present in solution and stable above pH 1.5, the formation of the dimeric Wells-Dawson derivative is slow.[80] This slow formation leads to the applciaiton of the trivacant lacuanry species as building blocks for mixed addenda polyoxometatle structures.[2] Increased solution stability can be achieved in organic media with polyoxometalates stable towards solvolysis at concetrations as low as 10^{-6} M.[2]

The mixed addenda Keggin structures have been previously studied and show a small increase in stability with the substitiouon of a single molybdneum(VI) for vanadium(V).[8] This is possibly due to a decrease in the overall steric strain upon the Kegign structure. Further substituion of molybdneum for vandium further decreases its solution stablilty in the order $\{PMo_{11}V\} > \{PMo_{10}V_2\} > \{PMo_9V_3\}$.[2,8] The mixed addenda system show an increased vulnarability to alkaline hydrolysis due to the incorporation of vandium, but also readily undergo acid hydrolysis in dilute (0.8 M) HCl.[2,81] Courtin[82,83] showed that increases in acidity results in the anions $\{PMo_{12-n}V_nO_{40}\}$ with n > 1 to lose vanadiums resulting in lower substitued heteroply anions. Between pH 1 and 3, the $\{PMo_{12-n}V_nO_{40}\}$ anions disporportionate and this has also been observed in tungston derivative.[84]

1.1.5 Acid Properties

1.1.5.1 Protonation Sites

The Keggin and Wells-Dawson heteropoly acids are classified as (strong) Brønsted acids, i.e. they donate protons.[1,4,27] The acid properties of the structures has been well documented over the years by Kozhevnikov,[4,27,28,60] Misono[3,] and Odyakov.[11,54,55] Here, we will briefly cover the acid properties of the Keggin structures.

The Keggin anion structure has two differing outer oxygen sites that can potentially undergo protonation; the terminal oxygen M=O present on each addenda atom and bridging oxygens (both edge and corner sharing). The specific oxygen site where protonation occurs has been studied in great detail by Kozhevnikov and co workers [85-87] with a more recent computational study by Neumann[47] investigating both the vanadium substituted and non-substituted phosphomolybdates. It was shown that the bridging oxygen atoms have a higher electron density in comparison to the terminal oxygen sites thus favouring protonation. Molecular orbital calculations showed that the bridging oxygens are more basic, hence favouring protonation. In the 12-heteropoly anions consisting of $[MoO_4^{2-}]$ and $[HPO_4]^{2-}$ in a 12:1 ratio, protonation occurs at the farthest bridging position from the metal (addenda) centre. However, in the vanadium substituted heteropoly anion the vanadium bound bridging oxygens show a higher proton affinity, resulting in protons bound to the nucleophilic sites around the vanadium atom.[47] This protonation cause a destabilization of the oxo-vandium bonding within the Keggin unit. These findings however were based upon calculations assuming a free Keggin in the gas phase; the protonation sites will vary in the solid phase. In this instance, the energy of the solid crystal lattice is considered as well as the basicity of available oxygens hence the terminal oxygens may undergo protonation.[2]

1.1.5.2 Behaviour in Solution

The solution properties of the heteropoly acids have been studied by Kozhevnikov[2,85] and more recently Okyakov,[59,60,88] focusing upon the mixed addenda (molybdenum and vanadium) heteropoly acids. Kozhevnikov characterised the acidic properties of a series of heteropoly acids in terms of their Hammett acidity function and dissociation constant. In aqueous media, Kozhevnikov successfully showed that

$H_3[PW_{12}O_{40}]$, $H_3[SiW_{12}O_{40}]$ and $H_3[PMo_{12}O_{40}]$ are fully dissociated and thus behaviour is analogous to that of a strong acid. It should be noted that Pope identified that the $[SiW_{12}O_{40}]^{4-}$ and $[PW_{12}O_{40}]^{3-}$ heteropoly acids remain fully dissociated even after being reduced by two and three electrons respectively.[89] Kozhevnikov measured the dissociation constants of a series of heteropoly anions (Table 1.1), but limited to only those with more than three protons due to no step-wise dissociation being observed for $H_3[PW_{12}O_{40}]$, $H_3[SiW_{12}O_{40}]$ and $H_3[PMo_{12}O_{40}]$ due to the solvent levelling effect. The use of organic solvents can overcome the levelling effect associated with water and allow for the differing pK_a of the respective dissociations to be studied in polyprotic acids.[90]

Table 1.1: Experimental dissociation constants of heteropoly acids at a) 25 ^{o}C and b) 20^{o}C in water.

Heteropoly Acid	pK_4	pK_5	pK_6	pK_7	pK_8
$H_5[PMo_{10}V_2O_{40}]^a$	1.2	2.1	-	-	-
$H_6[PMo_9V_3O_{40}]^a$	1.3	1.6	2.0	-	-
$H_8[NpMo_{12}O_{40}]^b$	3.2	3.4	3.6	4.3	5.7
$H_8[CeMo_{12}O_{40}]^b$	-	2.1	2.0	3.0	4.2

It should be noted that in organic solvents the $H_3[PW_{12}O_{40}]$, $H_3[SiW_{12}O_{40}]$ and $H_3[PMo_{12}O_{40}]$ heteropoly acids are no longer fully dissociated and thus no longer behave as a strong acid.[27]

The effect of the heteroatom upon the acid properties is essentially very weak despite that the respective acids of the individual heteroatoms can significantly differ (Table 1.2). The heteropoly acids however, are much stronger than the corresponding individual acids of the heteroatoms.[2] The reason for this is likely due to the heteropoly anion containing increased number of external oxygens that can sufficiently delocalise the increased charge of the anion upon dissociation.[27]

It is known that the tungsten derivatives of the Keggin motif are a stronger acid than there molybdenum counterparts, with the strongest acid being $H_3[PW_{12}O_{40}]$.[27] However, upon reduction acidity decreases hence why the tungsten based heteropoly acids are preferred for acid catalysis compared to the molybdenum counter parts due to their reduced oxidising ability.

Table 1.2: First dissociation constants for some common polyprotic acids in water at 25 ^{o}C. [90]

Acid	pK_1
H_2SO_4	-3
H_2SO_3	1.81
H_3PO_4	2.12
H_2S	6.88

The theory on the order of acidity of various heteropoly acids was supported by Izumi[91] who presented the following order of decreasing acidity based upon the chemical shift of hydroxyl protons in chloral hydrate ($Cl_3C_2H(OH)_2$):

$$H_3[PW_{12}O_{40}] > H_3[PMo_{12}O_{40}] > H_3[SiW_{12}O_{40}] \approx H_3[GeW_{12}O_{40}] > H_3[SiMo_{12}O_{40}]$$

1.1.6 Applications: Catalysis by Polyoxometalates

Polyoxometalates are very unique in the sense that they have been shown to be extremely useful in a number of applications as covered in a series of reviews and special editorial editions, although catalysis is by far their most important application.[4,6,92-94] The heteropoly acids have many advantages and are well known for have many functionalities as well as unique structural mobility.[2] The heteropoly acids have been employed as homogenous and heterogeneous catalysts for a series or organic reactions:[92-94,95]

- Alkylation
- Hydration of Alkenes
- Esterification
- Condensation
- Friedel Crafts
- Hydrolysis
- Beckmann rearrangement
- Diels-Alder reaction

The general principle of heteropoly acid catalysed reactions is that they can be expressed by the mechanism of Brønsted acid catalysis.[94,97] The general mechanism involves the protonation of the reactant (supplied form the dissociated heteropoly acid) to form a protonated intermediate which then undergoes dissociation to yield

the relevant products. The catalytic activity is pH dependent with the more acidic heteropoly acids showing a higher catalytic activity, this is related to the effectiveness of the acids as proton donors.

Although the heteropoly acids and there salts are used in a wide range of reactions and applications, in this work we focus upon their applications as electrocatalysts for the indirect reduction of oxygen.

1.1.6.1 Polyoxometalates in Electrochemical Reactions

It has been observed over the preceding sections that a wide variety of polyoxometalates can be used for catalysis. However, there has been limited use of these structures specifically for electrocatalysis.[96] Electrocatalysis is 'the relative ability of different substances, when used as/at electrode surfaces under the same conditions, to accelerate the rate of a given electrochemical process'.[111] The applicability of reduced heteropoly acids (and salts) as electrocatalysts for oxygen reduction is well documented (see section 1.1.6.2).

The redox ability of polyoxometalates is related to their molecular structure and can be divided into two subgroups based upon the addenda atoms displacement in the MO_6 octahedra.[1] In Type I or 'mono-oxo' structures, the addenda atom is always displaced towards a single, terminal oxygen atom whilst in Type II or 'cis-oxo' structures, the addenda atom is displaced towards two cis, usually but not always, terminal oxygens.[1] The two categories exist to distinguish between polyoxometalates that demonstrate reversible (Type I) and irreversible (Type II) electrochemical redox processes. Conveniently, the various structural types (see section 1.1.3) can be divided into these subgroups with Keggin, Wells-Dawson and their derivatives showing type I behaviour with only a single terminal oxygen present on each addenda atom. The Dexter-Silverton structure however contains two 'cis' terminal oxygens on each addenda atom and falls into the type II category.[1]

The reversibility of the redox process is dictated by the character of the lowest unoccupied molecular orbital (LUMO) i.e. does it have non-bonding or anti-bonding character. In the type I structure, the dz^2 and $dx^2 - y^2$ orbital's are antibonding, *dxy* and *dxz* are antibonding π component of the terminal oxygen bond and the *dxy* orbital

is essentially non bonding though may have some antibonding character depending upon the extent π-bonding interaction between the metal centre and the equatorial oxygens. In this instance, the LUMO is the nonbonding *dxy* orbital and occupation of this orbital by a single electron (or two) will have little effect upon the structure. However, in type II structures, the conversion of a single equatorial oxygen to a second terminal oxygen changes the *dxy* orbital character from non-bonding to antibonding. In this instance, the LUMO is now the antibonding *dxy* orbital. This theory is supported by Keggin structures undergoing reversible redox processes in which the oxidised state is isostructural to the reduced state in which one or more addenda atoms have a d^1 electron configuration.[1,2,6,8] On the other hand, the type II structures are irreversibly reduced with greater difficulty yielding structures which are no longer isostructural to their oxidised state. Based on this, only type I structures are considered suitable electrocatalysts for this work.[1,39,97]

The nature of the anion structure and charge as well and the nature of the addenda and heteroatom strongly dictate the redox potential of the type 1 polyoxometalates with particular emphasis laid upon the Keggin structure. It has been shown for the Keggin structure that the anion charge has the greatest influence upon the redox potential. This is supported by the work of Barteau et al.[104]who showed that heteroatoms that are not redox active can affect the oxidative ability of the Keggin structure. Substitution of heteroatoms with an increasing positive ionic charge reduces the overall anion charge. Hill and Musaev also showed similar trends in heteroatom substitution based on computational studies of substituted Keggin structures.[98]

Type I heteropoly anions can undergo multiple reversible one and two electron reductions resulting in the reduced 'heteropoly blues', conveniently named after the deep blue colour observed upon reduction.[2] In the case of only a single addenda atom type, then the electrons are delocalised on the addenda atoms octahedral at room temperature by rapid intermolecular electron transfer or electron hoping. At room temperature, the single addenda atom Keggin structures are electron spin resonance (ESR) silent with no observable/broad featureless lines are identified. However, upon cooling (< 60 K) these lines narrow and show the characteristics of $Mo^{(V)}/W^{(V)}$ metal centres as a consequences of the decreased rate of intermolecular electron hoping.[97]

The oxidation potentials of the polyoxometalates can be affected by the substitution of the heteroatom as previously seen, but to a greater extent, by the substitution of the addenda atom. The overall oxidising ability of the mixed addenda heteropoly anion can be arranged based upon the oxidising ability of the corresponding addenda atoms that make up the complete structure. The addenda atoms can be arranged in order of decreasing oxidising ability:

$$V^{(5+)} > Mo^{(6+)} >> W^{(6+)}$$

In the instance of reduced mixed addenda Keggin structures, the electrons are no longer delocalised over the entire structure but remain localised on the more reducible metal centre (at room temperature).[97] In the case of substituted or mixed addenda Keggin polyoxometalates the newly incorporated metal centre is commonly the active site for the catalytic reaction of interest.

The mixed addenda polyoxometalate series of the general formula $\{PMo_{12-x}V_xO_{40}\}$ have been studied in great detail in connection with their applications for catalytic oxidation[2,27-31,86,87,94] but also their redox properties have been well documented.[1-6,8,9,11] Weinstock's review[99] on homogenous-phase electron transfer in polyoxometalate structures is the most comprehensive review covering outer-sphere electron transfer mechanism, polyoxometalate self exchange, oxidation of organic and inorganic electron donors as well as reduction of oxygen by reduced polyoxometalates. The latter is by far the most remarkable feature of the vanadium substituted Keggin structures and is expanded in section 1.1.6.2.

1.1.6.2 Oxygen Reduction Catalysed by Phosphomolybdovanadates

The type I mixed addenda Keggin anions of the general formula $[PMo_{12-x}V_xO_{40}]^{(3+x)-}$ are the most effective and versatile polyoxometalate systems for the liquid phase oxidation by oxygen.[28,94,100-103] Matveev et al. were the first to employ these mixed addenda systems as liquid phase oxidation catalysts.[100] Although the vanadium substituted Keggins are the most common derivatives for this oxidation process, there have been attempts and Neumann co workers[46] to use ruthenium substituted polyoxometalates for activation of molecular oxygen.

For liquid phase oxidation, x is usually between 2 and 6 in $[PMo_{12-x}V_xO_{40}]^{(3+x)-}$ with the polyoxometalate catalysed reaction mechanism being represented by a stepwise redox mechanism. The stepwise process is highlighted in equations 1.3 and 1.4 with an initial reduction of the oxidised polyoxometalate species (POM_{ox}), which is accompanied by a stoichiometric protonation step to balance the increased anionic charge. This is followed by the reduction of O_2 via the reduced polyoxometalate (POM_{red}).

$$\left[PMo_{12-x}V_x^{(5+)}\right] + n\,e^- + n\,H^+ \longrightarrow H_n\left[PMo_{12-(x+n)}V_{x-n}^{(5+)}V_n^{(4+)}\right] \quad (1.3)$$

$$H_n\left[PMo_{12-(x+n)}V_{x-n}^{(5+)}V_n^{(4+)}\right] + {}^{n}/_{4}\,O_2 \longrightarrow \left[PMo_{12-x}V_x^{(5+)}\right] + {}^{n}/_{2}\,H_2O \quad (1.4)$$

The stoichiometric electron reduction of the POM_{ox} species can be achieved either by oxidation of a substrate or a direct electrochemical reduction at an electrode surface to yield the POM_{red} species. It is evident that the $V^{(V)}$ redox centre is essential to the mechanism thus rendering the 12-molybodphosphate anion inactive under mild conditions as well the mono substituted $[PMo_{11}VO_{40}]^{4-}$ anions due to the one electron reduction of O_2 being thermodynamically unfavourable.[2] When a substrate is used in equation 1.3, it is common for safety reasons to ensure that the reduction and oxidation reactions, equations 1.3 and 1.4 respectively, are carried out in separate vessels.[2] This can also be achieved when equation 1.3 is carried out via an electrochemical process, which would be reminiscent of fuel cell processes.

A consideration of the thermodynamic conditions for equations 1.3 and 1.4 to be successful can be explained on the basis of redox potentials. For this to be successful, the redox potential of the substrate (or electrode) must be less than that of the POM_{ox} species which in turn must be less than that of oxygen (O_2). To be clear, by "less", we are referring to the fact that the redox potential must be more negative than the redox potential of the species being reduced under the conditions employed and hence have a reduced tendency to accept electrons. Considering the simple case of an electrochemical reduction at an electrode surface, we can simply consider the thermodynamics of the POM_{ox} which has a reduction potential of approximately 0.7 V vs. standard hydrogen electrode where n = 1- 4.[58,104] The standard reduction

potential for the four electron reduction O_2 is 1.23 V vs. standard hydrogen electrode at 25 ^oC and 1 atm. Thermodynamically equations 1.3 and 1.4 are achievable.

The reduction of oxygen in acidic aqueous media does not just occur via a four electron process. Table 1.3 highlights the possible mechanistic pathways for oxygen reduction and their corresponding standard reduction potentials. It can be seen that the two, three and four electron reductions are all thermodynamically feasible, however, based on the argument outlined above the one electron reduction of oxygen is not a feasible process.

Table 1.3: Possible mechanistic pathways for the reduction of O_2 in acidic aqueous solutions and the associated standard reduction potentials (E^o) for each pathway.

Mechanism	E^o (vs. SHE)
$O_2 + e^- + H^+ \longrightarrow HO_2^\bullet$	- 0.05 V
$O_2 + 2e^- + 2H^+ \longrightarrow H_2O_2$	0.68 V
$O_2 + 4e^- + 4H^+ \longrightarrow 2H_2O$	1.23 V
$HO_2^\bullet + e^- + H^+ \longrightarrow H_2O_2$	1.44 V
$H_2O_2 + e^- + H^+ \longrightarrow HO^\bullet + H_2O$	0.71 V
$H_2O_2 + 2e^- + 2H^+ \longrightarrow 2H_2O$	1.76 V
$HO^\bullet + e^- + H^+ \longrightarrow H_2O$	2.81 V

Matveev et al. showed that the mechanism by which equation 1.4 was achieved was highly dependent upon the degree of reduction.[100] They successfully demonstrated that the highly reduced $\{PMo_8V_4^{(4+)}O_{40}\}$ was oxidised via the four electron reduction of oxygen involving the formation of an intermediate complex between the reduced POM and oxygen.[2] This was supported by the evidence of no acetone being formed when the reduction of O_2 was carried out in the presence of the highly reduced $\{PMo_8V_4^{(4+)}O_{40}\}$catalyst (in the presence of a radical scavenger (i-PrOH)).

Kozhevnikov extended this work to study weakly reduced polyoxometalates which contain only a single 'blue' electron e.g. $\{PMo_9V_2^{(5+)}V^{(4+)}O_{40}\}$. It has been explained that the one electron reduction of oxygen is not feasible. Kozhevnikov proposed the electron exchange between the one electron reduced species forming a three electron reduced species:

$$2\left[PMo_9V_2^{(5+)}V^{(4+)}\right] \longrightarrow \left[PMo_9V^{(5+)}V_2^{(4+)}\right] + \left[PMo_9V_3^{(5+)}\right] \quad (1.5)$$

$$\left[PMo_9V_2^{(5+)}V^{(4+)}\right] + \left[PMo_9V^{(5+)}V_2^{(4+)}\right] \longrightarrow \left[PMo_9V_3^{(4+)}\right] + \left[PMo_9V_3^{(5+)}\right] \quad (1.6)$$

The three electron reduced species is then slowly oxidised by oxygen.[2] Kozhevnikov also showed that the rate of oxidation for the weakly reduced $\{PMo_{10}V_2\}$, $\{PMo_9V_3\}$ and $\{PMo_8V_4\}$ occurred in the following order:

$$\{PMo_{10}V_2\} < \{PMo_9V_3\} > \{PMo_8V_4\}$$

This order was explained by the $\{PMo_{10}V_2\}$ species undergoing a disproportionation reaction prior to oxidation forming the more active $\{PMo_9V_3\}$ species.[2,94] The reduced kinetics of the $\{PMo_8V_4\}$ was explained by the reduced stability of this specie in solution.[2,94]

1.1.8 Applications in Proton Exchange Membrane Fuel Cells

Polyoxometalates have already proven that they are a practical and efficient alternative to some common fuel cell components with their initial application centred on proton exchange membranes.[105-108] The interest in these structures for potential fuel cell application was first reported by Nakamura[109] who demonstrated that conductivities of 0.2 S cm^{-1} were achievable with 12-tungstophosphoric acid. Although to achieve this level of conductivity the heteropoly acid is required to be in its solid, fully hydrated crystalline state. The reported high proton conductivity and high thermal stability[2] makes them a suitable candidate for the replacement of perfluorosulfonic acid membranes in high temperature proton exchange membrane fuel cells. However, heteropoly acids in their crystalline state have proven unstable in room temperature fuel cells due to them being readily soluble in aqueous media[2,109] More recent work by Trowbridge[110] investigated the effect of charge and counter ion type upon the conductivities.

Work by Herring et al.[105-108] has shown that heteropoly acids and their salts can have applications in fuel cell technology. In collaboration with Xcel Energy, Herring investigated the possible application of the mixed addend $[PMo_{12-x}V_xO_{40}]^{(3+x)-}$, iron substituted Well-Dawson structures $[(P_2W_{17}O_{61})Fe^{(III)}(H_2O)]$ and

$[(P_2W_{17}O_{61})Fe^{(III)}_4(H_2O)_2]$ as both anode and cathode catalysts. In all cases, the heteropoly acid/salt were incorporated as catalysts by adsorption onto Vulcan XC-72 carbon electrodes. In the case of the mixed addenda system, Herring reported these systems can be used as potential cathode catalysts but require much higher loadings and possible chemical modification which is not suited to the Vulcan carbon used. This work opens the door for the exploration of these mixed addenda systems as potential cathode catalysts to replace platinum based materials.

1.2 Fuel Cells

1.2.1 Why do we need Fuel Cell Technology?

The formation of fossil fuels occurs via a natural process through the decomposition of plants and organisms over a period millions of years and currently account for 80% of the world energy demand.[111] The argument of 'when' fossil fuel will run out is a long standing question, with the US producing reports showing increases in oil and natural gas reserves.[112] This is alongside the discovery of new reserves in Australia (reported January 2013) containing up to 233 billion barrels of oil and the introduction of new hydraulic fracturing techniques to remove gas trapped in shale. Although this looks promising, it is estimated that 'proven' oil, gas and coal reserves will run out by the year 2055, 2072 and 2128 respectively.[113] Based on this information, it is unlikely that fossil fuels will run out in this author's life time, but nonetheless, is a problem that cannot be left for future generations to fix.

Apart from the clear issue of fossil fuel supplies potentially running out, the consequences of using fossil fuels upon global warming are a much bigger issue. Global warming is described as a warming of the Earth's temperature climate system and is strongly linked to the increased concentrations of green house gasses (CO_2, CH_4, N_2O) and chlorofluorocarbons or (CFC's) produced from burning of fossil fuels and deforestation.

Hydrogen is potentially one the cleanest fuel sources with combustion in air producing only water, theoretically achievable in the hydrogen internal combustion engine vehicle (HICEV). Although, due to natural air containing a mixture of other gases such as N_2, it is possible that nitrous oxides will be formed. Hydrogen is a

unique gas and can be converted into electrical energy in a fuel cell via an electrochemical process with a higher efficiency than the conversion of fossil fuels to both mechanical and electrical energy respectively.

1.2.2 Fuel Cells: Overview

A fuel cell is described as an 'electrochemical energy converter which takes fuel as an input and produces electricity via a series of electrochemical processes'.[114,115] Generally in fuel cell technology, the reactants for the individual anodic and cathode reactions are fed into the respective chambers, separated by a conducting electrolyte layer. Electrons are created during the half cell reaction at the anode which are then transported, via an external circuit, to the cathode. The ions formed at the anode are transported through the conducting electrolyte media where they react with the cathodic reactants and electrons to produce water. (Figure 1.3).[114]

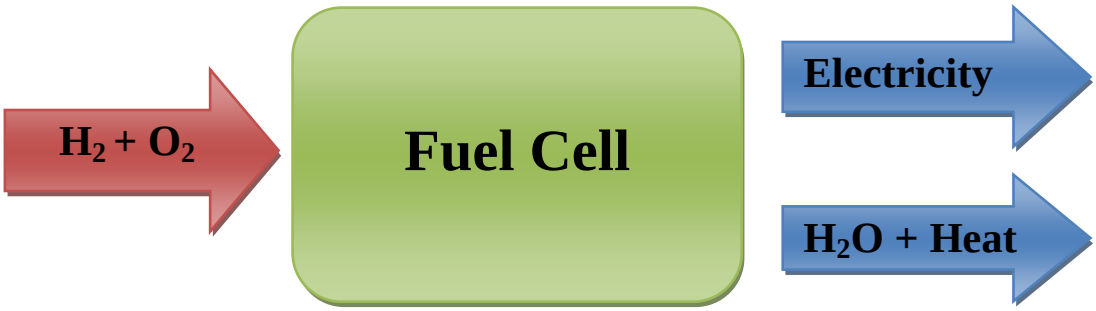

Figure 1.3: General concept of a hydrogen oxygen fuel cell.[114]

If we consider a simple hydrogen oxygen fuel cell in which the half cell equations for the anode and cathode are illustrated in equation 1.7 and 1.8 respectively with the overall reaction illustrated in equation 1.9.

$$2\,H_2 \longrightarrow 4\,H^+ + 4\,e^- \qquad E^o = 0 \text{ V vs. SHE (1.7)}$$

$$O_2 + 4\,H^+ + 4\,e^- \longrightarrow 2\,H_2O \qquad E^o = 1.23 \text{ V vs. SHE (1.8)}$$

$$2\,H_2 + O_2 \longrightarrow 2\,H_2O \qquad E^o_{(cell)} = 1.23 \text{ V vs. SHE (1.9)}$$

Considering the standard reduction potential for the two half cell equations (1.7 and 1.8), we can determine if the process in equation 1.9 is thermodynamically feasible based upon the Gibbs free energy. The standard Gibbs free energy, ΔG^o, is related to

the standard potential of the fuel cell, $E^{o}_{(cell)}$ by equation 1.10:

$$\Delta G^{o} = -nFE^{o}_{cell} \quad (1.10)$$

where n is the number of electrons transferred, F is faradays constant and $E^{o}_{(cell)}$ is the standard potential adopted by the fuel cell based upon the individual standard potentials of the individual oxidation and reduction processes (equation 1.11).

$$E^{o}\,(cell) = E^{o}_{reduction} - E^{o}_{oxidation} \quad (1.11)$$

The positive $E^{o}_{(cell)}$ equates to a negative Gibbs free energy which is indicative of a spontaneous reaction thus equation 1.9 is thermodynamically feasible. In a typical fuel cell, the overall efficiency for converting chemical energy into electricity is around 40 to 70 %. This is a significant improvement upon the 30 % efficiency of typical combustion engines.[114,115]

1.2.3 Fuel Cell Types

Fuel Cells come in various shapes, sizes and 'models' with the shape and size normally dictated by the number of cells compiled in a stack. The 'models' refers to the different types of fuel cells available and are commonly differentiated by the electrolyte used although there are other important differences. Table 1.4 illustrates the criteria data for each of the differing fuel cell types including the mobile ion within the electrolyte, operating temperature range, catalyst and fuel supply required. [114,115]

Table 1.4: Fundamental characteristics for the main fuel types.

Fuel Cell Type	Mobile ion	Operating Temperature	Catalyst	Fuel
Phosphoric acid	H^{+}	200 ^{o}C	Platinum	H_2
Alkaline	OH^{-}	60 – 220 ^{o}C	Platinum	CH_3OH
Molten carbonate	CO_3^{2-}	650 ^{o}C	Nickel	H_2, CH_4
Solid Oxide	O^{2-}	600 – 1000 ^{o}C	Perovskites	H_2,CH_4,
PEM	H^{+}	80 - 100 ^{o}C	Platinum	H_2

Phosphoric Acid Fuel Cell (PAFC): The phosphoric acid fuel cell uses concentrated liquid H_3PO_4, carbon based electrodes and expensive platinum catalysts. The fuel cell operates at very high temperatures in a bid to boost the rate of the anodic and cathodic reactions. At this time, PAFC's are well used across the USA and Europe with many 200 KW systems employed for terrestrial use.[114,115]

Alkaline Fuel Cell (AFC): The AFC produces electricity through the redox reaction involving hydrogen and oxygen, but is different from the example outlined in section 1.4.2. In this instance, hydrogen is oxidised at the anode by reaction with hydroxide anions from the electrolyte (equation 1.12) releasing electron and simultaneously forming water. The electrons travel via an external circuit to the cathode where they react with oxygen in the presence of water to form hydroxide anions (equation 1.13).[114,115]

$$2\,H_2 + 4\,OH^- \longrightarrow 4\,H_2O + 4\,e^- \quad (1.12)$$

$$2\,H_2O + O_2 + 4\,e^- \longrightarrow 4\,OH^- \quad (1.13)$$

It is essential that the electrolyte be an alkaline solution to provide hydroxide anions for the anodic reaction with sodium or potassium hydroxide commonly used.[115]

Molten Carbonate Fuel Cell (MCFC): The MCFC is a high temperature fuel cell, operating above 600 ^oC with a molten mixture of alkali metals, typically consisting of Li, Na or K carbonates held within a ceramic matrix. The high temperature results in the molten mixture forming a highly conductive molten salt with carbonate ions (CO_3^{2-}) being the mobile ions within the electrolyte. The anodic reaction again involves the oxidation of hydrogen (in the presence of carbonate ions) realising electrons, water and carbon dioxide (equation 1.14). The corresponding cathodic reaction involves the reduction of oxygen in the presence of carbon dioxide forming carbonate anions (equation 1.15). [114,115]

$$2\,H_2 + 2\,CO_3^{2-} \longrightarrow 2\,H_2O + 2\,CO_2 + 4\,e^- \quad (1.14)$$

$$O_2 + 2\,CO_2 + 4\,e^- \longrightarrow 2\,CO_3^{2-} \quad (1.15)$$

Solid Oxide Fuel Cell (SOFC): The solid oxide fuel cell has a much simpler concept than its counterparts due to it being classed as a two phase system. The entire fuel cell is a solid state device with the electrolyte being a ceramic material that shows high conductivities for oxide ions. The SOFC functions in an analogous manner to that of MOFC with negatively charge ions transporting across the electrolyte membrane as well as water formation at the anode. The high temperature of operation (1000 ^{o}C) results in any residual water produced being used for steam reformation of fuel.[114,115]

It is clear that each individual fuel type has its own unique mechanisms for the anodic and cathodic half cell reactions. Given the varying temperatures, fuels and catalysts used, the practical uses of each fuel cell type varies along with its individual power output. As we can see from Table 1.5, each fuel cell type has its own distinguishing features with varying power outputs available as well differing application suitability. It is clear that the proton exchange membrane fuel cell has the widest range of applications and is the fuel cell of choice for this work.

Table 1.5: Table summarising the power output range, main advantages and applications for individual fuel cell type. [114]

Typical Applications	Portable Electronics			Cars, boats and domestic CHP			Power Generation (Power plants)	
Power (Watts)	1	10	100	1k	10k	100k	1M	100M
Main Advantages	Higher energy density & faster recharging			Reduced emissions & higher efficiency			Higher efficiency, reduced pollution	
Application range for individual fuel cell type	DMFC			AFC			MCFC	
						SOFC		
	PEMFC							
						PAFC		

1.2.4 Proton Exchange Membrane Fuel Cell (PEMFC)

The fuel cell was developed in the 1960's for use by NASA on the first generation of manned space vehicles,[115] providing power for life support, guidance and communications. One key feature of the fuel cell in the space program was the production of water which could be recycled to provide clean drinking water for astronauts during space flight. [115]

As illustrated in Table 1.5, the PEM fuel cell can be applied to the widest range of applications, from laptops and other portable devices to cars and home heating and power systems. The polymer electrolytes used in the membranes are unique in that they function at low temperatures resulting in short start up time for PEMFC. [115] The overall thinness of the membrane electrode assembly allows for compact fuel cell stacks increasing the power to size ratio. In conjunction with no hazardous or corrosive fluids and the ability of the fuel cell to operate in any orientation makes this an ideal candidate for portable applications.[114,115]

The anodic and cathodic half cell reactions carried out in a PEM fuel cell are outlined in equations 1.7 to 1.9, shown again here for reference:

$$2\,H_2 \longrightarrow 4\,H^+ + 4\,e^- \qquad E^o = 0 \text{ V vs. SHE} \quad (1.7)$$

$$O_2 + 4\,H^+ + 4\,e^- \longrightarrow 2\,H_2O \qquad E^o = 1.23 \text{ V vs. SHE} \quad (1.8)$$

$$2\,H_2 + O_2 \longrightarrow 2\,H_2O \qquad E^o_{(cell)} = 1.23 \text{ V vs. SHE} \quad (1.9)$$

We have already discussed the thermodynamics of the above equations an established that equation 1.9 is a viable process. Here, we will briefly consider reactions carried out at the anode and cathode highlighting the causes of catalyst degradation and reduced performance which limit PEM fuel cell technology.

1.2.4.1 PEM Fuel Cell Anode

In standard hydrogen PEM fuel cells, the hydrogen oxidation reaction (HOR) occurs at the anode:

$$2\,H_2 \longrightarrow 4\,H^+ + 4\,e^-$$

Typically, the catalyst of choice is platinum due to its high activity for catalysing the HOR, this is aafforded to a nearly optimum bonding affintiy between the platinum metal and hydrogen gas.[111,114,115] The strength of the bond (between hydrogen and platinum) is sufficent for adsorption of hydrogen on to the platinum surface, but not too strong so that the adsorbed (oxidised) H^+ species become trapped. The protons readily desorb into the elctrolyte to take part in the corresponding cathode reaction. The relative cost of platinum is high (1522 \$ oz^{-1}), but it proves to be an extremely effective catalyst. Other metals such gold, silver and copper all form weak bonds with hydrogen resulting in minimal adsorption and thus a reduction in the rate of the HOR.[114,115]

The degradation drawbacks of the paltinum catalyst at the cathode in PEM fuel cells are severe. The platinum catalyst is subject to degradation via various process. The first to be considered is platinum dissolution and growth, which when combined, results in a decrease in the active surface area of the catalyst. [114,115] When exposed to air at high potentials, platinum oxide layers are formed, resulting in an insulation layer around the platinum catalyst particles, preventing disolution.[115] However, at lower potetnials, platinum particles which are not covered in the insulating oxide layer are prone to disolution, resulting in particle growth and a decrease in the active surface area. The second degradation issue is breakdown/corrosion of the carbon based catalyst support. When the fuel cell is operated at elevated temperatures, it is possible for the carbon support to react with oxygen, forming carbon mono/dioxide which is removed from the cell through the exhaust. This carbon corrosion can be accelerated during cell startup and shut down due to the local electrode potentials reaching as high as 1.5 V.

1.2.4.2 PEM Fuel Cell Cathode

Regardless of the fuel type employed in a PEM fuel cell, the cathode reaction always involves the oxygen reduction reaction (ORR)

$$O_2 + 4\,H^+ + 4\,e^- \longrightarrow 2\,H_2O$$

Analagous to the HOR reaction, platinum is the typical catalyst used for the ORR reaction at the cathode. However, in comparison with HOR reaction, platinum is

much less active for the ORR due to a high affinity for oxygen bonding upon the platinum surface. As a consequence, much higher loadings of platinum on the cathode side are required to achieve sufficient levels of performance from the fuel cell. It is these increased loadings upon the cathode side that make PEM fuel cells an expensive energy alternatitive.[114,115]

Investigations into the effect of particle size and catlayst support opon the ORR has been done, ultimatley to reduce the total platinum content of the PEM fuel cell.[117,118] The use of platinum alloys is of major interest which show increased activity for the ORR comapred to pure platinum[114,] Although increased activity is achieved with platinum alloy catalysts, these alloy catalysts have been difficult to disperse onto carbon based electrodes reducing the active surface area compared with pure platinum. The platinum alloys may also be susceptible to accelerated degradation and leaching of transiton metals, with the alloy poisoning the fuel cell and decreasing performance.[114,115]

Research into non-platinum based catalysts has also been insightful with metal macorcycles, heteropoly acids (see section 1.1.8) and doped carbon all showing romising signs.[114,115] However thus far, none of the alteratives have achieved 1/10th the acivity of the paltinum catalyst.

1.2.5 FlowCath® Technology: The Alternative Solution

The development of low cost PEM fuel cell systems is essential for them to be economically viable. ACAL Energy's proprietary FlowCath® platinum-free liquid cathode technology is one possible solutionFlowCath® technology focuses around the complete removal of platinum and precious metal catalysts from the cathode which accounts for approximately 80 % of the total platinum.[116] The basis of this technology is that the membrane electrode assembly (MEA) for the cathode is modified to accommodate a solution based redox system. The FlowCath® cell consists of a typical anode flow field and MEA which is very similar to that of a typical PEMFC. This allows fuels such as hydrogen and methanol that are typically used in PEM type systems to be employed here as well. Although the anode side may remain relatively unchanged, the key differences lie with the cathode.[116]

Figure 1.4 shows the schematic of the FlowCath® technology used in ACAL's novel fuel cell as well as an enhanced view of the FlowCath® MEA which does not incorporate of a traditional MEA. Here, the membrane is in direct contact with the aqueous solution based catalyst (catholyte solution). The catholyte solution is pumped through a porous carbon electrode material where the catalyst is reduced via an electrochemical redox process. Whilst pumped through the electrode, protons migrate from the membrane to the solution and protonate the reduced catalyst balancing the increased negative charge. The catholyte solution is then pumped to an external regenerator where oxygen is passed through the solution to react with the reduced catalyst forming water.

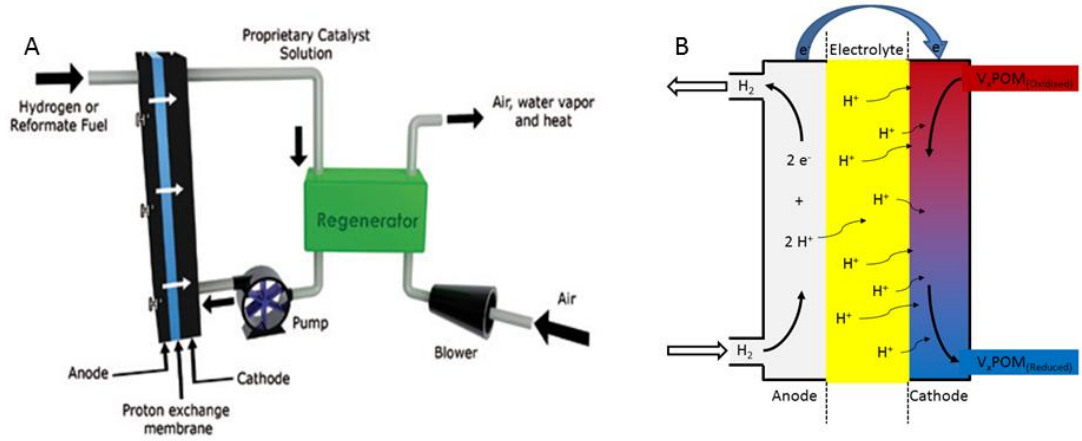

Figure 1.4: A) Schematic of the FlowCath® fuel cell technology, B) enhanced view of the membrane electrode assemble within FlowCath® Technology

In a standard PEM fuel cell, the overall thermodynamics of the system are controlled by water formation via oxygen reduction. In this instance, the separate ORR reaction effectively removes water formation from the thermodynamics equation thus the overall thermodynamics and kinetics are now dictated by the properties of the catalyst within the catholyte solution. This results in the open circuit potential (OCP) of the FlowCath® fuel cell no longer remaining at the theoretical value of 1.23 V vs. SHE (see section 1.2.2) but is now dictated by the OCP of the catalyst within the catholyte which is typically less than 1.23 V vs. SHE.[116]

Overall, the FlowCath® simplifies the standard PEM fuel cell technology. In standard PEMFC, the MEA on the cathode side is a complex challenge involving a three phase boundary. To successfully carry out the ORR protons, electrons and

oxygen all have to be present at the electrode surface. For this to be possible, electrons must travel through the porous carbon network whilst protons must travel along a network of interwoven ionomer to reach the carbon surface. Finally, the oxygen fed into the system must diffuse to the electrode surface after which water must diffuse away. In the FlowCath® system, the electrodes travel through the porous carbon to the electrode surface whilst all other transport networks are confined to the catholytes solution. This results in a much simpler two phase boundary at the electrode surface.[116]

Looking back to section 1.3 it can be see that the polyoxometalate compounds and in particular, the type I mixed addenda Keggin polyoxometalates of the general formula $\{PMo_{12-x}V_xO_{40}]^{(3+x)-}$, could be particularly advantageous in FlowCath® technology. Their excellent redox behaviour, unique oxidative abilities with oxygen and high solubility in aqueous media are the key properties that make them potentially suitable catholytes.

1.3 Justification and Objectives

The environmental impacts due to the dependence of fossil fuels to provide the majority of the worlds energy supply is becoming an increasing concern. With reports of increases in the rate of global warming due to increases in green house gasses arising from the burning of fossil fuels, the use renewable energy sources has never been more desirable. Current renewable sources include solar, wind, biomass and wave which all have their individual disadvantages. Solar power is only achievable during daylight hours and some areas of the planet, Antarctica for instance, do not see daylight for up to six months at a time. Hence thier use is somewhat geographically limited. Wind and sea power are only available when the wind blows and due to their unpredictable behaviour cannot be seen as a reliable and ready energy source. Given that the current energy economy revolves around electricity and liquid based fuel systems the use of biomass is somewhat limited as essentially obtained in a solid state.

A solution to this problem is fuel cell technology. The attractive prospect of fuel cell technology is that it is more efficient under practical operating conditions than the

conventional combustion engine. The fuel required for this technology is H_2 and is readily available in the atmosphere; however storage of this fuel is a small problem. There are numerous types of fuel cells but currently the proton exchange membrane (PEM) fuel cell is the most attractive for research and development due to high current densities being achieved at moderate temperatures. The major drawback to PEMFC is the use of highly expensive platinum catalysts for both the anode and cathode reactions. At the time of writing, the current cost of platinum is 1522.00 \$ oz^{-1} and with over 20 grams of platinum needed in a fuel cell stack for automotive use, the cost is staggering. This clearly demonstrates that for PEM fuel cells to be a realistic alternative for energy supply, cheaper alternatives or methods to reduce the required amount of platinum loading need to be investigated.

The main objectives for this work are as follows:

- Determine the applicability of V_xPOM species as catholytes for FlowCath® Technology
- Determine the electrochemical reversibility of the various V_xPOM species were x =1 – 4.
- Study the effects of FlowCath® Fuel Cell conditions on the speciation and electrochemical behaviour of the V_xPOM systems.
- Determine a suitable method for the direct comparison of catholyte performance.
- Identify structural and electrochemical changes in the catholyte system before, during and after use.
- Using knowledge of the standard V_xPOM catholytes, design and develop new and improved V_xPOM formulations that demonstrate improved fuel cell performance.

1.4 References

(1) Pope, M. T. *Heteropoly and Isopoly Oxometaltes*; Inorganic Chemistry Concepts; Springer-Verlag, Berlin, 1983; Vol. 8, pp. 1-1.

(2) Kozhevnikov, I. *Catalysis by Polyoxometalates*; Catalysis for Fine Chemical Synthesis; Wiley & Sons, LTD, 2002; Vol. 2.

(3) Misono, M. *Materials Chemistry and Physics* **1987**, *17*, 103-120.

(4) Okuhara, T.; Mizuno, N.; Misono, M. *Advances in catalysis* **1996**, *41*, 1-140.

(5) Mizuno, N.; Misono, M. *Journal of Molecular Catalysis* **1994**, *86*, 319-342.

(6) Hill, C. *Chemical reviews* **1998**, *98*, 1-2.

(7) Maksimov, G. *Russian Chemical Reviews* **1995**, *64*, 445-461.

(8) Souchay, P. *Polyanions et polycations*; Monographies de chimie mineerale; Gaithier-Villars, Paris, 1963.

(9) Tsigdinos, G.; Hallada, C. *Inorganic Chemistry* **1968**, *7*, 437 - 441.

(10) Grate, J. *Journal of Molecular Catalysis A: Chemical* **1996**, *114*, 93-101.

(11) Odyakov, V. F.; Zhizhina, E. G.; Maksimovskaya, R. I. *Applied Catalysis A: General* **2008**, *342*, 126-130.

(12) Nyman, M. *Dalton Transactions* **2011**, *40*, 8049 - 8058.

(13) Li, S.; Liu, S.; Liu, S.; Liu, Y.; Tang, Q.; Shi, Z.; Ouyang, S.; Ye, J. *Journal of the American Chemical Society* **2012**, *134*, 19716-19721.

(14) Müller, A.; Serain, C. *Accounts of Chemical Research* **2000**, *33*, 2-10.

(15) Berzelius, J. *Annalen der Physik* **1826**, *82*, 369-392.

(16) de Marignac, G. *Le fond d'un portefeuille*; Annales de Chimie et de Physique, 1864; Vol. 3, p. 1.

(17) Werner, Z.; Z; Werner, U.; Werner, A. *Berichte der deutschen chemischen Gesellschaft* 190**7**, *40*, 15-69.

(18) Miolati, A.; Turin, R.; Pizzighelli, R. *Journal for Praktische Chemie* **1907**, *77*, 417-456.

(19) Baker, L. C.; Glick, D. C. *Chemical Reviews* **1998**, *98*, 3-49.

(20) Pauling, L. *Journal of the American Chemical Society* **1929**, *51*, 1-13.

(21) Keggin, J. F. *Proceedings of the Royal Society A: Mathematical, Physical and Engineering Sciences* **1934**, *144*, 75-100.

(22) Varga, G.; Papaconstantinou, E.; Pope, M. *Inorganic Chemistry* **1970**, *9*, 662-667.

(23) Pope, M.; Varga, G. *Chemical Communications (London)* **1966**, 653-654.

(24) So, H.; Pope, M. *Inorganic Chemistry* **1972**, *11*, 1441 - 1443.

(25) Leparulo-Loftus, M.; Pope, M. *Inorganic Chemistry* **1987**, *26*, 2112 - 2120.

(26) Mbomekalle, I.; Keita, B.; Lu, Y.; Nadjo, L.; Pope, M. *European Journal of Inorganic Chemistry* **2004**, *2004*, 4132 - 4139.

(27) Kozhevnikov, I. *Russian Chemical Reviews* **1987**, *56*, 811-825.

(28) Kozhevnikov, I.; Matveev, K. *Russian Chemical Reviews* **1982**, *51*, 1075-1088.

(29) Kozhevnikov, I. *Catalysis Reviews* **1995**, *37*, 311-352.

(30) Kozhevnikov, I.; Matveev, K. *Applied Catalysis* **1983**, *5*, 135-150.

(31) Kozhevnikov, I. *Journal of Molecular Catalysis A: Chemical* **2007**, *262*, 86-92.

(32) Hill, C.; Prosser-McCartha, C. *Coordination Chemistry Reviews* **1995**, *143*, 407-455.

(33) Hill, C. *Journal of Molecular Catalysis A: Chemical* **2007**, *262*, 2-6.

(34) Geletii; Atalla; Bailey; Delannoy; Hill; Weinstock. *Journal of the American Chemical Society* **2004**, 126, 1-2.

(35) Grigoriev, V.; Hill, C.; Weinstock, I. *Journal of the American Chemical Society* **2000**, *122*, 3544 - 3545.

(36) Nicoara, A.; Patrut, A.; Margineanu, D.; Müller, A. *Electrochemistry Communications* **2003**, *5*, 511-518.

(37) Müller, A.; Roy, S. *Coordination Chemistry Reviews* **2003**, *245*, 153 - 166.

(38) Gouzerh, P.; Che, M. *l'actualité chimique* **2006**, *298*, 1 - 14.

(39) Pope, M.; Müller, A. *Polyoxometalate Chemistry From Topology via Self-Assembly to Applciations*; Kluwer Academic Publishers, **2002**.

(40) Weinstock, I. A.; Müller, A. *Israel Journal of Chemistry* **2011**, *51*, 176-178.

(41) Pope, M.; Muller, A. *Angewandte Chemie International Edition* **1991**, *30*, 34-48.

(42) Pope, M.; Müller, A. *Polyoxometalate chemistry: from topology via self-assembly to applications*; Kluwer Academic Publishers, 2001.

(43) Khenkin, A. M.; Leitus, G.; Neumann, R. *Journal of the American Chemical Society* **2010**, *132*, 11446-11448.

(44) Khenkin, A. M.; Weiner, L.; Wang, Y.; Neumann, R. *Journal of the American Chemical Society* **2001**, *123*, 8531-8542.

(45) Efremenko, I.; Neumann, R. *Journal of the American Chemical Society* **2012**, *134*, 20669-20680.

(46) Neumann, R.; Dahan, M. *Journal of the American Chemical Society* **1998**, *120*, 11969-11976.

(47) Efremenko, I.; Neumann, R. *The Journal of Physical Chemistry A* **2011**, *115*, 4811 - 4826.

(48) Hirao, H.; Kumar, D.; Chen, H.; Neumann, R.; Shaik, S. *Journal of Physical Chemistry C* **2007**, *111*, 7711-7719.

(49) Tsigdinos, G. *Topics in Current Chemistry* **1978**, *76*, 1-64.

(50) Hallada, C.; Tsigdinos, G. *The Journal of Physical Chemistry A* **1968**, *72*, 4304 - 4307.

(51) Tsigdinos, G.; Hallada, C. *Inorganic Chemistry* **1970**, *9*, 2488 - 2492.

(52) Tsigdinos, G.; Hallada, C. *Journal of the Less Common Metals* **1974**, *36*, 79 - 93.

(53) Maksimov, G. *Russian Chemical Reviews* **1995**, *64*, 445-461.

(54) Zhizhina, E.; Odyakov, V. *Reaction Kinetics and Catalysis Letters* **2008**, *95*, 301 - 312.

(55) Zhizhina, E. G.; Odyakov, V. F.; Simonova, M. V.; Matveev, K. I.; Matveev, K. I.; Catalysis, B. I.; Matveev, K. I. *Reaction Kinetics and Catalysis Letters* **2003**, *78*, 373-379.

(56) Zhizhina, E.; Odyakov, V.; Simonova, M.; Matveev, K. *Kinetics and Catalysis* **2005**, *46*, 380-389.

(57) Odyakov, F. V.; Zhizhina, E. G. *Russian Journal of Inorganic Chemistry* **2009**, *54*, 361-367.

(58) Odyakov, V.; Zhizhina, E.; Matveev, K. *Journal of Molecular Catalysis A:* **2000**, *158*, 453 - 456.

(59) Zhizhina, E. G.; Odyakov, V. F. *Applied Catalysis A: General* **2009**, *358*, 254-258.

(60) Zhizhina, E. G.; Odyakov, F. V. *Catalysis in Industry* **2010**, *2*, 217-224.

(61) Zhizhina, E.; Odyakov, F.; Matveev, K. *European Journal of Inorganic Chemistry* **1999**, 1009-1014.

(62) Kuznetsova, L.; Maksimovskaya, R.; Matveev, K. *Bulletin of the Academy of Sciences of the USSR Division of Chemical Science* **1983**, *32*, 660-665.

(63) Chernyshova, Y.; Kuznetsova, L.; Matveev, K. *Reaction Kinetics and Catalysis Letters* **1988**, *37*, 221-226.

(64) Long, D.; Burkholder, E.; Cronin, L. *Chemical Society Reviews* **2006**, *36*, 105.

(65) Müller, A.; Beckmann, E.; Bögge, H.; Schmidtmann, M.; Dress, A. *Angewandte Chemie International Edition* **2002**, *41*, 1162-1167.

(66) Lipscomb, W. *Inorganic Chemistry* **1965**, *4*, 132-134.

(67) Weakley, T.; Evans, H.; Showell, J.; Tourn, G.; Tourn, C. *Journal of the Chemical Society, Chemical Communications* **1973**, 139-140.

(68) Contant, R.; Teze, A. *Inorganic Chemistry* **1985**, *24*, 4610-4614.

(69) Alizadeh, M.; Harmalker, S.; Jeannin, Y.; Martin-Frere, J.; Pope, M. *Journal of the American Chemical Society* **1985**, *107*, 2662-2669.

(70) Li, Y.; Li, Y.; Wang, Y.; Feng, X.; Lu, Y.; Wang, E. *Inorganic Chemistry* **2014**, *48*, 6452-6458.

(71) Long, D.; Tsunashima, R.; Cronin, L. *Angewandte Chemie International Edition* **2010**, *49*, 1736-1758.

(72) Baker, L.; Figgis, J. *Journal of the American Chemical Society* **1970**, *92*, 3794-3797.

(73) Weinstock, I.; Cowan, J.; Barbuzzi, E.; Zeng, H.; Hill, C. *Journal of the American Chemical Society* **1999**, *121*, 4608 - 4617.

(74) Pope, M.; O'Donnell, S.; Prados, R. *Journal of the Chemical Society* **1975**, 1-2.

(75) Kehrmann, F.; Aachen, A. *Zeitschrift for anorganische Chemie* **1892**, *1*, 423-441.

(76) Dawson, B. *Acta Crystallographica* **1953**, *6*, 113-126.

(77) Evans, H. *Journal of the American Chemical Society* **1948**, *70*, 1291-1292.

(78) Luis, P.; Martín-Zarza, P.; Sanchez, A.; Ruiz-Pérez, C.; Hernández-Molina, M.; Solans, X.; Gili, P. *Inorganica Chimica Acta* **1998**, *277*, 139-150.

(79) Dexter, D.; Silverton, J. *Journal of the American Chemical Society* **1968**, *90*, 3589-3590.

(80) Pettersson, L.; Andersson, I.; Oehman, L. *Inorganic Chemistry* **1986**, *25*, 4726-4733.

(81) Ammam, M. *Journal of Materials Chemistry A* **2013**, *1*, 6291.

(82) Courtin, P. *Revue de Chimie Minerale* **1971**, *8*, 221.

(83) Courtin, P. *Revue de Chimie Minerale* **1971**, *8*, 75.

(84) Smith, D.; Pope, M. *Inorganic Chemistry* **1973**, *12*, 331 - 336.

(85) Kozhevnikov, I.; Sinnema, A.; Bekkum, H.; Fournier, M. *Catalysis letters* **1996**, *41*, 153-157.

(86) Kozhevnikov, I.; Sinnema, A.; Jansen, R.; Bekkum, H. *Catalysis letters* **1994**, *27*, 187-197.

(87) Kozhevnikov, I.; Sinnema, A.; Bekkum, H. *Catalysis letters* **1995**, *34*, 213-221.

(88) Zhizhina, E. G.; Odyakov, V. F. *Reaction Kinetics and Catalysis Letters* **2009**, *98*, 51-58.

(89) Pope, M.; Papaconstantinou, E. *Inorganic Chemistry* **1967**, *6*, 1147- 1152.

(90) Atkins, P.; Paula, J. *Physical Chemistry*; 8 ed.; Oxford University Press, 2006.

(91) Izumi, Y.; Matuso, K.; Urabe, K. *Journal of Molecualr Catalysis* **1983**, *18*, 229.

(92) Hill, C. L. *Journal of Molecular Catalysis* **1996**, *114*, 1-371.

(93) Mizuno, N.; Misono, M. *Chemical reviews* **1998**, *98*, 199 - 217.

(94) Kozhevnikov, I. *Chemical reviews* **1998**, *98*, 171-198.

(95) Kozhevnikov, I. *Applied Catalysis A: General* **2003**, *256*, 3-18.

(96) Sadakane, M.; Steckhan, E. *Chemical reviews* **1998**, *98*, 219-238.

(97) Pope, MT.; Müller, A. *Introduction to Polyoxometalates Chemistry*; Polyoxometalate Molecular Science, Nato Series; Kluwer Academic Publishers, 2003.

(98) Wang,Y.; Morokuma, K.; Lyuba, A.; Botar, B.; Hill, CL.; Musaev, G. *The Journla of Physical Chemistry B* **2006**, *110*, 170-173.

(99) Weinstck, IA. *Chemical reviews* **1998**, *98*, 113-170.

(100) Matveev, K.I. *Kinetics and Cataysisl* **1977**, *18*, 862.

(101) Kozhevnikov, I. *Catalysis Reviews, Science and Engineering* **1995**, *37*, 311.

(102) Neumann, R. *Progress in Inorganic Chemistry* **1998**, *47*, 317.

(103) Kozhevnikov, I. *Journal of Molecular Catalysis* **1997**, *117*, 51.

(104) Song, K.; Barteau, M. *Journal of Molecular Catalysis* **2004**, *212*, 229-236.

(105) Limoges, B; Turner, J.; Kuo, C.; Ferrell, J; Stains, R. J.; Herring, A *Electrochemical Society Transactions* **2006**, *1*, 61-67.

(106) Kuo, C.; Limoges, B; Turner, J.; Ferrell, J; Stains, R. J.; Herring, A *Electrochimica* **2007**, *52*, 2051-2061.

(107) Stains, R. J.; Kuo, C.; Limoges, B; Turner, J.; Ferrell, J; Herring, A *Electrochimica* **2008**, *53*, 8277-8286.

(108) Ferrell, J.; Stains, R. J.; Kuo, C.; Limoges, B; Turner, J.; Herring, A *Electrochimica* **2008**, *53*, 4927-4933.

(109) Sachdeva, S.; Turner, J.; Horan, J.; Herring ,A. *The use of Heteropoly acids in Proton Exchange Fuel Cells*; Fuel Cells and Hydrogen Storage; Springer, 2011.

(110) Harrup, M.; Stewart, F.; Luther, T.; Trowbridge, T *American Chemical Society Division of Energy and Fuels*, **2009**, *54*, 1-2

(111) Barbir, F. *PEM Fuel Cells: Theory and Practice*; Academic Press Sustainable World Series, Elsevier, 2005.

(112) US Energy Information Administration, www.eia.gov.

(113) McNerney, G. *Clean Energy Nation*, American Management Association, 2011.

(114) O'Hayre R, Cha S, Colella W, Prinz F. *Fuel Cell Fundamentals*. Wiley, 2009.

(115) Larminie, J L, Dicks, A D. Fuel Cell Systems Explained. 2nd ed. Wiley 2003.

(116) Creeth, A. *Fuel Cells Bulletin,* **2011**, *2011*(4), 12-15.

(117) Hayden BE, Suchsland J. *Support and Particle Size Effects in Electrocatalysis,* Fuel Cell Catalysis: A surface science approach, Wiley NY., **2009,** 567-592.

(118) Hayden B,; Pletcher D, Suchsl J,; Williams L.; *Physical Chemistry Chemical Physics.* **2009,** *11,*9141-9148.

Chapter 2

Characterization Methods and Theory

Table of Contents

2.1 Introduction

The work detailed in this thesis is based on aqueous phosphomolybdovanadate catholyte systems which have potential as catalysts in PEM Fuel cell technology. This work uses a variety of characterisation and analysis techniques, with the main focus upon electrochemical and spectrochemical analysis. This chapter covers the fundamental and theoretical aspects underlying the main characterization methods as well as highlighting other methods used in this work.

2.2 Electrochemistry

Electrochemical measurements were made using an Autolab PGSTAT128N potentiostat in conjunction with NOVA software. Cyclic voltammetry measurements were carried out using a three electrode system consisting of a glassy carbon working electrode, platinum wire counter electrode and a saturated calomel (SCE) reference electrode. Hydrodynamic measurements were carried out using a Radiometer Analytical EDI101 rotating glassy carbon working electrode, a platinum wire counter electrode and a saturated calomel reference electrode.

2.2.1 Introduction

Electrochemistry is a specific branch of chemistry which focuses on reactions occurring at the interface of an electrode and an electrolyte. The reactions at the interface involve the transfer of electrons between the electrode and the electro active species within the electrolyte solution. Electrochemical reactions can be driven by the application of an external direct electric current (DC) which can in turn drive an otherwise non-spontaneous reaction. This method is known as electrolysis. The electrical potential across the electrode and electrolyte interface, which is known as the interfacial potential difference, greatly influences which electrochemical reaction occurs and its rate. Indeed, this potential difference between the electrode and electrolyte provides the driving force for electrochemical processes. The ability to control and quantify the interfacial potential and study the charge transport across the interface is essential to understanding electrochemistry processes.

2.2.2 Thermodynamics

The thermodynamics of system can be explained in terms of chemical potential. In this case, the simple reaction shown by equation 2.1 in a homogenous solution will be considered:

$$A \rightleftharpoons B \tag{2.1}$$

Here the chemical potential of species *i*, μ_i, is described by equation 2.2:

$$\mu_i = \mu_i^\circ + RT \ln Q \tag{2.2}$$

where μ_i° is the standard chemical potential of species *i*, *T* is temperature, *R* is the molar gas constant and *ln Q* is the reaction quotient, which is a function of the activity and concentration of species involved in the reaction.[1] At equilibrium the chemical potential of the two chemical species must be equal:

$$\mu_A = \mu_B \tag{2.3}$$

When considering the electron transfer reaction at the electrode solution interface, the fundamental laws of thermodynamics are upheld and predict the position of equilibrium but do not predict how the system responds to a change in equilibrium.

2.2.3 Electron Transfer at the Electrode-Solution Interface

An electrode reaction typically involves the transfer of charge from an electrode to a species present in solution (electrolyte) at the electrode surface. Considering the one electron transfer shown in equation 2.4 where species A and B exist in the solution phase and the source of electrons is the electrode in the solid phase:

$$A^{n+} + e^- \rightleftharpoons B^{(n-1)+} \tag{2.4}$$

To describe this heterogeneous reaction we need to introduce a new parameter, electrochemical potential, $\overline{\mu_i}$ described in equation 2.5:

$$\overline{\mu_i} = \mu_i^\circ + z_i F \phi_\beta + RT \ln a_i \tag{2.5}$$

where z_i is the charge of species *i*, F is Faraday constant, ln a_i is the activity of species *i* and ϕ_β is the potential of phase β, within which species *i* is located.[2,3,4] When the system in equation 2.4 is at equilibrium we obtain:

$$\left(\mu_A^\circ + nF\phi_S + RT\ln a_A\right) + \left(\mu_e^\circ - F\phi_M + RT\ln a_e\right)$$

$$= \left(\mu_B^\circ + (n-1)F\phi_S + RT\ln a_B\right) \quad (2.6)$$

Here ϕ_S is the potential of the solution phase and ϕ_M is the potential of the electrode phase. In this instance (equation 2.6) *n* refers to the charge upon the complex. Upon re-arrangement we obtain:

$$(\phi_M - \phi_S) = \frac{1}{F}\left(\mu_A^\circ + \mu_e^\circ - \mu_B^\circ\right) - \frac{RT}{F}ln\left(\frac{a_B}{a_A}\right) \quad (2.7)$$

where $(\phi_M - \phi_S)$ is known as the interfacial potential of the redox couple at the electrode surface. Equation 2.7 is an alternative form of equation 2.2 known as the Nernst equation, more commonly expressed as:

$$E = E^\circ - \frac{RT}{F}ln\,Q \quad (2.8)$$

$$Q = \frac{\gamma_B\,[B]}{\gamma_A\,[A]} \quad (2.9)$$

Where *E* is the electrode potential, E^o is the standard electrode potential, *n* is the number of electrons transferred and γ_i is the activity coefficient of species A or B.[4] The electrode potential *E* is equivalent to the interfacial potential $(\phi_M - \phi_S)$ when the redox system in question is coupled with the standard hydrogen electrode.[1-5,6] The Nernst equation relates the actual cell potential to the standard potential and reaction quotient. Equation 2.8 can be further simplified by substitution of the standard potential, E^o, with the formal potential $E^{o'}$ (equation 2.10). The formal potential is the actual measured potential of the half cell when the concentration of the oxidised and reduced species is equal. The formal potential also incorporates activity coefficients of the respective species in the half cell reactions.[2,4]

$$E = E^{\circ\prime} - \frac{RT}{nF}ln\frac{[B]}{[A]} \quad (2.10)$$

It can be seen from equation 2.10 that any variation in the interfacial potential will result in a shift in the position of equilibrium and a change in the concentration of species A and B adjacent to the electrode surface. Hence the application of an external voltage induces an electron transfer reaction at the electrode solution interface. The response of the system from the applied external voltage is of great interest and how quickly equilibrium is reached is determined by the electrode kinetics.

2.2.4 Electrochemical Cell

Electrochemical cells can be split into two general categories, Galvanic cells and electrolytic cells; here we will first consider the electrolytic cell. Experimentally, the direct measurement of the interfacial potential $(\phi_M - \phi_S)$ is not possible. Ultimately a situation where the potential difference between two half cell reactions is measured is needed.[4] The two half cells comprise of a) the redox active species and b) a reference cell or reference electrode. The reference electrode forms part of an impedance circuit whose interfacial potential remains constant. In Figure 2.1 the reference electrode is the standard hydrogen electrode. The potential difference, *E*, for the redox process in equation 2.4 is given by:

$$E = (\phi_M - \phi_S)_{AB} + IR_s + (\phi_M - \phi_S)_{ref} \quad (2.9)$$

where $(\phi_M - \phi_S)_{ref}$ is the interfacial potential of the reference electrode, *I* is the current which flows via the circuit and R_s is the solution resistance.[2] In electrochemical reactions where a current is generated/flows, the IR_s term is minimised by using small electrodes to reduce *I*.[7] Electronic compensation can be used by the potentiostat to mitigate for the effect of R_s.[8] In addition, due to the fundamental properties of a reference electrode the term $\left(\phi_M - \phi_S\right)_{ref}$ remains constant thus equation 2.9 can be re-expressed as:

$$E = (\phi_M - \phi_S)_{AB} + constant \quad (2.10)$$

By definition the SHE (standard hydrogen electrode) interfacial potential is zero, leading to the case of *E* being equal to $(\phi_M - \phi_S)_{AB}$.

A potentiostat can vary the voltage applied to the working electrode and measure the flow of resulting current as well as simultaneously recording the potential difference. A key function of the potentiostat is to ensure that $(\phi_M - \phi_S)_{ref}$ remains constant for a current potential experiment and that it varies in the desired way during a potentio-dynamic experiment. This is achieved by the use of counter/auxiliary electrode. The counter electrode functions as an anode when the working electrode functions as a cathode. This ensures that current flow is between the working and counter electrode and no current is passed through the reference electrode circuit which would compromise its stability.

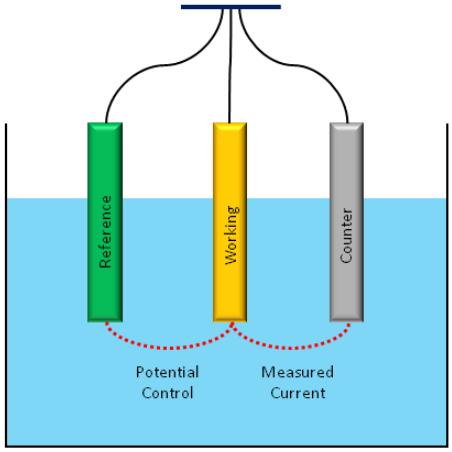

Figure 2.1: Diagram of a simple three electrode cell where the reference electrode is the standard hydrogen electrode.

Galvanic cells are two electrode systems and hence both oxidation and reduction processes are observed, with oxidation occurring at the anode and reduction at the cathode.[4] The separate oxidation and reduction process constitute the two half cell reactions that are required for a complete circuit. In this instance electrons will flow from the anode to the cathode if a spontaneous reaction occurs when the two electrodes are connected. For this to be the case a viable path for the transport of ions between the two electrolytes compartments is needed, for example Figure 2.2. The transport of ions across the porous membrane is balanced by the flow of electrons through the external circuit, with the transport of electrons ultimately being used to power electronic devices. The Daniel cell (Figure 2.2) is a typical example of a galvanic cell which uses zinc and copper electrodes immersed in zinc and copper sulphate, respectively.[9]

The cell reaction is described by:

Overall: $Zn_{(s)} + Cu^{2+}_{(aq)} \longrightarrow Zn^{2+}_{(aq)} + Cu_{(s)}$ $E^{o}_{(cell)} = 1.10$ V vs. SHE

Anode: $Zn_{(s)} \longrightarrow Zn^{2+}_{(aq)} + 2e^{-}$ $E^{o} = -0.76$ V vs. SHE

Cathode: $Cu^{2+}_{(aq)} + 2e^{-} \longrightarrow Cu_{(s)}$ $E^{o} = 0.34$ V vs. SHE

$E^{o}_{(cell)}$, is the standard electrode potential incorporating both half cell reactions under standard conditions (1 M concentration, 1 atm pressure and 298.15 K). E^{o} on the other hand is the standard electrode potential of the individual half cell reactions under standard conditions. The cell potential can be calculated by:

$$E^{o}\,(cell) = E^{o}_{reduction} - E^{o}_{oxidation} \tag{2.11}$$

When E_{cell} is positive the cell reaction is spontaneous. Considering chemical energy it is Gibbs free energy, ΔG, which determines the spontaneity of a reaction.[10] The relationship between E_{cell} and ΔG is evident in equation 2.12. When E_{cell} is positive the resulting Gibbs energy is negative, hence the corresponding reaction is spontaneous.

$$\Delta G = -nFE_{cell} \tag{2.12}$$

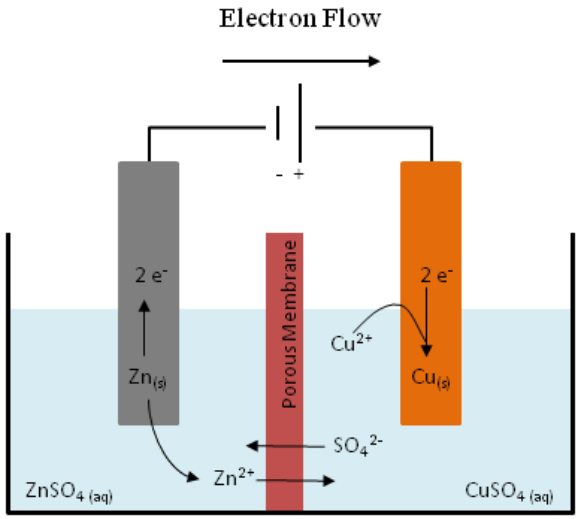

Figure 2.2: Processes observed in a Daniell cell. The cell consists of half cells connected via a porous membrane each containing a single electrode immersed in a electrolyte solution .

Under standard conditions equation 2.12 can be re-written to give equation 2.13:

$$\Delta G^o = -nFE^o_{cell} \tag{2.13}$$

Gibbs free energy and standard Gibbs free energy of a reaction can be related by equation 2.14,

$$\Delta G = \Delta G^o + RTlnQ \tag{2.14}$$

where ΔG^o Gibbs free energy under standard conditions. By substituting equation 2.12 and 2.13 in to 2.14 we obtain the Nernst equation (equation 2.8), illustrating the relationship between Gibbs free energy and electrode potential.[2,4,10]

2.2.5 The Structure of Electrode-Solution interface

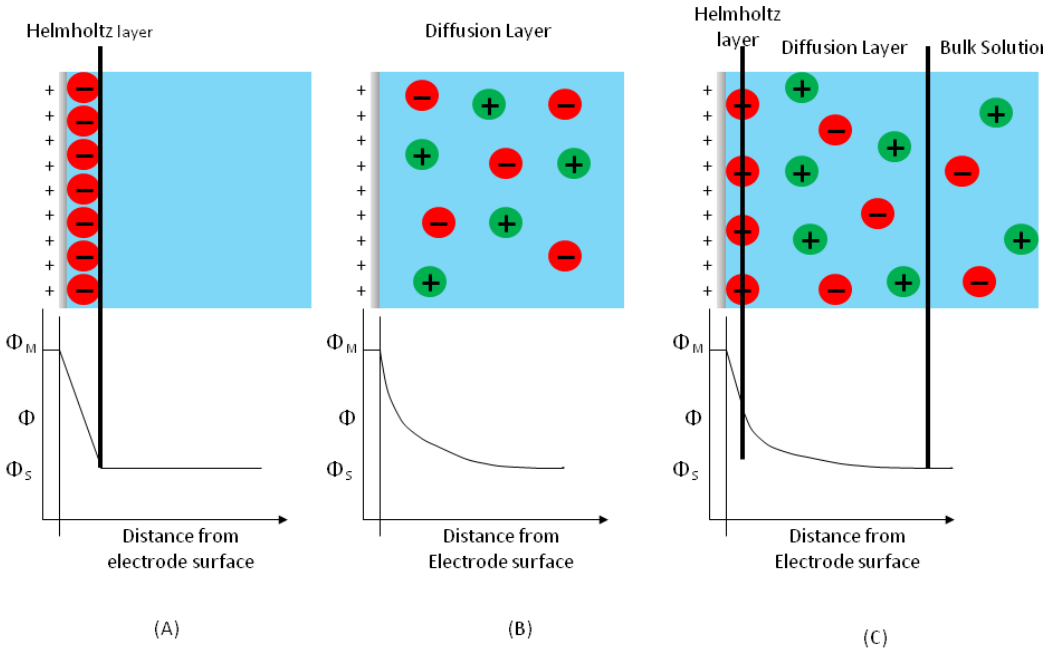

Figure 2.3: Illustration of the models that describe the electrode - electrolyte interface, green circles are cations, red circle are anions. (A) Helmholtz model, (B) Gouy-Chapman model and (C) Stern model.

The generation of an electrode potential at the electrode-electrolyte interface results from a breakdown in electroneutrality in the electrolyte solution adjacent to the electrode surface.[11] There are various models (Figure 2.3) to describe this region, the first and simplest by Helmholtz (Figure 2.3A), describes the electrode and electrolyte interface as a capacitor were the charge on the electrode is balanced in solution by a

rigid layer of oppositely charged ions which lie in a sheet parallel to the electrode surface. This rigid layer marks the boundary of the Outer Helmholtz Plane (OHP). The Helmholtz model doesn't take into account the dependence of measured capacity on the potential or solution concentration.[12]

The Gouy–Chapman model (Figure 2.3B) which includes a diffuse double layer model which gives a dependence of the double layer capacitance on both the potential electrode and the electrolyte concentration. Ultimately the model showed that excess charge density does not only reside at the OHP and that double layer thickness may vary. The model fails to explain capacity-potential curves for all concentrations and the dependence on concentration is not observed.[12,13,14]

The Stern model (Figure 2.3C) combined the ideas from the Helmholtz and Gouy-Chapman models with ions forming a rigid OHP (~1 nm from the electrode surface) parallel to the electrode and a Gouy-Chapman type diffusion layer. In this case the potential drop is experienced across the entire diffuse layer as shown in Figure 2.3C, which extends to a distance less than ~100 $\dot{A}$ for electrolyte concentrations greater than 0.01 M.[12,15] In some instances ions can lose their solvation shell and adsorb directly to the electrode surface. This results in an Inner Helmholtz Plane (IHP) and was described by Grahame.[16] This phenomenon is known as 'specific adsorption' commonly observed for weakly solvated ions.[16]

We can identify two key points from the Stern model. Firstly, the redox active species present in solution can approach the electrode surface to within a distance imposed by the OHP. Here electron transfer can occur via electron tunnelling across this region, the probability of this then decrease exponentially with increasing distance from the electrode surface. For accurate quantitative analysis it is essential that the majority, if not the entire potential drop, occurs in the region where electron tunnelling is highly probable.[2,4,12] Secondly, the electrode and the OHP can act as a capacitor meaning current can flow without the transfer of electrons (i.e. charging of a capacitor).[2-5] This ultimately shows that there are two types of current contributing to the observed redox process and it is important to draw a clear distinction between the two. The first current process is known as faradaic current, in which a heterogeneous electron transfer across the electrode solution interface occurs. This electron transfer results in an oxidation or reduction of the electroactive species. The

total faradaic current is equal to the change in charge with time:

$$I = \frac{dQ}{dt} \tag{2.15}$$

Where I is total current, t is time and Q is the charge given by $Q = nFN$, where N is the number of moles of analyte electrolyzed. The second process results from non-faradaic current which arises from changes in the electrode solution interface upon changing the applied potential or solution composition.[2-4] This is commonly referred to as the background current.

2.2.6 Electrode Kinetics

As discussed in section 2.2.2, thermodynamics can only predict the position of equilibrium in the redox system. It is the electrode kinetics that describes how the redox system responds towards a change in the equilibrium position. If we consider the redox process equation 2.16 and introduce two new terms k_{red} and k_{ox} which correspond to the rate of reduction and oxidation respectively:

$$A + e^- \underset{k_{ox}}{\overset{k_{red}}{\rightleftharpoons}} B \tag{2.16}$$

The total current, I, recorded is a combined contribution from the oxidation and reduction. The cathodic current, I_c, has a negative contribution from the reduction of species A, whilst the anodic current, I_a, has a positive contribution from the oxidation of species B.

$$I = I_a + I_c \tag{2.17}$$

Both the anodic and cathodic current are dependent upon the flux, j, of the respective species A and B to the electrode surface. Assuming a uniformly accessible electrode:

$$I_c = F\,A\,j_A \tag{2.18}$$

$$I_a = F\,A\,j_B \tag{2.19}$$

where A is the electrode area and j is the flux of electroactive species, in this specific case A or B. The flux is also directly dependent upon the rates of the two separate heterogeneous redox processes given by:

$$j_A = k_{red}[A]_o \tag{2.20}$$

$$j_B = k_{ox}[B]_o \tag{2.21}$$

Where $[A]_o$ and $[B]_o$ are the initial concentration of species A and B, respectively. It is important to note that the heterogeneous rate constant is dependent upon pressure, temperature, potential and the transition state of the redox reaction.[2-6]

If we consider Figure 2.4A which shows the complete profile from reactants to products whilst Figure 2.4B shows a close up view of the transition state highlighted in yellow. The reaction pathway is shown at two different potentials, $E^{o'}$ and E. At $E^{o'}$ (blue line) the Gibbs energy for reaction ($\Delta_r G$) is zero hence no net reaction occurs and the two respective parabolas are aligned. An increase in the potential to a new value E, results in a change in the Gibbs energy of the electron, by a value which is equal to $F(E\text{-}E^{o'})$. All other species remain unaffected as it is ϕ_M which is increased, whilst ϕ_S remains unaffected. The effect of this potential increase is that $\Delta_r G$ becomes negative by a value $F(E\text{-}E^{o'})$ for the oxidation of species B and concordantly the activation energy for reaching the transition state for oxidation, $\Delta G_{ox}^{\ddagger E^{o\prime}}$, also decreases (becomes more negative) to a new value $\Delta G_{ox}^{\ddagger E}$. The fraction by which $\Delta G_{ox}^{\ddagger \mathrm{E}^{o\prime}}$ decrease by is dependent upon the symmetry of the respective reaction profile. For a given oxidation, in this case species B, this fraction is denoted by (1-α) where α is the transfer coefficients which ranges from zero to one.[2,4,6,17-19]

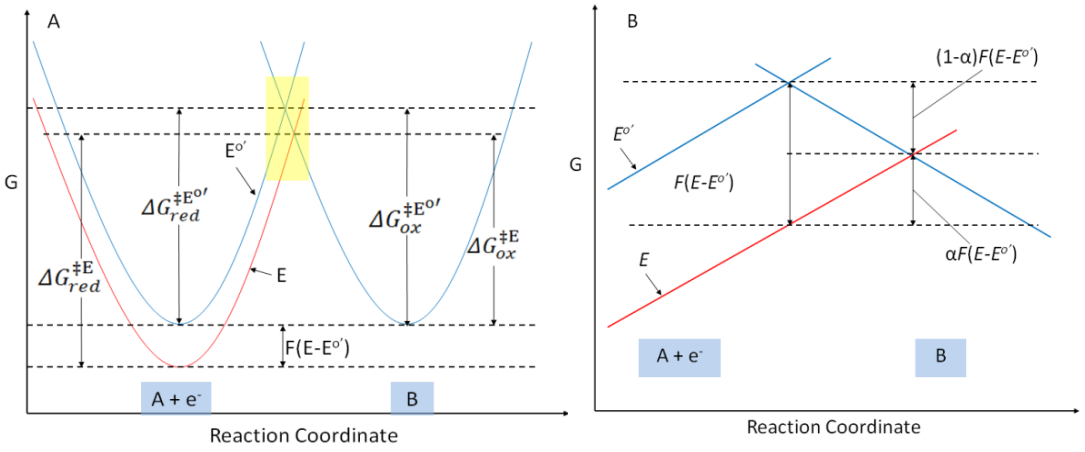

Figure 2.4: A) Diagram of the redox reaction profile for the reaction shown in equation 2.16. B) Close up view of the highlighted transition state in A.

Hence $\Delta G_{ox}^{\ddagger E}$ can be described by:

$$\Delta G_{ox}^{\ddagger E} = \Delta G_{ox}^{\ddagger E^{o\prime}} - (1-\alpha)F(E-E^{o\prime}) \quad (2.22)$$

A decrease in $\Delta G_{ox}^{\ddagger E^{o\prime}}$ also results in an increase in the energy of $\Delta G_{red}^{\ddagger E^{o\prime}}$ by $\alpha F(E\text{-}E^{o'})$:

$$\Delta G_{red}^{\ddagger E} = \Delta G_{red}^{\ddagger E^{o\prime}} + \alpha F(E-E^{o\prime}) \quad (2.23)$$

From the relationship described in equation 2.22 and 2.23, one can consider that the application of voltage alters the energy of the electron within the electrode. Metals do not possess individually defined electron energy levels, but consist of many closely packed atoms with strong electronic overlaps leading to a continuum of energy levels (bands) being created.[4,6,20] These energy levels are filled from the bottom up (lowest energy levels filled first); with to a reasonable approximation the upper most level containing electrons being know as the Fermi level (E_F). In this instance bands above the E_F are largely empty while just below there is a high density of electronic states. Figure 2.5 shows the effect of changing the Fermi level within an electrode (metal) in comparison with the HOMO (Highest Occupied Molecular Orbital) LUMO (Lowest Unoccupied Molecular Orbital) gap of a reactant, assuming the electrode reactant distance is small enough to allow electron transfer.

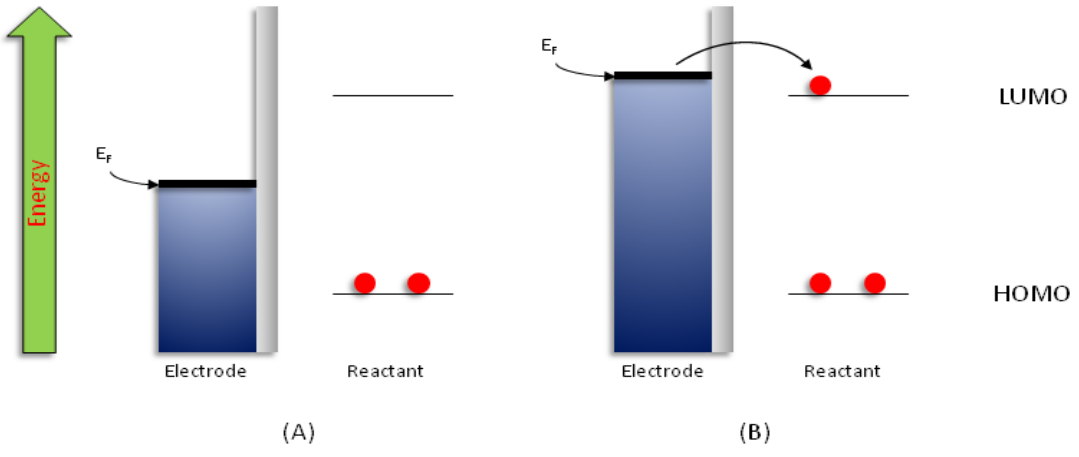

Figure 2.5: Illustration showing electron transfer to a redox couple in solution following the raising of E_F. A) E_F not high enough to allow electron transfer from the electrode to the redox species. B) E_F high enough to allow electron transfer from the electrode to the LUMO of the redox species.

Figure 2.5A shows that at a low potential (voltage) the energy of the E_F is below that of the LUMO of the reactant; in this case it is energetically unfavourable for an electron transfer from the electrode to the reactant to occur. However, Figure 2.5B shows that an increase in potential effectively increases the energy of E_F so that the Fermi level is higher than or equal to that of the LUMO. At this point it is thermodynamically favourable for an electron transfer to occur from the electrode to the LUMO of the reactant.[2,4,6]

If we assume that the rate constants for the respective heterogeneous reactions adopt an Arrhenius form where $\Delta G^{\ddagger}_{red/ox} = E_a$, where E_a is the activation energy for the reaction in question, then k_{ox} and k_{red} can be described by equations 2.24 and 2.25;[4,10]

$$k_{ox} = A_{ox}\, e^{\frac{-\Delta G^{\ddagger}_{ox}}{RT}} \tag{2.24}$$

$$k_{red} = A_{red}\, e^{\frac{-\Delta G^{\ddagger}_{red}}{RT}} \tag{2.25}$$

Where A is the pre-exponential factor for the oxidation and reduction reactions respectively. Substituting equations 2.22 and 2.23 into 2.24 and 2.25 yields:

$$k_{ox} = A_{ox}\, e^{\frac{-\Delta G^{\ddagger}_{E^{o\prime}_{ox}}}{RT}} e^{\frac{(1-\alpha)F(E-E^{o\prime})}{RT}} \tag{2.26}$$

$$k_{red} = A_{red}\, e^{\frac{-\Delta G^{\ddagger}_{E^{o\prime}_{red}}}{RT}} e^{\frac{-\alpha F(E-E^{o\prime})}{RT}} \tag{2.27}$$

Equations 2.26 and 2.27 are representative of k at a given potential, if we consider the case when $E = E^{o'}$ then we can write:

$$A_{ox}\, e^{\frac{-\Delta G^{\ddagger}_{ox}}{RT}} = A_{red}\, e^{\frac{-\Delta G^{\ddagger}_{red}}{RT}} = k^{o} \tag{2.28}$$

Where k^o is the standard electron transfer rate constant. From equation 2.28 it can be seen that k^o is not dependant on potential and thus k_{ox} and k_{red} can be expressed in terms of k^o:

$$k_{ox} = k^{o} e^{\frac{(1-\alpha)F(E-E^{o\prime})}{RT}} \tag{2.29}$$

$$k_{red} = k^o \, e^{\frac{-\alpha F(E-E^{o'})}{RT}} \tag{2.30}$$

Substitution of equations 2.29 and 2.30 into 2.20 and 2.21 yields the current-potential relationship commonly known as the Butler-Volmer equation.[18,19] This requires equations 2.18 and 2.19 to hold true.

$$I = I_a + I_c = F\,A\,k^o \left\{ [\mathrm{B}]_o e^{\frac{(1-\alpha)F\left(E-E^{o'}\right)}{RT}} - [\mathrm{A}]_o e^{\frac{-\alpha F\left(E-E^{o'}\right)}{RT}} \right\} \tag{2.31}$$

The value of k^o strongly depends on the energetics of the transition state. k^o has been determined for many well characterised electrochemical systems and it typically ranges from $1 - 10^{-4}$ cm s^{-1}, although it lies outside this range for very fast and slow electrode kinetics. Systems that demonstrate a relatively high value of k^o respond rapidly to a change in potential whilst systems with low values require much larger changes in potential to drive the electron transfer. The change in potential is known as overpotential, η and is a measure of how much the potential deviates from the formal potential ($\eta = E\text{-}E^{o'}$).[21,22]

The Butler-Volmer equation (equation 2.31) shows the complete relationship between potential and current, however it has limitations. The concentration terms in the Butler-Volmer equation are strictly concentrations of the redox species at the electrode surface. How the redox species are transported to the electrode surface is a separate issue, but it is essential to realise that the Butler-Volmer equation requires surface concentrations and these may be different from the bulk.

2.2.7 Mass Transport

Mass transport describes the movement of the electroactive species to and from the electrode surface. This can be split into three separate modes, diffusion, migration and convection, with each one contributing to the total current.

2.2.7.1 Diffusion

Diffusion is the movement of a species through a solution due to a concentration gradient. This movement is governed by Fick's first law which describes the flux of ions as a change in concentration with respect to a specific position/coordinate

(equation 2.32). The second law describes the change in concentration at a specific position/coordinate with respect to time (equation 2.33),[4,23]

$$j_A(x,t) = -D_A \frac{\partial[\mathrm{A}](x,t)}{\partial x} \tag{2.32}$$

$$\frac{\partial[\mathrm{A}](\mathrm{x,t})}{\partial t} = D_A \left(\frac{\partial^2[\mathrm{A}](\mathrm{x,t})}{\partial x^2}\right) \tag{2.33}$$

Where D_A is the diffusion coefficient of species A. Equations 2.32 and 2.33 are based upon a single coordinate. When considering various geometries then other coordinates are considered and the equation generally includes the Laplace operator. This incorporates the function of all coordinates within a specified geometry.

A concentration gradient develops when a species becomes depleted or produced at the surface of an electrode. The concentration gradient exists in a small area that lies between the bulk solution and the electrode surface and is known as the diffusion layer. The size of the diffusion layer, δ_N, was estimated by Nernst by extrapolation through the linear region of the diffusion profile (Figure 2.6) to a concentration which was equal to that of the bulk solution.[2,6,10]

$$\frac{\partial[A]_0}{\partial x} = \frac{[A]_{bulk} - [A]_0}{\delta_N} \tag{2.34}$$

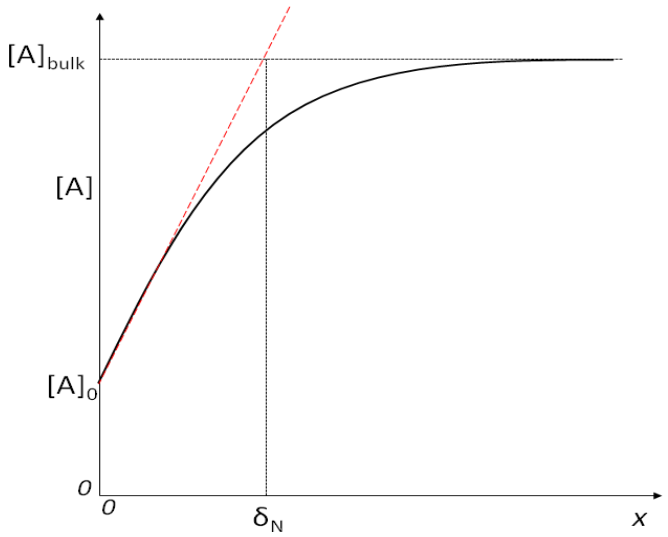

Figure 2.6: Diffusion profile at an electrode surface showing the diffusion layer adjacent to the electrode.

Hence the current produced in a reaction due to species A, is related to the diffusion layer by:

$$I_A = n\,F\,A\,j_a = n\,F\,A\,D_A\frac{[A]_{bulk}-[A]_0}{\delta_N} \quad (2.35)$$

2.2.7.2 Migration

Migration is the movement of a charged species through a solution due to a potential gradient. The flux of species A^z, where z is the charge associated with A in a single dimension, x, is given by:[2,4,6]

$$j_A = -\frac{z_A F}{RT} D_A[A]\left(\frac{\partial E}{\partial x}\right) \quad (2.36)$$

where z_A is the charge on species A, and all other symbols have been identified previously. It is fitting to simplify the mathematical treatment of an electrochemical system by reducing the contribution of migration so that it becomes negligible. This is achieved by addition of an electrochemically inert background electrolyte with a concentration typically greater than 0.1 M.[4] The high concentrations of background electrolyte successfully carry nearly all of the current in the bulk solution, thus it is migration of the background electrolyte that occurs and not of the electroactive species. This then leaves diffusion as the only mode of transport for the electroactive species. In addition to reducing the effect of migration the background electrolyte provides many other important benefits;

a) Addition of excess background electrolyte lowers the solution resistance reducing the observed ohmic drop.[2,4,6] The ohmic drop (solution resistance) can distort the current voltage response and prevent the electroactive species from experiencing the full potential difference.

b) The background electrolyte ensures a clear and defined double layer is observed and importantly remains thin in comparison with the diffusion layer. This ensures that the entire potential drop occurs across the double layer.[3]

c) The excess of electrolyte aids in maintaining a fixed ionic strength within the solution leading to activity coefficients of the respective electroactive species remaining constant. Thus allows the electrode potentials to be quoted as formal potentials.

2.2.7.3 Convection

Convection can be split in to two separate categories, natural or forced convection. Natural convection occurs as a result of gradients due to density, temperature or pressure.[24-26] Natural convection can be difficult to predict and interpret in a quantitative manor due to its unpredictable and random nature. However it is possible to avoid this as its contributions are not significant over a short time scale.[4] Forced convection occurs via an external force agitating the solution, commonly from stirring, pumping or hydrodynamic flow. The latter refers to a typical flow cell were solution is flowed over a stationary electrode[27] or the rotating disc electrode where the electrode is moved to induce laminar flow bringing solution to the electrode surface.[28]

2.3 Voltammetry

During electrochemistry experiments the primary focus is the reaction occurring at the surface of the working electrode. The heterogeneous electron transfer reaction occurring at the electrode can be studied in two ways, potentiostaticly and galvanostaticly. Potentiometric experiments involve controlling the potential at the working electrode, usually sweeping from an initial potential to second desired potential and recording the change in current. Galvostatic experiments involve controlling the current and the change in potential is recorded. Both methods can provide accurate and qualitative data, but in this instance potentiometric experiments are preferred. There are numerous potentiometric techniques available but the most widely used is cyclic voltammetry (CV) due to its relatively straight forward experimental setup and quantitative results. A second commonly used technique is the rotating disc electrode in conjunction with hydrodynamic processes. Both of the fore mentioned techniques are widely used in this work and will be covered in more detail.[2-4,6]

2.3.1 Cyclic Voltammetry

Cyclic voltammetry (CV) can be applied as a solution based analysis with the species under investigation being dissolved in solution containing a sufficient background electrolyte. CV can also be used when the species is absorbed on the surface of the

working electrode. In the situation where the species is dissolved in solution there are a number of characteristics that can be determined,[4] such as:

a) Formal potential ($E^{o'}$)

b) Reversibility of the system

c) Peak currents (I_p) and potentials (E_p) (oxidation and reduction)

d) Diffusion coefficient (D_o)

e) Estimation of standard rate constant (k^o) for electron transfer

A typical cyclic voltammogram is obtained by applying an external potential to the working electrode (E_1), where no redox process (of the electroactive species in question) takes place. The potential is then swept to a second potential (E_2) at a given scan rate, *v*, where the kinetics of the redox process are more rapid and give raise to a faradaic current. Once the potential reaches E_2, it is swept back to E_1 at the same rate as the forward sweep (Figure 2.7). If the experiment is concluded at potential E_2, this would correspond to a linear sweep voltammogram.

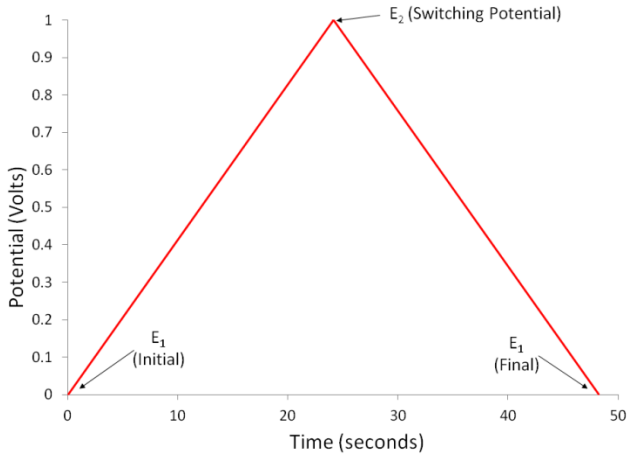

Figure 2.7: Change in voltage with time during a cyclic voltammetry experiment.

As can be seen from Figure 2.7 this results in a triangular wave shape representing the change in voltage with time. The current is a function of the applied potential and is measured after each specified increment. It is the change in current as a function of potential which is plotted to obtain the voltammogram. The applicable scan rate to these experiments can vary ranging from a few millivolts up to 1 megavolt per second.[29] The lower limit is restricted by the onset of natural convection due to the

time scale of the measurement being longer so that it is no longer negligible and leads to non-reproducible mass transport.[4] The upper limit can be restricted by charging effects upon the double layer and solution resistance lead to distortions in the voltammograms.[4]

Figure 2.8A shows a typical cyclic voltammogram one would obtain for the redox couple in equation 2.16. Where in this instance $E^{o'}$ = - 0.22 V, $[A]_{bulk}$ = 0.001 M with species B being absent prior to the reaction, see figure legend for all other parameters. The onset of the CV begins with the forward scan (reduction of species A) and as we approach $E^{o'}$ the current increases exponentially as described by equation 2.31. As the reaction continues, species A becomes depleted and a concentration gradient is established at the electrode surface. Continuing the reaction we reach a potential where the flux needed to sustain the exponential increase can no longer be sustained by diffusion and the exponential increase is no longer achieved. Eventually the diffusion layer has grown to a sufficient size as to decrease the concentration gradient and hence $j_{A,}$ to the electrode surface. The resulting decrease in flux resulted in the system passing through a maximum resulting in a peak reduction (cathodic) current, I_p^{red}.

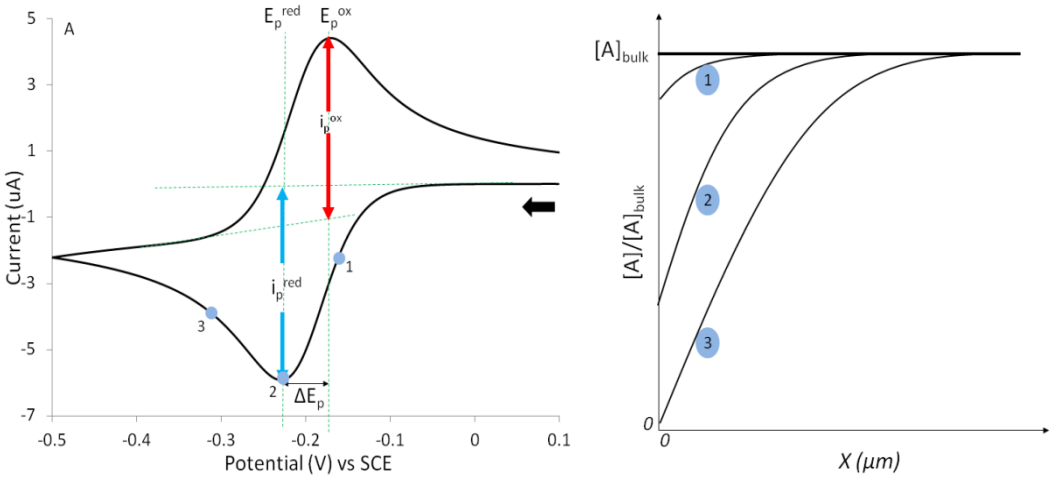

Figure 2.8: A) Typical CV obtained for a reversible one electron transfer process. $E^{o'}$ = -0.2 V, [A] = 0.001 M. D_o = 1 x 10^{-6} cm^2 s^{-1}, k^o = 0.1cm s^{-1}, v = 0.1 V s^{-1} and A = 0.076 cm^2. B) Change in concentration at three different stages of the cyclic voltammogram.

Figure 2.8B illustrates the concentration profiles at various stages through the reduction wave with respect to species A. At point 1, the concentration gradient is sufficient to maintain the current predicted by the Butler-Volmer equation. Upon

reaching point 2, the gradient is at its steepest and the rate of diffusion is no longer sufficient to maintain the exponential increase in current, hence a peak current is observed. Upon reaching point 3, the diffusion layer has grown significantly into the solution resulting in a shallower gradient and hence lower currents. Upon reaching potential E_2 the potential is swept in the reverse direction resulting in more positive potential being achieved. Initially at the electrode surface there is a large concentration of species B which undergoes oxidation at the electrode surface resulting in an anodic current. The concentration of B decreases in the same manner as seen for species A, resulting in a peak oxidation (anodic) current, I_p^{ox}, when the flux of B to the electrode surface via diffusion is no longer sufficient to maintain the exponential increase in current. The two separate waves give the CV its characteristic shape with the two peaks at two different peak potentials, E_p^{red} and E_p^{ox} respectively. The peak separation, ΔE_p, is the difference between the two peak potentials.

The cyclic voltammogram observed in Figure 2.8A is an example at a specific scan rate, *v*. By varying the scan rate we observe significant changes in the voltammetry (Figure 2.9). The increase in current with scan rate is shown by the relationship between the Nernst diffusion layer thickness and time (Equation 2.37). Based on this principle at higher scan rates electrolysis occurs over a much shorter time period resulting in a thinner diffusion layer. As seen from Figure 2.8B, the shorter time scale results in steeper concentration gradients resulting in an increased flux of material to the electrode surface, inevitably leading to larger faradaic currents.

$$\delta_N = \sqrt{2Dt} \tag{2.37}$$

Figure 2.9 shows the influence of scan rate upon the CV shape. Essentially this is the effect the rate of mass transport has upon the voltammogram shape. Electrode kinetics also affects the shape of the final voltammograms and in conjunction with mass transport dictates the shape of the forward and reverse waves. In the redox process outlined in equation 2.16, the change in potential experienced during the cyclic voltammetry experiment results in a constant shift in the equilibrium position brought about by changes in the concentration of both species (A and B). The rate at which the system reaches equilibrium is an important parameter and determines the electrochemical reversibility of the system. There are two extremes that describe the reversibility of a system which are a) electrochemically reversible and b)

electrochemically irreversible. It is important to note that the expressions of electrochemical reversibility in this context do not refer to the thermodynamics of the system, but simply the kinetics at the electrode solution interface.[10]

For an electrochemically reversible system the electron transfer is facile, such that the rate of electron transfer is faster than the rate of diffusion to the electrode surface.[2,4] This results in the system remaining at equilibrium during the potential sweep, thus to say the concentrations of the reactant and product at the electrode surface are maintained in order to satisfy the Nernst equation (equation 2.10). In this case where redox kinetics are so fast that no activation effects are seen and because the system constantly lies in a state of equilibrium no kinetic data for the electron transfer can be ascertained. Due to this reason electrochemically reversible systems are referred to as being diffusion controlled. A reversible system should demonstrate the characteristics outlined in Table 2.1.[6] Point 1 is a key parameter in the determination of electrochemical reversibility and should remain at 57 mV at all scan rates (for a single electron transfer).

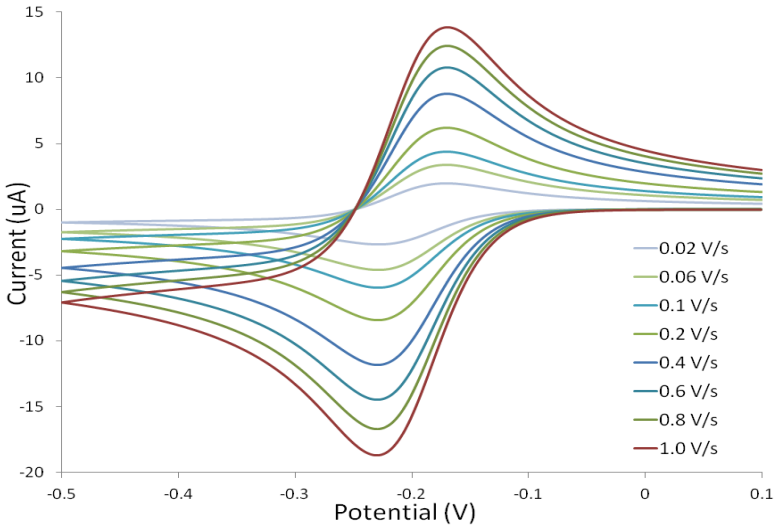

Figure 2.9: Effect of varying scan rate upon the cyclic voltammogram of the one electron redox process in equation 2.16. $E^{o'}$ = -0.2 V, [A] = 0.001 M. D_o = 1 x 10^{-6} cm^2 s^{-1}, k^o = 0.1cm s^{-1}, range of v 0.02 - 0.1 V s^{-1} and electrode area (A) = 0.076 cm^2.

The electrochemical reversible system is based upon fast electrode kinetics, however when we have the situation where the electrode kinetics are much slower than diffusion the system is described as electrochemically irreversible. This is on the basis of the system not obeying the Nernst equation and equilibrium at the electrode

surface is not maintained. In this case the flux of species A is no longer a diffusion boundary condition but a kinetic one. Combining equation 2.20 and 2.32 we obtain:

$$j_A = -D_A \frac{\partial[\mathrm{A}]}{\partial x} = k_{red}[A]_o \tag{2.39}$$

Table 2.1: Diagnostic tests for an electrochemically reversible system

Diagnostic tests for a reversible system
1) $\Delta E_p = \lvert E_p^c - E_p^a \rvert = 59$ mV/n
2) $\lvert I_p^a / I_p^c \rvert = 1$
3) E_p is independent of scan rate
4) I_p is proportional to $v^{1/2}$ (equation 2.38)

$$I_p = 2.69 \times 10^5 \, n^{3/2} A \, D_O^{1/2} C^* \, v^{1/2} \tag{2.38}$$

Figure 2.10 is an example of a typical voltammogram obtained for an electrochemically irreversible process. In this instance k^o is much lower compared to the value obtained for a reversible process. It is evident from Figure 2.10 that a much larger overpotential is needed to drive the reduction of species A. Typically only a single wave peak is observed due to ΔE_p being too large for peaks in both the forward and reverse waves to be within the desired potential range of interest. Here we can see that the primary characteristic determining electrochemical reversibility is the magnitude of k^o.

The domain between these two limits is known as quasi reversible. If we again consider the process in equation 2.16 and that k^o is sufficient to allow for a reversible process. It is has been shown that an increase in v does not affect ΔE_p (Figure 2.9), however if we continue to increase the scan rate we observe that ΔE_p no longer remains constant and increases with v (Figure 2.11). This is representative of a quasi-reversible behaviour. When the system is subject to the scan rates illustrated in (Figure 2.9) the electrode kinetics are fast enough to maintain equilibrium at the electrode surface. In Figure 2.11 at these relatively high scan rates ΔE_p no longer remains at 59 mV. Here we see that the rate of the electrode kinetics is no longer sufficient to maintain the equilibrium at the electrode surface and begin to limit the

current response. In this instance, the kinetics is the limiting factor making it possible for estimations to be made about the kinetic parameters. Figure 2.12 shows the effect of k^o upon the shape of the cyclic voltammogram based on equation 2.16 with all other parameters remaining the same as in Figure 2.8A.

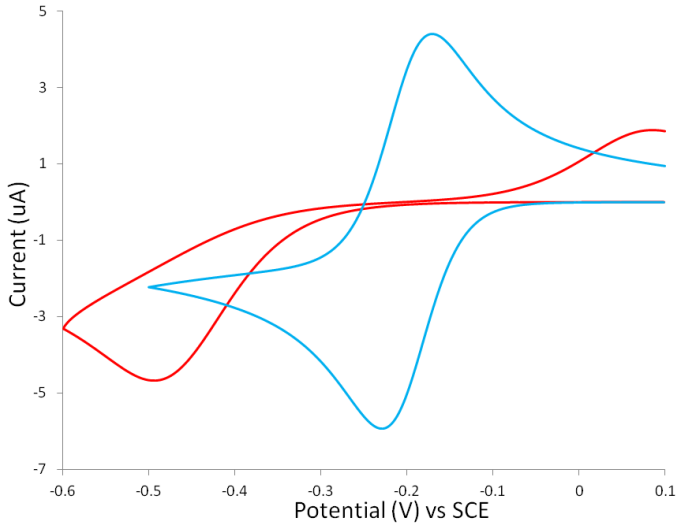

Figure 2.10: Overlay of a reversible, blue (k^o = 0.1 cm s^{-1}) and irreversible, red (k^o = 1 x 10^{-5} cm s^{-1}) cyclic voltammetry. Other parameters, $E^{o'}$ = -0.2 V, [A] = 0.001 M. D_o = 1 x 10^{-6} cm^2 s^{-1}, v = 0.1 V s^{-1} and A = 0.076 cm^2.

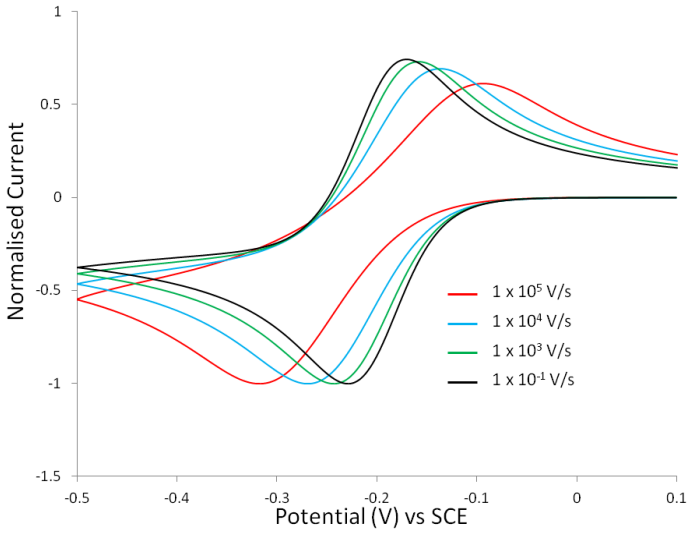

Figure 2.11: Overlay of cyclic voltammograms at significantly high scan rates. Other parameters $E^{o'}$ = -0.2 V, [A] = 0.001 M. D_o = 1 x 10^{-6} cm^2 s^{-1}, k^o = 0.1 cm s^{-1} and A = 0.076 cm^2.

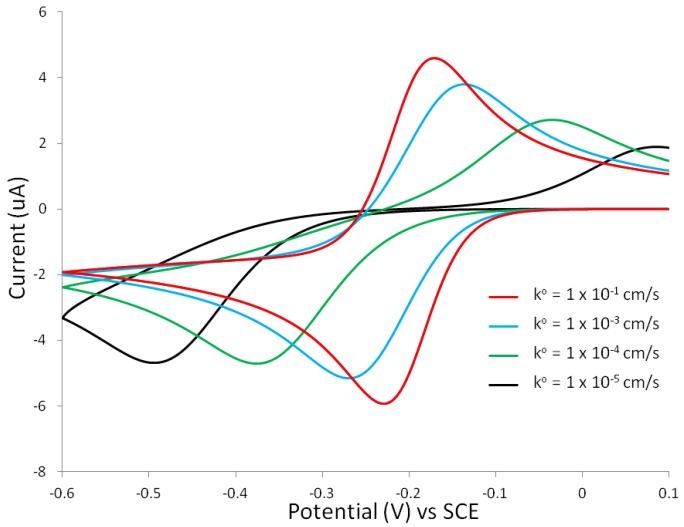

Figure 2.12: Overlay of cyclic voltammograms with varying values of k^o ranging from 0.1 to 1 x 10^{-5} cm s^{-1}.

The resulting trend seen is solely based upon the effect of varying k^o and shows the transition from a reversible to an irreversible system. It is evident that the value of k^o dictates the extent of reversibility and the 'category' in which the respective system is placed.

Reversible: $k^o \geq 0.3v^{1/2}$

Quasi-reversible: $0.3v^{1/2} \geq k^o \geq 2 \times 10^{-5}v^{1/2}$

Irreversible: $k^o \leq 2 \times 10^{-5}v^{1/2}$

The characteristics of a quasi-reversible system are shown in Table 2.2:[6]

Table 2.2: Diagnostic tests for an electrochemically quasi-reversible system

Diagnostic tests for a quasi-reversible system
1) $\Delta E_p \geq 59$ mV/n and increases with increasing v
2) $\lvert I_p^a / I_p^c \rvert = 1$ provided $\alpha_a = \alpha_c = 0.5$
3) E_p^c shifts negatively with increasing v
4) $\lvert I_p \rvert$ increase with $v^{1/2}$ but is not proportional

It has been stated previously that due to a reversible system being diffusion controlled it is not possible to ascertain any kinetic data. However in the case of a quasi-reversible system, electrode kinetics influence the rate of the electrode reaction

and therefore it is possible to obtain kinetic data. Based on the cyclic voltammetry it is possible to determine the experimental heterogeneous standard rate constant for electron transfer, k^o. There a numerous methods developed to calculate k^o on the basis of peak potential separation ΔE_p.[2,4] Here we will briefly consider the method of Nicholson.[30]

The method of Nicholson relates k^o to ΔE_p through the dimensional parameter Ψ, described in equation 2.40

$$\Psi = \frac{\gamma k^o}{(\pi a D_o)^{1/2}} \tag{2.40}$$

where γ and a are given by:

$$\gamma = \frac{D_{o(ox)}}{D_{o\,(Red)}} \qquad a = \frac{nFv}{RT}$$

Where $D_{o(ox)}$ and $D_{o(Red)}$ are the diffusion coefficients for the oxidised and reduced species. If γ the diffusion coefficients of the respective oxidised and reduced species are equal then equation 2.40 simplifies to;

$$\Psi = \frac{k^o}{\left(\pi D_o \frac{nFv}{RT}\right)^{1/2}} \tag{2.41}$$

Figure 2.13 shows the relation between Ψ and experimental peak separation.

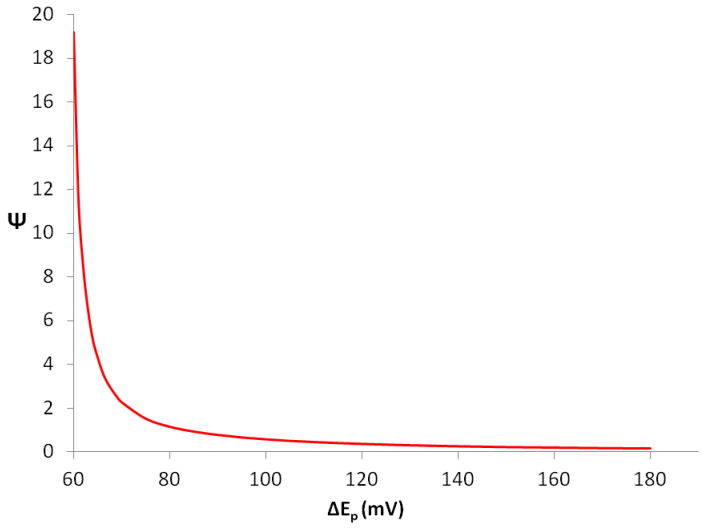

Figure 2.13: Dependence of Ψ on peak separation.

2.3.2 Hydrodynamic Voltammetry

2.3.2.1 Modification of Fick's Law

Section 2.4.7 illustrated the general equations for the flux of species A based on the individual mass transport effects and Ficks law. Overall the flux of species A in a single dimension is given by;[4]

$$j_A = -D_A \frac{\partial[\mathrm{A}](x,t)}{\partial x} - \frac{z_A F}{RT} D_A[\mathrm{A}]\left(\frac{\partial E}{\partial x}\right) + V_{\mathrm{x}} \frac{\partial[\mathrm{A}]}{\partial x} \quad (2.42)$$

where the right hand side of the equation contains the contributions from diffusion, migration and convection. For reasons described in section 2.2.7 we are able to eliminate the migration term from the flux equation. Equation 2.42 describes the flux of species A at a given point. Equation 2.43 describes the change in concentration at a given point with time (Fick's second law).

$$\frac{\partial[\mathrm{A}]}{\partial t} = D_A \left(\frac{\partial^2[\mathrm{A}])}{\partial x^2}\right) - V_{\mathrm{x}} \frac{\partial[\mathrm{A}]}{\partial x} \quad (2.43)$$

In the absence of convection, V_{x} = 0, equation 2.44 is reduced to the simplified diffusion equation (equation 2.33).

2.3.2.2 The Rotating Disc Electrode

A small metallic (often platinum or glassy carbon) disc is embedded centrally within a large insulated cylinder and acts as the working electrode. The cylinder is placed in solution and rotated at a constant speed. This rotation causes the solution to move in a well defined pattern. The rotation of the electrode acts as a pump and draws (fresh) solution up vertically (along the x axis) to the electrode surface and then dispersed outwards (Figure 2.14).[31]

The rotation of the electrode enables a steady supply of fresh electrolyte to the electrode allowing for steady state voltammetry. For steady state voltammetry a laminar flow must be established, if rotation is too slow the flow is not sufficient. If rotation is too fast then turbulent flow is observed and steady state voltammetry is not possible. The range of rotation can be calculated based up the Reynolds number which is given by equation (2.44) and (2.45):[7]

Upper rotation limit: $$Re = \frac{\omega r_1}{v} \quad (2.44)$$

Lower rotation limit: $$\omega > 10\ \frac{v}{r_1^2} \quad (2.45)$$

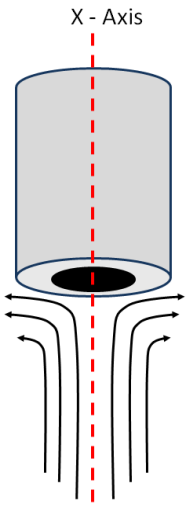

Figure 2.14: Radial dispersion and laminar flow of a solution at the rotating disc electrode solution interface.

Where ω is the rotation speed (Hz), r_1 is the radius of the electrode (cm) and in this instance; v is the kinematic viscosity of the solution. Laminar flow is established providing the Reynolds number does not exceed the critical value of ca. 2 x 10^3 but is sufficient to satisfy equation 2.45. The hydrodynamics of the rotating disc electrode when under the conditions of laminar flow were derived by Von Karman and Cochran,[32] respectively. They identified a hydrodynamic layer thickness and described its relationship with the kinematic viscosity and rotation speed of the electrode:

$$x_H = \sqrt{v/2\pi\omega} \quad (2.46)$$

where x_H the hydrodynamic layer thickness and v is the kinematic viscosity. Note that ω is converted to radians through the multiplication by 2π. Equation 2.46 leads to estimations of x_H and for typical rotations speeds that fall within the range of 1 -50 Hz yields x_H to range from 0.1 to 1 mm^2. This leads to the notation that this is roughly an order of magnitude larger than a typical diffusion layer. It is important to note the velocity components that arise from each of the three cylindrical

coordinates, V_x V_r and V_ϕ which correspond to the RDE. The three components correspond to the velocity for the axial, radial and azimuthal components. At the electrode surface the velocity contributions from the radial and axial contributions are zero resulting in the azimuthal velocity being the sole contributor. This allows the velocity at the electrode surface or how fast the solution is spun about the disc with radius r, to be expressed as;

$$V_\phi = 2\pi\omega_r \tag{2.47}$$

The axial velocity profile, V_x (along the x axis, Figure 2.14) is independent of V_r and V_ϕ, hence the velocity profile supplying fresh solution to the electrode surface is uniform over the entire surface. This simplifies the treatment of the rotating disc in comparison to other hydrodynamic techniques, leading to equation 2.43. Levich used the understanding of the solution velocity being only dependent upon a single coordinate to estimate the diffusion layer thickness at the rotating disc electrode;

$$\delta_D = 0.643\ \omega^{1/2}\nu^{1/6}D^{1/3} \tag{2.48}$$

Where δ_D is the diffusion layer and ν is again the kinematic viscosity. The ratio of the diffusion to the hydrodynamic layer thickness is given by manipulation of equations 2.46 and 2.47 to give:[2,31]

$$\frac{\delta_D}{x_H} = 1.61\left(\frac{\mathrm{D}}{\nu}\right)^{1/3} \tag{2.49}$$

Based on typical values of D_o = 1 x 10^{-5} cm^2 s^{-1} and ν = 0.01 cm^2 s^{-1} we obtain,

$$\frac{\delta_D}{x_H} = 0.16 \tag{2.50}$$

This illustrates that the diffusion layer is significantly small compared to the hydrodynamic layer. This provides a model for the change in concentration near the electrode surface, analogous to that of the diffusion process (Figure 2.6). In this instance we see an efficiently mixed bulk phase and a stagnant diffusion layer (Figure 2.15).[31]

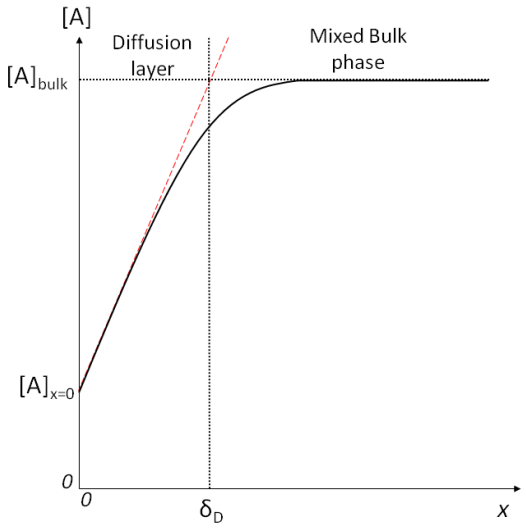

Figure 2.15: Diffusion layer thickness at a rotating disc electrode showing the clear separation between the diffused and mixed bulk layers.

Figure 2.15 suggests that the steepest gradient and hence highest current that can be attained when the $[A]_{x=0}$ is zero. This is achieved when a significantly large overpotential is applied to reduce all of species A that can diffuse to the electrode surface, based upon the redox process outlined in equation 2.16.

$$A + e^- \underset{k_{ox}}{\overset{k_{red}}{\rightleftharpoons}} B$$

The corresponding limiting current is given by equation 2.51, known as the Levich equation:[4]

$$I_L = 0.62\, n\, A\, F\, D_o^{2/3}\, \nu^{-1/6} C^*\, \omega^{1/2} \tag{2.51}$$

Where I_L is the limiting or Levich current and A is the electrode area. The Levich equation describes how the limiting current of a system varies with rotation speed. It shows that current should be proportional to rotation speed provided laminar flow is observed. This allows the experimentalist to manipulate the concentration profile and compress or extend the diffusion layer by varying the rotation speed.

When the conditions of the Levich equation are met, a plot of I_L vs. $\omega^{1/2}$ should be linear and pass through the origin, with the slope being used to calculate the diffusion coefficient of the electro active species. If the relationship between rotation rate and

the Levich current is not linear this signifies that mass transport effects are not the rate limiting factor and that the electron transfer kinetics are the rate limiting step.

2.3.2.3 Applying the Butler-Volmer Equation

The Butler-Volmer equation may be applied to simple electrochemical reactions that are not limited by mass transport effects; hence electron transfer kinetics is the rate limiting step. Assuming the solution is sufficiently stirred to ensure that concentrations at the electrode surface do not differ from that in the bulk, we can describe the reaction using the following Butler Volmer equation, expressed here in terms of exchange current, I_o as opposed to k^o seen previously.

$$I = I_o \left[e\left(\frac{\alpha_a n F}{RT}\eta\right) - e\left(-\frac{\alpha_c n F}{RT}\eta\right) \right] \tag{2.52}$$

The Butler Volmer equation is valid over a wide range of overpotentials but can be expressed differently depending on the magnitude of η. Assuming a one electron transfer, at small overpotentials (η < 0.01 V) and when $\alpha_c = \alpha_a = 0.5$ we observe linear characteristics. When x is small in the term e^x this can be simplified to 1 + x and we obtain:

$$I = I_o \frac{n F}{RT} \eta \tag{2.53}$$

At large values of η it is possible to exclude one of the bracketed terms in equation 2.52 as it becomes negligible. For example;

Large negative overpotentials;

$$I = I_o e\left(-\frac{\alpha_c n F}{RT}\eta\right) \tag{2.54}$$

And at large positive overpotentials;

$$I = I_o e\left(\frac{\alpha_a n F}{RT}\eta\right) \tag{2.55}$$

Equations 2.54 and 2.55 are known as the Tafel[33] equations and will hold true providing the backward reaction contributes less than 1 % of the overall current.

Using equation 2.56 this gives that an overpotential of approximately 118 mV at room temperature to meet this condition.[4]

$$\frac{e^{(1-\alpha)f\eta}}{e^{-\alpha f\eta}} = e^{f\eta} \leq 0.01 \tag{2.56}$$

The Tafel equation is normally expressed in the base 10 log form, hence by plotting Log *I* *vs.* η (Figure 2.16) we can extract the exchange current of the electrochemical process.

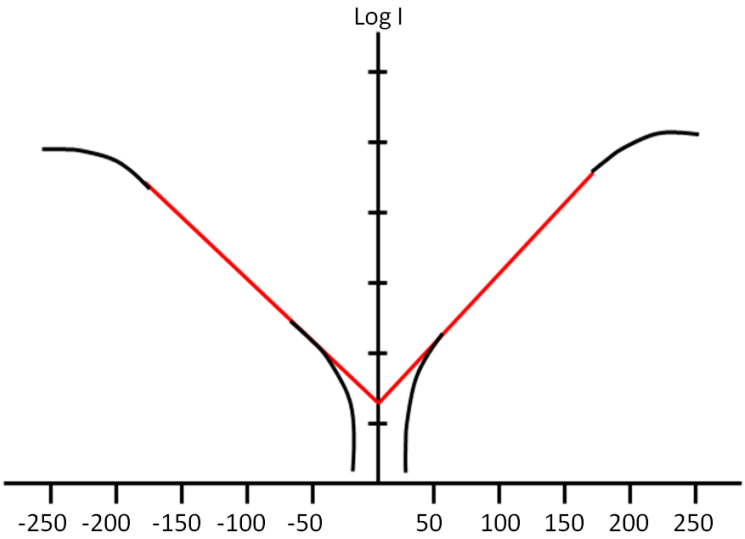

Figure 2.16: Example Tafel plot identifying the linear region (redline) for extrapolation of I_o.

Tafel plots contain three distinct regions; at low overpotentials the plots deviate from the linear behaviour due to the overpotential approaching zero, where the opposing reaction can no longer be considered negligible. Hence equation 2.54 and 2.55 are no longer valid and must take on the form of equation 2.52 as total current $I = I_a + I_c$. At large overpotential the current rises rapidly (due to the exponential factors dominating behaviour in equation 2.54 and 2.55), but at extreme overpotentials the current plateaus. In these regions current is no longer limited by electron transfer kinetics but by mass transfer, hence surface concentrations will differ from those of the bulk and equation 2.52 is no longer valid.[4] At these overpotentials the surface and bulk concentrations are no longer in unity and this must be considered.

$$I = I_o \left[\frac{C_O(0,t)}{C_O^*} e\left(\frac{\alpha_a\, n\, F}{RT}\eta\right) - \frac{C_R(0,t)}{C_R^*} e\left(-\frac{\alpha_c\, n\, F}{RT}\eta\right) \right] \tag{2.57}$$

The concentration factors in equation 2.57 now moderate the exponential factor hence the rapid increase in current is subdued at higher overpotentials. At extreme overpotentials it is still possible to remove one of the terms as its contribution to overall current remains negligible.

2.5.2.4 Exchange Current

The exchange current (I_o) is a fundamental property of an electrode's behaviour when the net current is zero and the electrode adopts a potential based on the concentrations of the oxidised and reduced species within the bulk solution. Though there is no net current at this equilibrium potential, we can imagine that the faradaic currents ascribed to the anodic and cathodic processes are equal in magnitude to the exchange current I_o;

$$I_o = nFAk^o C_O^* e^{-\alpha f(E_{eq} - E^{o\prime})} \tag{2.58}$$

Equation 2.58 shows that the exchange current is proportional to the standard rate constant can be substituted for k^o in kinetic equations.[4] The advantage of this being that the current can now be described in terms of the deviation from the equilibrium potential, also known as overpotential. The exchange current is dependent upon a number of factors, particularly the electrodes surface and its physical parameters, thus the exchange current is commonly normalised to the area of the electrode surface to give the exchange current density (J_o), which is expressed as current per unit area e.g. mA cm^{-2}.

The effect of the exchange current density upon overpotential is evident in equation 2.58. A redox system demonstrating a large exchange current density can generate larger currents at a given overpotential than an analogous system with a small exchange current density at the same overpotential (Figure 2.17). It is this relationship that makes the exchange current a key parameter in fuel cell catalysis. The key aim in fuel cell kinetics is to achieve the highest current with minimal overpotential or activation polarization. In short the higher the exchange current density the smaller the activation polarization.

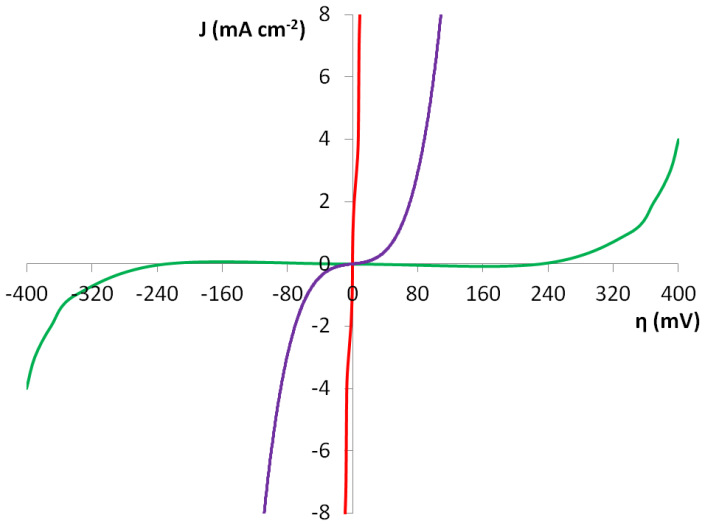

Figure 2.17: Effect of the exchange current density upon the current density generated at varying overpotential. Red, $J_o = 10^{-3}$ mA cm^{-2}, purple, $J_o = 10^{-6}$ mA cm^{-2} and green, $J_o = 10^{-9}$ mA cm^{-2}

2.4 UV-Visible Spectroscopy

2.4.1 Instrument

UV-Visible spectroscopy measurements were carried out on a PowerWave HT Micro plate Spectrophotometer at wavelengths ranging from 250 – 900 nm. Samples were placed into well plates at a known concentration and their absorbance as a function of wavelength recorded.

2.4.2 Background and Theory

When comparing different compounds, be it in solution or the solid state one obvious difference is their colour. $CuSO_{4(aq)}$ is blue, $NiCl_{2(aq)}$ is green and $PbI_{2(s)}$ is yellow. These colours are not just limited to transition metal based structures but are also observed in organic structures such as quinone (yellow), chlorophyll (green) and aspirin (colourless). Sunlight or white light is seen as a uniform colour by the human eye but is actually a composite of a broad range of wavelengths that span the visible (VIS) region of the electromagnetic spectrum. The composite of visible colours can be observed when passing white light through a prism (Figure 2.18) which consequently refracts the light in varying degrees (dispersion angle) according to wavelength.[34,1]

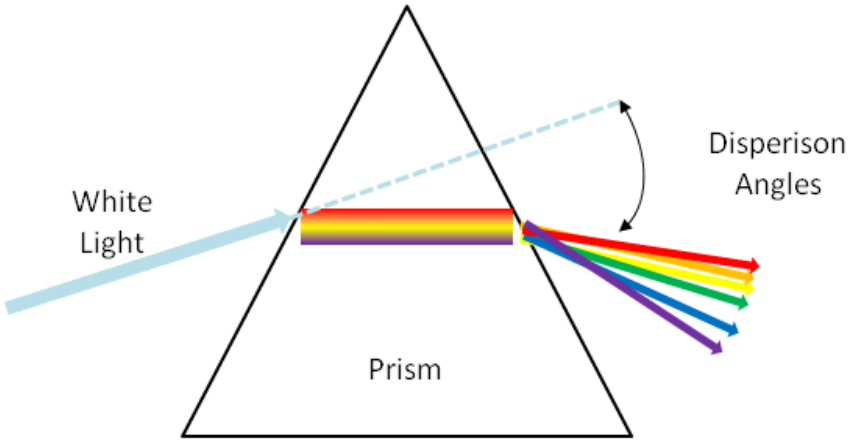

Figure 2.18: Separation of white light when passed through a prism.

It is normal to think of electromagnetic radiation as a wave containing the fundamental properties wavelength, frequency and amplitude (Figure 2.19).[35] The wavelength is the distance between two adjacent peaks usually given in meters, while the amplitude is the height of the peaks with respect to the zero point line. Frequency is a measure of the number of waves that pass a specific point within a given time. Frequency and wavelength are related by:[1,35]:

$$v = \frac{c}{\lambda} \tag{2.59}$$

Where λ is wavelength in metres, *v* is frequency in Hertz and *c* is the speed of light in m s^{-1} and the at a specific frequency the energy of the wave is given by:

$$E = hv \tag{2.60}$$

where *E* is energy, *h* is Plank constant and *v* is frequency.[1,34,35]

The absorption of electromagnetic radiation within the UV-Vis region can be sufficient to cause a transition in the electron energy levels of a molecule. This results in an electron being promoted from an occupied orbital (ground state or HOMO) to an empty orbital (excited state or LUMO) as illustrated in Figure 2.20.

However, this will only occur providing the energy of the radiation (wave) is equal to that of the transition.[34] It is evident from equations 2.59 and 2.60 that waves of

shorter wavelength are higher in energy. In organic (and inorganic depending upon electron configuration) molecules there are several possible transitions with energy differences between the transitions typically falling within the range of 152 – 650 kJ/mole. The σ orbitals are commonly the lowest energy orbitals resulting in σ bonds, followed by π orbitals, non-bonding (n) orbitals and finally antibonding orbitals (σ^* and π^*). Figure 2.21 illustrates the relative energy of specific orbitals and transitions available.[34,35]

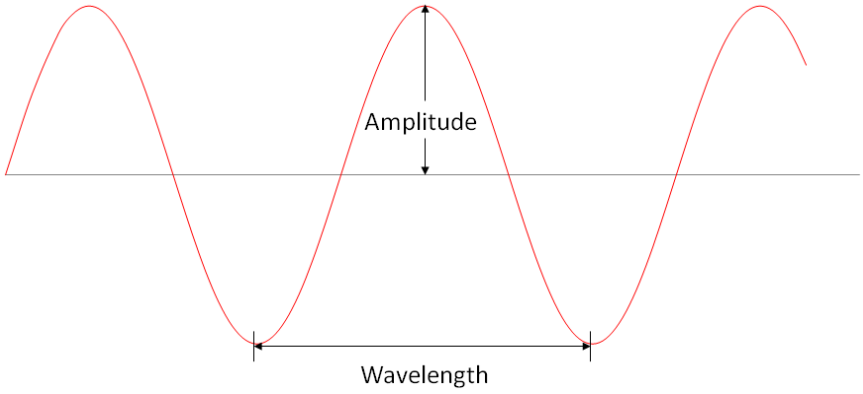

Figure 2.19: Characteristics of single wave showing the magnitudes of wavelength and amplitude respectively.

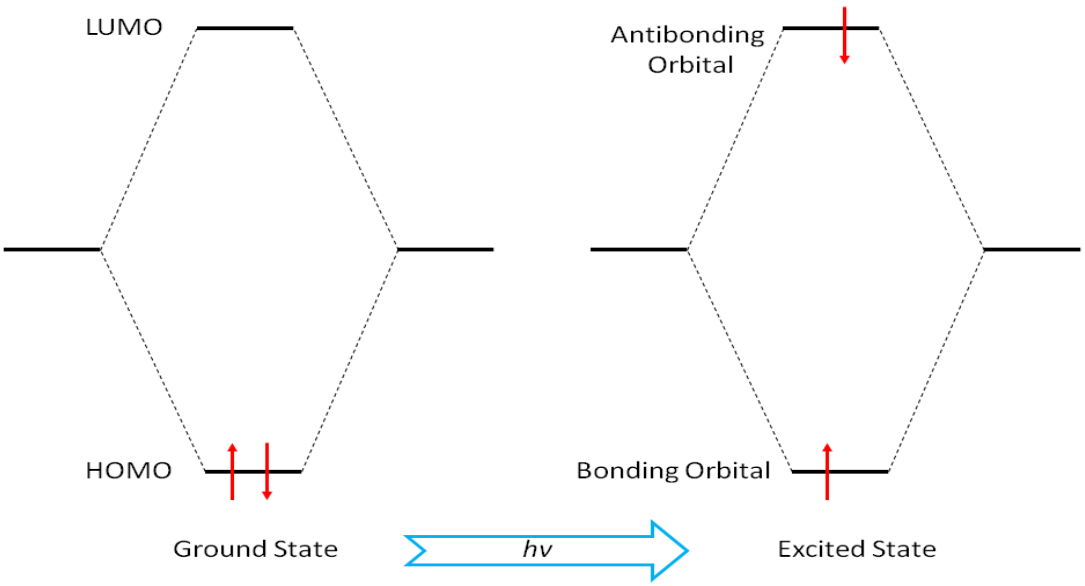

Figure 2.20: Excitation process on an electron from the HOMO to the LUMO during the absorption of an electromagnetic wave with energy equal to that of the transition.

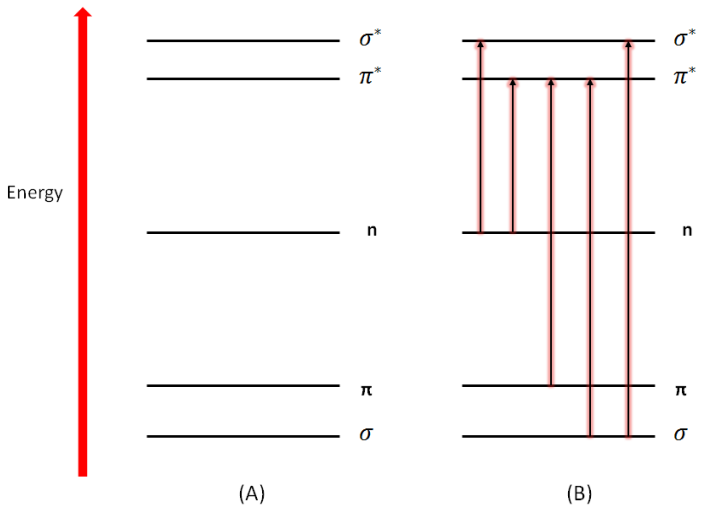

Figure 2.21: A) Energy of various orbital's within a molecule B) Possible transitions from occupied to empty orbitals. The magnitude of the arrow between each transition is a comparison of the energy required to make the transition.

Figure 2.21B shows the potential transitions from occupied to empty orbitals with the magnitude of the transition arrow indicating the energy required for each individual transition. It is also evident that the energy required to bring about a transition from the highest occupied molecular orbital (HOMO) to the lowest unoccupied molecular orbital (LUMO) is less compared to the resulting transition originating from a lower occupied orbital. Thus a $\pi \longrightarrow \pi^*$ transition would have lower energy than a $\sigma \longrightarrow \pi^*$ transition. Table 2.3 outlines typical compounds which observe these possible transitions.

Table 2.3: Compounds associated with the respective energy level transitions.[34]

Transition	Compound
$\boldsymbol{\sigma \longrightarrow \sigma^*}$	Alkanes
$\boldsymbol{\sigma \longrightarrow \pi^*}$	Carbonyl Compounds
$\boldsymbol{\pi \longrightarrow \pi^*}$	Alkenes, Carbonyls, Alkynes, Azo compounds
$\mathbf{n} \longrightarrow \boldsymbol{\sigma^*}$	Oxygen, Sulphur, Nitrogen and Halogen compounds
$\mathbf{n} \longrightarrow \boldsymbol{\pi^*}$	Carbonyl compounds

The transitions outlined in Table 2.3, which result from an excitation from the ground state to an excited state result from absorbance of ultraviolet radiation i.e. wavelengths below 400 nm. The visible electromagnetic spectrum lies between 400 and 750 nm. As seen from Figure 2.18 when white light is refracted through a prism

we observe all wavelengths in the visible region and hence the array of colours associated with these wavelengths (Figure 2.22). Some organic compounds absorb visible light but are usually highly conjugated systems resulting in shifts to longer wavelengths.[36] Simple alkenes contain a single double bond and the $\pi \longrightarrow \pi^*$ transition absorbs ultraviolet light at a wavelength of approximately 175 nm.[34] Increasing conjugation within the structure reduces the HOMO- LUMO gap hence the energy of the transition is reduced e.g. β-carotene which contains 11 double bonds and absorbs visible light at a wavelength of 465 nm.[37,38] However it is not just highly conjugated systems that absorb visible light and appear coloured to the naked eye; transition metals (and complexes) also absorb visible light.

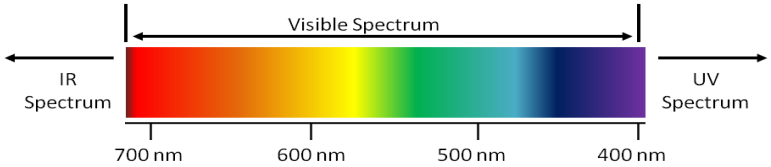

Figure 2.22: Visible region of the electromagnetic spectrum identifying the corresponding wavelngths associated with each observed colour

The transitions experienced in transition metal complexes are due to either d-d transitions, ligand to metal charge transfer (LMCT) or metal to ligand charge transfer.[39] This phenomenon of 'colour' within a compound however is a little more complex than first perceived. If a compound absorbs visible light then it naturally appears to have colour. However if the compound absorbs light in the visible region it does not possess the colour corresponding to the wavelength absorbed[34,39]. The colour observed for an object or solution is not due to the substance emitting light, this is reserved for fluorescence and phosphorescence. The case in this instance is we see the light that is reflected (e.g. solids) or for substances that are transparent we see light that is transmitted (e.g. solutions). The colour observed is not that which is absorbed but its complementary colour.

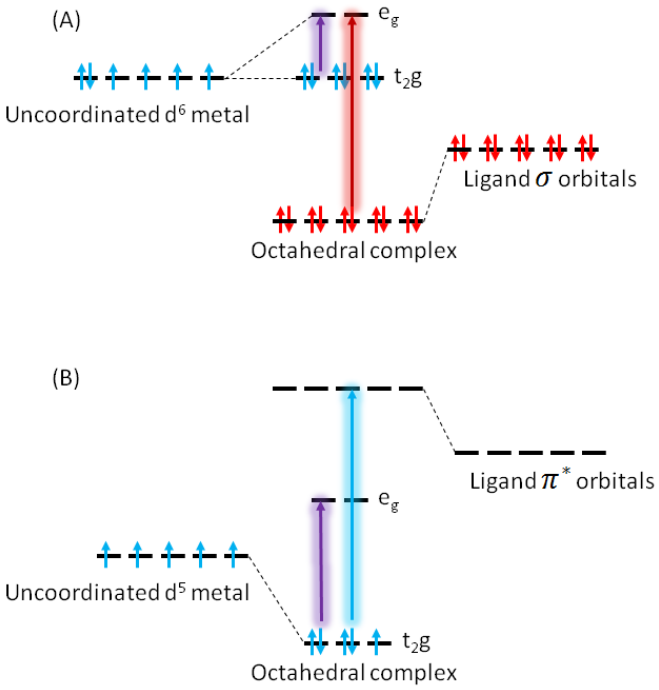

Figure 2.23: A) Ligand to metal transfer from a low lying filled ligand molecular orbital to a vacant d-orbital shown (red arrow) as well as the possible d-d transition (purple arrow). B) Metal to ligand transfer from a d-orbital to a low lying vacant ligand orbital (blue arrow) and the possible d-d transition (purple arrow).

2.5 Solution Nuclear Magnetic Resonance Spectroscopy

NMR data was collected on a Bruker Avance 400 MHz system fitted with a 5 mm broadband inverse (BBFO) probe with automatic tuning and matching capability (ATM) and a SampleJet autosampler. Data was collected at 25 ^{o}C at a frequency of 161.97 MHz for ^{31}P, 105.24 MHz for ^{51}V and 400.13 MHz for ^{1}H. Deuterated solvents were used as obtained from Sigma-Aldrich and all spectra are referenced to specified standards.

2.6 Fourier Transform Infrared Spectroscopy (Attenuated Total Reflectance)

FT-IR measurements were performed on a Bruker Tensor 27 spectrometer fitted with an Attenuated Total Reflectance attachment. Samples were analysed as either KBr discs or using the ATR attachment for 16 scans with a resolution of 4 cm^{-1}. All spectra were recorded in transmission mode.

2.7 Raman Spectroscopy

Raman spectroscopy measurements were carried out on a Renishaw inVia Raman microscope. Samples analysed in the solid phase between 150 and 1200 cm^{-1} with a resolution of 5 cm^{-1}. All samples were kindly run by Mr Iain Aldous

2.8 X-ray Diffraction

Single crystal X-ray data was collected in the department using a Rigaku VariMax rotating anode fitted with a Saturn724+ CCD detector and graphite monochromated Mo radiation at 93 K. Analysis was carried out by Dr. M. Little.

2.9 Scanning Electron Microscopy and Energy Dispersive X-ray Spectroscopy

SEM and EDX measurements were run using a Hitachi-S4800 Scanning Electron Microscope. A small piece of the sample was adhered to a stud using Araldite resin and coated with gold using an EMITECH K550X sputter coater for 2 minute at 20 mA prior to measuring. All samples were kindly run by Dr Tom Hasell.

2.10 pH and Conductivity

Conductivity and pH measurements were carried out using a Mettler Toledo S47-K SevenMulti dual meter. All measurements were carried out in solution with equipment calibrated daily using standard pH and conductive solutions.

2.11 Thermogravimetric Analysis

Thermogravimetric analysis (TGA) was performed on a TA instruments Q5000IR TGA which incorporated an automated overhead thermo balance. Samples were heated at a rate of 10 ^{o}C up to 800 ^{o}C.

2.12 Inductively Coupled Plasma Optical Emission Spectroscopy

Inductively Coupled Plasma Atomic Emission Spectroscopy (ICP-AES) was performed by Mr. George Miller within the departmental service. Sample measurements were performed utilising a Spectro Ciros ICP-OES radial view instrument.

Instrument parameters from optimisation were, plasma power 1360 W with a nebulising flow of 0.9 L min^{-1}, coolant flow of 13.0 L min^{-1} and auxiliary flow of 0.8 L min^{-1}. Line selection for each element was P 177.495 nm, S 180.731 nm, B 249.773 nm, Mo 202.030 nm, Nb 309.418 nm, Co 228.616 nm, V 292.464 nm, Ni 231.604 nm, Ta 240.063 nm, Sn 189.991 nm. Typical RSD values were between 1-1.5 % indicating a stable plasma with consistent sample injection and aspiration.

2.13 Molecular Similarity Testing

Molecular models were created based on X-ray crystallographic data using Accelrys Materials Studio 5.0. Similarity was determined using the consensus method within the software. This method aligns the inputted structures to find the best overall fit. Structural analysis was performed by Mr. D Holden.

2.14 Digital CV simulation

Cyclic Voltammetry simulations were carried out using DigiElch 7.2 software. Simulated data was fitted to experimental data to obtain or confirm standard rate constants for electron transfer and diffusion coefficients. CV simulations were constructed under room temperature conditions with all other parameters described within the chapter in question.

2.15 References

(1) Atkins, P.; Paula, J. *Physical Chemistry*; W H Freeman & Company, 2006.

(2) Compton, R.; Banks, C. *Understanding Voltammetry*; World Scientific Publishing, 2007.

(3) Koryta, J.; Dvořák, J.; Kavan, L. *Principles of electrochemistry*; John Wiley & Sons Inc, 1992.

(4) Bard, A.; Faulkner, L. *Electrochemical Methods: Fundamentals and applications*; 2nd ed.; Wiley, New York, 2000.

(5) Fisher, A. *Electrode Dynamics (Oxford Chemistry Primers)*; 1st ed.; Oxford University Press, 1996.

(6) Pletcher, D. *Instrumental Methods in Electrochemistry*; Horwood Pub Limited, 2000.

(7) Zoski, C. *Handbook of Electrochemistry*; 1st ed.; Elsevier Science Limited, 2007.

(8) Rubinstein, I. *Physical Electrochemistry*; CRC Press Llc, 1994.

(9) Martins, G. *Journal of Chemical Education* **2005**, 482-483.

(10) Atkins, P.; Paula, J. *Physical Chemistry*; 8 ed.; Oxford University Press, 2006.

(11) Dickinson, E. J.; Compton, R. G.; Limon-Petersen, J. G. *Journal of Solid State Electrochemistry* **2011**, 1335-1345.

(12) Srinivasan, S. *Fuel Cells: Fundamentals and Applications* **2006**, 27-92.

(13) Chapman, D. *Philosophical Magazine* **1913**, *25*, 475-481.

(14) Gouy, M. *Jounral of Theoretical and Applied Physics* **1910**, 457 - 468.

(15) Stern, O. *Elecktrochem* **1927**, *30*, 508.

(16) Grahame, D. *Journal of The Electrochemical Society* **1951**, *98*, 343.

(17) Butler, J. *Transactions of the Faraday Society* **1924**, 659-665.

(18) Butler, J. *Transactions of the Faraday Society* **1924**, 729-733.

(19) Butler, J. *Transactions of the Faraday Society* **1924**, 734-739.

(20) Gerischer, H.; Ekardt, W. *Applied Physics Letters* **1983**, *43*, 393-395.

(21) Marcus, R. In *Advances in Chemical Physics*; Advances in Chemical Physics, 1999; Vol. 106, pp. 1-6.

(22) Marcus, R. *Journal of Electroanalytical Chemistry* **2000**, *483*, 2-6.

(23) Fick, A. *Philosophical Magazine* **1855**, *10*, 30-39.

(24) Taylor, J.; Hanratty, T. *Electrochimica Acta* **1974**, *19*, 529-533.

(25) Incropera, F.; Dewitt, D. *Introduction to heat transfer*; John Wiley and Sons,: New York, NY, 1985.

(26) Kays, W.; Crawford, M.; Weigand, B. *Convective heat and mass transfer*; McGraw-Hill Higher Education, 2005.

(27) Tokuda, K.; Aoki, K.; Matsuda, H. *Journal of Electroanalytical Chemistry and Interfacial Electrochemistry* **1977**, *80*, 211-222.

(28) Jordan, J.; Javick, R. *Electrochimica Acta* **1962**, *6*, 23-33.

(29) Amatore, C.; Maisonhaute, E.; Simonneau, G. *Electrochemistry Communications* **2000**, *2*, 81-84.

(30) Nicholson, R. *Analytical Chemistry* **1965**, *37*, 1351-1355.

(31) Nikolic, J.; Expósito, E.; Iniesta, J. *Journal of Chemical Education* **2000**, *77*, 1191 - 1194.

(32) Cochran, W.; Goldstein, S. *Mathematical Proceedings of the Cambridge Philosophical Society* **1934**, *30*, 365.

(33) Tafel, J. *Zeitschrift für Physikalische Chemie* **1905**, 641 - 712.

(34) Donald, P. L. *Introduction to Spectroscopy*; 4 ed.; Brooks/Cole Publishing Company, 2008; pp. 381-417.

(35) Harwood, L.; Claridge, T. *Introduction to Organic Spectroscopy*; Oxford University Press, USA, 1996.

(36) Eakins, G. L.; Alford, J. S.; Tiegs, B. J.; Breyfogle, B. E.; Stearman, C. J. *J. Phys. Org. Chem. 24*, 1119-1128.

(37) Liu, R. *Journal of Chemical Education* **2002**, *79*, 183-185.

(38) Sklar, A. *Reviews of Modern Physics* **1942**, *14*, 232-245.

(39) Shriver, D.; Atkins, P. *Inorganic Chemistry*; 4 ed.; W. H. Freeman, 2006.

Chapter 3

Determining the Applicability of Mixed Addenda Polyoxometalate Systems of the General Formula $Na_xH_3PMo_{12-x}V_xO_{40}$ (x = 1 - 4) as Catholytes for FlowCath® Technology: Electrochemical Analysis and Simulation.

Table of Contents

3.1 Introduction

The chemistry of polyoxometalates has been well studied by Pope, Muller, Kozhevnikov, Neumann and co-workers over the past forty years with the main research focused upon their catalytic properties.[1-8] A specific subset of the polyoxometalate family, phosphomolybdovanadates, have been well investigated not only for their catalytic properties as highlighted in chapter 1, but also for their unique ability to undergo oxidation via the oxygen reduction reaction (ORR).[8-13,14] Combining the well documented redox properties of the vanadium centres,[15-19] and their capabilities in the ORR make these compounds ideal candidates for FlowCath® technology. Although the electrochemistry of the phosphomolybdovanadate series has been investigated previously, there are still questions that remain. Previously the electrochemistry, in particular their cyclic voltammetric behaviour has been studied. However, a consideration of the effect the natural speciation in aqueous solution of these compounds has upon the electrochemical properties and cyclic voltammetry response has not been considered.

The application of polyoxometalates in fuel cell technology has been studied with an initial focus upon their specific proton conductivity[20] with a more recent review on their application by Herring.[21] Work by Herring and co-workers also investigated the catalytic behaviour of various polyoxometalates as catalysts for reactions on both the fuel cell anode and cathode.[22-24] Herring's research focused on the polyoxometalates being in the *solid phase* and their application to *conventional* proton exchange membrane fuel cells (PEMFC). Key results from their research highlighted that vanadium substituted polyoxometalates only showed significant activity on the fuel cell cathode and that they can increase the platinum tolerance against carbon monoxide poisoning. Ultimately they were limited to solid state catalysis. However, in conjunction with FlowCath™ technology we are able to investigate the potential of *aqueous* phosphomolybdovanadates as a platinum replacement for catalysis on the fuel cell cathode.

This chapter concerns the applicability of the phosphomolybdovanadate series as potential catholytes in FlowCath® technology. In particular the electrochemical behaviour of the catholytes is investigated with a particular focus on the effects of

speciation upon the electrochemical properties. This chapter also investigates the effect non-platinum based electrode materials may have on the electron transfer reaction kinetics.

3.2 Results and Discussion

3.2.1 Effect of Non-Platinum Based Electrodes Upon Electron transfer in $Ru(NH_3)_6^{3+/2+}$ System

As described in chapter 1 a key objective of FlowCath® technology is the elimination of precious metals from the system. This not only applies to the catalyst but to all materials that make up the complete system, which leads to the cathodes comprising of solely carbon based materials. It is well documented that electron transfer is commonly slower at glassy carbon surfaces compared to platinum[25] with various comparisons drawn based upon the $Ru(NH_3)_6^{3+/2+}$ redox system.

Figure 3.1A shows an overlay of 0.001 M $Ru(NH_3)_6Cl_3$ in 0.1 M KCl at varying scan rates ranging from 20 – 400 mV s^{-1} using a platinum working electrode. The CV features the redox processes associated with the Ru^{3+}/Ru^{2+} redox couple. The formal potential ($E^{o'}$) of the $Ru^{3+/2+}$ redox couple is -0.171 V vs. SCE with a peak to peak separation (ΔE_p) of 61 mV at lower scan rates. Peak cathodic current (I_p^c) increases proportionally with the square root of scan rate ($v^{1/2}$) (Figure 3.1B), the peak anodic and cathodic current ratios are equal to ~1 and ΔE_p reaming constant at 61 mV across the series of scan rates. This points to or close to an electrochemically reversible system with ΔE_p being only very slightly higher than the expected 59 mV for an ideal reversible system. Based on the Randles Sevcik equation (section 2.3.1) we obtain a diffusion coefficient of 6.57 x 10^{-6} cm^2 s^{-1} and a standard rate constant for electron transfer (k^o) calculated using the method of Nicholson[26] of 0.1 cm s^{-1} (based upon a scan rate of 0.1 V s^{-1}) which is in agreement with previous results obtained by steady state electrochemical methods[27]. The magnitude of k^o is comparable with that of a electrochemically reversible system with the slightly larger ΔE_p probably being caused by lower solution conductivity which can directly affect the interfacial potential.[28-30]

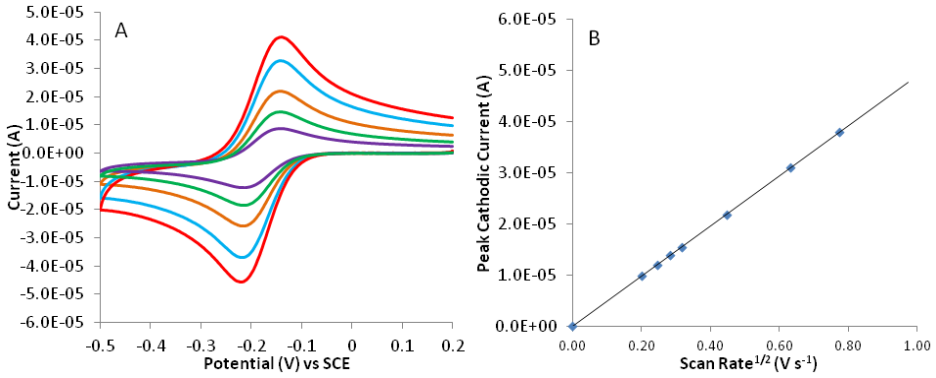

Figure 3.1: A) Overlay of cyclic voltammetry of the $Ru(NH_3)_6Cl_3$ system at varying scan rates in 0.1 M KCl at Pt disc electrode. Purple = 0.04, Green = 0.1, Orange = 0.2, Blue = 0.4, Red = 0.6 V s^{-1}. B) Plot of peak cathodic current vs. the square root of scan rate.

Analysis of the same redox system at a glassy carbon electrode (GC) produces analogous results to that at platinum (Figure 3.2), with only slight variations in peak currents and potentials (Table 3.1) resulting in an increase in ΔE_p from 61 mV at Pt electrode to 62 mV (v = 0.1 V s^{-1}) at GC. This increases further with increasing scan rate reaching a maximum of 69 mV at a scan rate of 0.6 V s^{-1}. Calculation of k^o by the method of Nicholson gives a value of 0.057 cm^2 s^{-1} and a diffusion coefficient of 3.77 x10^{-6} cm^2 s^{-1} obtain via the Randles Sevick equation (equation 2.38).

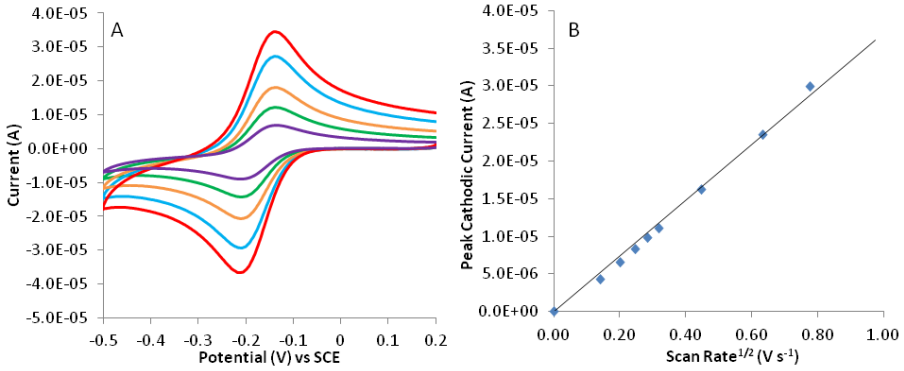

Figure 3.2: Overlay of cyclic voltammetry of $Ru(NH_3)_6Cl_3$ at varying scan rates in 0.1 M KCl at a glassy carbon disc electrode. Purple = 0.04, Green = 0.1, Orange = 0.2, Blue = 0.4 and Red = 0.6 V s-1. B) Plot of peak cathodic current vs. scan rate.

A comparison of the electrochemical properties obtained from the CVs at the GC and Pt electrodes is shown in Table 3.1 and Figure 3.3. The diffusion coefficient (D_o) of 3.77 x10^{-6} cm^2 s^{-1} obtained on the GC electrode is approximately half that calculated at Pt electrode. A change in D_o will result in a decrease in the peak current based on the experimental values, however, with only the electrode material

Table 3.1: Summary of electrochemical properties obtained at a scan rate of 0.1 V s^{-1} at platinum and glassy carbon electrodes. E_p = Volts, I_p = Amps, ΔE_p = mV and k^o = cm s^{-1} .

Electrode Material	E_p^c	I_p^c	E_p^a	I_p^a	ΔE_p	k^o
Platinum (Pt)	-0.210	1.58E-05	-0.149	1.54E-05	61	0.102
Glassy carbon (GC)	-0.203	-1.11-05	-0.139	1.27E-05	62	0.057

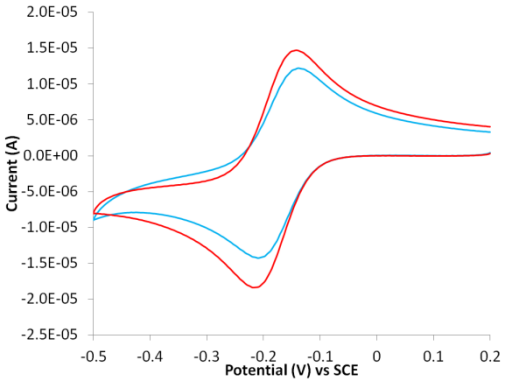

Figure 3.3: Comparison of cyclic voltammetry response at GC and Pt electrode using 0.001M $Ru(NH_3)_6Cl_3$ in 0.1 M KCl at 0.1 V s^{-1}. Red = Pt electrode Blue = GC electrode. Area of both electrodes (A) = 0.076 cm^{-2}

changing between measurements the solution properties will remain unchanged and hence the diffusion coefficient should remain unchanged. With the I_p and $v^{1/2}$ relationship not truly proportional (Figure 3.2B), it raises questions of how accurate the D_o values are based on the Randles Sevcik equation at a GC electrode, as strictly speaking this analysis should only be applied to electrochemically reversible systems. Figure 3.3 shows an overlay of CVs obtained at a scan rate of 0.1 V s^{-1} on both Pt and GC. The small changes in E_p can be seen as well as large differences in I_p, but notably at the GC electrode side reactions occur with the cathodic current increasing at -0.4 V.

The $Ru(NH_3)_6^{3+/2+}$ redox system is considered to be a classical outer sphere electron transfer with no significant interaction between the inorganic complex and electrode surface, so is less dependent on the nature of the electrode material compared with an inner sphere electron transfer.[30] However the electrode material can still affect the outer sphere mechanism as the following factors are dependent on electrode material a) structure of the Helmholtz layer, b) energy distribution and density of electronic states and c) number/coverage of active sites.[30]

Between a metal and non-metal e.g. platinum and carbon, the difference in the density of electronic states can determine the rate of heterogeneous electron transfer as described by Marcus-Hush theory.[31,32] Compton et al. have shown that this theory can be applied to diffusion controlled processes.[33] One could argue that a decrease in surface oxide coverage (the active sites for adsorption on GC electrodes)[34] at the GC electrode leads to reduced activity. However McCreery et al. have shown that an outer sphere mechanism is unaffected by surface oxide coverage at GC electrode using the $Ru(NH_3)_6^{3+/2+}$ redox couple as a specific example.[34] But Deakin et al. showed pH can effect some outer sphere reactions at carbon electrodes due to protonation of surface carboxyl groups thus changing the surface groups and the interfacial charge distribution. It is believed in this instance that firstly, the increase in the density of electronic states at the Fermi level results in the increased I_p on Pt electrodes compared to glassy carbon. Hence the surface groups and interfacial charge distribution remains consistent at both electrode surfaces. Secondly the ratio of basal plane and edge plane ratio at the carbon electrode surface can also affect the current signal.

Simulation of CVs obtained at the GC electrode allow for an accurate determination of the diffusion coefficient and confirmation of k^o. The simulated fit focuses on the first redox wave which is the one electron reduction of Ru^{3+} to Ru^{2+}. Initially, the parameters used were those obtained from data in Figure 3.2, C_{ox} = 0.001 M, C_{red} = 0, $D_o = D_{ox} = D_{red}$ = 3.77 x 10^{-6} cm^2 s_{-1} and k^o = 0.057 cm s^{-1}. The fit of the simulated data was not perfect with peak currents less than those observed in the experimental data and the peak to peak separation being larger than anticipated. This indicates that the diffusion coefficient based on the Randles Sevcik equation is much lower than the actual value suggested. The error in D_o is manifested by the deviation from linearity and breakdown in the I_p vs. $v^{1/2}$ proportionality relationship in Figure 3.2B. The simulations were refitted using a diffusion coefficient obtained at the Pt electrode and this then showed good correlation with experimental data. Final simulation parameters are shown in Table 3.2 and overlays of experimental and simulation data in Figure 3.4.

Table 3.2: Summary of parameters used for cyclic voltammetry simulations at glassy carbon electrode with C_{ox} = 0.001 M, C_{red} = 0.

Scan Rate (V s^{-1})	$E^{o'}$ (V vs. SCE)	D_o (cm^2 s^{-1})	k^o (cm s^{-1})
0.02	-0.173	7.1 x 10^{-6}	0.071
0.06	-0.173	6.1 x 10^{-6}	0.069
0.1	-0.173	6.2 x 10^{-6}	0.070
0.2	-0.173	6.5 x 10^{-6}	0.069
0.4	-0.173	6.5 x 10^{-6}	0.069
0.6	-0.173	6.5 x 10^{-6}	0.073

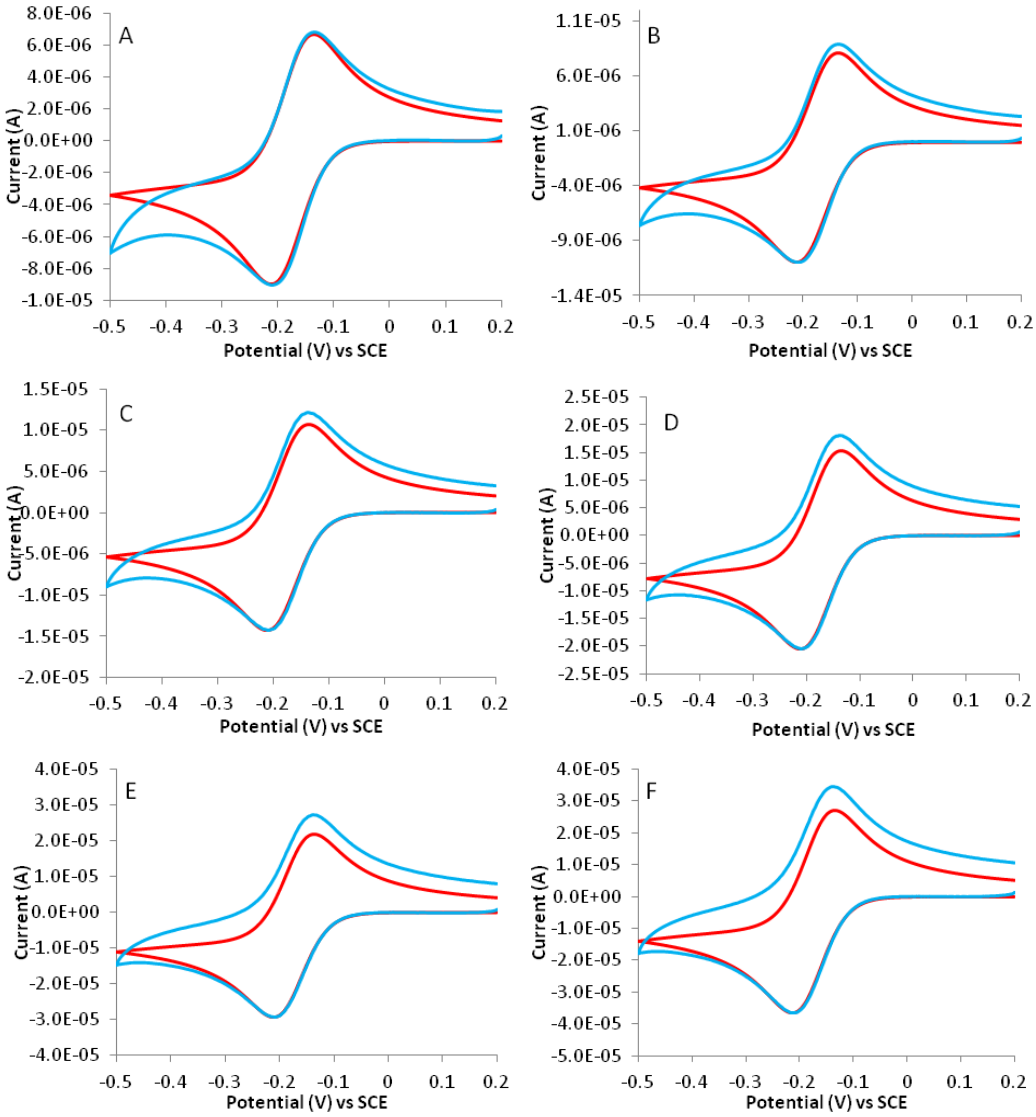

Figure 3.4: Overlay of simulation and experimental cyclic voltammetry responses of 0.001 M $Ru(NH_3)_6Cl_3$ CV in 0.1 M KCl at a GC electrode at varying scan rates. Red = simulation and Blue = experimental. A = 0.04, B = 0.06, C = 0.1, D= 0.2, E = 0.4 and F = 0.6 V s^{-1}.

Based on the simulated fit we obtain an average diffusion coefficient of 6.4 x 10^{-6} cm^2 s^{-1} and 0.070 cm s^{-1} (0.074 cm^2 s^{-1} using method of Nicholson) for the standard rate constant for electron transfer. These values are concordant with those obtained at the platinum electrode showing that the diffusion coefficient does not change with the electrode material and thus, the change in electrode material leads to the reduced electron transfer kinetics when moving from Pt to GC.

3.2.2 The Effect of Supporting Electrolyte on Electron Transfer in the $Ru(NH_3)_6^{3+/2+}$ System

It was established in the preceding section that the GC electrode has slower electron transfer kinetics compared to platinum and this ultimately will result in an effect on the kinetics observed for the catholyte systems. It is known that the nature of the supporting electrolyte employed during an electrochemical analysis can greatly affect the electron transfer kinetics and overall shape of the cyclic voltammogram.[35-39] With the effect of supporting electrolyte upon the redox potential resulting in significant shifts of up to 1.0 V.[38]

CV analysis of the $Ru(NH_3)_6^{3+/2+}$ complex was carried out in three different (acidic) background electrolytes, namely, H_2SO_4, H_3PO_4 and $HClO_4$ with pH ranging from 1 to 1.6. The acids are suitable supporting electrolytes as a constant pH of ~1 is required for the analysis of the phosphomolybdovanadate series. At GC electrodes there is a pH dependence of the CV response resulting from a change in the double layer charge, however this same pH dependence is not observed at metallic electrodes indicating that this is a property of carbon based electrodes and not the electroactive species.[40] There is no significant change in the formal potential of the $Ru^{3+/2+}$ couple at lower pH indicating no protonation of the redox species.[40] Figure 3.5 shows the CV response of $Ru(NH_3)_6^{3+/2+}$ in the afore mentioned electrolytes at a GC electrode with electrochemical properties summarised in Table 3.3.

It can be seen from Figure 3.5 that there are significant differences between I_p and E_p (thus, k^o) for the same redox species in different supporting electrolytes. Figure 3.5B shows a decrease in peak cathodic current across the entire scan rate range when in acidic electrolytes compared to the neutral KCl electrolyte. The reason for the difference in k^o is not due to a change in electrode material nor is it due to a

(significant) change in the percentage of surface oxide groups, as each electrode was prepared in the same way.

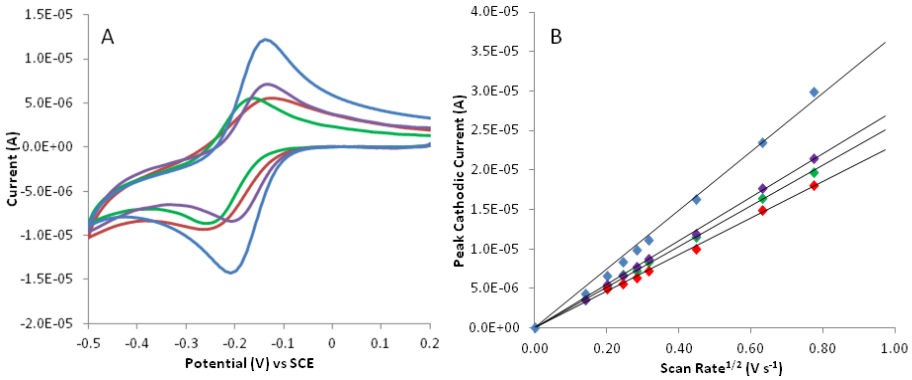

Figure 3.5: A) CV responses of 0.001 M $Ru(NH_3)_6Cl_3$ in Red =0.1 M H_3PO_4, Green = 0.1 M H_2SO_4, Purple = 0.1M $HClO_4$ and Blue = 0.1 M KCl all at v = 0.1 V s^{-1}. B) Comparison of peak cathodic currents obtained across a range of scan rates. GC electrode used during analysis.

Table 3.3: Summary of electrochemical properties for the $Ru(NH_3)_6^{3+/2+}$ redox system in 0.1 M supporting electrolytes[(a)]. ΔE_p obtained at a scan rate of 0.1 V s^{-1}.

Electrolyte	$E^{o'}$ (V)	D_o (cm^2 s^{-1})	ΔE_p (mV)	k^o (cm s^{-1})	pH
H_3PO_4	-0.187	1.46 x 10^{-6}	119	1.51x 10^{-3}	1.62
H_2SO_4	-0.206	1.82 x 10^{-6}	82	4.35 x10^{-3}	0.99
$HClO_4$	-0.167	2.08 x 10^{-6}	61	5.81 x10^{-2}	1.00
KCl	-0.173	6.10 x 10^{-6}	62	7.9 x10^{-2}	6.1

The decrease in k^o associated with the pH change for the $Ru(NH_3)_6^{3+/2+}$ couple was reported by Deakin and may be due to, a) an increase in the specifically adsorbed hydronium ion or b) protonation of surface chemical functional groups.[40] This may explain the changing CV response when moving from a neutral to acidic pH in Figure 3.5. An increase or surface excess of specifically adsorbed hydronium ion or protonation of surface groups results in an increase in the positive charge (or decrease in negative charge) on the surface which may have a detrimental effect on the electron transfer between the $Ru(NH_3)_6^{3+/2+}$ couple and the surface as this species may not be able to closely approach the electrode surface.[30] The apparent difference in D_o and k^o between the three acidic electrolytes could be due to a number of factors.

[a] Diffusion coefficient is based on the results obtained from simulations of the respective experimental

The pH varies between the three electrolytes and this may cause the fraction of surface oxide groups which are protonated to vary, but this would not support the trend seen by Deakin.[40] Ion pairing between the ruthenium complex and the electrolyte anions will vary and likely effect diffusion coefficients. It could be argued that the degree of ion pairing is manifested in the relative diffusion coefficients with increased paring reducing the respective diffusion coefficient in each electrolyte. A change in k^o could also result from ion pairing. Reduction of the ruthenium centre reduces the overall positive charge of the complex thus changing the degree of ion pairing. How quickly the solvation shell and ion pairings respond to this change will affect the rate of electron transfer. Specific adsorption of anions on to the electrode surface as well as hydrogen bonding between surface oxides and protons still associated with $H_2PO_4^-$ and HSO_4^- will also change the structure/thickness of the electrical double layer, hence, affecting the true interfacial potential experienced by the redox species. Based on these observations $HClO_4$ can be viewed as the most suitable electrolyte due to its minimal effect on the kinetics of electron transfer at the electrode surface.

3.2.3 The speciation of the Phosphomolybdovanadate Systems

The structure and speciation of vanadium substituted polyoxometalates (POM) involves a complex equilibria which is strongly affected by both pH and concentration.[7] Hence, an understanding of the effects of pH and solvent on the classic outer sphere electron transfer of $Ru(NH_3)_6^{3+/2+}$ at GC electrodes is an important first step towards understanding the electrochemistry of the complex $Na_xH_3PMo_{12-x}V_xO_{40}$ systems used in this work. The series of POMs used are all based on the Keggin structure with x ranging from 1- 4. Figure 3.6 shows IR and Raman spectra obtained for each of the POM series 'as synthesised' in the solid phase. Solid samples used in FT-IR and Raman measurements were dried in a desiccator for 24 hours prior to analysis.

The FT-IR (Figure 3.6A) spectra shows IR bands that are characteristic of the Keggin structure at 1053, 950, 880 and 760 cm^{-1} which are assigned to P – O, M-O(where M = Mo or V), inter-octahedral M-O-M and intra-octahedral M-O-M vibrations. These absorptions are present in each of the four systems in question. Bands located at ~1600 and ~3200-3400 cm^{-1} correspond to the presence of water

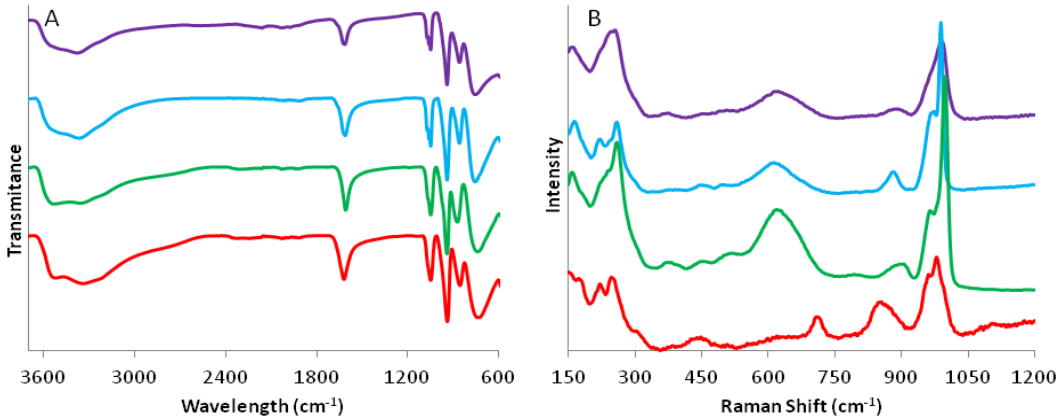

Figure 3.6: A) FT-IR spectrum of $Na_xH_3PMo_{12-x}V_xO_{40}$ and B) Raman spectrums of $Na_xH_3PMo_{12-x}V_xO_{40}$ where x = 1 (purple), x = 2 (blue), x =3 (green) and x = 4 (red).

within the coordination sphere.[41] The Raman spectrum (Figure 3.6B) shows bands at 980, 850 and 700 cm^{-1} which are assigned to M=O, M-O-M (asymmetric) and M-O-M (symmetric) which are characteristic of the Keggin structure and again present in each of the four systems.[42] The FT-IR and Raman analysis is relatively simple and indicates that the structure observed is that of (or at least dominated by) the Keggin motif. The ^{31}P NMR however shows the complexity of these systems and the observed dynamic equilibrium present in each case.

The Pettersson group and others have previously studied the speciation of POMs in great detail using combined NMR and potentiometric titration techniques.[43-46] The work by Pettersson, provided a basis and understanding of POM speciation in aqueous media to be taken forward and deployed in conjunction with the POM systems used in this work. In POM systems of the general formula $Na_xH_3PMo_{12-x}V_xO_{40}$, with $x \geq 2$, the POM species is not a single pure species but consists of a distribution of $Na_xH_3PMo_{12-x}V_xO_{40}$ species usually with x ranging from 1 – 4. Under acidic conditions the chemical shift in the ^{31}P spectra are sufficiently different to allow a clear distinction between the various species.[46] The resulting distribution/equilibrium is assigned to the decrease in stability with increasing substitution of vanadium into the Keggin structure, caused by the increase in negative charge on the Keggin.[9] Figure 3.7 shows the ^{31}P NMR of the synthesised $Na_xH_3PMo_{12-x}V_xO_{40}$ samples. It is evident that $Na_1H_3PMo_{11}V_1O_{40}$ (V_1POM) is predominately only a single species system represented by a singlet at –4.08 ppm due to a single positional isomer and two small satellite peaks. $Na_2H_3PMo_{11}V_2O_{40}$

(V_2POM) however contains both V_1 (-4.1 ppm) and V_2 species with peaks between –3.9 and -3.6 ppm representing the various V_2 positional isomers. This is in agreement with the work by Pettersson et al. The same scenario is observed with $Na_3H_3PMo_9V_3O_{40}$ (V_3POM) and $Na_4H_3PMo_8V_4O_{40}$ (V_4POM) with each comprising of $V_{1\text{-}4}$ species. Based on the most stable α isomers there are 5, 13 and 27 positional isomers possible for the V_2, V_3 and V_4POM species, respectively.[9,11] Other peaks can also be assigned to β isomers which are stable enough to be present in sufficient quantities to be detected. Careful analysis of the ^{31}P NMR spectra allows an integration of the peaks associated with each individual POM species and allows an estimation of the total concentration of individual species which make up the target POM system[b]. Table 3.4 highlights the results obtained by Herbet with respect to specific concentrations of individual POM species in a given POM system. The V_1POM system is excluded for reasons stated. Herbet used mathematical integration to calculate the concentration of individual V_xKeggin. The integration of each peak associated with a particular V_xKeggin and its isomers was determined and hence the percentage of each V_xKeggin within the overall V_xPOM can be determined. Any phosphorus unaccounted for is assigned to residual H_3PO_4 present in solution.

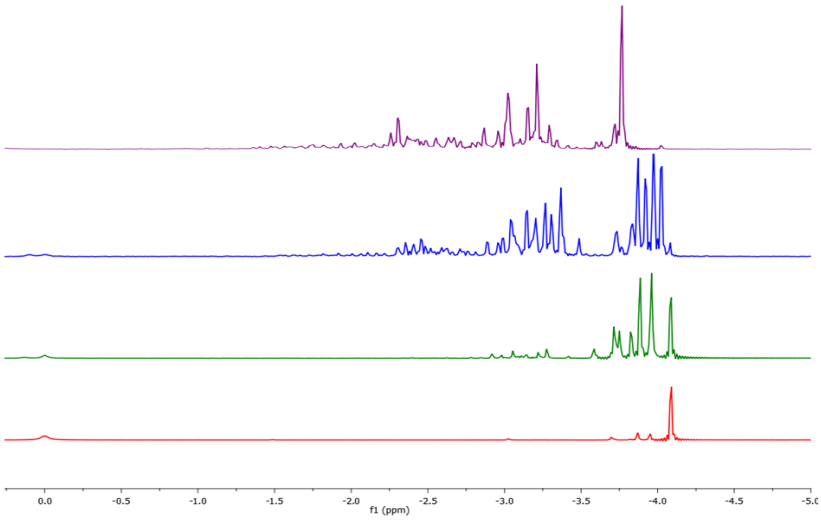

Figure 3.7: ^{31}P NMR of $Na_xH_3PMo_{12\text{-}x}V_xO_{40}$ aqueous systems. Samples used at 0.3 M concentration pH ~ 1 for all samples, 1 % H_3PO_4 as external reference. Red = $Na_1H_3PMo_{11}V_1O_{40}$, Green = $Na_2H_3PMo_{10}V_2O_{40}$, Blue = $Na_3H_3PMo_9V_3O_{40}$ and Purple = $Na_4H_3PMo_8V_4O_{40}$

[b] Speciation analysis of the $V_{1\text{-}4}$POM systems by ^{31}P NMR was carried out by Dr. M. A. Herbet at ACAL Energy. Speciation data was obtained form 0.3 M sample sand normalised to obtain values reported in Table 3.4. Results are presented in internal report MAH-REP015.

It is evident from Table 3.4 that the V_2 and V_3POM systems are dominated by the corresponding species but V_4POM remains to be dominated by the V_3 species however there is a drastic increase in the V_4 specie concentration when moving from the V_3 to V_4 POM system.

The increased number of positional isomers is unlikely to significantly affect the electrochemical properties of the individual species; however the distribution of individual species present in each system along with multiple redox centres will have more profound effects. Table 3.4 contains the speciation's data for the relevant V_xPOM systems. For clarity the following definitions are used to describe each term used:

- **V_xPOM (system)**: This refers to the overall experimental formula of the synthesised system with x representing the number of vanadium's contained within the general formula; $Na_xH_3PMo_{12-x}V_xO_{40}$. For example V_2POM refers to the system with the experimental formula, $Na_2H_3PMo_{10}V_2O_{40}$
- **V_xKeggin**: This refers to the specific Keggin species within the overall system. For example in the V_2POM (experimental formula $Na_2H_3PMo_{10}V_2O_{40}$) system consists of the individual V_1, V_2 and V_3Keggin species respectively.

Table 3.4: Estimated concentrations of individual POM species in each POM system based on a total [Keggin] = 0.001 M

POM System	[V_1 Keggin] mM	[V_2 Keggin] mM	[V_3 Keggin] mM	[V_4 Keggin] mM	[Free VO_2^+] mM
V_2POM	3.2×10^{-1}	5.6×10^{-1}	8.6×10^{-2}	0	2.8×10^{-1}
V_3POM	4.6×10^{-2}	5.0×10^{-1}	3.2×10^{-1}	8.3×10^{-2}	6.6×10^{-1}
V_4POM	3.6×10^{-3}	1.9×10^{-1}	4.0×10^{-1}	3.1×10^{-1}	1.16

3.2.4 Effect of In-Situ Oxygen Reduction on the Cyclic Voltammetry Behaviour of the V_{1-4}POM Systems.

The oxidation of reduced vanadium substituted polyoxometalates by molecular oxygen is well documented with in depth analysis carried out by Kozhevnikov[5-7], Neumann[10-12,14] and Matveev[8,13]. The mechanism behind the oxidation is not of importance at this point, but what is, is the effect (if any) the oxidation will have

upon the CV measurements. Typically CV measurements are carried out at 1 mM concentration (redox active species) in the presence of excess background electrolyte.[30,47] DigiElch Cyclic voltammetry simulation software[64] enables the effect that molecular oxygen will have upon the CV to be simulated prior to experimental analysis.

The simulations are based around the model shown in equations 3.1-3.3 with initial parameters outlined in Table 3.5. Equation 3.1 is the reduction of an arbitrary POM species at the electrode surface (that can undergo a four electron reduction), equation 3.2 highlights the relatively simple four electron reduction of oxygen and equation 3.3 illustrates the possible homogeneous reaction between O_2 and reduced POM species (POM_{red}):

$$POM_{ox} + 4e \longrightarrow POM_{red} \quad (3.1)$$

$$O_2 + 4H^+ + 4e \xrightarrow{k_f} 2\,H_2O \quad (3.2)$$

$$POM_{red} + O_2 + 4H^+ \longrightarrow 2\,H_2O + POM_{ox} \quad (3.3)$$

The parameters used (D_o, $[O_2]$) in the model for O_2 oxidation are typical values reported in literature for aqueous solutions with the exception of k_f which is set at an extremely high value.[48,49] Figure 3.8 shows a series of simulated CVs at varying POM concentrations with oxygen reduction effectively switched 'on' and 'off'[c] to observe its effect at the given concentration. Figure 3.8A and B are taken at 0.3 and 0.03 M respectively and show that the homogeneous reaction in equation 3.3 has

[c] Switched 'on' and 'off' refers to the value of k_f in equation 3.3 being set to 1 x10^6 and 0 M s^{-1} respectively.

little or no effect. This is due to the difference in concentration between diffused O_2 (0.2 mM) and POM (0.3-0.03 M). As the POM concentration approaches the dissolved O_2 concentration, the O_2-POM reaction (Equation 3.3) begins to affect the voltametric signal causing an increase in reduction current associated with an EC' mechanism.[30] At 0.003 M observe a slight increase in I_p^c when the oxygen reduction reaction is switched on. Reducing the initial concentration of POM_{ox} to 0.0003 M shows distinct changes in the CV with I_p^c increasing by a factor of 3.81 when the oxygen reduction reaction is switched on.

The oxygen reduction reaction regenerates POM_{ox} near the electrode surface leading to a steeper concentration gradient and consequently increased flux of POM_{ox} to the electrode surface. Because the reaction is so fast in the simulations and O_2 is consumed in the reaction, the effective increase in concentration of POM_{ox} is similar to the concentration of O_2 i.e. similar to 0.2 mM.

Table 3.5: Parameters used in the simulation to investigate the effect of oxygen reduction upon POM cyclic voltammetry.

Parameters	Equation 3.1	Equation 3.3
$E^{o'}$ (V vs. SCE)	0.47	1
Transfer Coefficient	0.5	0.5
k^o (cm s^{-1})	0.01	0
$K_{eq}^{(d)}$	-	2.27 x10^{35}
$k_f^{(d)}$ (M s^{-1})	-	1 x10^6
$k_b^{(d)}$ (M s^{-1})	-	4.41 x10^{-30}
$[O_2]$ (M)	2.2 x10^{-4}	2.2 x10^{-4}
[POM] (M)	Varies	Varies
D_o POM (cm^2 s^{-1})	1 x10^{-6}	1 x10^{-6}
D_o O_2 (cm^2 s^{-1})	2 x10^{-5}	2 x10^{-5}
Electrode Area (cm^2)	0.0706	0.0706
Scan rate (V s^{-1})	0.05	0.05

[d] Parameters specific to the homogeneous reaction shown in equation 3.3

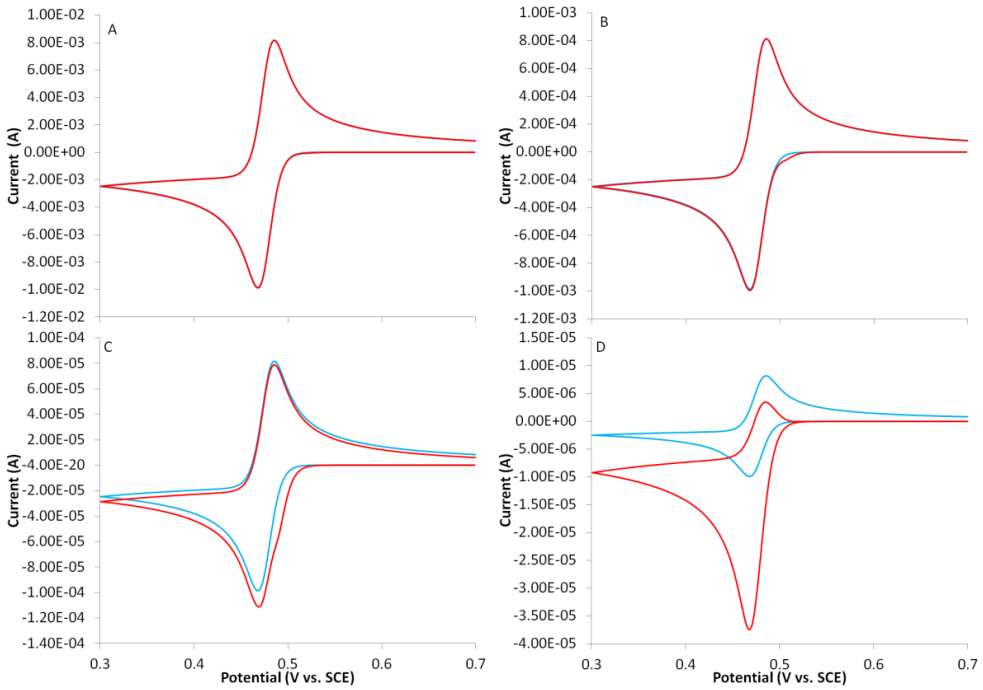

Figure 3.8: Simulation of the effects of molecular oxygen upon the CV of the POM systems. A) [POM] = 0.3 M, B) [POM] = 0.03 M, C) [POM] = 0.003 M and D) [POM] = 0.0003 M. In each instance the red CV represents equation 3.3 switched 'on' (k_f = 1 x10^6) and blue equation 3.3 is switched 'off' (k_f = 0)

At the higher POM concentrations the extra POM_{ox} generated by the O_2 reaction is insignificant to the bulk concentration of POM so a minimal change is observed in the concentration gradient hence a minimal change in flux of POM_{ox} to the electrode surface. By maintaining the higher concentrations of POM_{ox} at the electrode surface we effectively observe steeper concentration gradients and thus an increase in the flux of POM_{ox} to the electrode surface. The increased flux of POM_{ox} at varying time intervals when comparing to the situation when oxygen reduction is switched off, leads to the higher currents being generated.

It is apparent from Figure 3.8 that the initial concentration of POM species has to be reduced to 0.003 M before the effects of oxygen reduction significantly affects the shape of the CV. Although that said, the small increase in current at 0.003 M is linked with a k_f value that is much larger than one would expect for the oxygen reduction reaction. From Figure 3.9 it is clear that k_f for equation 3.3 can be reduced to 1 x10^3 M s^{-1} ([POM_{ox}] = 0.0003 M) at which point oxygen reduction has very little effect on the overall CV; the reductive peak current increases and the back, oxidative current, decreases which is typical of a classic EC' mechanism.[30,50]

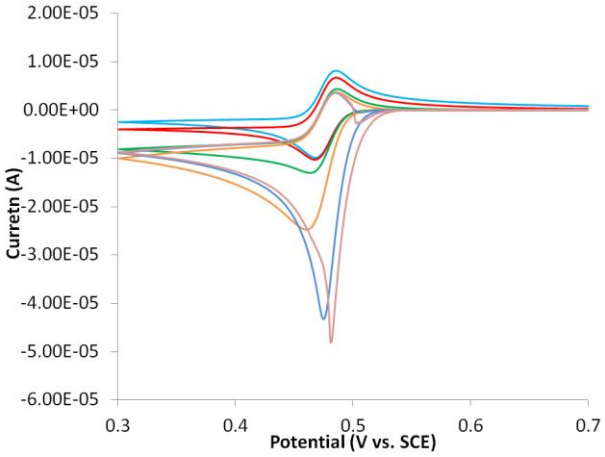

Figure 3.9: Simulated cyclic voltammetry of POM system varying k_f value for the simultaneous oxygen reduction. Parameters outlined in Table 3.5 are employed with k_f values of; light blue = 0, red = 1 x10^3, green = 1 x10^4, yellow = 1 x10^5, dark blue = 1 x10^7 and pink = 1 x10^9.

The minimum value for k_f needed to observe a change in the simulated POM CV at the 0.0003 mM POM concentration is approximately 1 x10^3 M s^{-1} which is still relatively fast. With the concentration of the redox active species present in solution during experimental analysis being nearly ten times greater than that of the simulations, minimal affects are expected to be observed due to O_2 reduction. In such simulations the effect of oxygen reduction upon the V_xPOM CV under typical experimental conditions (0.001 mM V_xPOM in 0.1 M supporting electrolyte at room temperature and pressure) is minimal. However to prevent ambiguity, solutions will be degassed with N_2 prior to CV analysis.

3.2.5 Cyclic Voltammetry Analysis of $V_{1\text{-}4}$ POM Systems

The supporting electrolyte can have a major impact on the shape of the CV obtained and the measured E_p and I_p are consequently shifted. A shift in E_p due to solvent effects could be misinterpreted as an improvement in the POM system which would not be reproducible in the fuel cell, with no additional supporting electrolytes are present in the catholyte solution. For the study of the POM systems in this case it is necessary to maintain a constant pH, since the POM's speciation is pH sensitive, hence a pH similar to that of the fuel cell catholyte is needed. For this reason we use acids as supporting electrolytes, specifically H_3PO_4, $HClO_4$ and H_2SO_4 to maintain a pH of 1, the pH of V_4POM. The effect of these acids upon the outer sphere electron transfer of the ruthenium hexamine system was discussed in section 3.2.2. It is

believed that the heterogeneous reduction of polyoxometalates at an electrode surface also involves outer sphere electron transfer.[51] Hence an electrolyte with minimal effects on electrochemical parameters is imperative for a meaningful analysis. Figure 3.10 illustrates the effects of the various electrolytes upon the CV response of the V_1POM.

Figure 3.10A shows the CV obtained for the V_1POM system in the three acidic electrolytes. There are clear shifts in the formal potentials corresponding to V^{5+}/V^{4+} redox couple in each case, which were estimated as average values of E_p^a and E_p^c. The decreasing formal potential (becomes less positive) with respect to supporting electrolyte is in the following order $HClO_4$ > H_2SO_4 > H_3PO_4; i.e. reduction of the POM becomes more difficult when moving from $HClO_4$ to H_3PO_4. The decrease in ΔE_p follows the same trend as that of the formal potential indicating an increase in the electron transfer kinetics in $HClO_4$ compared with H_3PO_4. The CV of V_1POM in $HClO_4$ is in agreement with literature when comparing values for $E^{o'}$ and E_p for the Keggin bound vanadium redox couple.[19,22] The increase in peak separation observed in the H_3PO_4 and H_2SO_4 supporting electrolytes indicate they are less suitable in this instance, analogous to the results for the ruthenium system. In the ruthenium system ion pairing could give rise to the slower kinetics, however given the negative charge on the POM species this is unlikely to be the case here. However specific adsorption of anions on the electrode surface could affect electrode kinetics.

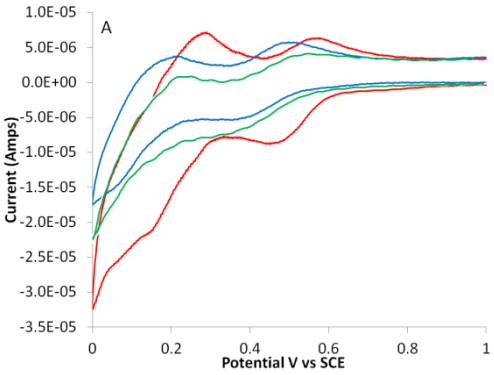

B

Electrolyte	$E^{o'}$ (V)	ΔEp (mV)	pH
H_3PO_4	0.430	161	1.00
H_2SO_4	0.470	139	0.99
$HClO_4$	0.512	124	1.00

Figure 3.10: A) Cyclic voltammetry of 0.001 M V_1POM in 0.1 M $HClO_4$ (red), 0.6 M H_3PO_4 (green) and 0.1 H_2SO_4 (blue). B) Table highlighting selected electrochemical properties obtained in the various supporting electrolytes. $E^{o'}$ and ΔE_p are based on the vanadium redox couple.

A comparison between the four POM systems (Figure 3.11) in question yields a number of distinct differences with key properties summarised in Table 3.6. It is

important to note, that it was previously established that each system is a complex distribution of V_1-V_4 species (with the exception of V_1 which solely consists of the V_1). This should be taken into account when considering the electrochemical properties quoted here are not of the specific species but an 'average' result of the system. The V_1POM shows peaks at 0.575, 0.450, 0.149, and 0.271 V vs. SCE. The first pair of peaks correspond to the $V^{(4+)}/V^{(5+)}$ redox couple whilst the second set corresponds to reduction of the molybdenum backbone ($Mo^{(5+)}/Mo^{(6+)}$ redox couple) within Keggin structure. The V_2POM system is very similar as we observe three peaks at 0.569, 0.447 and 0.279 V vs. SCE assigned again to the vanadium and molybdenum redox centres, respectively. It should be noted that the peak at 0.149 V assigned to the reduction of the molybdenum centre is no longer evident in the V_2POM system, but is now merely an inflection. The cyclic voltammograms of the V_3 and V_4 systems are very different in comparison with $E^{o'}$ shifting negatively by approximately 0.1 V (compared to V_1) with the Keggin-bound molybdenum reduction oxidation also shifted in the same direction by a similar amount. The negative shift in $E^{o'}$ can be assigned to the increase in negative charge on the Keggin structures.[17] Interestingly the V_1/V_2 and V_3/V_4 systems adopt similar formal potentials. This is due to the speciation equilibrium found in each system (Table 3.4Table 3.4), with V_1 and V_2 systems mainly consisting of the V_1 and V_2 Keggins whereas the V_3 and V_4 Keggins dominate the V_3 and V_4POM systems.

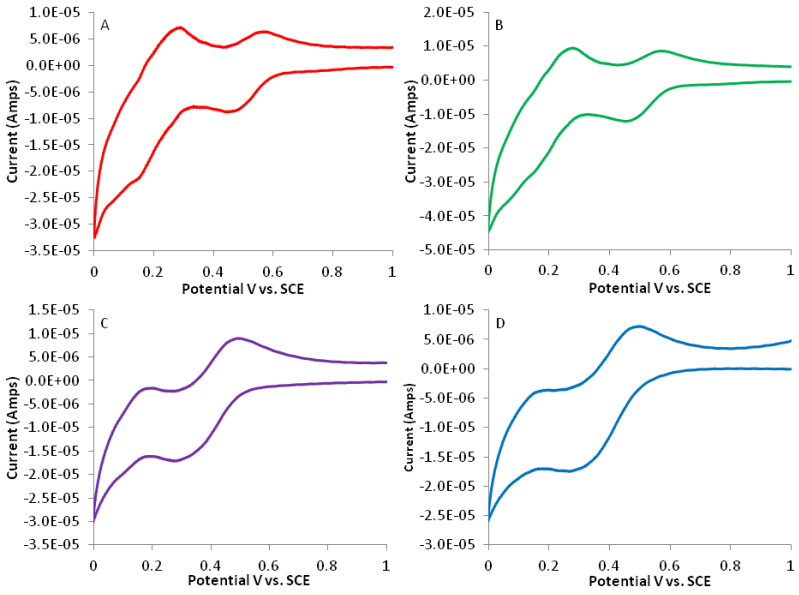

Figure 3.11: Cyclic Voltammetry of 0.001 M POM in 0.1 M HClO4 at 0.04 V s^{-1}. A) V_1POM, B) V_2POM, C) V_3POM and D) V_4POM

On moving from V_1 to V_4POM there is an increase in the peak to peak separation, which usually indicates slower kinetics. However the V_3 and V_4POM CV's are broader and sometimes inflections are observed in the reduction wave implying the difference is caused by something more complicated than slower electrode kinetics. As we change from the V_1 to V_4 system there is an increase in concentration of vanadium (redox active centre in the potential range observed) from 1 mM to 4 mM accounting for the increase in peak currents (Table 3.6). This is the situation observed for I_p^c however I_p^a decreases from V_3 to V_4 which could be a result of free vanadium present in solution.

If we consider the reaction shown in equation 3.4, where V_xPOM undergoes a one electron reduction:

$$V_xPOM_{ox} + e^- \longrightarrow V_xPOM_{red} \quad (3.4)$$

Table 3.6: Electrochemical properties $E^{o'}$, E_p, I_p (V vs.SCE) and ΔE_p (mV) of V_xPOM systems (x=1-4) obtained at 0.001 M POM in 0.1 M $HClO_4$ at 0.04 V s^{-1}

System	$E^{o'}$	E_p^c	I_p^c	E_p^a	I_p^a	ΔE_p
V_1	0.515	0.450	7.27 x10^{-6}	0.574	2.91 x10^{-6}	124
V_2	0.512	0.460	1.02 x10^{-5}	0.570	4.25 x10^{-6}	110
V_3	0.387	0.284	1.58 x10^{-5}	0.489	9.54 x10^{-6}	205
V_4	0.372	0.265	1.75 x10^{-5}	0.479	8.08 x10^{-6}	215

Here we are considering the one electron reduction of a single vanadium centre so we can show equation 3.4 as:

$$V^V_{POM} + e^- \longrightarrow V^{IV}_{POM} \quad (3.5)$$

Based on data obtained in Table 3.6 and conditions outlined in the table legend the redox potential of the $V^{V/IV}$ redox couple in the V_{1-4}POM systems ranges from 0.574 to 0.479 V vs. SCE (0.818 to 0.723 vs. SHE) respectively. Table 3.4 also highlights the concentration of free vanadium (existing as the vanadate ion) in each of the V_x systems which increases from V_2-V_4 with the concentration believed to be zero in the V_1 system. Free vanadium also undergoes a one electron reduction (equation 3.6) at a

more positive redox potential (0.88 V vs. SHE at pH 1)[e] than the vanadium redox centre with in the Keggin structure.

$$V^{V}_{Free} + 2H^{+} + e^{-} \longrightarrow V^{IV}_{Free} + H_2O \quad (3.6)$$

Hence free vanadium can sufficiently oxidise the reduced vanadium within the Keggin structure, combining equations 3.5 and 3.6:

$$V^{IV}_{POM} + V^{V}_{Free} + 2H^{+} \longrightarrow V^{IV}_{Free}\, V^{V}_{POM} \quad (3.7)$$

The effect of equation 3.7 upon the cyclic voltammetry of the V_xPOMs in Figure 3.11 is only sufficiently evident when x = 3 or 4, as here the concentration of free vanadium is substantial in comparison with POM species present in solution. The electrochemical kinetics for the electrochemical reduction of free vanadium are well documented and renowned for being 'sluggish'.[52-54] It is also possible for dissociation of the vanadium metal centre from the Keggin structure upon reduction which in turn would also affect the peak anodic current observed.

3.2.6 Determination of Electrochemical Reversibility and Diffusion Coefficients for the V_xPOM Systems

The electrochemical 'reversibility' of a system describes the electron transfer kinetics of a redox system at the electrode surface (see section 2.3.1). The four systems in question are undoubtedly not chemically irreversible as they show a clear reversible redox process (both oxidation and reduction peaks observed). Table 3.7 and 3.8 highlight the properties associated with each characteristic of an electrochemically reversible and quasi-reversible system. It is clear that none of the V_xPOMs in question are truly electrochemically reversible as they fail to meet all of the criteria outlined. However, each of the V_xPOMs fails to meet all of the criteria that describe a quasi-reversible system. We cannot clarify the reversibility of each system based on the criteria in Tables 3.7 and 3.8 and ultimately only quantification of k^o will clarify this. To calculate k^o via the method of Nicholson firstly D_o for the respective systems needs to be ascertained.

[e] Standard redox potential of free vanadium is 1.0 V vs. SHE. Value quoted is the theoretical value calculated using the Nernst equation at pH 1.

$$I_{p} = 2.69 \text{ x} 10^{5}\ n^{3/2}\ A\ D_{O}^{1/2} C^{*}\ v^{1/2} \quad (3.8)$$

Table 3.7: Diagnostic parameters describing an electrochemically reversible system and corresponding values ascertained for individual 0.001 M V_xPOM systems in 0.1 M $HClO_4$ based on a one electron transfer. ΔE_p measured at v = 0.04 Vs^{-1}

Parameters	V_1POM	V_2POM	V_3POM	V_4POM
ΔE_p = 59 mV/n	124	110	205	215
$\lvert I_p^a / I_p^c \rvert$ = 1	0.42	0.41	0.61	0.46
E_p independent of v	No	No	No	No
I_p proportional to $v^{1/2}$	No	No	No	No

Table 3.8: Diagnostic parameters describing an electrochemically quasi-reversible system and corresponding values ascertained for individual 0.001 M V_xPOM systems in 0.1 M $HClO_4$ based on a one electron transfer. ΔE_p measured at v = 0.04 Vs^{-1}

Parameters	V_1POM	V_2POM	V_3POM	V_4POM
$\Delta E_p \geq$ 59 mV/n	124	110	205	215
$\lvert I_p^a / I_p^c \rvert$ = 1	0.42	0.41	0.61	0.46
E_p^c shifts negatively with v	Yes	Yes	Yes	Yes
I_p not proportional to $v^{1/2}$	Yes	Yes	Yes	Yes

As I_p increases proportionally with $v^{1/2}$ and the Randles Sevcik equation (Equation 3.8) can be used to calculate D_o based on the linear relationships (Figure 3.12). However as observed previously the Randles Sevcik equation consistently underestimates the diffusion coefficient if the system is not a true electrochemically reversible system.

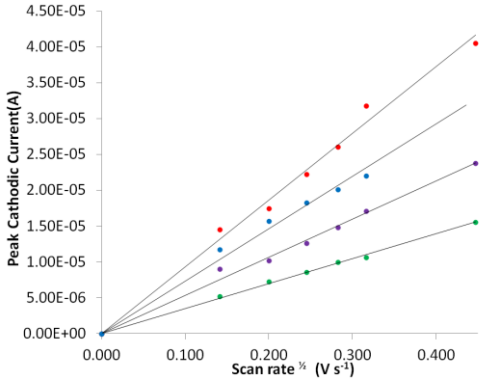

Figure 3.12: Overlay of change in peak cathodic current with increasing scan rate for 0.001 M V_1-V_4POM systems in 0.1 M $HClO_4$ at pH 1. Green = V_1, purple = V_2, blue = V_3 and red = V_4

3.2.6.1 Simulation of V_xPOM Systems: Model A

Simulation of the V_xPOM systems using model A is carried out using DigiElch simulation software[64] with the following assumptions:

- Each of the V_xPOM systems contains only a single Keggin species which is that of its experimental formula i.e. V_2POM contains only the V_2Keggin, V_3POM contains only the V_3Keggin etc.
- In all V_xKeggin only a single electron transfer is observed which involves the Keggin-bound vanadium redox centre

Using data from Figure 3.12 and assuming n = 1 for the V_1, V_2, V_3 and V_4 systems we obtain values for D_o of 3.35 x10^{-6}, 7.81 x10^{-6}, 1.47 x10^{-5} and 2.38 x10^{-5} cm^2 s^{-1} respectively. Although the V_2-V_4POM systems could potentially undergo multiple electron transfer we observe only a single redox couple associated with the vanadium centres in the cyclic voltammetry. This could indicate that the vanadium metal centres are independent (non-interacting in the redox sense) and that a single electron transfer can be assumed.[55]

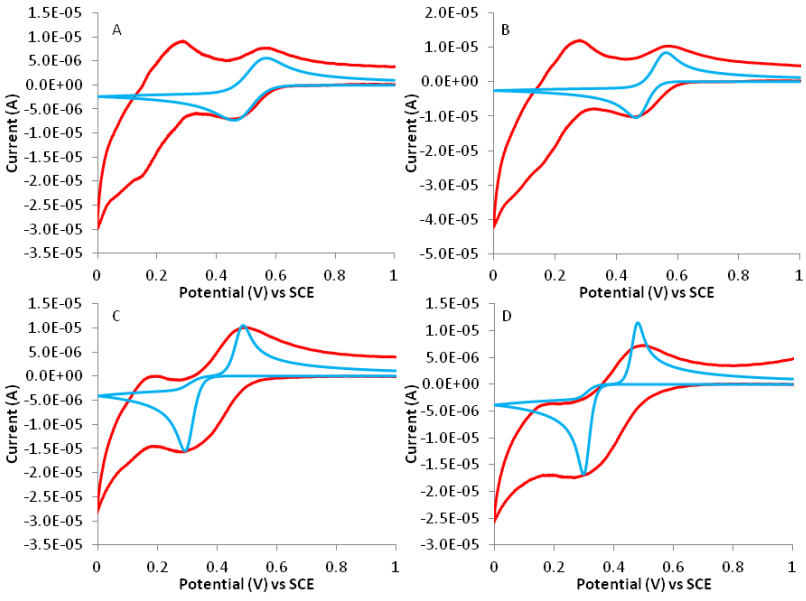

Figure 3.13: Comparison of Simulated (blue line) and Experimental (red line) cyclic voltammetry of V_xPOM systems based on a one electron transfer model described in equation 3.4. Parameters used for simulations are $E^{o'}$ = 0.515 (V_1/V_2) and 0.412 (V_3/V_4) volts vs. SCE, transfer coefficient = 0.5, [V_xPOM] = 0.001 M, [Electrolyte($HClO_4$)] = 0.1 M, Electrode Area (A) = 7.62 x10^{-2} cm^2, n = 1 and v = 0.04 V s^{-1}. A) V_1POM, B) V_2POM, C) V_3POM and D) V_4POM

However it is noted that although the I_p of V_1 and V_2 POMs does appear proportional with the square root of scan rate, V_3 and V_4 deviate from linearity. Simulations of the four systems in question based upon a one electron transfer (model A, described in equation 3.4) were performed to ensure the trend observed for D_o was not due to deviations observed in Figure 3.12 and a breakdown in the Randles Sevcik equation. The simulations show excellent correlation with the experimental peak cathodic currents which are assigned to the reduction of the V^V redox centre within each of the Keggin structures (Figure 3.13). Simulated D_o for the V_1, V_2, V_3 and V_4 system are 4.6 $x10^{-6}$, 1.05 $x10^{-5}$, 2.28 $x10^{-5}$ and 3.46 $x10^{-5}$ cm^2 s^{-1}, respectively[f]. The overall negative charge upon the fully dissociated V_1, V_2, V_3 and V_4 structures is -4, -5, -6 and -7 respectively. It is unlikely that the Keggins are fully dissociated as the pH of the fresh Keggin would be less, with the increase in negative charge leading to an increase in the degree of solvation around the respective anion (Figure 3.14).[56] This increase in solvation results in a larger resistance to movement in solution for the more highly saturated anions and hence slower diffusion expected. This suggests the number of electrons transferred is more than one for V_xKeggin when x >1.

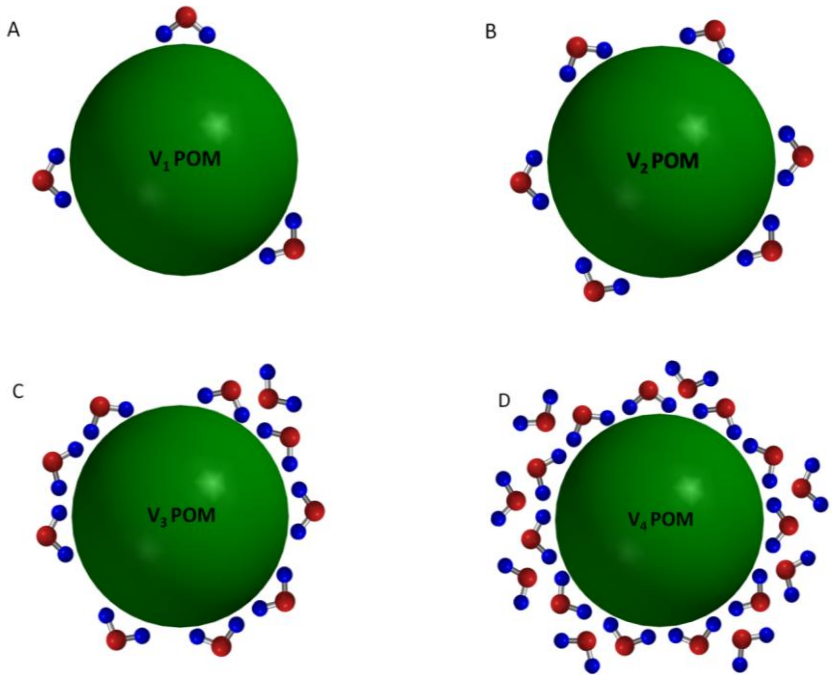

Figure 3.14: Illustration of the varying degree of solvation across the POM systems. A) V1POM, B) V2 POM, C) V3 POM and D) V4 POM

[f] Simulated diffusion coefficients calculated as an average taken across a range of simulations with scan rate ranging from 0.02 – 0.2 V s^{-1}

3.2.6.2 Simulation of V_xPOM Systems: Model B

Simulation of the V_xPOM systems using model B is carried out using DigiElch simulation software[64] with the following assumptions:

- Each of the V_xPOM systems contains only a single Keggin species which is that of its experimental formula i.e. V_2POM contains only the V_2Keggin, V_3POM contains only the V_3Keggin etc
- Here the number of electrons transferred (n) varies between the V_xKeggin species. V_1Keggin n = 1, V_2Keggin n = 2, V_3Keggin n = 3, V_4Keggin n = 4

A re-calculation has been made for the diffusion coefficients based on the number of electrons involved ranging from 1-4, where we assume n = 1, 2, 3 and 4 for the V_1, V_2, V_3, and V_4 respectively. The new model (model B) is based upon equations 3.9 – 3.12, taking into account the possibility of a varying number of electrons transferred, but maintaining a single species preset in each system. Simulations of the V_xPOM systems based upon model B are shown in Figure 3.15 with comparisons between experimental and simulated values highlighted in Table 3.9.

$$V_1POM_{ox} + e^- \longrightarrow V_1POM_{red} \quad (3.9)$$

$$V_2POM_{ox} + 2e^- \longrightarrow V_2POM_{red} \quad (3.10)$$

$$V_3POM_{ox} + 3e^- \longrightarrow V_3POM_{red} \quad (3.11)$$

$$V_4POM_{ox} + 4e^- \longrightarrow V_4POM_{red} \quad (3.12)$$

Figure 3.15 shows that model B, like model A, has a good correlation between the experimental and simulation CV when comparing the cathodic peaks associated with the reduction of the vanadium redox centres. The D_o values based upon model B (experimental and simulation) show a decrease when moving from V_1 to V_4 which is in agreement with the work of Chaumont et al.[56] Although model B successfully predicts the trend in D_o (based on theory and literature) the model is still solely based upon a single species present in each system with the correlation between simulated

and experimental peak widths still remaining very poor. Assuming that model B is correct with regards to the number of electrons transferred for each individual species and the trend displayed in D_o, it is possible to expand the model to incorporate the varying concentrations of species present in each system as well as the homogenous reactions in solution.

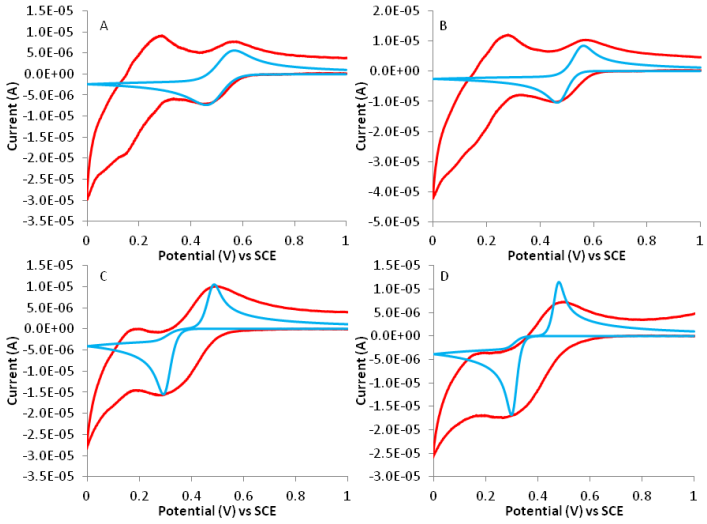

Figure 3.15: Comparison of Simulated (blue line) and Experimental (red line) cyclic voltammetry of V_xPOM systems based on model B, described in equations 3.10-3.13. Parameters used for simulations are $E^{o'}$ = 0.515 (V_1/V_2) and 0.412 (V_3/V_4) volts vs. SCE, α = 0.5, [V_xPOM] = 0.001 M, [Electrolyte($HClO_4$)] = 0.1 M, Electrode Area = 7.06 x10^{-2} cm^2, n = 1 for V_1, 2 for V_2, 3 for V_3 and 4 for V_4 and v = 0.04 V s^{-1}. A) V_1POM, B) V_2POM, C) V_3POM and D) V_4POM

Table 3.9: Comparison of simulated and experimental D_o values obtained from models described in equation 3.4 and 3.10 - 3.13. D_o = cm^2 s^{-1} determined via Randles Sevcik and DigiElch simulation

POM System	Electrons Transferred (n)	D_o Randles Sevcik	D_o Simulation
V_1	1	3.5 x10^{-6}	4.63 x10^{-6}
V_2	1	7.81 x10^{-6}	1.05 x10^{-5}
V_3	1	1.47 x10^{-5}	2.28 x10^{-5}
V_4	1	2.38 x10^{-5}	3.46 x10^{-5}
V_1	1	3.5 x10^{-6}	4.63 x10^{-6}
V_2	2	9.76 x10^{-7}	1.56 x10^{-6}
V_3	3	5.44 x10^{-7}	8.91 x10^{-7}
V_4	4	3.72 x10^{-7}	6.23 x10^{-7}

3.2.6.3 Simulation of V_xPOM Systems: Model C

Simulation of the V_xPOM systems using model C is carried out using DigiElch simulation software[64] with the following assumptions:

- Each of the V_xPOM systems (when x > 1) contains multiple V_xKeggin species based upon ^{31}P NMR data (Table 3.4) which is that of its experimental formula i.e. V_2POM contains V_1Keggin, V_2Keggin and V_3Keggin species.
- Here the number of electrons transferred (n) varies between the VxKeggin species. V_1Keggin n = 1, V_2Keggin n = 2, V_3Keggin n = 3, V_4Keggin n = 4

Model C is a complex expansion of the model B and involves not only the incorporation of multiple species present in each system but also the effect of the free vanadate species (equations 3.13 - 3.16). Here we incorporate the possibility of a homogeneous electron transfer from the reduced POM to the free vanadium in solution. This additional electron transfer changes the electrochemical mechanism to an EC mechanism, where the POM undergoes an initial heterogeneous electron transfer at the electrode surface and then a second homogeneous electron transfer in solution. It is important to note that this new model is only applicable to V_x systems were n > 1 due to the assumption of multiple species present within the system. Figure 3.16 shows the stages in the development of model C using the V_2POM system.

The initial parameters are based upon those of the V_1POM system, as these are determined for a single species and are accurate for the V_1 POM. Figure 3.16A shows the first stage of development of model C for the V_2POM system where the specific concentrations of each individual species is set (Table 3.4) and D_o, k^o and n are 4.63 x10^{-6} cm^2 s^{-1}, 0.0026 cm s^{-1} and 1 respectively, obtained from previous simulations. It is clear that the magnitude of the cathodic current is not equal to that of the experimental indicating that the properties for each individual V_xKeggin species are not the same. The V_2 and V_3Keggin species were changed from a one to a two electron transfer mechanism resulting in the simulated cathodic current exceeding the experimental (Figure 3.16B).

$$V_1POM_{red} + V^{V}_{Free} \longrightarrow V_1POM_{ox} + V^{IV}_{Free} \quad (3.13)$$

$$V_2POM_{red} + 2\,V^{V}_{Free} \longrightarrow V_2POM_{ox} + 2\,V^{IV}_{Free} \quad (3.14)$$

$$V_3POM_{red} + 3\,V^{V}_{Free} \longrightarrow V_3POM_{ox} + 3\,V^{IV}_{Free} \quad (3.15)$$

$$V_4POM_{red} + 4\,V^{V}_{Free} \longrightarrow V_4POM_{ox} + 4\,V^{IV}_{Free} \quad (3.16)$$

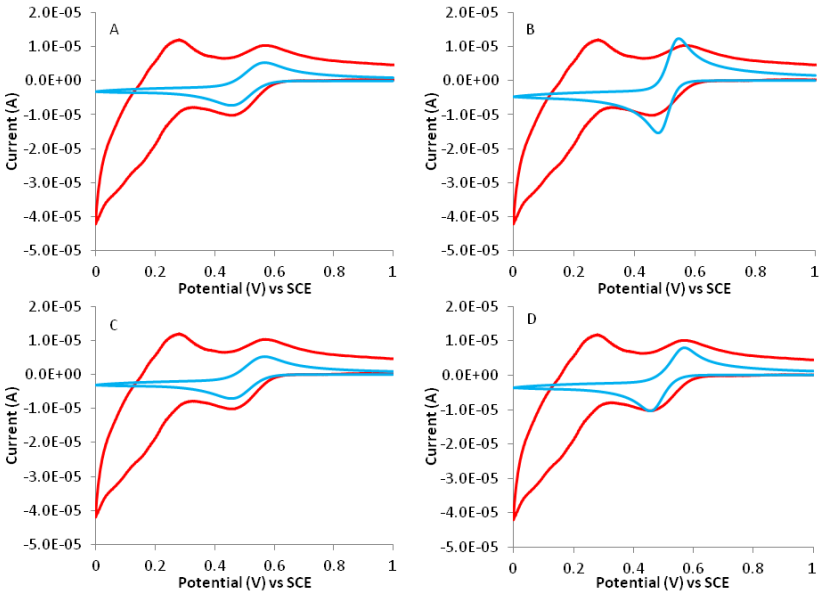

Figure 3.16: Development of model C (equations 3.10-3.17) using the V_2POM system. Initial parameters used for simulations are $E^{o'}$ = 0.515 volts vs. SCE, α = 0.5, [V_1POM] = 96 mM, [V_2POM] = 170 mM, [V_3POM] = 26 mM and [V_{Free}] = 84 mM, [Electrolyte ($HClO_4$)] = 0.1 M, Electrode Area = 7.62 x10^{-2} cm^2 and v = 0.04 V s^{-1}. Red = experimental and blue = simulated.

Applying the diffusion coefficient obtained for the V_2 species based on a two electron transfer (simulation 1.56 x10^{-6} cm^2 s^{-1}) to the V_2 and V_3Keggins in this model results in the simulated cathodic current once again being less than the experimental (Figure 3.16C). The V_3Keggin was changed to a three electron transfer mechanism with a D_o of 8.91 x10^{-7} cm^2 s^{-1} yielding an increase in the cathodic current but not sufficient to match that of the experimental data. An increase in D_o of the V_2Keggin (2.2 x10^{-6} cm^2 s^{-1}) results in a good agreement between the simulated and experimental data (Figure 3.16D). An increase in the V_3Keggin D_o also increased the cathodic current but to a much lesser extent compared to the V_2Keggin due to the difference in concentrations ([V_2Keggin] = 5.6 x10^{-1},

[V_3Keggin] = 8.6 x10^{-2}). The simulations in Figure 3.16 support the idea that the number of electrons transferred is not in unity across all species and that to ascertain the experimental current, *n* increases from V_1 to V_4. This increase in *n* leads to D_o for each species having to be reduced in order to achieve agreement with experimental data, also, a more accurate D_o is obtained as we are simulating the effects of individual species upon the overall CV. Most noticeably, the model agrees with what would be expected form a logical approach:

- Diffusion coefficients of V_xKeggin decreases as x increases
- Number of electrons transferred increases as x increases.

The same model was applied to the V_3 and V_4 systems substituting in the respective concentrations of each respective species, with the final simulations shown in Figure 3.17.

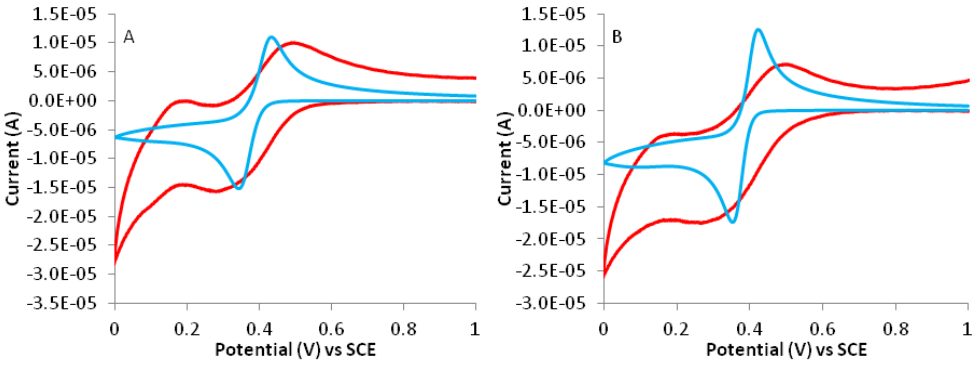

Figure 3.17: Experimental and simulation comparison based on model C. A) V_3POM system and B) V_4POM System. Parameters used for simulations; $E^{o'}$ = 0.412 volts vs. SCE, α = 0.5, V_3POM system; [V_1POM] = 14 mM, [V_2POM] = 150 mM, [V_3POM] = 98 mM, [V_4POM] = 25 and [V_{Free}] = 200 mM, V_4POM system; [V_1POM] = 1.1 mM, [V_2POM] = 56 mM, [V_3POM] = 120 mM, [V_4POM] = 95 mM and [V_{Free}] = 350 mM, [Electrolyte($HClO_4$)] = 0.1 M, Electrode Area = 7.62 x10^{-2} cm^2 and 4 for V_4 and *v* = 0.04 V s^{-1}. Red = experimental and blue = simulated.

In both systems the formal potential for the simulation was shifted to 0.412 V vs. SCE and the four electron transfer mechanism of the V_4 species introduced. The same effect was observed where by increasing the number of electrons the corresponding D_o had to be reduced in order for the simulated and experimental cathodic peak currents to be comparable. The D_o obtained for the V_1, V_2, V_3 and V_4 Keggins based on this model are 4.63 x 10^{-6}, 2.2 x10^{-6}, 9.91 x10^{-7} and 8.4 x10^{-7} cm^2 s^{-1} with values for the $V_{2\text{-}4}$Keggins being the minimum possible values.

The values obtained here are slightly higher than those based on the assumption of a single species in solution, probably due to the effect of the slower diffusing species being removed when considering the effect of individual species have upon the overall CV. Although the magnitude of the cathodic currents for the V_3 and V_4 systems show good correlation, (Figure 3.17A and B, respectively) the peak to peak separation is extremely poor as well as peak width. Interestingly, to obtain an acceptable peak to peak separation, a k^o value of 2 $x10^{-5}$ cm s^{-1} is needed which is a magnitude more commonly associated with an electrochemically irreversible process[30]. In this instance this is highly unlikely as we observe both a reduction and oxidation peak within a narrow potential range resulting in a relatively small peak to peak separation compared with the values (peak to peak separation) expected for an irreversible process.

It has been previously highlighted that the formal potential of the vanadium redox couple within the Keggin changes when moving from the V_1 to the V_4 system. The change in formal potential is reflected in the increase in negative charge of the Keggin structures. The V_1 system has the most positive formal potential with a single electron transfer occurring at said potential, however the remaining species undergo several electron transfers with the initial electron transfer at a given potential. The formal potential of the successive reductions could account for the broadening of the observed peaks and increase in the peak to peak separation. If we consider the simple heterogeneous electron transfer process at an electrode surface:

$$A + e^- \longrightarrow B \qquad (3.18)$$

The CV simulation of the one electron reduction of species A in equation 3.18 is shown in Figure 3.18A where a single oxidation and reduction peak is observed. This would be analogous of the V_1POM with the magnitude of k^o dictating the peak separation. If we now consider a two electron transfer at the electrode surface where:

$$A + 2e^- \longrightarrow C \qquad (3.19)$$

Here a simultaneous two electron reduction occurs (Figure 3.18B) where we observe sharp narrow peaks and a small peak to peak separation. This is not representative of the V_2POM systems which have a relatively large peak to peak separation and a

broad reduction and oxidation peak. Quantum mechanics predicts that more than one electron transferring at the same time is highly unlikely. Rather, a classical multi electron transfer where two sequential one electron transfers occur with the second being much easier than the first. In all cases the two electron reduction occurs by two successive one electron reductions:

$$A + e^- \longrightarrow B + e^- \longrightarrow C \qquad (3.20)$$

The two electron reduction outlined in equation 3.20 can occur via two scenarios, a) $E^{o'}_{(BC)}$ is more positive then $E^{o'}_{(AB)}$ i.e. it is easier to reduce the intermediate species B than species A (Figure 3.18C) or b) $E^{o'}_{(AB)}$ is more positive then $E^{o'}_{(BC)}$ i.e. it is more difficult to reduce the intermediate species B than species A (Figure 3.18D). In Figure 3.18C we observe a sharp oxidation and reduction peak; however Figure 3.18D shows drastic broadening of both the oxidation and reduction peaks, analogous to the V_2POM system. Although the example in Figure 3.18D is an extreme example with a distinct second reduction peak observed, small changes in the formal potential of successive reductions will lead to a broadening of individual peaks and an increase in peak to peak separation.

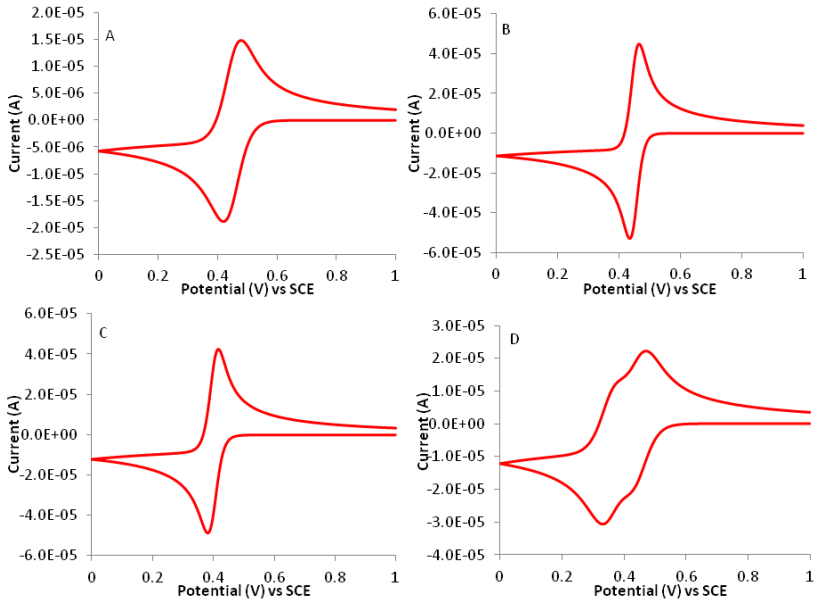

Figure 3.18: Simulations of the possible mechanisms associated with single and multiple electron transfer. A) Single electron transfer (Equation 3.18), B) Two electron transfer (Equation 3.19), C) Successive one electron transfers $E^{o'}_{(BC)} > E^{o'}_{(AB)}$ and D) Successive one electron transfers $E^{o'}_{(BC)} < E^{o'}_{(AB)}$

Considering the case of the V_2POM system we identified from ^{31}P NMR that there are V_1, V_2 and V_3 Keggin species present which all undergo multiple electron reductions as shown above. The CV observed for the V_2 system can now be observed as an 'outline' or average response of the sequential reductions that occur. This is highlighted in Figure 3.19A where we see the true complexity of the cathodic peak consisting of the individual multiple electron transfers. The case of the V_4 system (Figure 3.19B) is similar with the increased broadening due to the number of reductions within the peak increasing. One must also consider the effect of the free vanadate ion upon the broadening of the observed peak. The free vanadate ion situated in the outer sphere of the Keggin structure is more easily reduced than the substituted vanadium within the structure. This leads to another redox process at a more positive formal potential resulting in further broadening of the observed peaks. It is also likely that approaching the formal potential of the molybdenum redox couple also contributes to this phenomenon.

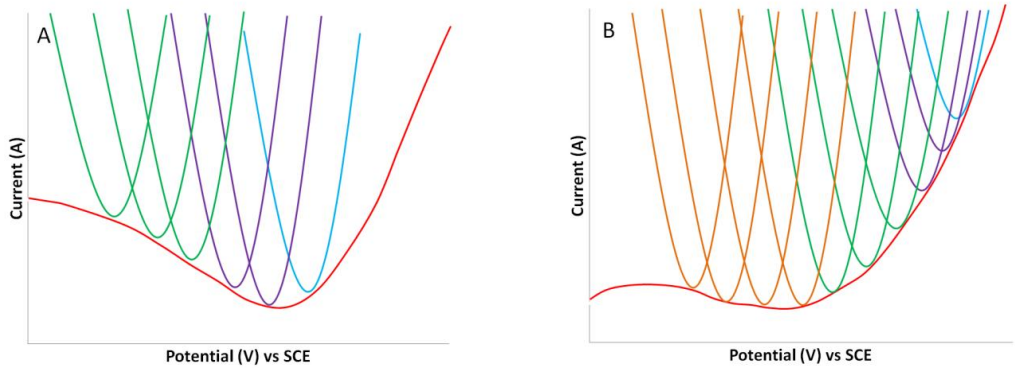

Figure 3.19: Magnified view of the reduction peak showing the separate reduction peaks for the individual Keggin species within each system. Red line is the experimental CV wave whilst blue = V_1, purple = V_2, green = V_3 and orange = V_4 are the successive reductions associated with each individual species. A) V_2POM system and B) V_4POM system.

It is shown that the multiple redox process occurring in a very small potential window account for the broadening and the increase in separation of the peaks observed in the CV. This explanation no longer requires the need for k^o to decrease to values expected for irreversible electron transfer. However, the diffusion coefficients derived from model C are more representative of individual Keggin species (V_2 – V_4) and not the overall system thus making it difficult to calculate k^o via the method of Nicholson based on these calculations. However, based on the V_1 system we obtain an experimental k^o calculated by the method Nicholson of 0.0015

cm s^{-1} which is in agreement with simulations (0.0021 cm s^{-1}). Based on the value of k^o (and data in Table 3.7 and 3.8) it can be assumed that V_1 behaves as an electrochemically quasi-reversible system. With k^o not decreasing beyond 2 x10^{-5} cm s^{-1} (for reasons outlined above) across the V_xPOM series it can be assumed the V_1-V_4 systems are all electrochemically quasi-reversible.

3.2.7 Rotating Disc Electrode Analysis of the $Ru(NH_3)_6^{3+/2+}$ Redox System

As discussed in chapter 1 FlowCath® technology is focused around a liquid catholyte being continuously pumped around the fuel cell. This essentially means that a constant supply of fresh electrolyte is brought to the electrode surface analogous to hydrodynamic methods for electrochemical analysis. While the voltammetric studies have provided an understanding of these systems, this analysis has been based upon the interplay between diffusion and electrode kinetic processes. However the rotating disc electrode analysis (RDE) allows for an analysis which is more comparable to fuel cell conditions where the catalyst is brought to the cathode via other means of mass of transport (convection). For high rates of mass transport, the electrode kinetics limits the rate of the electrochemical reaction over a wide operating range. The RDE allows for the effects of mass transport (diffusion, migration and convection) to be effectively removed from the 'equation' and allow for a better understanding of the electron transfer mechanism.

The current voltage curves for the $Ru(NH_3)_6^{3+/2+}$ redox couple at rotating speeds ranging from 500 – 5000 rpm under a nitrogen atmosphere are illustrated Figure 3.20 and are a typical example of data obtained from a RDE. Figure 3.20A shows a series of linear sweeps from 0.1 to -0.4 V vs. SCE for the reduction of $Ru(NH_3)_6^{3+}$ studied previously. As can be seen when increasing the rotation speed of the RDE we see an increase in I_L, the limiting current or Levich current which is in agreement with relationship outlined in equation 3.21 (Levich equation) for RDE.

$$I_L = 0.62\, n\, A\, F\, D_o^{2/3}\, v^{-1/6} C^*\, \omega^{1/2} \qquad (3.21)$$

The Levich equation describes the relationship between the maximum (Levich) current and the square root of the rotation speed of the RDE and is shown in Figure 3.20B for $Ru(NH_3)_6$. The diffusion coefficient calculated from the gradient is

3.683×10^{-6} cm^2 s^{-1}which is in agreement with literature and that obtained via Randle Sevcik analysis at the glassy carbon electrode.[27]

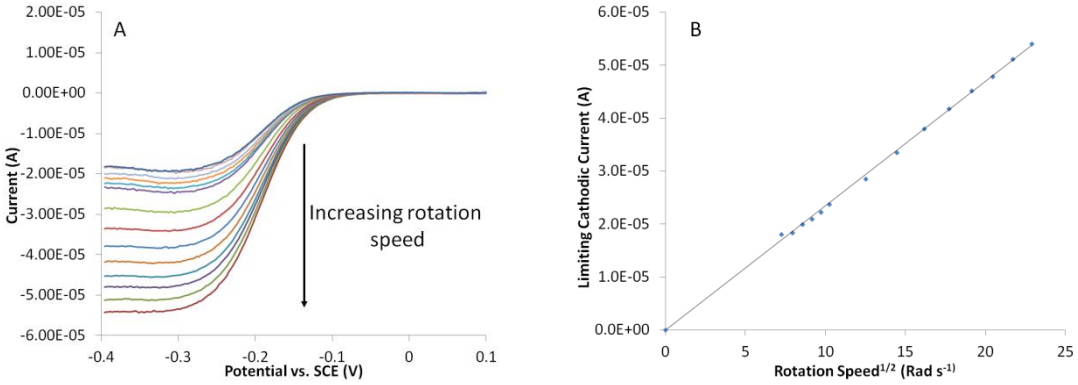

Figure 3.20: A) Overlay of linear sweeps for the reduction of 0.001 M $Ru(NH_3)_6Cl_3$ in 0.1 M KCl at rotation speeds ranging from 500 to 5000 rpm. B) Limiting cathodic current taken at 0.3 V vs. SCE at varying rotation speeds ranging from 500 to 5000 rpm. ν = 0.005 Vs^{-1}.

Here we see that the current is mass transport limited indicating the rate of electron transfer is faster than that of mass transport and the concentration of $Ru(NH_3)_6^{3+}$ at the electrode surface is zero. Figure 3.21 illustrates the Tafel plot obtained for the $Ru(NH_3)_6^{3+}$ reduction. The Tafel plot represents the $Ru(NH_3)_6^{3+}$ reduction with the contributions of mass transport removed (see section 3.4.2 for details of Tafel plot construction). Here we can see three distinct regions associated with a typical Tafel plot. A linear region between ~ 0.12 and 0.22 V is observed associated with pure charge transfer control. Below this region (0.11 – 0 V) we observe the deviation from linearity caused by the electrode potential approaching that of the formal potential and the anodic reaction no longer being negligible in the Butler-Volmer equation. At higher overpotentials (> 0.22 V) we again observe the deviation from linearity caused by mass transport effects i.e. the supply of the electroactive species is no longer sufficient to sustain the exponential increase in current at the given overpotential.[57] Tafel plots based upon a system with fast electrode kinetics may not produce linear regions due to only small overpotentials required to drive the reaction and subsequently reach a mass transport limited current at relatively low overpotentials.[30,57] This is likely to be case if the Tafel plot was obtained using a Pt electrode; however the glassy carbon electrode shows slower electron transfer kinetics (observed during CV analysis) and larger overpotentials are required to drive the reaction, hence a linear region in the Tafel plot is observed.

For a typical one electron transfer we would expect a transfer coefficient of around 0.5 and a Tafel slop of 118 mV decade^{-1},[30] however in this instance we obtain a transfer coefficient of 0.3 and a slope of 140 mV decade^{-1}. The shallower gradient (compared to the theoretical value) is a result of slower kinetics at the glassy carbon electrode. This is supported by the standard rate constant calculated from equation 3.22 (0.028 cm s^{-1}) being in agreement with that calculated via the method of Nicholson based upon the cyclic voltammetry data obtained for the GC electrode.

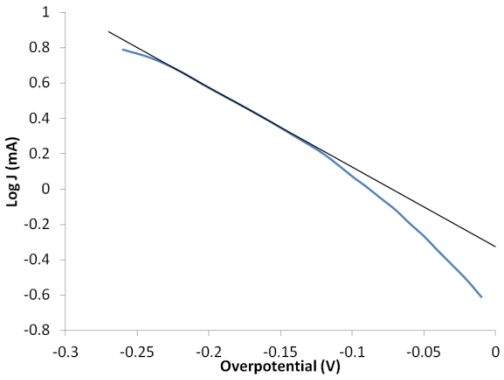

Figure 3.21: Cathodic branch of the Tafel plot obtained for 0.001 M Ru(NH3)6 in 0.1 M KCl at a glassy carbon electrode. Transfer coefficient = 0.3, Tafel slope = 140 mV decade^{-1}, J_o = 0.4 mA cm^{-2} and k^o = 0.011 cm s^{-1}.

$$I_o = F\,A\,k^o\,C_o^*\,e^{(-\alpha f(E_{eq}-E^{o\prime}))} \tag{3.22}$$

Where I_o is the exchange current obtained from the experimental Tafel plot by extrapolation to zero overpotential, k^o is the standard rate constant for electron transfer, F is Faraday's constant, C_o^* is the initial concentration of the oxidised species and F is Farday's constant. The two parameters I_o and k^o are fundamental in assessing a catalyst's fuel cell performance (see Chapter 2). However careful consideration of the Tafel slope highlights that a small curvature still remains. Figure 3.22A shows the experimental and polynomial fit for the Tafel plot of 0.001 M $Ru(NH_3)_6Cl_3$ in 0.1 M KCl with a slight curvature visible in the charge transfer region (highlighted yellow). When plotting the error curve for the difference between the raw experimental data and the linear fit (Figure 3.22B), this transformation results in a parabolic type fit. Here ΔLog J is the difference between the values obtained based on the polynomial and linear fits and a given overpotential. In this instance the red line (connecting the points) is here merely to highlight the data, not to highlight any possible trends. It was believed that the decrease in the standard rate

constant on glassy carbon would indeed result in a classic Tafel slope, this is not the case.

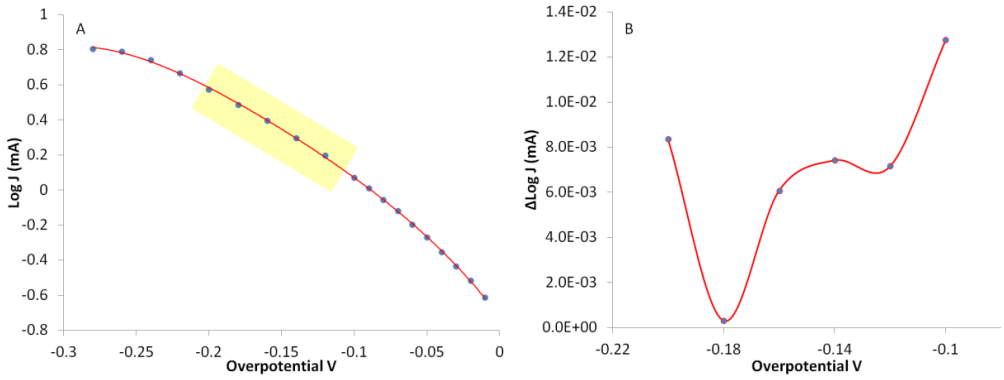

Figure 3.22: A) Tafel plot of $Ru(NH_3)_6$ showing raw data (blue dots) and the polynomial fitted data (red line). B) Difference between polynomial and linear fits in the 'linear' charge transfer region highlighted (yellow) in A.

The curvature that still remains is only slight indicating that the re-organization energy must be large enough to minimise the effect of overpotential upon the symmetry factor/transfer coefficient (equation 3.23)[g]

$$\alpha = \frac{1}{2}\left(1 + \frac{\Delta G}{\lambda}\right) \tag{3.23}$$

This leads to the assumption that contributions to the re-organisation energy may arise from inner and outer sphere effects via fluctuations in bond lengths and charge distribution, respectively.

3.2.8 Rotating Disc Analysis of the $V_{1\text{-}4}$POM Systems

It is discussed in chapter 2 that the exchange current and the standard rate constant are key parameters when comparing the suitability of potential catalysts. However to extrapolate this data from a Tafel plot one needs to ensure that a suitable charge transfer region is observed. The ruthenium system studied in section 3.4.7 showed a slight curvature in the cathodic branch of the experimental Tafel plot with the re-organisation energy being large enough to reduce the effect of overpotential on the symmetry factor. A slight curvature might also be expected in the POM Tafel plots

[g] Here the Gibbs energy term is not a pure standard Gibbs energy as the energy of the electron changes with electrode potential.

since the vanadium centres may undergo re-organization upon electron transfer analogous to that of the ruthenium centre with only small changes in bond lengths upon reduction when bound in the Keggin.

Initially considering the V_1POM system used for CV experiments in the presence of 0.001 M V_1POM in 0.1 M $HClO_4$ (measurements are carried out under a N_2 atmosphere) we observe a linear relationship between the limiting current and square root of rotation speed (Figure 3.23A) indicating the system is under mass transport control in the limiting current plateau region. Within each potential scan at the respective rate of rotation a number of limiting current plateaus are observed. These are associated with the various redox processes in the system. The Keggin-bound vanadium redox couple has the most positive redox potential hence is believed to be the source for the first limiting current plateau at approximately 0.2 V vs. SCE. This is the same for the remaining V_xPOMs with the first limiting current observed at between 0.2 and 0.25 V vs. SCE (Figure 3.23B-D). It is apparent however that in the case of V_3 and V_4POM systems the potential sweeps have only a single limiting current plateau within the potential range observed. Here a mass transport limited current is not observed for the molybdenum redox centres but the beginning of the reduction is observed.

A clear increase in limiting cathodic current is observed when moving from the V_1 to V_4 (2.73×10^{-2}, 5.63×10^{-2}, 6.72×10^{-2} and 1.04×10^{-1} mA respectively) system as a result of the increased concentration of the redox active vanadium centre present within the Keggin/system. This is consistent with the relationship observed in the Levich equation illustrating that peak current increases with concentration. Figure 3.23E-G shows the relationship between the limiting cathodic current and the rate of rotation for the RDE for the four POM systems. It is clear the two properties are not strictly proportional (analogous to I_p vs. $v^{1/2}$) indicating that the current is not solely limited by mass transport effects but the kinetics of the electron transfer mechanism may also contribute.[58] The diffusion coefficients calculated for this data set are much lower than those obtained from the simulation data (Table 3.10) and do not show the same expected trend. It should be noted that it is difficult to identify the limiting currents for the V_xPOM systems as there is always a contribution from more than one single redox process, even for the V_1POM system. At 0.2 V vs. SCE, the

potential perceived at which the limiting current occurs, is negative enough for the reduction of the molybdenum redox centres to be observed. Hence if multiple redox processes are occurring simultaneously, a linear plot is not expected.

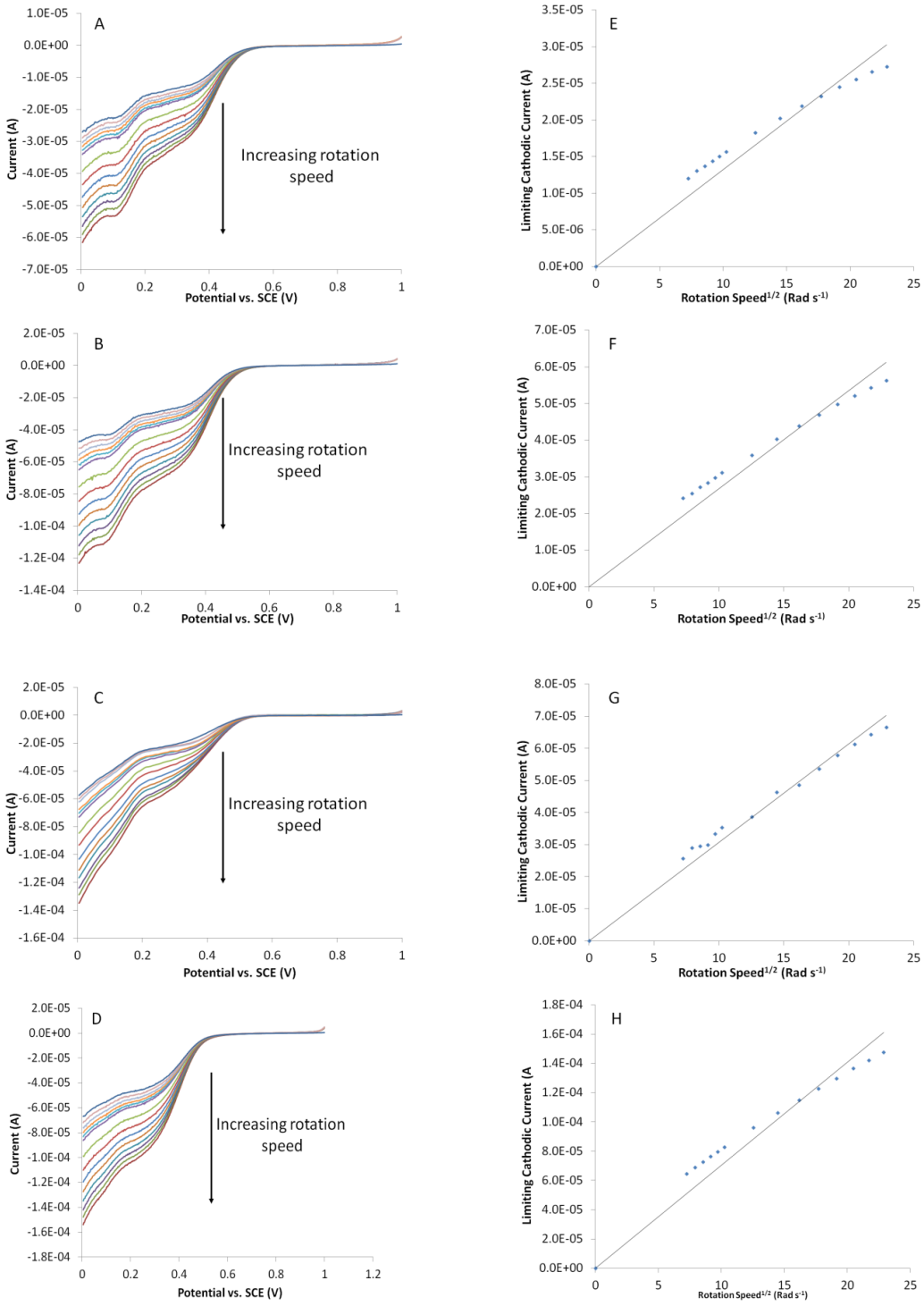

Figure 3.23: Overlay of linear sweeps for the reduction of 0.001 M A)V_1POM, B) V_2POM, C) V_3POM and D) V_4POM in 0.1 M $HClO_4$ at rotation speeds ranging from 500 to 5000 rpm. Plot of limiting cathodic current at varying rotation speeds ranging from 500 to 5000 rpm E) V_1POM, F) V_2POM, G) V_3POM and H) V_4POM.

The Tafel plot constructed based on the ruthenium system showed a clear Tafel region for the charge transfer process, where it was possible to extrapolate to zero overpotential to obtain the exchange current. Figure 3.24 depicts the cathodic branches of Tafel plots obtained for the reduction of the V_xPOM systems at a GC electrode, with each again showing the three regions of a typical Tafel plot.

Table 3.10: Comparison between simulated and experimental D_o values. Experimental values obtained under hydrodynamic conditions at glassy carbon RDE. [V_xPOM] = 0.001 M in 0.1 M $HClO_4$. D_o = cm^2 s^{-1}. Simulated D_o values obtained from simulation using model C, electrons transferred for each system are also concordant with those used in model C.

POM System	Simulated D_o (cm^2 s^{-1})	RDE D_o (cm^2 s^{-1})
V_1	4.63×10^{-6}	1.55×10^{-6}
V_2	2.20×10^{-6}	1.57×10^{-6}
V_3	9.91×10^{-7}	1.17×10^{-6}
V_4	8.40×10^{-7}	1.42×10^{-6}

However it is apparent that the Tafel plots obtained here are not 'classical' as the charge transfer region is small and a slight curvature is evident from the naked eye which becomes more prominent in the V_4POM system. This curvature is more evident when observing the error curve for the difference between the experimental data and the linear fit for the Tafel slope (Figure 3.25). For a truly linear fit one would expect zero error across the range of overpotential in question. The standard rate constant for the V_1POM is approximately one order of magnitude less than the of the ruthenium system thus faster electron transfer is not the cause for the enhanced curvature. Curvature in Tafel plots that are based upon steady state measurements can occur for a number of reasons. Work done by Fletcher and Varley[59] highlights the stringent criteria a system must obey in order for a curvature on this basis to be observed. The three key parameters being: a) slow irreversible electron transfer b) no inner sphere ligand substitution of the reactive species, c) a single reactant species and d) no coupled homogenous kinetics.

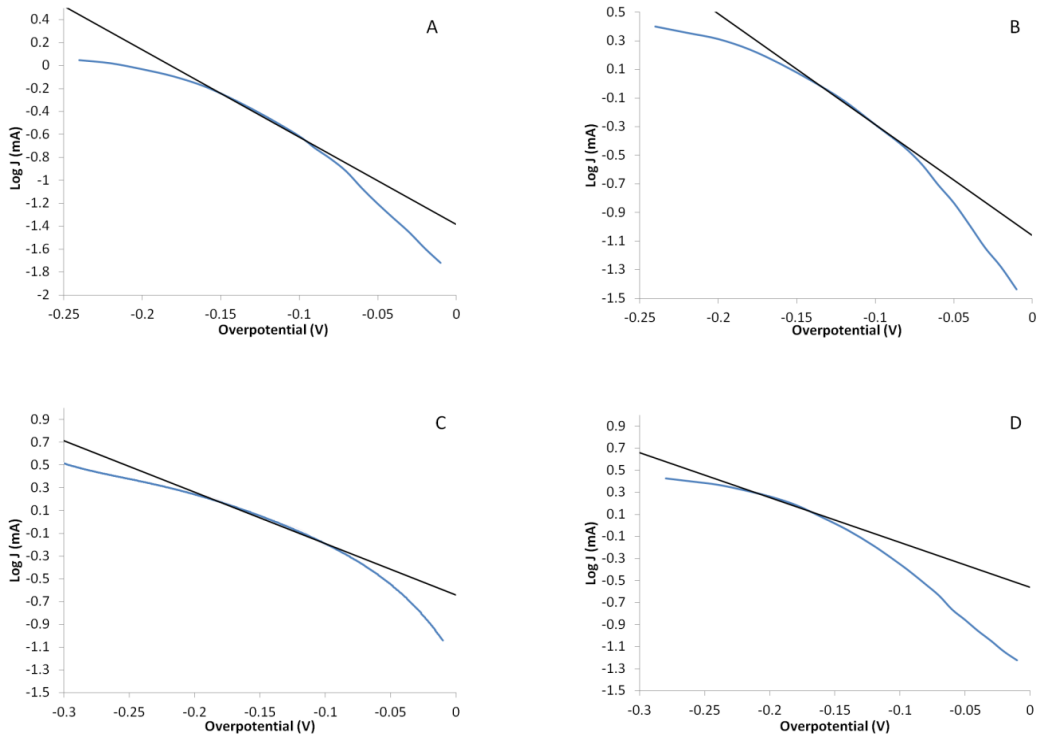

Figure 3.24: Cathodic branch of the Tafel plots obtained for 0.001 M V_xPOM in 0.1 M $HClO_4$ at a glassy carbon RDE. A) V_1POM, B) V_2POM, C) V_3POM and D) V_4POM.

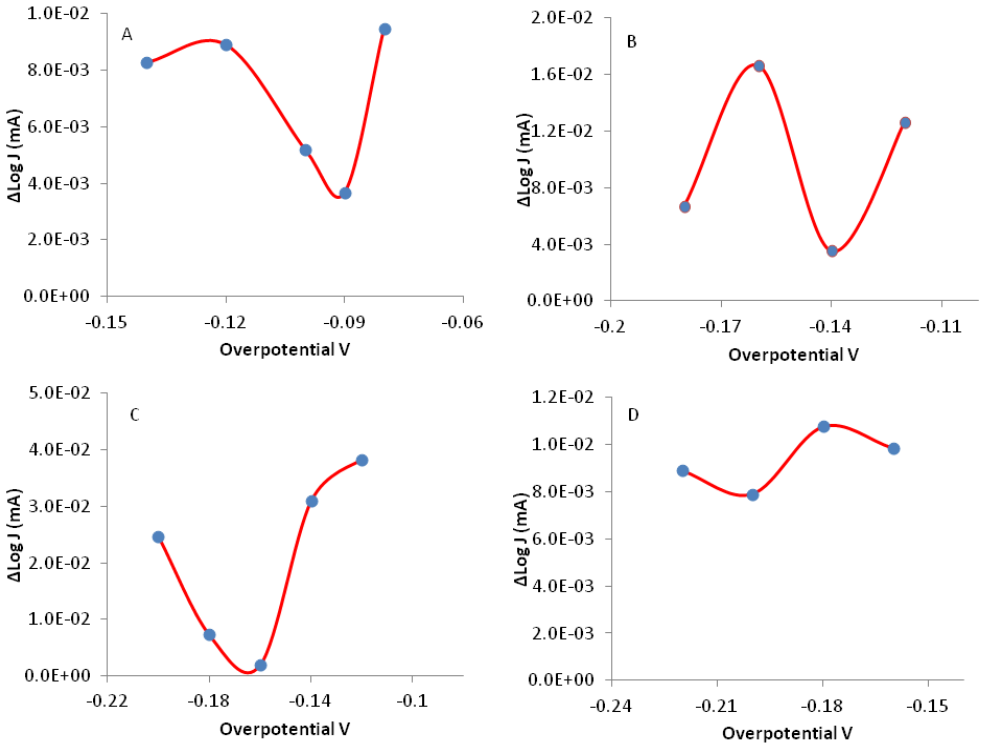

Figure 3.25: Error curves showing the difference between the experimental and linear fit for the corresponding Tafel slopes in the VxPOM systems. A) V_1POM, B) V_2POM, C) V_3POM and D) V_4POM

This is clearly not the case in the V_xPOM systems as we do not observe irreversible electron transfer, nor is there a single species present in solution and continuous substitution of metal centres within the Keggin due to the dynamic equilibrium present. However there are several other reasons for curvature in Tafel plots;

a) Solution resistance can result in a potential drop resulting in errors in the predicted kinetics. This effect can be corrected with IR compensation.

b) Surface layer formation upon the electrode surface, be it a passive layer or not, can lead to changes in the structure of the surface and interaction with the electrochemically active species.

c) Mixed control processes, where more than one reaction occurs simultaneously through multiple reactions of the various species.

The effect of solution resistance is unlikely to be the cause due to a large excess of supporting electrolyte (0.1 M $HClO_4$) used during the analysis. The adsorption of polyoxometalates on to electrode surfaces however, has been shown to inhibit electron transfer to the solution phase species.[60] These monolayers can spontaneously form from acidic aqueous solutions of polyoxometalates[61] and with the natural speciation of the V_xPOMs leading to multiple species undergoing reduction, these phenomena are the likely source of the observed curvature.

The extrapolation of the exchange current is a key parameter for characterising potential catalysts for FlowCath® technology. In the case of the V_xPOM systems the pure charge transfer regions (linear section of cathodic branch) are small and the observed curvature lead to a non-ideal Tafel plot, thus the accuracy of the extrapolated values is questionable. If we consider the V_3POM as an example, it can be seen from Figure 3.26 that uncertainties in determining to the perceived linear section can give significant deviations in the extrapolated value resulting in an upper and lower limit for the Log J_o extrapolation. The deviations arise with a small change (10 mV) in the linear section being extrapolated, even though this remains within the perceived ‘pure’ electron transfer region. Consequently rather, than an exchange current density value, we obtain a range within which the exchange current density falls. This still allows for a comparison between systems even though there is a

spread in any given J_o value determination. Table 3.11 summaries the range for exchange current density[h] and k^o values obtained for the individual systems.

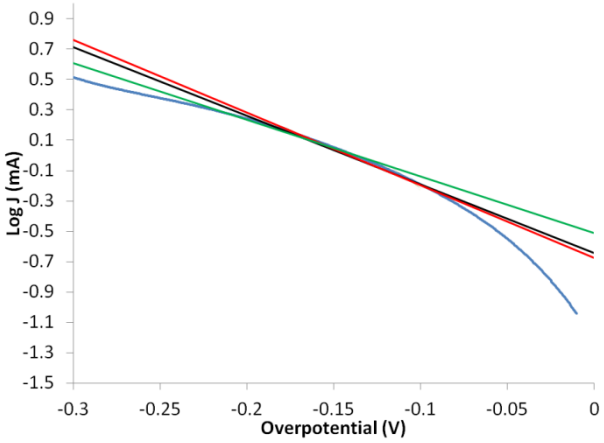

Figure 3.26: Cathodic branch of the Tafel plot for a 0.001 M V_3POM system in 0.1 M $HClO_4$ showing the upper (green) and lower (red) limit extrapolations of J_o whilst remaining within the charge transfer region.

Table 3.11: Values for J_o and k^o obtained for the 0.001 M V_xPOM systems in 0.1 M $HClO_4$.

POM System	J_o range (mA cm^2)	k^o range (cm s^{-1})	Electrons transferred
V_1	1.65 – 2.94 x10^{-2}	7.90 – 9.92 x10^{-4}	1
V_2	2.76 – 6.67 x10^{-2}	0.53 – 1.08 x10^{-3}	2
V_3	0.66 – 1.36 x10^{-1}	0.93 – 1.74 x10^{-3}	3
V_4	1.76 – 4.42 x10^{-1}	2.41 – 5.40 x10^{-3}	4

Although the cyclic voltammetry analysis focused on obtaining the parameters for the individual species in this instance the value obtained based on the average response of the system will be considered. Considering the values in Table 3.11 it is apparent that the J_o and k^o values increase from the V_1 to the V_4 system. Equation 3.22 shows the relationship between the two parameters and their dependence upon concentration. At this POM concentration (0.001 M) the increased vanadium substitution appears to have only a small effect upon J_o and k^o with values only changing by one order of magnitude across the V_xPOM series.

[h] The exchange current density is the exchange current extrapolated at zero overpotential and normalised with respect to the surface area of the electrode. This gives a current value per unit area.

The exchange current density is a measure of the amount of overpotential required to drive a reaction and one may have expected the four electron reduction of the V_4POM system to require a much larger overpotential compared with the V_1POM thus a much lower exchange current density. Based on the assumption of a various number of electrons transferred in the V_xPOM systems the relatively constant standard rate constant and exchange current density would suggest that this may not necessarily be the case. In this instance it may be possible that a multi electron reduction of the V_xPOM where $x > 1$, does not become more thermodynamically unfavourable with each successive reduction, i.e. the formal potential does not shift to more negative reduction potentials and that only a single heterogeneous electron transfer occurs due to the homogeneous electron transfers between oxidised POM and free vanadium.

The V_1POM in its oxidised state has a charge of 4- (fully dissociated) which increases to 5- upon reduction of the single vanadium centre. On going to the V_4 POM which has an initial charge of 7- (fully dissociated), the increase in vanadium substitution and negative charge causes a negative shift in the formal potential.[17] This effect would then continue to be observed after each successive reduction, but based on the simulation results in section 3.2.6**,** the change in the formal potentials is not believed to be significant enough as to define a series of redox waves but merely broaden the observed redox peak. This supports the idea of the vanadium centres being non-interacting in the redox sense.[55] For successive reductions to be significantly less favourable (thermodynamically), a more prominent shift in the formal potential would be observed as is the case of $PMo_{12}O_{40}$ and $PW_{12}O_{40}$.[60]

The electron transfer also requires a consideration of the stability of the oxidised POM. The increasing substitution of vanadium within the Keggin structure causes a general decrease in stability by not only increasing the negative charge on the overall structure but increasing bond strain. The effective ionic radii of the Mo^{VI} ion is 59 pm and is ideal for the Keggin structure whereas the V^{V} ion has a smaller radi of 54 pm[62]. Increasing the number of smaller ions within the Keggin structure increases the overall strain and thus leads to a decrease in stability. However it is has been proven that a partially reduced vanadium substituted Keggin structure can have an increased stability compared to its oxidised counterpart.[9] By reducing a single vanadium centre

the stability of the Keggin anion can be increased even though the overall negative charge also increases. The resulting successive reductions in the V_2, V_3 and V_4POMs could have a similar stabilising effect on the Keggin structure leading to only small shifts in formal potential with the increased negative charge. In the RDE analysis where fresh oxidised POM is brought to the electrode surface and the reduced species is removed. If on this time scale of the RDE experiment only a single electron transfer to the Keggin was observed at the electrode surface then there would be no variation in limiting current across the V_xPOM series.

The free vanadium present in the V_2, V_3 and V_4 systems could play a pivotal role in the electron transfer and be key to understanding the observed standard rate constants. It was stated earlier that free vanadium that is coordinated in the outer sphere of the Keggin may be reduced more easily than the vanadium coordinated within the Keggin itself. In the RDE analysis where fresh oxidised POM is brought to the electrode surface and reduced POM removed, given the time scale that the oxidised species is at the electrode surface, it may be the case that a two, three or four electron reduction of the Keggin may not be achieved. However the vanadium coordinated within the outer sphere of the Keggin could be reduced (and dissociate) more easily accounting for the increase in current across the V_x systems. If however the POM species remains at the electrode surface sufficiently long enough then the multiple electron reduction of the V_xKegign species could occur which would result in increased cathodic currents for V_xPOMs with increasing x.

3.2.9 Oxidation of Reduced $Na_xH_3PMo_{12-x}V_xO_{40}$ Systems by O_2.

The oxidation (regeneration) of the reduced polyoxometalate catalysts is a fundamental concept in FlowCath® technology. With the electrochemical behaviour of the V_xPOM systems being somewhat similar under the conditions observed it may prove to be the regeneration capabilities of the individual V_xPOM systems that limit the overall performance. To screen the regeneration capabilities of the four systems at low concentrations we employed a method developed at the Centre for Materials Discovery, see section 3.4.2.3 for details. In brief the method is based upon analysing the *d-d* transitions observed in the reduced POM species. In the fresh POM systems the Keggin-bound vanadium is in its 5+ oxidation state which contains no *d* electrons (d^0), thus no *d-d* transitions are observed. However upon reduction of the vanadium

centre the oxidation number decreases and a single d-electron (d^1) is present, which now exhibits *d-d* transitions when absorbing light at a wavelength of approximately 775 nm. It is the rate at which this peak diminishes by which we screen the regeneration capabilities of the POM systems.

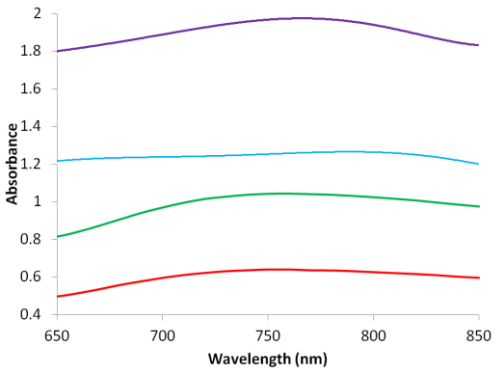

Figure 3.27: UV-Vis spectrum of the four V_xPOM systems. Each system has 50 % of the total vanadium in its 4+ oxidation state. Total POM concentration for each system is 4.6 mM. Red = V_1POM, Green = V_2, Blue = V_3 and Purple = V_4POM system.

Figure 3.27 shows the UV-Vis spectrum obtained for each of the VxPOM systems where in each case 50 % of the total vanadium is in the 4+ oxidation state resulting in the broad peak at 776 nm. The intensity of this peak increases when moving from the V_1 to V_4 system. Based on the concentration of the POM species (4.6 mM) the calculated molar absorbtivity is not constant indicating that Beer's law is not obeyed. However considering the change in concentration of the active species (vanadium) in the four systems adjusting the calculations accordingly we obtain a consistent molar absorbtivity of 240 M^{-1} cm^{-1}. This is consistent with the theory of d-d- transitions being Laporte forbidden resulting in only weak transitions.[63] The regeneration of reduced V_xPOMs with oxygen (O_2) is an extremely complex process. For highly reduced V_xPOMs where $x \geq 4$ and all are in the +4 oxidation state, follow first order kinetics in both the reduced POM and O_2. However it is important to note that within the fuel cell, the POM systems are never 100 % reduced with respect to vanadium i.e. not all vanadium centres are in the 4^+ oxidation state. This is due to[i]:

[i] The issues here are those that arise during fuel cell testing.

1) In the particular of case of the V_4POM, 100 % reduction would lead to a pH increase above 3.5 leading to a decrease in stability. [7] Over reducing the POM leads to precipitation within the fuel cell.

2) Given the rate at which the catalyst solution is pumped around the electrode, it is unlikely that a four or three electron reduction would occur and would rely on fast electron exchange between weakly reduced V_xPOMs to form the more highly reduced V_xPOM.

With these considerations the regeneration comparison is carried out on partially reduced POM's where 50 % of the vanadium is in the 4+ oxidation state. This however, results in an extremely complex mechanism involving several elementary steps including electron transfer between mono reduced POMs, forming a highly reduced single species[j] which can then be oxidised by O_2 by a stepwise electron transfer.[9] Due to the complexity of O_2 reduction, the reaction is third order with respect to the partially reduced V_xPOM systems.[7,9] The possible pathways for successful reduction of O_2 in acidic aqueous solution are illustrated in Table 3.12.

Table 3.12: Possible mechanistic pathways for the reduction of O_2 in acidic aqueous solutions and the associated standard reduction potentials (E^o) for each pathway.

Mechanism	E^o (vs. SHE)
$O_2 + e^- + H^+ \longrightarrow HO_2^\bullet$	- 0.05 V
$O_2 + 2e^- + 2H^+ \longrightarrow H_2O_2$	0.68 V
$O_2 + 4e^- + 4H^+ \longrightarrow 2H_2O$	1.23 V
$HO_2^\bullet + e^- + H^+ \longrightarrow H_2O_2$	1.44 V
$H_2O_2 + e^- + H^+ \longrightarrow HO^\bullet + H_2O$	0.71 V
$H_2O_2 + 2e^- + 2H^+ \longrightarrow 2H_2O$	1.76 V
$HO^\bullet + e^- + H^+ \longrightarrow H_2O$	2.81 V

The one electron reduction of O_2 forming the $HO_2^\bullet$ radical via the oxidation of a reduced V_1POM species is thermodynamically very unfavourable. For this reason the V_1POM system is not used in the comparison due to its inability to regenerate. Using the integrated rate law equation for n^{th} order (equation 3.23) it was first essential to determine the order of reaction for each of the V_x systems. Table 3.13 summarises the linear fit (R^2) for various orders of reaction with respect to the reduced V^{4+}

[j] Highly reduced species are the V_xPOMs where all vanadiums are in the 4+ oxidation state.

concentration with Figure 3.28 showing the final linear plot based on the calculated order of reaction for determination of the rate constant, k.

$$\frac{1}{[A]^{n-1}} = \frac{1}{[A]_0^{n-1}} + (n-1)kt \quad (3.23)$$

Where [A] should be the concentration of V^{4+} but in this instance is substituted for the absorbance recorded at 776 nm, *k* is the rate of reaction and *t* is time in seconds.

Table 3.13: R^2 values obtained for the linear fit of kinetic data for each V_xPOM based of various orders of reaction.

Order of Reaction	V_2	V_3	V_4
1.1	0.91	0.91	0.85
2	0.92	0.96	0.94
3	0.91	0.99	0.98

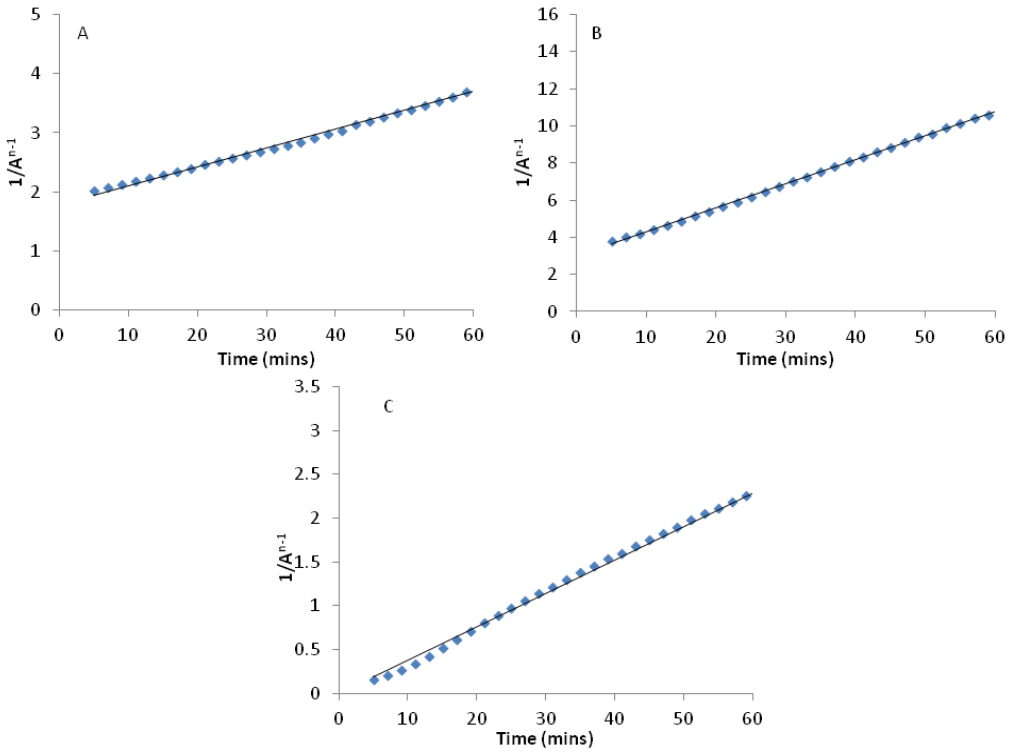

Figure 3.28: Linear plots for determination of rate constant (k) based upon the order of reaction obtain with respect to [$V4^+$]. A) V_2POM, order of reaction = 2.6, B) V_3POM, order of reaction = 3 and C) V_4POM, order of reaction = 3.1.

The order of reactions obtained for the V_2, V_3 and V_4POM systems are 2.6, 3 and 3.1 with respect to [V^{4+}], respectively. These results are consistent with those obtained by Kozhevnikov for the regeneration of partially reduced V_xPOM systems.[7] Based

on the calculated order of reaction the rate constants calculated are 2.0 $x10^{-2}$, 6.5 $x10^{-2}$ and 1.5 $x10^{-2}$ M^{-1} min^{-1} for the V_2, V_3 and V_4POM systems respectively which again is in agreement with the work by Kozhevnikov.[7]

3.3 Conclusions

This chapter has highlighted that the phosphomolydovanadate polyoxometalate series ($Na_xH_3PMo_{12-x}V_xO_{40}$ where x = 2 - 4) are suitable catalysts for FlowCath® technology. The electrochemistry of the of the $Na_xH_3PMo_{12-x}V_xO_{40}$ compounds was studied with distinct differences observed in cyclic voltammetry behaviour. The V_1 and V_2 show multiple redox process assigned to the $V^{4+/5+}$ and $Mo^{5+/6+}$ redox couples, however the V_3 and V_4 show predominately, only a single redox process assigned to the $V^{4+/5+}$. The observed increase in peak separation and broadness is not due to a decrease in the standard rate constant for electron transfer but a consequence of natural speciation and multiple redox species undergoing simultaneous reductions each with an increasingly more negative formal potential. This results in a broadening of the observed peaks and an apparent increase in peak to peak separation as we move from the V_1 to V_4 system. Simulation of the V_xPOM systems cyclic voltammetry allowed for model systems to be constructed that successfully simulated diffusion coefficients for the individual POM species present in V_x systems. Here the diffusion coefficient decreased from V_1 to V_4 which is attributed to the increase in the hydration sphere of the respective systems.

Rotating disc analysis confirmed no significant change in the k^o between the V_1 and V_4 systems as well as an increase in cathodic current with the highest achieved in the V_4 system. The role of free vanadium (vanadate ion) upon the electrochemistry of the POM systems was highlighted and shown to play a pivotal role in the observed behaviour. Not only is it able to readily oxidise the reduced POM (in-situ), but is also readily reduced when coordinated in the outer sphere of the POM structure. The fast electron transfer kinetics of the coordinated free vanadium result in the almost constant k^o across the series. Finally, non-platinum based electrode materials showed a clear decrease in electrode kinetics as demonstrated for the model $Ru(NH_3)_6^{3+/2+}$ system. This demonstrates the potential decrease in performance when removing Pt based materials from the fuel cell cathode even with liquid based catalyst systems.

This chapter clearly demonstrates the potential of $Na_xH_3PMo_{12-x}V_xO_{40}$ based materials as suitable candidates for FlowCath® technology, specifically when x > 1 due to $NaH_3PMo_{11}V_1O_{40}$ not being successfully oxidised by O_2, crucial to FlowCath® technology.

3.4 Experimental

All chemicals used were purchased from Sigma–Aldrich and used without further purification.

3.4.1 Synthesis of $Na_xH_3PMo_{12-x}V_xO_{40}$ series

Example based upon synthesis of 500 ml 0.3 M $Na_4H_3PMo_8V_4O_{40}$:

$$2\,V_2O_5 + 2\,Na_2CO_3 \longrightarrow 4\,NaVO_3 + CO_2$$

$$4\,NaVO_3 + 8\,MoO_3 + H_3PO_4 \longrightarrow Na_XH_3PMo_{(12-x)}V_xO_{40} + H_2O$$

Vanadium pentaoxide (54.56 g, 0.3 mol) was suspended in 275 ml distilled water in a 500 ml round bottom flask equipped with a magnetic stirrer bar heated to 60 ^oC. To the slurry, sodium carbonate (31.80 g, 0.3 mol) was added slowly, liberating carbon dioxide. Upon complete addition the slurry was heated to 100 ^oC and refluxed for 60 minutes. The solution was cooled to room temperature and approximately 3 ml of 30% hydrogen peroxide was added drop wise with stirring to oxidise residual V^{4+}. The solution was refluxed for a further 60 minutes to ensure completion conversion to the sodium vanadate and decompose residual hydrogen peroxide. Impurities were removed by filtration. The clear red sodium vanadate solution was returned the 500 ml round bottom flask to which molybdenum oxide (172.73 g, 1.2 mol) was added with stirring. The mixture was heated to 60 ^oC and 85% phosphoric acid (17.29 g, 0.15 mol) was added. The mixture was heated to 100 ^oC and refluxed for 5 hours. The mixture was cooled to room temperature and volumetrically diluted to 500 ml with distilled water.[3] For analysis the salt was isolated by evaporating to dryness (using a rotary evaporator) and twice re-crystallised from hot H_2O.

$Na_4H_3(PMo_8V_4O_{40})$ ICP analysis Calc. Na: 5.29, P: 1.78, Mo: 44.19, V: 11.72 %. Found Na: 5.31, P: 1.76, Mo:44.15, V:11.69 %. $Na_3H_3(PMo_9V_3O_{40})$ ICP analysis

Calc. Na: 3.92, P: 1.76, Mo: 49.09, V: 8.69 %. Found Na: 3.96, P: 1.77, Mo: 49.12. V: 8.66 %. $Na_2H_3(PMo_{10}V_2O_{40})$ ICP analysis Calc. Na: 2.58, P: 1.74, Mo: 53.87, V: 5.72 %. Found Na: 2.56, P: 1.78, Mo: 53.82, V: 5.68 %. $NaH_3(PMo_{11}VO_{40})$ ICP analysis Calc. Na: 1.27, P: 1.72, Mo: 58.53, V: 2.82 %. Found Na: 1.26, P: 1.73, Mo: 58.55, V: 2.84 %.

3.4.2 Experimental Methods

The following methods where used for the all cyclic voltammetry and rotating disc analysis investigated in this chapter.

3.4.2.1 Cyclic voltammetry

Measurements were carried out using a standard three electrode arrangement consisting of a glassy carbon working electrode, a saturated calomel reference electrode and a platinum wire counter electrode. The working electrode was prepared by polishing with 3 and 1 micron diamond paste with sonication in distilled water between and after each polish. The reference electrode was cleaned with distilled water whilst the platinum wire was flamed annealed and cleaned in concentrated sulphuric acid to remove impurities. 10 ml of the redox active (0.001 M) species dissolved in 0.1 M $HClO_4$ was added to the cell and the electrodes connected to the potentiostat. Cyclic voltammetry analysis was carried out within the potential range of 0 – 1.0 V vs. SCE. Each CV was initiated at the OCP measured prior to the analysis.

3.4.2.2 Rotating Disc Analysis

A three electrode arrangement was used consisting of a glassy carbon RDE working electrode, a saturated calomel reference electrode and a platinum wire counter electrode. The working electrode was again polished using 3 and 1 micron diamond paste with sonication between and after polishing. 70 ml of the redox active species (0.001 M) dissolved in 0.1 M $HClO_4$ was added to the cell and the electrodes connected to the potentiostat. A series of linear voltammograms at 0.005 V s^{-1} were recorded at varying rotation speeds ranging from 500 to 5000 rpm within the potential range of 0 to 1.0 V vs. SCE.

3.4.2.3 Regeneration of V_xPOM

The regeneration of the reduced V_xPOM series was measured using the following method. A 10 ml aliquot of the 0.3 M V_xPOM was added to a 40 ml glass vial to which a stoichiometric amount of 20% hydrazine hydrate was added to sufficiently reduce 50 % of the total vanadium concentration to its V^{4+} oxidation state. The aliquot was then stirred under nitrogen for 30 minutes at 50 ^oC to ensure the reduction was complete.

15.4 ul of the reduced V_xPOM was then added to 1 ml of 0.1 HCl giving a final V_xPOM concentration of 4.6 mM. This sample was then transferred to a 96 well plate for UV-Vis measurements. The absorption measurements involved the absorption at 776 nm being recorded every 2 minutes for a total period of 60 minutes. During the measurement the 96 well plate was agitated continuously (except when the actual measurement was being recorded) with a constant flow of air maintained throughout. The temperature inside the well plate chamber was maintained at 50 ^oC for the duration.

3.4.2.4 Construction of Tafel Plot

Tafel plots were constructed by measuring a series of linear voltammetry sweeps with an RDE at varying rotation speeds across a given potential range. The reciprocal the current at specific potential or overpotential at each rotation speed was the plotted versus the reciprocal of the rotation speed. This produced a linear trend which then allowed for the current at infinite rotation speed to be extrapolated. The current obtained for each specific potential/overpotential measured is then used as a single point in the Tafel plot.

3.5 References

(1) Keita, B.; Contant, R.; Milalane, P.; Secheresse, F.; Deoliveira, P.; Nadjo, L. *Electrochemistry Communications* **2006**, *8*, 767-772.

(2) Evtuguin, D.; Neto, C.; Rocha, J. *Applied Catalysis A: General* **1998**, *167*, 123 - 139.

(3) Grate, J. *Journal of Molecular Catalysis A: Chemical* **1996**, *114*, 93-101.

(4) Vazylyev, M.; Sloboda-Rozner, D.; Haimov, A.; Maayan, G.; Neumann, R. *Topics in Catalysis* **2005**, *34*, 93-99.

(5) Kozhevnikov, I. *Catalysis Reviews* **1995**, *37*, 311-352.

(6) Kozhevnikov, I. *Russian Chemical Reviews* **1987**, *56*, 811-825.

(7) Kozhevnikov, I. *Chemical reviews* **1998**, *98*, 171-198.

(8) Zhizhina, E. G.; Odyakov, V. F.; Simonova, M. V.; Matveev, K. I.; Matveev, K. I.; Catalysis, B. I.; Matveev, K. I. *Reaction Kinetics and Catalysis Letters* **2003**, *78*, 373-379.

(9) Kozhevnikov, I. *Catalysts For Fine Chemical Synthesis, Volume 2, Catalysis By Polyoxometalates*; Wiley, 2002.

(10) Neumann, R. *Inorganic Chemistry* **2010**, *49*, 3594-3601.

(11) Khenkin, A.; Ben-Daniel, R.; Rosenberger, A.; Vigdergauz, I.; Neumann, R. *Aerobic Oxidations Catalyzed by Polyoxometalates*; Polyoxometalate Chemistry From Topology via Self-Assembly to Applications; Springer Netherlands; pp. 347-362.

(12) Neumann, R.; Khenkin, A. M. *Chemical Communications* **2006**, 2529.

(13) Kuznetsova, L.; Maksimovskaya, R.; Matveev, K. *Bulletin of the Academy of Sciences of the USSR Division of Chemical Science* **1983**, *32*, 660-665.

(14) Khenkin, A. M.; Weiner, L.; Wang, Y.; Neumann, R. *Journal of the American Chemical Society* **2001**, *123*, 8531-8542.

(15) Odyakov, V.; Zhizhina, E.; Matveev, K. *Journal of Molecular Catalysis A:* **2000**.

(16) Li, C.; Zhang, Y.; O'Halloran, K. P.; Zhang, J.; Ma, H. *Journal of Applied Electrochemistry* **2009**, *39*, 421-427.

(17) Song, I. K.; Barteau, M. A. *Journal of Molecular Catalysis A: Chemical* **2004**, *212*, 229-236.

(18) Rusu, D.; Baban, O.; Hauer, I.; Gligor, D. *REVUE ROUMAINE* **2010**, 1-8.

(19) Nambu, J.; Ueda, T.; Guo, S.; Boas, J.; Bond, A. *Dalton Transactions* **2010**, *39*, 7364.

(20) Katsoulis. *Chemical reviews* **1998**, *98*, 359-387.

(21) Sachdeva, S.; Turner, J.; Horan, J. *Fuel Cells and Hydrogen* **2011**.

(22) Limoges, B.; Stanis, R.; Turner, J.; Herring, A. *Electrochimica Acta* **2005**, *50*, 1169-1179.

(23) Kuo, M.; Stanis, R. J.; Ferrell, J. R., III; Turner, J. A.; Herring, A. M. *Electrochimica Acta* **2007**, *52*, 2051-2061.

(24) Kuo, M.; Limoges, B.; Stanis, R.; Turner, J. *Journal of Power* **2007**, *171*, 517-523.

(25) Taylor, R.; Humffray, A. *Journal of Electroanalytical Chemistry and Interfacial Electrochemistry* **1973**, *42*, 347-354.

(26) Nicholson, R. *Analytical Chemistry* **1965**, *37*, 1351-1355.

(27) John, B.; Mark, W. *Journal of Electroanalytical Chemistry* **1991**, 73-81.

(28) Compton, R.; Banks, C. *Understanding Voltammetry*; World Scientific Publishing, 2007.

(29) Atkins, P.; Paula, J. *Physical Chemistry*; 8 ed.; Oxford University Press, 2006.

(30) Bard, A.; Faulkner, L. *Electrochemical Methods: Fundamentals and applications*; 2nd ed.; Wiley, New York, 2000.

(31) Marcus, R. *The Journal of Chemical Physics* **1956**, *24*, 966.

(32) Hush, N. *The Journal of Chemical Physics* **1958**, *28*, 962.

(33) Nissim, R.; Batchelor-McAuley, C.; Henstridge, M.; Compton, R. *Chemical Communications* **2012**, *48*, 3294.

(34) Chen, P.; McCreery, R. *Analytical Chemistry* **1996**, *68*, 3958-3965.

(35) Jaworski, J.; Leniewska, E.; Kalinowski, M. *Journal of Electroanalytical Chemistry and Interfacial Electrochemistry* **1979**, *105*, 329-334.

(36) Ajloo, D.; Yoonesi, B.; Soleymanpour, A. *Int J Electrochem Sci* **2010**, 1-19.

(37) Sahami, S.; Weaver, M. *Journal of Electroanalytical Chemistry and Interfacial Electrochemistry* **1981**, *124*, 35-51.

(38) Gutmann, V.; Gritzner, G.; Danksagmuller, K. *Inorganica Chimica Acta* **1976**, *17*, 81-86.

(39) Riahi, S.; Eynollahi, S.; Ganjali, M. *International Journal of Electrochemical Science* **2009**, *4*, 1128 - 1137.

(40) Deakin, M.; Stutts, K.; Wightman, R. *Journal of Electroanalytical Chemistry and Interfacial Electrochemistry* **1985**, *182*, 113-122.

(41) Arichi, J.; Pereira, M. M.; Esteves, P. M.; Louis, B. *Solid State Sciences* **2010**, *12*, 1866-1869.

(42) Cuentas-Gallegos, A. K.; Frausto, C.; Ortiz-Frade, L. A.; Orozco, G. *Vibrational Spectroscopy* **2011**, *57*, 49-54.

(43) Selling, A.; Andersson, I.; Grate, J. H.; Pettersson, L. *European Journal of Inorganic Chemistry* **2000**, 1509-1521.

(44) Pettersson, L. *Molecular Engineering* **1993**, *3*, 29-42.

(45) Pettersson, L.; Andersson, I.; Oehman, L. *Inorganic Chemistry* **1986**, *25*, 4726-4733.

(46) Pettersson, L.; Andersson, I.; Grate, J. *Inorganic Chemistry* **1994**, *33*, 982 - 993.

(47) Dickinson, E.; Limon-Petersen, J.; Rees, N.; Compton, R. *Journal of Physical Chemistry* **2009**, *113*, 11157 - 11171.

(48) Jamnongwong, M.; Loubiere, K.; Dietrich, N.; Hébrard, G. *Chemical Engineering Journal* **2010**, *165*, 758-768.

(49) Evans, D.; Claiborne, J. *The Physiology Of Fishes*; CRC Press, 2005.

(50) Pletcher, D. *Instrumental Methods in Electrochemistry*; Horwood Pub Limited, 2000.

(51) Weinstock, I. *Chemical reviews* **1998**, *98*, 113 - 170.

(52) Gattrell, M.; Park, J.; MacDougall, B.; Apte, J.; McCarthy, S.; Wu, C. *Journal of The Electrochemical Society* **2004**, *151*, A123.

(53) Gattrell, M.; Qian, J.; Stewart, C.; Graham, P.; MacDougall, B. *Electrochimica Acta* **2005**, *51*, 395-407.

(54) Freund, M.; Lewis, N. *Inorganic Chemistry* **1994**, *33*, 1638 - 1643.

(55) Ghosh, K.; Hu, J.; White, H. S.; Stang, P. J. *Journal of the American Chemical Society* **2009**, *131*, 6695-6697.

(56) Chaumont, A.; CNRS, U.; Wipff, G. *European Journal of Inorganic Chemistry* **2013**, *2013*, 1835-1853.

(57) Kear, G.; Walsh, F. *Corrosion Materials 30*, 51-55.

(58) Zoski, C. *Handbook of Electrochemistry*; 1st ed.; Elsevier Science Limited, 2007.

(59) Fletcher, S.; Varley, T. S. *Physical Chemistry Chemical Physics* **2011**, *13*, 5359.

(60) Choi, S.; Kim, J. *Bulletin of the Korean Chemical Society* **2009**, *30*, 810-816.

(61) Tang, Z.; Liu, S.; Wang, E.; Dong, S. *Langmuir* **2000**, *16*, 4946-4952.

(62) Speight, J. *Lange's Handbook of Chemistry, 70th Anniversary Edition*; McGraw-Hill Professional, 2004.

(63) Donald, P. L. *Introduction to Spectroscopy*; 4 ed.; Brooks/Cole Publishing Company, 2008; pp. 381-417.

(64) Manfred, R.; Reddy, D.P.; Feldberg, S.W. *Analytical Chemistry* **1994**, 65, 589-600.

Chapter 4

Bridging the Gap between Lab and Fuel Cell Analysis: The Transition to Self-Supported High Concentration Systems

Table of Contents

4.1 Introduction

Chapter 3 focused upon the electrochemical analysis of the $Na_xH_3PMo_{12-x}V_xO_{40}$ series under dilute conditions, specifically 1 mM of the redox active species in the presence of an excess of supporting electrolyte, typically at a concentration of 0.1 M. This allowed for the investigation into electrochemical parameters in an ideal solution i.e. fully supported media and a large excess of protons compared to the redox active species. Diffusive and kinetic parameters were investigated with quiescent cyclic voltammetry and the RDE. However when the catalysts in question are used in the fuel cell, the conditions are very different from those used for typical lab-based analysis. Under fuel cell conditions there is no supporting electrolyte added to the aqueous catalyst which we refer to as 'self-supporting' as well as a 300 times increase in concentration, from 0.001 to 0.3 M. With no supporting electrolyte present in the aqueous catalyst solution there is the possibility of increases in solution resistance (as well as large increases in current) and changes in the electrochemical response. The increase in concentration has the potential to change the observed electrochemistry as this simultaneously increases the concentration of not only the individual V_xPOM Keggin species but also the free VO_2^+/VO^{2+} cation species. In Chapter 3 we observed the affect of free vanadium upon the reduced POM species (as an oxidant) is minimal under ideal conditions but that it could play a positive role by increasing the cathodic current when present in the outer sphere of the Keggin species. Increasing the concentration of the V_xPOM may also have detrimental effects on electrode kinetics by increasing the coverage of the adsorbed layer on the electrode surface. In addition, the relative concentration of protons can also affect the voltammetry as each reduction of the Keggin is associated with a subsequent protonation. Under ideal conditions this factor was not considered due the excess of protons present (relative to POM concentration), however under fuel cell conditions the availability of protons is somewhat limited.

This chapter investigates the effect of the currently used fuel cell conditions used in conjunction with FlowCath® has upon the observed kinetics of the electrode reaction. Specifically we will investigate the influence of no supporting electrolyte on the V_xPOM upon the resistance of the solution and its effects upon the observed voltammetry. Here we will use the ferri/ferrocyanide redox couple as a comparison.

The effects of increased concentration will be carefully considered with Gattrell reporting the detrimental effects of the VO_2^+ species upon electrode kinetics in the vanadium redox flow battery.[1,2] The final section aims to devise a suitable method to allow a comparison of the electrochemical properties of the V_xPOM systems and hence determination of a lead catalyst to take forward for formulation development.

4.2 Results and Discussion

4.2.1 Standard System for Fuel Cell Comparison: $Fe(CN)_6^{3-/4-}$

In chapter 3 the ruthenium hexamine system was deployed as the standard electrochemically reversible system and compared with the V_xPOM systems investigated. As discussed in Chapter 3, the ruthenium complex served this role by highlighting that the V_xPOM systems do no behave as a model redox system. However given the nature of the ruthenium system, it is not possible to observe the effect of a 300 times increase in concentration due to its poor solubility at high concentrations in aqueous media. The ferricyanide complex is a well known and studied compound and is highly soluble with stable solutions of up to 1 M possible. This makes the ferricyanide system ideal to form the basis of this investigation. The electrochemistry of the ferricyanide complex is not as straightforward as its ruthenium counterpart with Tafel analysis identifying a definitive curvature in the standard plots.

4.2.1.1 Analysis Under Ideal conditions

To observe the effects of fuel cell conditions upon the electrochemistry one needs to observe the electrochemical response under ideal conditions. Figure 4.1 shows the CV of 0.001 M $K_3Fe(CN)_6$ in 0.1 M KCl undergoing a one electron reduction at a glassy carbon electrode and the corresponding peak currents obtained at varying scan rates. The CV (Figure 4.1A) shows a typical response with peak anodic and cathodic potentials observed at 0.26 and 0.17 V vs. SCE respectively resulting in a peak to peak separation, $\Delta E_{p,}$ of 95 mV which is greater than the 59 mV expected for an ideal one electron process.[3] The standard rate constant (k^o) calculated from the peak

separation is 0.002 cm s^{-1}.[a] The value of k^o is in agreement with previous work[3] which determined the electrochemical behaviour of the $Fe(CN)_6^{3-/4-}$ system as quasi-reversible and that the corresponding k^o obtained at glassy carbon electrodes was strongly linked with electrode preparation. However the value of 0.002 cm s^{-1} is slightly less than the value of 0.005 cm s^{-1} obtained at a GC electrode using an analogous electrode preparation to this work.[3] This may be a result of the increased concentration of supporting electrolyte used, 1 M KCl compared to 0.1 M used in this investigation.

Figure 4.1B shows the linear relationship between peak (cathodic) current and scan rate expected for a system under diffusion control. The corresponding diffusion coefficient calculated using the Randles Sevick equation for the $Fe(CN)_6^{3-}$ species yields a value of 4.06 x10^{-6} cm^2 s^{-1} which is slightly lower than the reported literature value of 6.32 x10^{-6} cm^2 s^{-1}.[3] Again due to the system not being a truly electrochemically reversible, the Randles Sevcik analysis underestimates the diffusion coefficient.

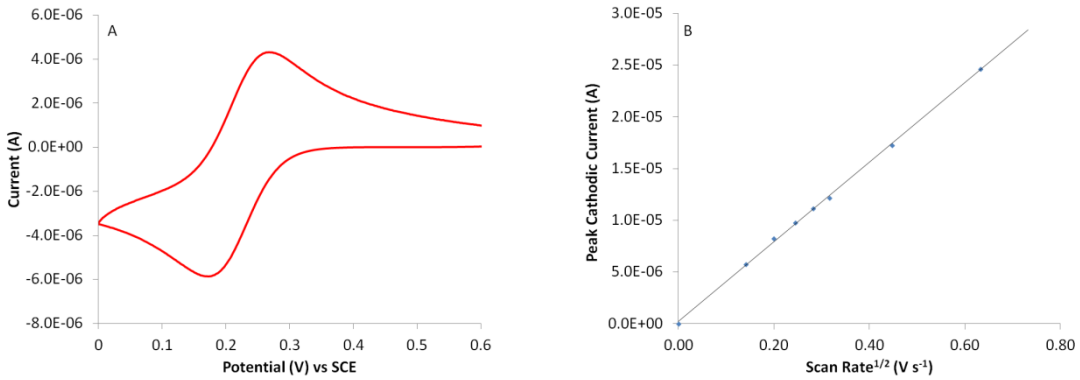

Figure 4.1: A) Cyclic voltammetry of 0.001 M $K_3Fe(CN)_6$ in 0.1 M KCl. The working electrode is a glassy carbon, counter electrode is a platinum wire and reference electrode is saturated calomel electrode. Scan rate = 0.02 V s^{-1} B) Plot of I_p^c vs. $v^{1/2}$ at scan rates ranging from 0.02 – 0.4 V s^{-1}.

To confirm the reliability of the obtained values for D_o and k^o we again employed CV simulation analysis using DigiElch simulation software. Simulation of the experimental data (Figure 4.2) confirmed the experimentally obtained values and are in agreement but slightly less than reported in literature, D_o = 5.7 x10^{-6} cm^2 s^{-1} and k^o = 0.002 cm s^{-1}.[3]

[a] Standard rate constant obtained via comparison with simulation

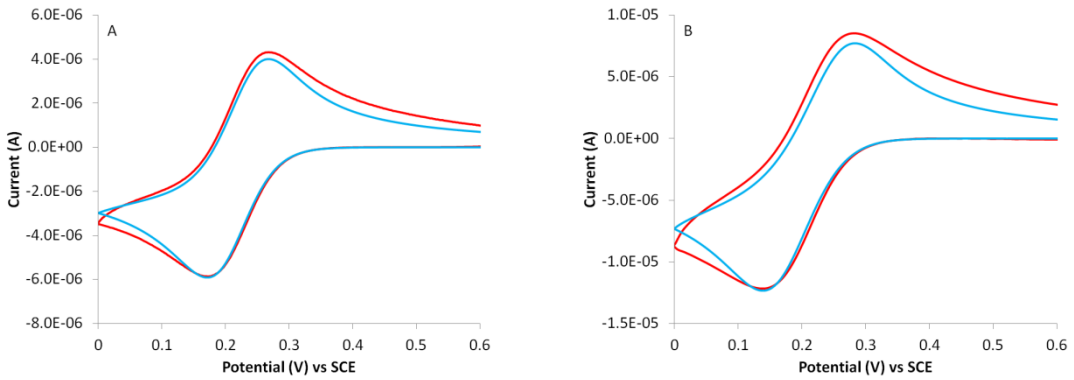

Figure 4.2: Comparison between experimental (red) and simulated (blue) CV of 0.001 M $K_3Fe(CN)_6$ in 0.1 M KCl. A) scan rate = 0.02 V s^{-1} and B) scan rate = 0.1 V s^{-1}.

4.2.1.2 Analysis under Fuel Cell Conditions

It is important to clarify the exact nature of the proposed fuel cell conditions. For CV analysis the compound in question will be present as an aqueous solution at a concentration of 0.3 M with no further supporting electrolytes added, 'self-supporting', with the analysis being carried out at room temperature.

The CV obtained for the self-supported 0.3 M ferricyanide system (Figure 4.3A) initially appears very similar to that obtained under ideal conditions. Peak oxidation and reduction potentials have shifted to 0.29 and 0.13 V vs. SCE respectively resulting in an increased peak separation of 158 mV. This points to the possibility of slower kinetics at the electrode surface.[4,5] Comparing the CVs obtained at both ideal and fuel cell conditions (Figure 4.3B) shows some very distinct differences. Firstly there is an increase in peak current under fuel cell conditions as expected by the significant increase in concentration. However there is not the 300 times increase as would be theoretically expected for a model system.[4-6] As well as the shifts in peak potentials, the anodic current (during the back sweep) decays rather rapidly to zero which does not occur for a typical diffusion controlled process.[4-6]

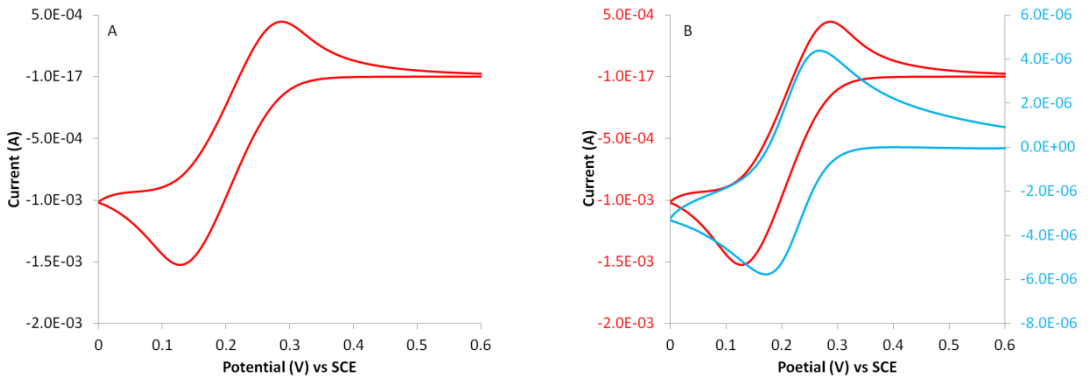

Figure 4.3: A) Cyclic voltammetry of aqueous 0.3 M $K_3Fe(CN)_6$ at 0.02 V s^{-1} on a glassy carbon electrode. B) Comparison between CV's of $K_3Fe(CN)_6$ at ideal conditions (blue line) and fuel cell conditions (red line) at v=0.02 V s^{-1}.

The change in the observed current in a CV under diffusion control at a planar electrode can be described by the Cottrell equation (equation 4.1).

$$I = \frac{nFAC_{ox}\sqrt{D_{ox}}}{\sqrt{\pi t}} \tag{4.1}$$

Where I is current, n is the number of electrons transferred, C_{ox} is the concentration of the oxidised species, D_{ox} is the diffusion coefficient of the oxidised species and t is time. Equation 4.1 can be simplified;

$$I = rt^{-1/2} \tag{4.2}$$

where r is the constants for a given redox system from equation 4.1 collected together. Foe equation 4.2, the mathematical principles show that the current should decrease at a rate proportional to $t^{1/2}$ when under diffusion control i.e. it should not rapidly drop to zero. This is the case for the CV in Figure 4.3B under ideal conditions (blue line) where on the back sweep the current does not return to zero. However under fuel cell conditions (red line) this is not the case as the current drops to zero during the back sweep. This suggests another factor may be affecting the voltametric response in addition to the inter play of kinetics and diffusion. If physical changes such as ligand substitution where the reason then this same anomaly would be observed under ideal conditions. The more likely cause is the lack of supporting electrolyte present in the solution leading to the mass transport contributions to the redox species arising from not only diffusion but also migration.[7,8]

Secondly, consider the ionic current flowing in the solution. With no supporting electrolyte, it is the redox active species that must not only undergo the redox process of interest at the working electrode but also act as the charge carrier. The reduction of the $Fe(CN)_6^{3-}$ species at the electrode surface results in (more) negatively charged ions flowing from the working electrode to the counter or positive (less negative) ions must flow in the opposite direction. The movement of the ferri/ferrocyanide ions in solution is extremely fast.[9] When reduction of the $Fe(CN)_6^{3-}$ species occurs, the $Fe(CN)_6^{4-}$ is acting as the current carrier, so is being removed from the electrode surface faster than if just diffusion controlled. This migration contribution to the mass transport is probably contributing to the decrease in anodic current. Table 4.1 shows the mobility of various ions and ionic complexes in water at room temperature and it can be seen that protons have the highest ionic mobility with the $Fe(CN_6)^{3-/4-}$ ions having the highest mobility in water of the remaining ionic species.

Table 4.1: Ionic motilities of selected ions in water at 298 K, u (10^{-8} m^2 s^{-1} V^{-1})

Ion species	Mobility
Ag^+	6.24
Ca^{2+}	6.17
H^+	36.23
NH_4^+	7.63
Br^-	8.09
Co_2^{3-}	7.46
$Fe(CN_6)^{3-}$	10.5
$Fe(CN_6)^{4-}$	11.4

Simulation of this redox process highlights that indeed the interplay between diffusion and kinetics is not controlling the observed CV response. The fundamentals of the simulation assume that the system is under diffusion control (with respect to mass transport) and it is evident that the observed current in the 0.3 M simulation (Figure 4.4) does not return to zero. This suggests the increase in concentration is not the cause and that other processes (migration) are occurring. The simulations of the 0.3 M self-supporting $Fe(CN)_6^{3-/4-}$ system at scan rates ranging from 0.02 – 0.2 V s^{-1} yield a diffusion coefficient of 5 x10^{-6} cm^2 s^{-1} (2.74 x10^{-6} calculated using Randles Sevcik equation using data in Figure 4.4B) and k^o of 6.2 x10^{-3} cm s^{-1} (6.4 x10^{-3}

calculated via Nicholson method) which in both cases are less than the respective values under ideal conditions. The slight decrease in D_o could be due to an increase in viscosity with diffusion and viscosity related via the Stokes-Einstein equation.

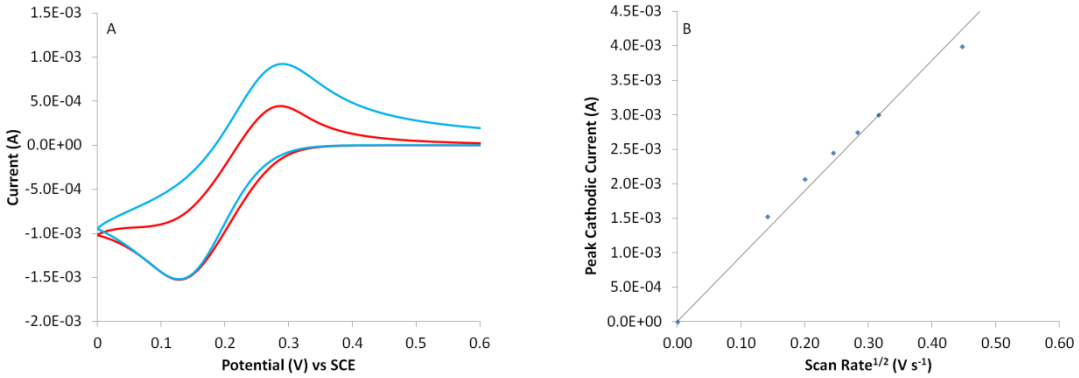

Figure 4.4: A) Comparison between simulation (blue) and experimental (red) cyclic voltammetry of 0.3 M $K_3Fe(CN)_6$ under fuel cell conditions. Simulation is modelled on a diffusion controlled process. B) Experimental change in I_p with $v^{1/2}$ for 0.3 M $K_3Fe(CN)_6$ under fuel cell conditions.

In particular k^o is nearly one order of magnitude lower than that observed under ideal conditions. This suggests the lack of supporting electrolyte is not only affecting the mass transport processes within the system but also the observed kinetics of the electrode reaction with an increase in the peak to peak separation. However, it is possible that the kinetics remain unchanged but that migration and other factors contributing to the voltammetry resulting in a larger peak to peak separation. The lack of supporting electrolyte will contribute to a poorly defined double layer but also, only a fraction of the potential drop $(\phi_M - \phi_S)$ driving the reaction is experienced by the active species as described by Frumkin.[10,11] This lower interfacial potential drop results in lower currents being achieved. The increase in concentration from 1 mM to 300 mM when moving from ideal to fuel cell conditions should readily have a 300 times increase in current associated with it. However we only observe an increase in current of 207 times that under ideal conditions, showing that the reaction is not proceeding at the rate required to attain the theoretically expected currents.

4.2.1.3 Effect of Solution Resistance

One has to consider the effect of solution (or uncompensated) resistance, based upon Ohms law[4] (equation 4.3). This resistance (R_u) occurs between the working and reference electrodes due to the distance between the two electrodes and poor conductivity in an electrochemical cell. This resistance can never be fully avoided and is usually minimised with the addition of a supporting electrolyte and reducing the distance between the reference and working electrode. Furthermore typical voltammetry experiments use mM concentrations (redox active species) and electrodes of the order 3 mm diameter resulting in currents of the order 10^{-5}-10^{-4} A. This leads to a lower IR drop. Here the increased currents observed under fuel cell conditions result in a larger uncompensated resistance and hence a larger potential drop (V_{iR}) compared to ideal conditions.

$$I = \frac{V_{iR}}{R_u} \tag{4.3}$$

We can compensate for the two effects discussed. In order to take account of the Frumkin effect knowledge of the double layer structure is required where as *iR* compensation for solution resistance can be readily applied to most systems either during the measurement or post analysis.[12]

The current interrupt method is a relatively simple procedure used to measure the potential drop associated with uncompensated resistance. A method was employed by where a known current was applied (1 mA) and a steady potential is measured, the current is then switched off (set to zero) resulting in the potential across the uncompensated resistance instantaneously becoming zero. Extrapolation of the potential decay to the point of the current interrupt allows for calculation of the voltage drop caused by solution resistance. The current interrupt data for the 0.3 M $Fe(CN)_6^{3-}$ system is shown in Figure 4.5 where between 0 and 0.1 seconds a 1 mA current is generated. The nearly instantaneous voltage drop due to uncompensated resistance is observed around 0.1 seconds. The voltage then continues to decay with time due to polarisation resistance. In this case the calculated voltage drop at the current interrupt was 0.051 V resulting in a resistance of 51 ohms.

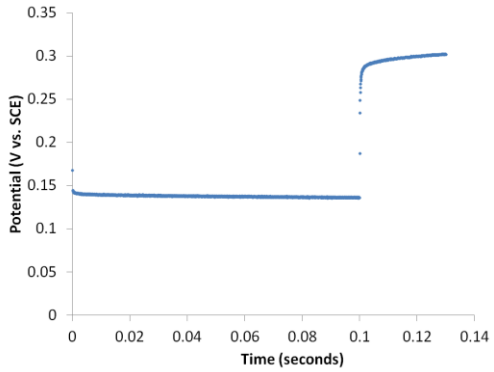

Figure 4.5: Graph showing the voltage decay as a result of the current interrupt method for 0.3 M $K_3Fe(CN)_6$. A cathodic current equal to 1 mA was applied for 0.1 seconds at which point the current was switched off and potential decay observed.

With the magnitude of the uncompensated resistance now known we can record an *iR* compensated cyclic voltammetry for the 0.3 M $Fe(CN)_6^{3-/4-}$ system. It is common to only compensate for approximately 85 % of the uncompensated resistance due to the possibility of positive feedback from the potentiostat resulting in oscillation and distortion of the CV (Figure 4.6A). The comparison between the compensated (85 % or 43.8 ohms) and uncompensated CV reveals key points with regards to the fuel cell conditions.[35]

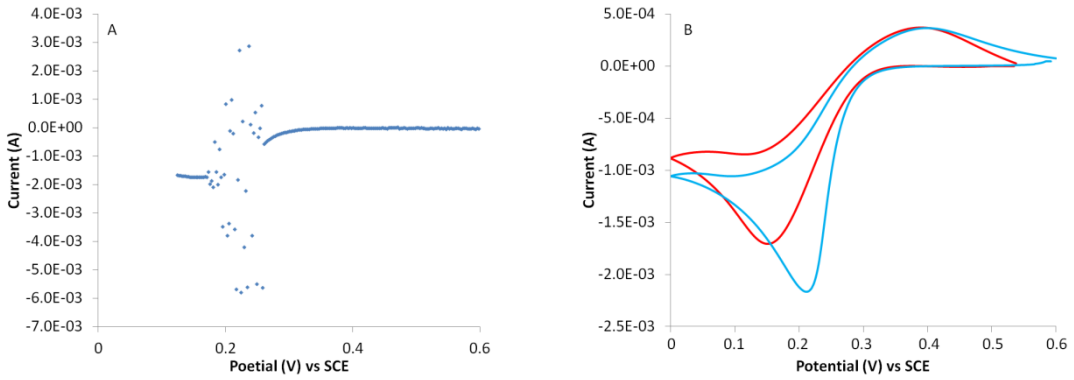

Figure 4.6: A) CV of 0.3 M $K_3Fe(CN)_6$ at a glassy carbon electrode with 100 % *iR* compensation (51 Ohms) B) Comparison between CVs of the 0.3 M $K_3Fe(CN)_6$ system with zero *iR* compensation (red) and 85 % *iR* compensation (43.4 ohms, blue).

When *iR* compensation is taken into account the peak to peak separation is significantly reduced by 90 mV and a significant increase is also observed in I_p^c (Figure 4.6B). With this *iR* compensation, the simulation model gives a diffusion coefficient of 5.7 $x10^{-6}$ cm^2 s^{-1} and k^o of 0.0022 cm s^{-1}. This demonstrates that the increase in uncompensated resistance but more significantly the large increase in the

observed currents affects the peak to peak separation giving the impression of slower electrode kinetics. This is supported by the increase in the peak current ratio between ideal and fuel cell conditions, increasing from 207, without *iR* compensation, to approximately 264 with *iR* compensation. Although the theoretical value of 300 is not quite achieved it should be noted that only 85 % *iR* compensation was applied If 100 % *iR* compensation was possible the ratio would be closer to the factor of 300.

Addition of supporting electrolyte to the 0.3 M $Fe(CN)_6^{3-/4-}$ system (Figure 4.7) yields very little change in the observed peak separation which remains constant at ~160 mV regardless of KCl concentration. However, with the increased supporting electrolyte concentration, the observed I_p^c and I_p^a values decrease. This is probably a result of the migration effect having less of a contribution upon mass transport resulting in a more diffusion limited process. Upon addition of KCl the total volume increases thus the concentration of the redox active species decreases ($Fe(CN)_6$) as well as a possible decrease in D_o with solution viscosity increasing. The slight change in formal potential is possibly due to an increase in the K^+ concentration to sufficiently balance the increased negative charge upon reduction.[13]

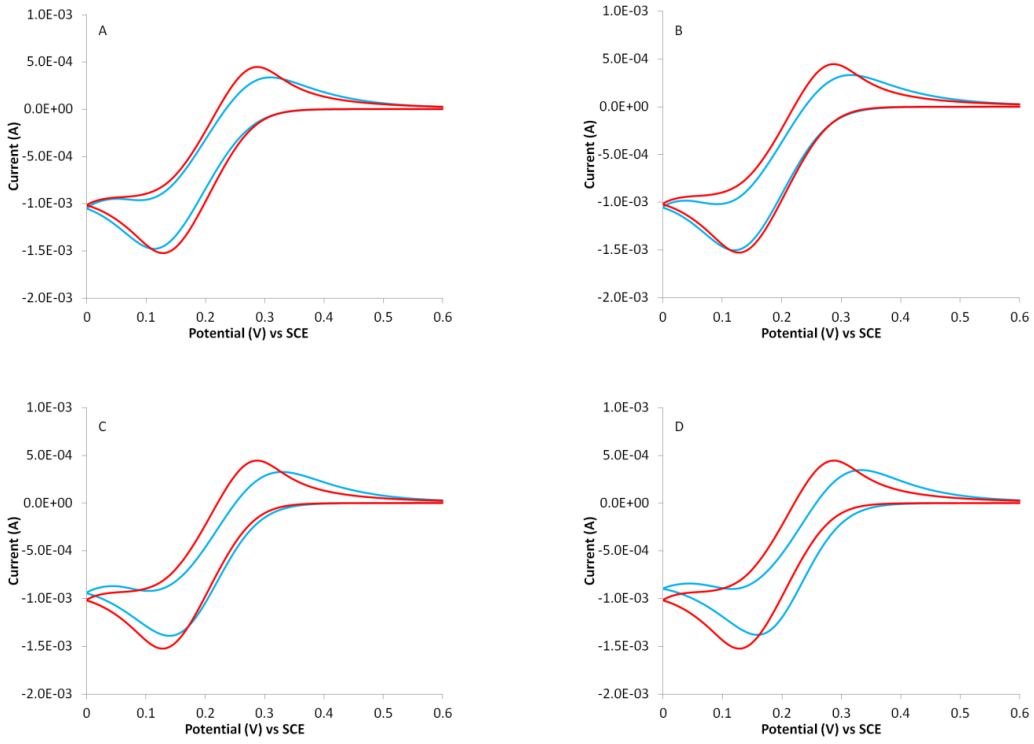

Figure 4.7: Effect of adding supporting electrolyte to the 0.3 M $K_3Fe(CN)_6$ system. In each case the red CV is the 0.3 M $K_3Fe(CN)_6$ with no supporting electrolyte and the blue CV contained various quantities of KCl. A) 0.1 M KCl, B) 0.3 M KCl, C) 0.9 M KCl and D) 1.5 M KCl.

4.2.2 V_xPOM Systems

4.2.2.1 From Ideal to Fuel Cell Conditions

The V_xPOM systems display similar voltammetry characteristics to the $Fe(CN)_6^{3-/4-}$ system when moving from ideal to fuel cell conditions. In Chapter 3, under ideal conditions we observe a well-defined diffusion controlled (with respect to mass transport) redox processes (Figure 4.8A-D). Under fuel cell conditions this is still the case as we still maintain well defined redox processes, however, these are not solely under diffusion control. The vanadium redox couple in all four systems remains the dominant process with formal potentials ranging from 0.55 – 0.35 V vs. SCE for the V_1 – V_4 systems respectively, indicating the shift in formal potential with increased vanadium substitution is still observed at higher V_xPOM concentrations.

The three distinct changes observed under fuel cell conditions are:

- There is a distinct increase in ΔE_p for the vanadium redox couple.
- A significant increase in peak current when comparing the changes in conditions for each respective system.
- The process is no longer a solely diffusion controlled with respect to mass transport.
- Oxidative current goes to zero too quickly for signal to be controlled by interplay of diffusion and kinetics.

Peak separation under ideal conditions ranged 110 to 215 mV (Chapter 3, Table 3.6) for the V_xPOM systems and under fuel cell conditions this increases significantly with all four systems demonstrating a peak to peak separation of approximately 300 mV. The increase in peak separation is not surprising in the absence of supporting electrolyte and is clearly analogous to the ferri/ferrocyanide system.

There is a clear increase in peak current under fuel cell conditions however this is not representative of the 300 times increase in concentration and much higher currents are expected than those observed. Finally, in the $V_{2\text{-}4}POM$ systems the observed current returns to zero as seen in the $Fe(CN)_6^{3-/4-}$ system but this same phenomena are not observed in the V_1POM system. Previously this was attributed to migration

and high ionic mobility in aqueous media for the ferro/ferricyanide system. If these same phenomena were observed across the entire V_xPOM then it is likely to be the effects of migration being observed once again. However this is not the case and all though migration will play a role, there must be other contributing factors.

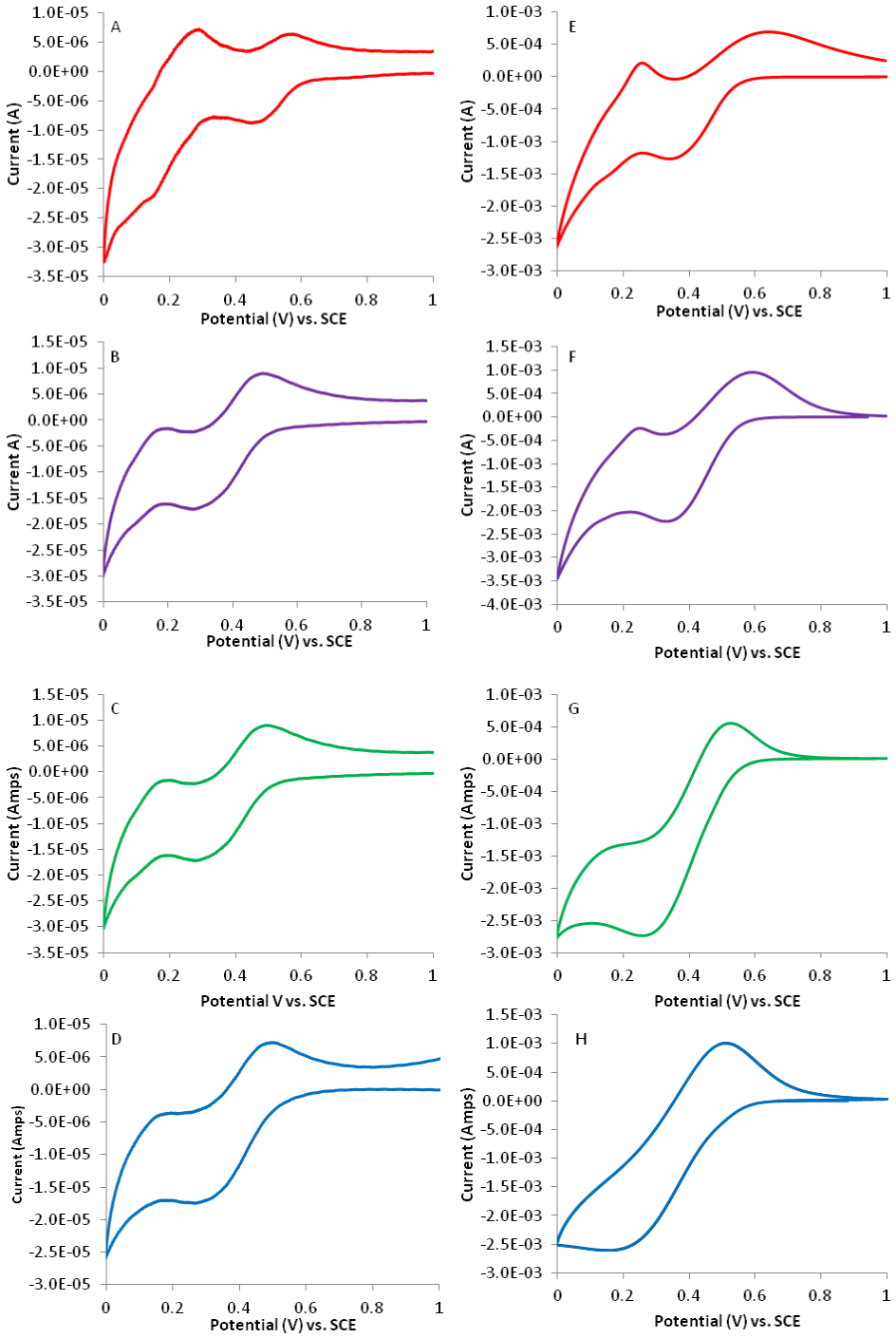

Figure 4.8: Comparison of cyclic voltammetry obtained for the V_xPOM systems where x = 1- 4 under ideal conditions (0.001 M V_xPOM in 0.1 M $HClO_4$), A) V_1POM, B) V_2POM, C) V_3POM and D) V_4POM and fuel cell conditions (0.3 M V_xPOM in H_2O), E) V_1POM, F) V_2POM, G) V_3POM and H) V_4POM. All CVs obtained on a glassy carbon electrode at a scan rate of 0.04 V s^{-1}.

4.2.2.2 Uncompensated Resistance

As observed in the ferro/ferricyanide system the effect of uncompensated resistance and more significantly the large increase in observed currents upon the CV was detrimental. With the same increase in concentration it is likely that the increased currents are having the same effect upon the V_xPOM systems, however with an increased counter ion concentration and an increased molar conductivity of the respective ions in the V_xPOM systems (H^+, Na^+)[14] the total solution resistance should be less than the respective ferro/ferricyanide system. Figure 4.9 shows the voltage-time response for the current interrupt method for determination of the uncompensated resistance associated with each V_xPOM system.

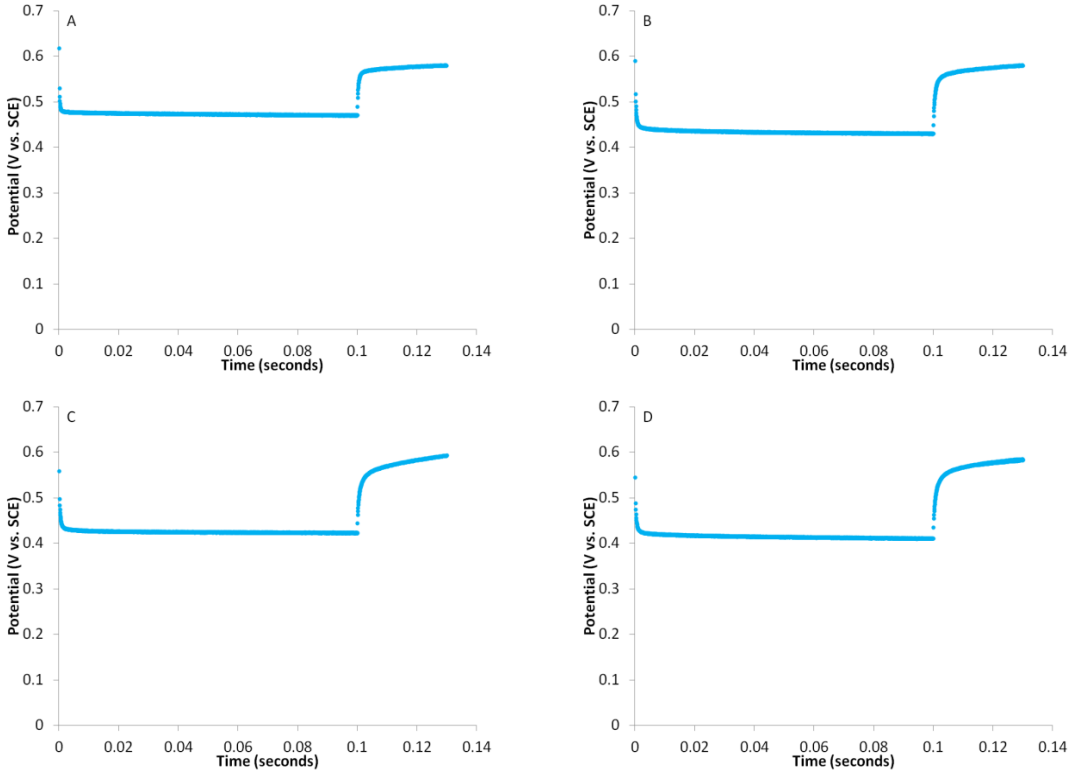

Figure 4.9: Graphs showing the voltage for the current interrupt method and 0.3 M V_xPOM, A) V_1POM, B) V_2POM, C) V_3POM and D) V_4POM. A cathodic current equal to 1 mA was applied for 0.1 seconds at which point the current was switched off and potential decay observed.

As previously observed for the $Fe(CN)_6^{3-/4-}$ system when the applied current is switched off the uncompensated resistance instantaneously becomes zero resulting in a suddendrop in voltage which is directly related to the magnitude of uncompensated resistance by equation 4.3. The four V_xPOM systems were analysed, giving resistance values of 18.9, 18.3, 21.9 and 24.1 ohms for the V_1, V_2, V_3 and V_4

systems, respectively. Although the respective counter ion concentration increases with vanadium substitution it is the $Na^{+}_{(aq)}$ and $VO_2^{+}{}_{(aq)}$ ions which begin to dominate the system. In the POMs with increased vanadium substitution the charge is carried by the $Na^{+}_{(aq)}$ and $VO_2^{+}{}_{(aq)}$ ions which have a lower molar conductance than H^{+},[14] which is the dominant charge carrying ion in V_1POM. The *iR* compensated CVs (Figure 4.10) show improvement with a reduced peak separation (Table 4.2), however, the peak separation remains in excess of 200 mV for each system, still larger than that observed under ideal conditions, indicating apparently slower electrode kinetics even with *iR* compensation. Unlike the ferro/ferricyanide system, uncompensated resistance is not the only limiting factor upon the voltammetry under these conditions.

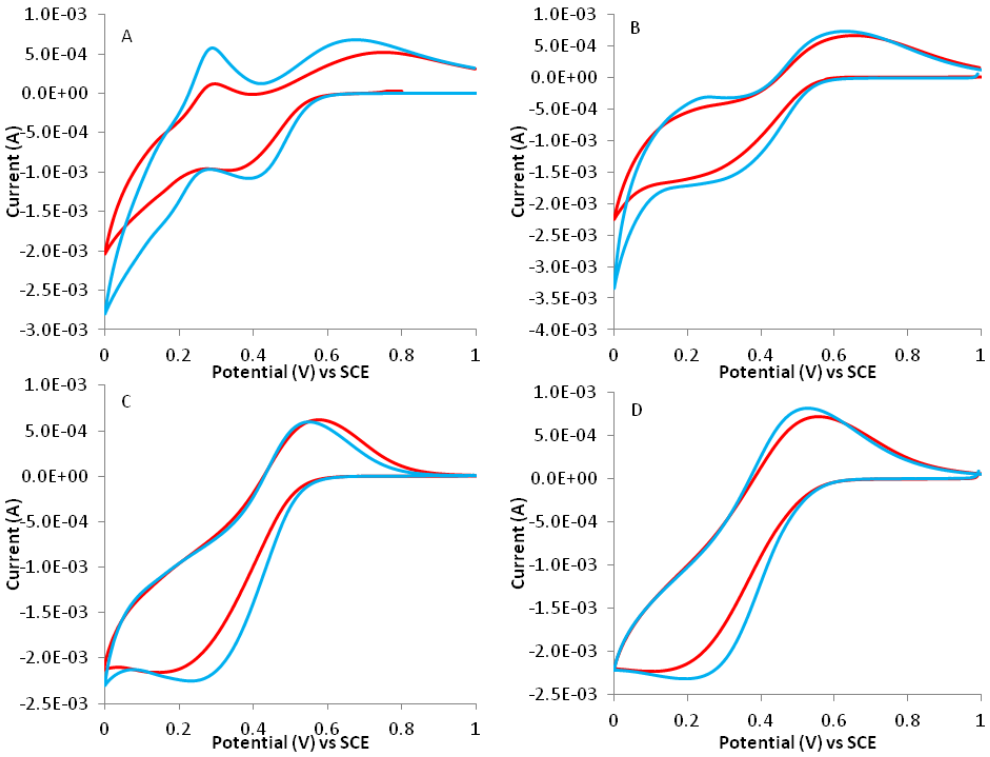

Figure 4.10: Comparison between uncompensated (red) and *iR* compensated (blue) cyclic voltammetry of V_xPOM. A) V_1POM, *iR* compensation 15 Ohms, B) V_2POM, *iR* compensation 16 ohms, C) V_3POM, *iR* compensation 17.5 ohms and D) V_4POM, *iR* compensation 23 ohms.

Table 4.2: Comparison of peak separation for the vanadium redox couple in the 0.3 M V_xPOM systems with and without *iR* compensation. Scan rate = 0.04 V s^{-1}

V_x System	ΔE_p (With)	ΔE_p (Without)
V_1	305 mV	241 mV
V_2	310 mV	256 mV
V_3	300 mV	229 mV
V_4	290 mV	224 mV

The reduction step of the V_xPOMs highlighted in chapter 3 showed the multi electron transfer process at the electrode surface with each successive reduction followed by a protonation step of the Keggin to balance the increased negative charge.[15,16] Under ideal conditions this is not considered to be a rate limiting step due to the excess proton concentration supplied by the supporting electrolyte, e.g. 1 mM POM in 0.1 M $HClO_4$ results in 100 protons for each redox molecule. However, under fuel cell conditions there is no supporting electrolyte present to supply protons for the successive protonation steps after each reduction. This is highlighted in Table 4.3 which shows that for a complete reduction of the V_4POM system i.e. all vanadiums reduced to the 4+ oxidation state, 1.48 M of protons is required, however, only 0.1 M are available in solution based on a pH of 1. Although POMs have the unique ability to undergo successive reductions without protonation[17] this increased charge upon the Keggin will further hinder the subsequent second third and fourth electron transfer.

Table 4.3: Table comparing the total concentration of protons required for a complete reduction of the V_4POM system (all vanadium reduced to the 4+ oxidation state) with protons available in the 0.3 M self supporting V_4 system. pH = 1. Protons required for each Keggin species is calculated based upon speciation data of V_4POM in Table 4.4.

V_4POM System	Protons required
V_1 Keggin	1.1 x10^{-2} M
V_2 Keggin	1.1 x10^{-1} M
V_3 Keggin	3.6 x10^{-1} M
V_4 Keggin	3.8 x10^{-1} M
VO_2^+	7.0 x10^{-1} M
Total $[H^+]$ required	1.48 M
Total $[H^+]$ available	0.1 M

It is also notable that there is an evidently lack of increased peak current under *iR* compensated conditions. With solution resistance compensated for, the POM systems would be expected to show an increase of approximately 300 times. This is not the case and is summarised in Figure 4.11. Here we see the comparison for the ratios of peak cathodic current between ideal and fuel cell conditions. The red bars show the ratio without solution resistance compensated and it is clear that none of the V_xPOMs nor the $Fe(CN)_6^{3-/4-}$ systems approach the ideal ratio of 300. Also the ratio progressively decreases as we move from V_1 to V_4 indicating a significant decrease in performance with the V_4 effectively working at less than 50 % efficiency (ratio less than 150). The extended yellow bars represent the increase in peak current with solution resistance compensated and hence an increase in the ratio of the two peak currents. The ferro/ferricyanide system reaches a ratio of 260 and given that only 85 % of the total uncompensated resistance is compensated for this is close to the expected value. If we were able to achieve 100 % compensation without positive feedback and distortion of the CV then the theoretical increase of 300 times in peak current might be possible.

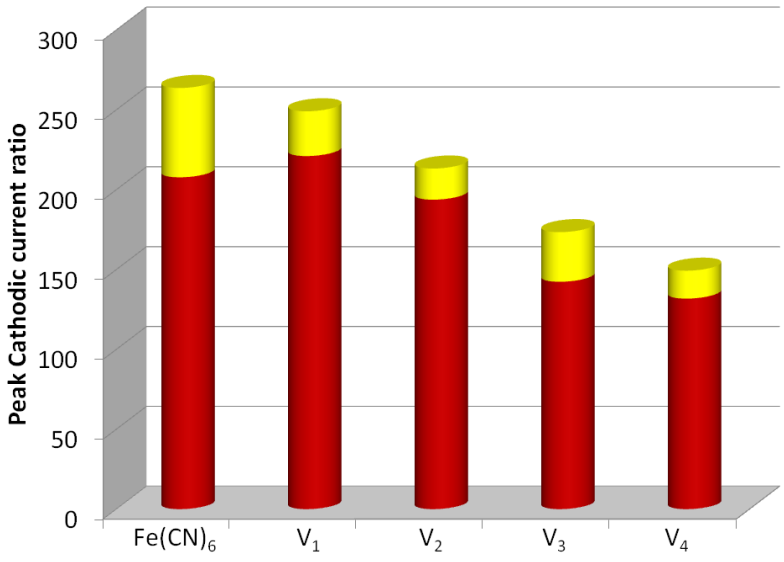

Figure 4.11: This illustrates the ratio between peak cathodic currents under ideal conditions (0.001 M redox species in 0.1 M supporting electrolyte) and fuel cell conditions (0.3 M redox species and no supporting electrolyte). Red bars indicate ratio between peak currents without *iR* compensation and additional yellow bars indicate the increase in peak cathodic current with 85 % *iR* compensation.

The V_1POM is very similar to the ferro/ferricyanide system with a resistance compensated ratio for peak current of 250, close to that of the 260 determined for

ferro/ferricyanide. The remaining POM systems show a drastic decrease in the (compensated) peak current ratio with values of 213, 173 and 149 for the V_2, V_3 and V_4POM systems respectively. With solution resistance not mitigating against the slower electrode kinetics or the reduced peak currents under fuel cell conditions the cause of this phenomenon lies elsewhere. The only other significant property which changed when moving to fuel cell conditions is the concentration of the redox active species. Not only is there an increase in the concentration of individual POM species but there is an increase in the free vanadium ion (VO_2^+) present in solution.

4.2.2.3 Effect of Concentration on Voltammetry

The significant increase in concentration changes the dynamics of each individual V_xPOM system. As can be seen from Table 4.4 there are significant quantities of VO_2^+ (free vanadium) present in the V_2, V_3 and V_4 systems and its effect upon the electrochemistry has already been discussed in the preceding chapter.

Table 4.4: Estimated concentrations of individual POM species in each POM system based on a V_xPOM concetration of 0.3 M. See Chapter 3 for details.

System	[V_1Keggin]	[V_2Keggin]	[V_3Keggin]	[V_4Keggin]	[Free V]
V_2POM	9.6 x10^{-2} M	1.7 x10^{-1} M	2.6 x10^{-2} M	0 M	8.4 x10^{-2} M
V_3POM	1.4 x10^{-2} M	1.5 x10^{-1} M	9.8 x10^{-2} M	2.5 x10^{-2} M	2.0 x10^{-1} M
V_4POM	1.1 x10^{-3} M	5.6 x10^{-2} M	1.2 x10^{-1} M	9.5 x10^{-2} M	3.5 x10^{-1} M

However, although the effect of free vanadium upon the electrochemistry has been observed previously, its effect under ideal conditions (lower concentrations) is minimal compared to fuel cell conditions. This concentration effect is evident in Figure 4.12 where the simulation model developed in Chapter 3 (model C) is utilised. Figure 4.12A shows the comparison between the simulation run at a scan rate of 0.04 V s^{-1} at two different concentrations, red = 0.1 M and blue = 0.001 M. The changes in I_p^c and I_p^a are not relative to the factor of 100 by which the concentration increases.

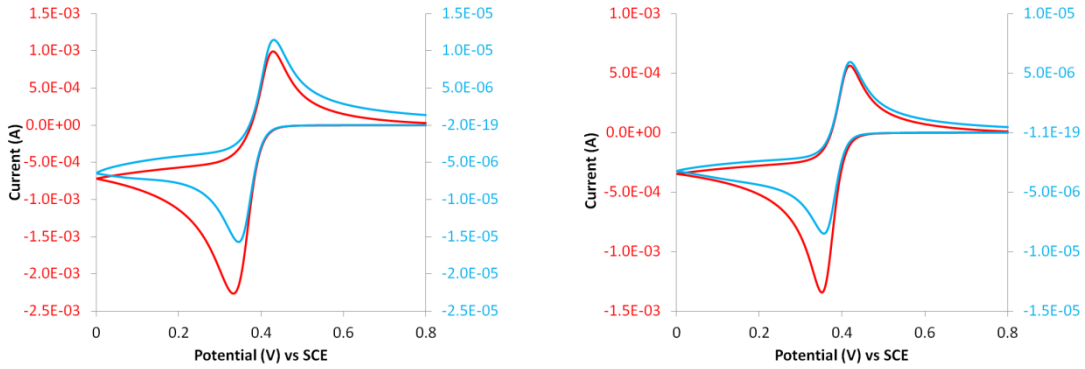

Figure 4.12: Simulated dependence of the VO_2^+ cation in solution upon the cyclic voltammetry response of the V_3POM system. Model C developed in chapter 3 was used. A) CV response at a scan rate of 0.04 V s^{-1} for 0.1 M V_3POM (red) and 0.001 M (blue). B) CV response at a scan rate of 0.01 V s^{-1} for 0.1 M V_3POM (red) and 0.001 M (blue).

Specifically I_p^c increases in magnitude by a factor of approximately 150 on moving from 1 mM to 0.1 M V_4POM concentration. The resulting peak current ratio for the anodic and cathodic process reduces from 0.73 at 1 mM concentration to 0.43 at 0.1 M. This same situation is observed for different scan rates, with the ratio changing from 0.70 to 0.43 at 1 mM and 0.1 M respectively at a scan rate of 0.001 V s^{-1} (Figure 4.12B). The reason for this lies in the availability of VO_2^+ ion to oxidise the reduced POM species. Consequently at these increased concentrations we have two separate redox systems working in tandem, the POM system(s) and the free vanadium system. With the concentration of free vanadium so high in an acidic media, the chemistry of this species is analogous to that of the vanadium redox flow battery.[18,19]

Gattrell and co workers[1,2] investigated the reduction of VO_2^+ (free vanadium in acidic media) and the reasons for the apparent low symmetry factor at high overpotentials on carbon electrodes. Here they proposed a reaction model which is applicable to the systems being investigated in this work. Consider the following reactions of reference for the reduction of VO_2^+ to VO^{2+}:

$$[VO_2 \bullet 4H_2O]^+ + e^- \rightleftharpoons [VO_2 \bullet 4H_2O]^0 \quad (4.4)$$

$$[VO_2 \bullet 4H_2O]^+ + POM_{red} \rightleftharpoons [VO_2 \bullet 4H_2O]^0 + POM_{ox} \quad (4.5)$$

$$[VO_2 \bullet 4H_2O]^0 + H^+ \rightleftharpoons [VOOH \bullet 4H_2O]^+ \quad (4.6)$$

$$[VOOH \bullet 4H_2O]^+ + H^+ \rightleftharpoons [VO \bullet 5H_2O]^{2+} \quad (4.7)$$

At glassy carbon electrodes the direct reduction of VO_2^+ is kinetically slow (equation 4.4) however the catalytic reduction using polyoxometalates has been shown to drastically increase the rate of reduction VO_2^+ at low overpotentials (equation 4.5).[20] POM_{red} is oxidised during the catalytic reduction of VO_2^+ toVO^{2+}. It is this catalytic reduction that is observed in the voltammetry of the V_xPOM systems as well as the direct reduction of the VO_2^+ species. The successive protonation steps (equations 4.6 and 4.7) occur regardless of which mechanism (equations 4.4 or 4.5) is used for VO_2^+ reduction. The direct reduction is highly dependent upon the carbon surface, which includes the type of carbon used and surface polishing. This strong dependence on the nature of the electrode surface is typical of an inner sphere electron transfer.[21] This leads to the expansion of equation 4.4:

$$VO_{2\,(aq)}^+ \rightleftharpoons VO_{2\,ads}^+ \quad (4.8)$$

$$VO_{2\,ads}^+ + e^- \rightleftharpoons VO_{2\,ads}^0 \quad (4.9)$$

$$VO_{2\,ads}^0 \rightleftharpoons VO_{2\,(aq)}^0 \quad (4.10)$$

There is no protonation of the absorbed intermediate species as this would result in a pH dependence if rate determining. This issue has been proven by Gattrell as no pH dependence is observed for the reduction of VO_2^+ at high overpotentials (>150 mV).[2] Here the electron transfer (equation 4.9) is the rate determining step.[2] The neutral vanadate intermediate (VO_2^0) is also generated via the catalytic reduction of VO_2^+ (equation 4.5) resulting in large quantities of intermediate species which would be expected to have a low solubility in the aqueous media. The formation of these absorbed layers upon the electrode, as well the potential blocking effect of the neutral intermediate species, form the basis of Gattrell's model. They describe that the electron transfer to the active species in solution involves electron transfer through the adsorbed intermediates which are evidently slow to desorb. This would lead to the entire applied potential not being available to drive the reduction.[1,2] This model forms the basis of our expansion whereby we incorporate the adsorption of POM species upon the electrode surface. Kim and Kovács[22,23] studied the electrochemical effects of these absorbed layers and found that they inhibit the

electron transfer to solution phase species. The POM structures can also spontaneously form self assembled monolayers upon electrode surfaces from acidic aqueous solutions.[24] Evidence for adsorbed POM layers from analysis of the V_xPOM systems under investigation here is seen in Figure 4.13. In both Figure 4.13A and B a freshly polished GC electrode is used to run a 'blank' CV of the $HClO_4$ electrolyte. The electrode is then cycled with V_1 and V_4POM before being rinsed with distilled water and the resulting CV in the same $HClO_4$ electrolyte shows evidence of residual V_1 (A) and V_4 (B) POM species remaining on the electrode surface.

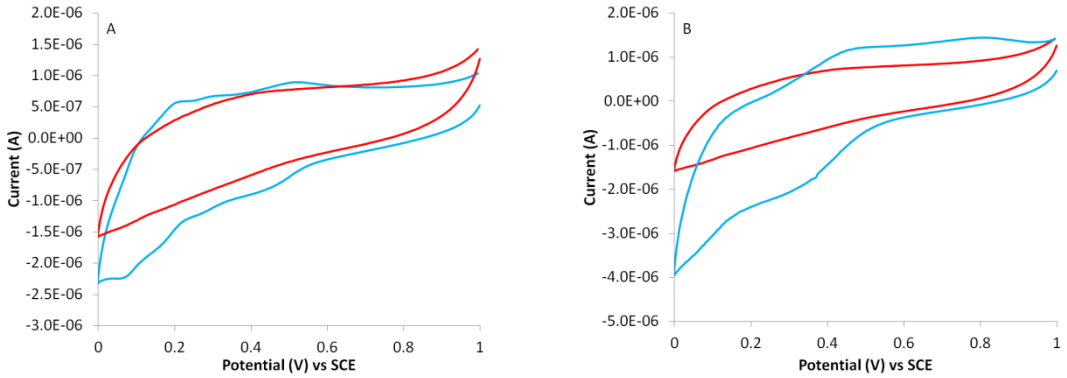

Figure 4.13: Evidence of adsorption of adsorbed POM layers on the GC electrode surface after exposure to V_xPOM. A) CV of blank GC electrode in 0.1 M $HClO_4$ (red) and after exposure to V_1POM (blue). B) CV of blank GC electrode in 0.1 M $HClO_4$ (red) and after exposure to V_4POM.

Combining the initial model proposed by Gattrell for free vanadium and the knowledge of adsorbed POM species on the electrode surface, we are able create a clearer picture of the factors affecting the electron transfer at the electrode surface. The model proposed in Figure 4.14 represents the layering effect observed at the electrode surface in the V_xPOM systems were x = 2-4. This does not apply to the system when x = 1 as no free VO_2^+ present in solution. The first adsorbed layer upon the electrode surface is shown to be the POM monolayer, however it could quite easily be a mixture of the various species forming the initial adsorbed layer. Work by Kim and Choi showed that not only do molybdenum based POMs exhibit a higher adsorption compared to its tungsten counterpart but that the relative surface coverage ranges from 0.43 to 0.63.[22] There may be defects in the adsorbed POM layer resulting in specific adsorption of the VO_2^+ species. The absorbed POM layer may act as a mediator in the electron transfer between the electrode and solution phase species.

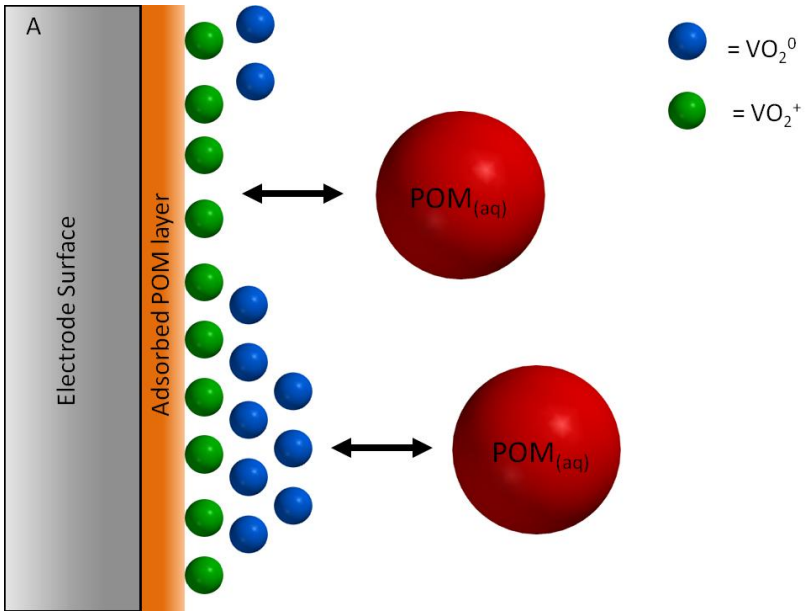

Figure 4.14: Proposed model for the electrode solution interface for the V_xPOM systems when x > 1. Spheres represent the various species present at the interface. Blue; VO_2^0, green; VO_2^+ and red; V_xPOM species.

Equations 4.8-4.10 describe the adsorption and reduction of the VO_2^+ adsorbed on the electrode surface. This same process can be assumed for the POM layer with VO_2^+ coordinating to the adsorbed POM layer (outer sphere)[25] and undergoing reduction via mediation from the POM layer. This allows the reduction of VO_2^+ leading to the intermediate species VO_2^0 without specific adsorption on the electrode surface. The three mechanisms by which the intermediate VO_2^0 species is produced (direct reduction of VO_2^+ at the electrode surface, dissociation of reduced vanadium centres coordinated to the Keggins outer sphere and dissociation of Keggin bound reduced vanadium) ensure that there is a sufficient concentration of VO_2^0 present at the electrode surface (in conjunction with the adsorbed POM layer) to inhibit the electron transfer from the electrode to the solution phase species. This effectively blocks the POM species from the electrode and hence the POM does not experience the full applied potential (Figure 4.15) which will ultimately reduce the current generated. For the case of the V_1POM we expect the electrode solution interface to be much simpler as it is a single species system with no VO_2^+ present. This effectively means that only an adsorbed POM layer upon the electrode surface would act as a potential inhibitor of the electron transfer to the solution phased species.

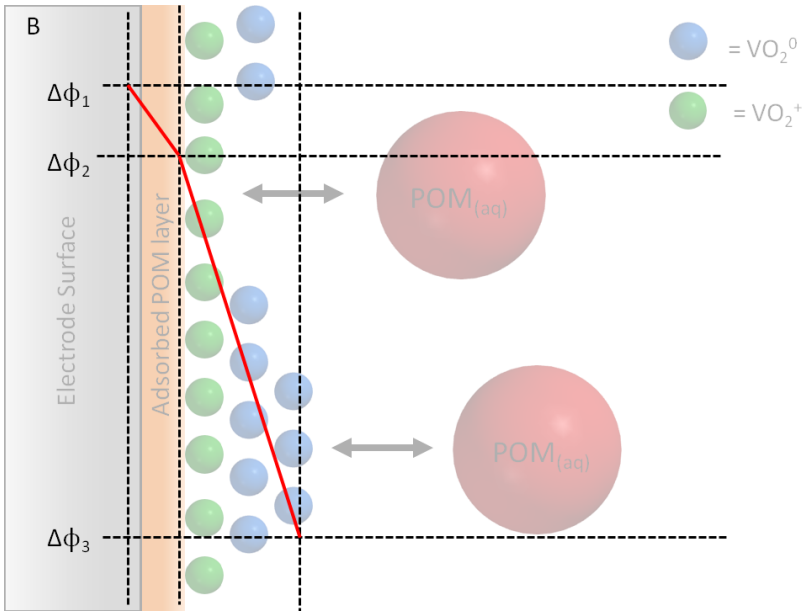

Figure 4.15: Overlay of proposed changed in the applied potential at the electrode surface across the adsorbed/ blocking layers.

This model supports the observed trend in data in Figure 4.11. The increase in [VO_2^+] subsequently leads to an increased thickness of the apparent 'blocking layer' resulting in a reduction in the fraction of the applied electrode potential the solution phase species experiences. Hence the expected increase in currents with concentration will not be achieved as the same applied potentials to drive the reaction at the increased concentrations are not available to the active species. This model is unlikely to severely affect the electrode kinetics under ideal conditions due to the initial and subsequent concentrations of VO_2^+ and VO_2^0 concentrations not being sufficient to cause the VO_2^0 driven blocking at the electrode surface. Also under ideal conditions the VO_2^0 species is likely to be readily protonated due to the large excess of protons available.

4.2.2.4 Rotating Disc Analysis: Fuel Cell Conditions

It is clearly evident from this chapter thus far that the effect of the increased concentration and lack of supporting electrolyte upon the electrode kinetics is substantial. The rotating disc analysis under fuel cell conditions should give more realistic values of the fuel cell's fundamental electrochemical parameters J_o and k^o as here the analysis will be carried out with no supporting electrolyte and in the presence of the perceived blocking layer. We first consider the scenario of the

V_1POM system where we assume only an adsorbed POM layer is present on the electrode surface when under fuel cell conditions.

The V_1POM still shows a general dependence of the limiting current upon rotation speed at higher concentrations although a plateau is not observed (Figure 4.16). However, the limiting current is not proportional to the square root of rotation speed and begins to plateau (Figure 4.16 inset) indicating that the Levich equation no longer (quantitatively) describes the limiting current and that the electrode kinetics are rate limiting.[4,5] It is noted that in the current-voltage sweeps (Figure 4.16A) we observe only a single limiting current unlike under ideal conditions where we observed separate limiting current plateaus for the vanadium and molybdenum redox species. However it is difficult to identify specific potential where the limiting current is observed. As discussed in the previous chapter the limiting current at the RDE coincides with the concentration of the redox species undergoing electron transfer at the electrode surface approaching zero.[4] However the increase in concentration at the electrode leads to the surface being essentially saturated so that the concentration of the redox species (in this case vanadium) approaches zero at much lower potentials thus we do not strictly observe a limiting current plateau but more of a deviation from the exponential increase in the observed potential range.

The Tafel plot obtained based upon the rotating disc data is shown in Figure 4.16B with extrapolation for J_o shown. As was the case in chapter 3, Tafel plots allow the for the electrode kinetics to be observed in the absence of any mass transport effects. The Tafel plot shows the most apparent linear section in the overpotential region of 120 – 220 mV, which is much higher compared with the analysis carried out under ideal conditions (80 – 140 mV). A large change in the apparent Tafel slope is also observed, under ideal conditions we obtained 140 mV decade^{-1}, however under fuel cell conditions this increases to >250 mV decade^{-1}. Walsh described the characteristics of a true Tafel slope and identified that large Tafel slopes are not representative of conventional Tafel behaviour and could result from film resistance upon the electrode surface. [26]

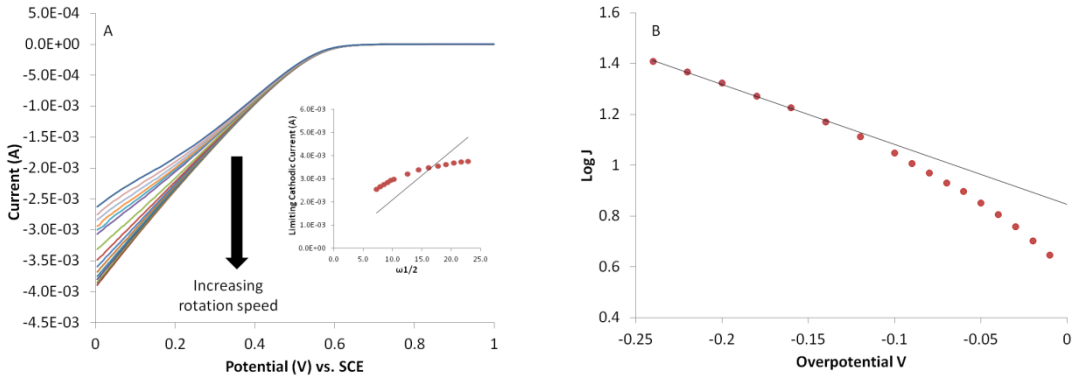

Figure 4.16: A) Potential vs. current curves for V_1POM with inset showing the relationship between the limiting cathodic current and $\omega^{1/2}$. B) Tafel plot constructed based on RDE data in Figure 4.16A showing extrapolation for J_o.

The corresponding error curve analysis for the linear fit in Figure 4.16B (Figure 4.17) shows the clear difference between the two conditions. Although both show the same inverted parabola shape, the shift in overpotential for extrapolation of J_o is apparent and an increased error in the linear fit is observed under ideal conditions, resulting in poorer correlation between the linear fitted data under both ideal and fuel cell conditions. With the clear shift in the linear section for J_o extrapolation to higher overpotentials, an increase in the Tafel slope and a large discrepancy between the fitted and raw data (under both sets of conditions) shown by the curve analysis, one has to seriously consider how valid an extrapolated value from these curved plots would be. The increase in concentration is likely to lead to an increased coverage of the electrode surface with respect to adsorbed POM layer. This ultimately increases the blocking layer at the electrode surface and hence lower currents are achieved at the higher overpotentials resulting in the increased Tafel slope.

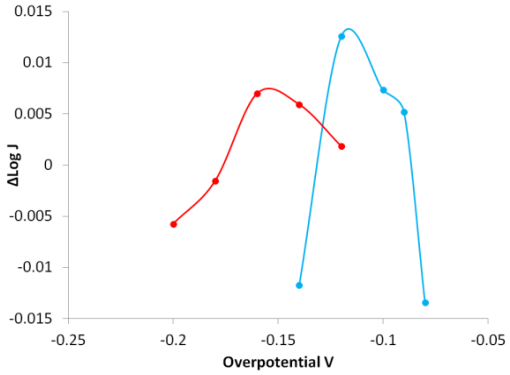

Figure 4.17: Comparison of curve analysis for V_1POM between ideal (blue) and fuel cell (red) conditions showing the deviation between the linear fit and raw data across the extrapolated overpotential range for extrapolation of J_o. Red

If we consider the V_4POM, we have an adsorbed POM layer, $VO_2^{+}{}_{(ads)}$ and $VO_2^{0}{}_{(ads)}$ as well as the desorbed $VO_2^{0}{}_{(aq)}$ species and a huge shortage of protons. Under ideal conditions the V_4POM already demonstrated very complex electrochemistry with an observed curvature in the Tafel plot as well as the perceived linear section being observed at high overpotentials (180-240 mV). Under these circumstances any extrapolated data based on linear fits for the V_4POM would be plagued with error and ambiguity, thus under fuel cell conditions this data would be unfit for analysis to obtain the desired parameters (J_o, k^o) should it follow the same trend as the V_1POM. The limiting current of the V_4POM shows a decreased dependence upon the rotation speed with no significant change observed between 500 and 5000 rpm (Figure 4.18A).

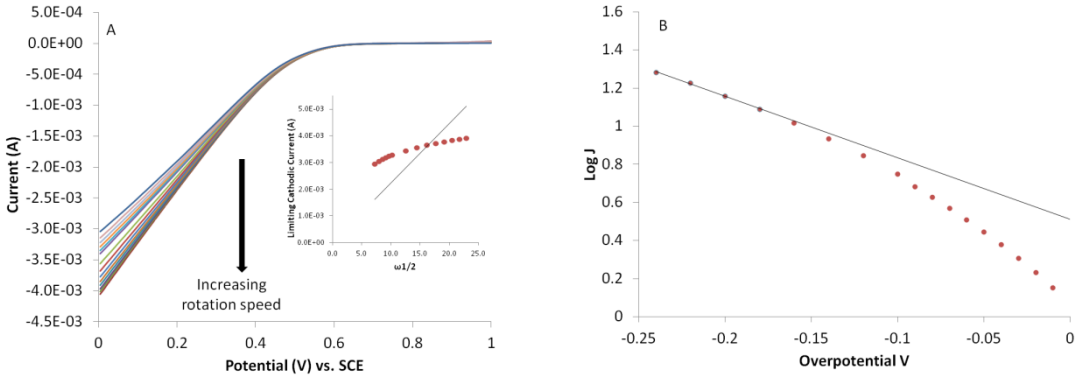

Figure 4.18: Potential vs. current curves for V_4POM with inset showing the relationship between the limiting cathodic current and $\omega^{1/2}$. B) Tafel plot constructed based on RDE data in Figure 4.18A showing extrapolation for J_o.

This is highlighted in the plot of limiting current versus $\omega^{1/2}$ (inset Figure 4.18A) where it is clear that the limiting current is not proportional to $\omega^{1/2}$, indicating that the electrode kinetics are rate limiting. It should be noted that larger limiting currents are observed in the V_4POM in comparison with the other V_xPOM even with the increased blocking expected at the V_4POM electrode surface. Analogous to the V_1POM it is difficult to assign a potential at which the rate liming current is observed. We again only observe a single limiting current for the V_4POM which is apparent under both ideal and fuel cell conditions.

The curve analysis for the extrapolation of J_o based on the data in Figure 4.18 shows a slight shift in the linear section to higher overpotentials with a smaller error observed between the raw and fitted data under fuel cell conditions. An increase in

the calculated Tafel slope from 200 to 240 mV decade^{-1} when moving from ideal to fuel cell conditions further raises the question of how valid the extrapolated exchange current density and standard rate constants are under these conditions.

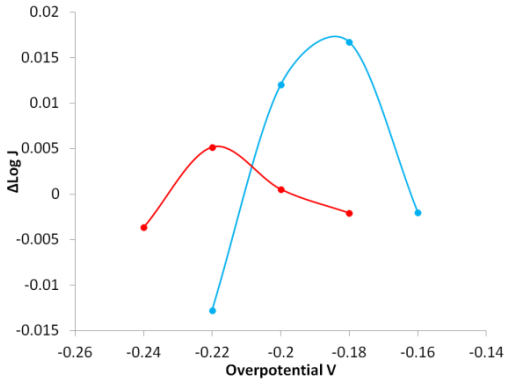

Figure 4.19: Comparison of the curve analysis for V_4POM between ideal (blue) and fuel cell (red) conditions showing the deviation between the linear fit and raw data across the extrapolated overpotential range for extrapolation of J_o (Red).

4.2.2.5 *iR* Compensated Rotating Disc Electrode Analysis

The compensation for solution resistance showed substantial improvements in the CV behaviour of the V_xPOMs, drastically reducing the peak to peak separation and increasing the observed peak currents. Compensation could allow for an improved Tafel plot and thus enable us to more confidently extrapolate J_o. The nature of the RDE setup employed results in an increased distance between the working and reference electrodes and consequently, an increase in uncompensated resistance. Table 4.5 illustrates the calculated solution resistance at the RDE for the V_1 and V_4POMs at varying rotation speeds.

The slight variation in resistance across the range of rotation speeds for the respective POMs is minimal and to prevent positive feedback when using IR compensation, 85 % of the resistance at 5000 rpm for each respective system will be employed.

Figure 4.20 shows the linear voltammograms for the V_1 and V_4POM with and without (solution resistance) compensation at 5000 rpm. It is clear that with compensation we observe an increase in current along with a more defined limiting current at potentials similar to those under ideal conditions.

Table 4.5 Calculated uncompensated resistance at the RDE at rotation speeds ranging from 0 – 5000 rpm for the V_1 and V_4POM systems. Current supplied prior to interrupt, 1 mA. Electrode setup was identical to that used for the RDE analysis of V_xPOMs

Rotation speed (RPM)	V_1POM (ohms)	V_4POM (ohms)
0	52.6	89.5
1000	52.6	86.4
2000	51.9	85.8
3000	51.0	85.5
4000	51.6	84.3
5000	50.7	84.0

Although we observe the same dramatic increase in peak current when taking into account the uncompensated resistance, it is clear that we still do not observe a 300 times increase in current when comparing the linear sweep voltammetry scans obtained under ideal conditions. In this instance the improvement may seem significant; however, more important, is the effect that *iR* compensation has upon the resulting Tafel plot.

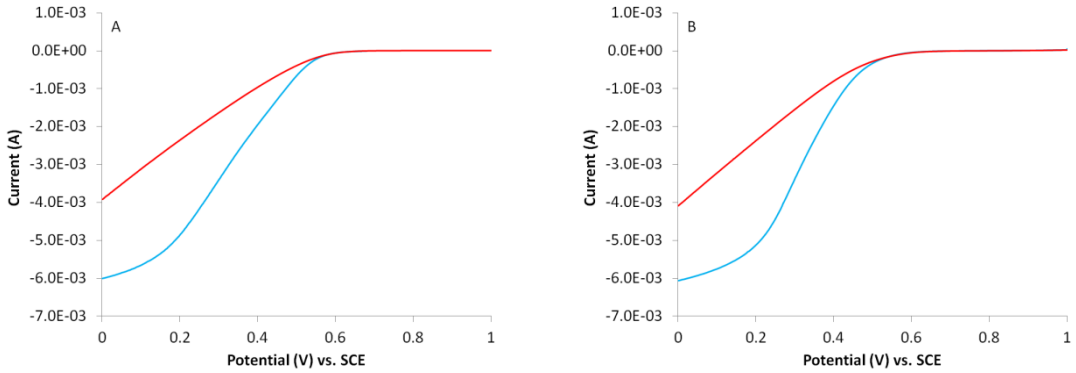

Figure 4.20: Uncompensated (red) and 85 % compensated resistance (blue) current potential curves at the RDE electrode. Rotation speed = 5000 rpm. A) 0.3 M V_1POM, IR compensation = 43 ohms, B) 0.3 M V4 POM, IR compensation = 71 ohms. v = 0.005 V s^{-1}.

The resistance compensated Tafel plots show little improvement with a curvature still clearly evident in both the V_1 and V_4POMs (Figure 4.21). Even with *iR* compensation there is no significant change in the observed Tafel slopes, as in both cases, values still exceed 200 mV $decade^{-1}$, which is not representative of a true Tafel plot.[26,27] It is apparent that the initial aim of using the fundamental electrokinetic property J_o as a means of comparison between the V_xPOM is not feasible due the

potential large errors in extrapolation and ambiguity in the final quoted value. An alternative comparison is needed in order to highlight improved/decreased performance between catalysts and to form a basis by which new formulations/catalysts can be compared. It is also apparent that for a true comparison between catalysts, ideally the comparison needs to be drawn under fuel cell conditions as the speciation of the systems has significant effects the electrochemical behaviour.

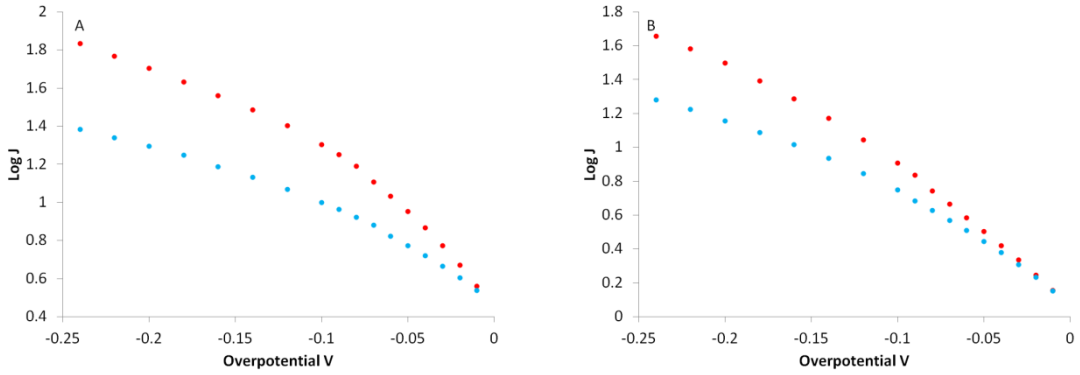

Figure 4.21: Uncompensated (blue) and *iR* compensated (red) Tafel plots for A) 0.3 M V_1POM and B) 0.3 M V_4POM.

4.2.2.6 Alternative Method: Overpotential vs. Current

Exchange current density is a fundamental property in fuel cell catalysis as it gives an insight into the kinetics of an electrochemical reaction.[28,29] Large values for J_o indicate fast kinetics, large active surface area, high concentration and that minimal overpotential is required to drive a reaction and vice versa. Evaluating J_o from the obtained Tafel plot is not viable in these systems but measuring the overpotential needed to attain a given current density (Figure 4.22) is an alternative method for comparing the catalytic systems as well as quantitative ranking of different catalyst formulations. This method uses the raw data employed to construct the Tafel plots already considered and results in an analytical method that can be applied to the V_xPOM series studied and any future formulations/catalyst developments. The aim of this method is to select a series of currents that will test the complete range of current output and observe the change in overpotential (Figure 4.22) between the four systems. The current densities to be observed are 5, 10, 20 and 50 mA cm^{-2}.

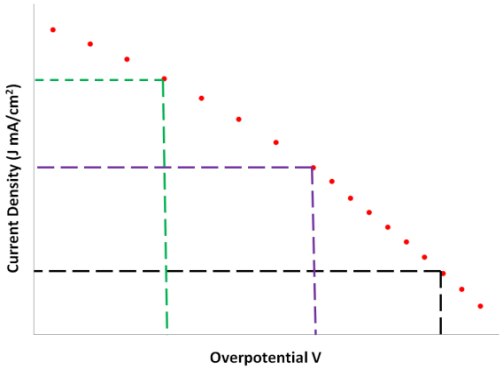

Figure 4.22: Example of data interpolation via alternative method. Specific current densities will be selected and the magnitude of the overpotential required to reach the given current density is quantified. Dashed lines (green, purple and black) show examples of extrapolation at increasing current densities

4.2.2.7 Effect of Temperature on Catalyst Performance

The thermodynamics and kinetics of the system are greatly affected under fuel cell conditions. We have so far considered the effect of concentration upon the system and its importance when comparing the V_xPOMs. The final factor to consider when comparing these systems is temperature. Under ideal and fuel cell conditions we have observed the V_xPOMs at room temperature, however, the fuel cell operates at 80 ^oC and for a true comparison the RDE analysis would need to be carried out at this elevated temperature. Using the V_4POM as an example we can see the effect of temperature upon the resulting current at varying overpotentials (Figure 4.23).

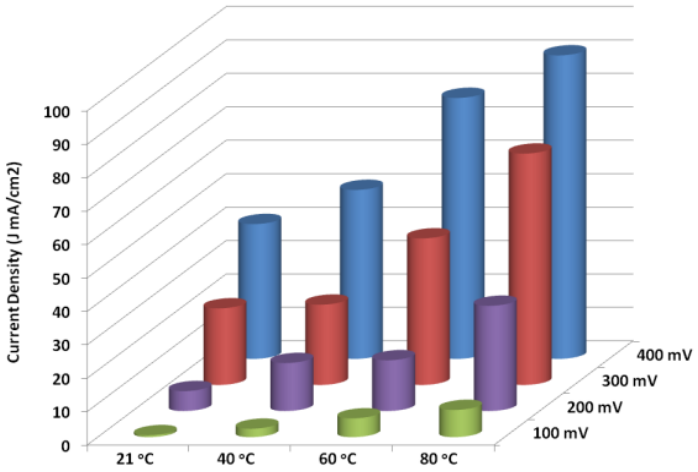

Figure 4.23: Change in current density for the V_4POM with increasing temperature ranging from 21 - 80 ^oC. The four overpotentials measured where 100 mV (green bars), 200 mV (purple bars), 300 mV (red bars) and 400 mV (blue bars).

At the four overpotentials observed (100, 200, 300 and 400 mV) we can see that there is a clear and drastic increase in current density between room temperature (21 ^{o}C) and a typical fuel cell operating temperature (80 ^{o}C). To truly compare the four systems in questions and identify a lead catalyst, the comparison must be done at fuel cell conditions and fuel cell temperature.

4.2.2.8 Comparison and Normalisation of V_xPOM Data

The four POM systems in question were analysed using the proposed alternative method. To facilitate a complete analysis a wide range of currents were analysed. Specifically we observed the magnitude of overpotential required to generate 5, 10, 20, 50 and 80 mA cm^{-2} (Figure 4.24). Figure 4.24 only illustrates data for four of the five current densities being considered; this is simply due to only the V_1POM system successfully reaching 80 mA cm^{-2} at an overpotential equal to 240 mV. The remaining three systems were not able to reach this higher current density within the potential range observed. At the three lower current densities (5, 10 and 20 mA cm^{-2}) we observe following trends, a) the respective overpotential applied to each system increases when the desired current density increases and b) for the first three current densities the overpotential required by the respective system to achieve the corresponding current density is in the order $V_1 < V_2 < V_3 < V_4$. At these current densities we observed a trend in overpotential which would represent a decrease in the exchange current density of the respective POMs as we move from the V_1 to V_4 POM system. This is the opposite from what we identified under ideal conditions based on extrapolations from the constructed Tafel plots. However, it has been noted that concentration has greatly affected the apparent kinetics and double layer structure, which could very easily change the measured electrochemical properties of a system. The increase in overpotential across the four systems could result from an increase in the blocking layer thickness reducing the actual potential experienced by the redox species compared to the actual applied potential at the electrode surface. Also with the self-supporting systems being proton limited, it is possible a localised pH change (increase) is observed at the electrode surface which again could change the electrochemistry of the POM system.

At a current density of 50 mA cm^{-2} we do not observe this same trend in overpotential with the increasing overpotential required from the respective systems

following the order V1 < V_4 < V_3 < V_2. At these higher overpotentials the VO_2^+ can be directly reduced (considering a similar electrode potential in each system) at the electrode surface and can contribute to the current achieved. This will then become an issue of concentration and with [VO_2^+] increasing in the order of V_2 < V_3 < V_4 then increased currents at a specific overpotential would be higher in the V_4POM system. For the V_1POM the free VO_2^+ specie does not play a role and as explained previously does not create a blocking layer at the electrode surface thus not hindering the electrode kinetics. Although the adsorbed POM layer is still present, the V_1POM experiences a potential much closer to that of the applied potential at the electrode surface.

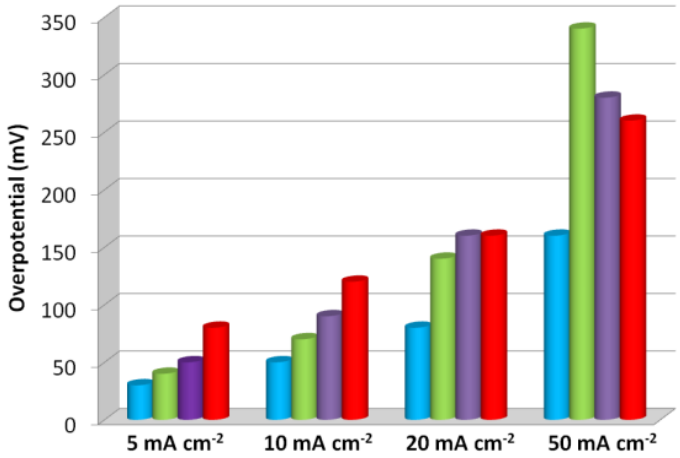

Figure 4.24: Comparison of overpotential required by individual V_xPOMs to generate the desired current densities. Blue = V_1POM, Green = V_2POM, Purple = V_3POM and Red = V_4POM. Analysis carried out at 80 ^oC.

Considering the concentration effects observed at 50 mA cm^{-2} one needs to further consider the effects of concentration across all current ranges. Normalisation of the data with respect to the vanadium concentration in each system allows this 'concentration term' to be taken into account. Figure 4.25 shows the normalised data shown in Figure 4.24 with respect to the vanadium concentration of the V_1POM. Once normalised, there is a significant change in the overpotential required to generate the desired currents across the V_xPOM systems. Considering the normalised data at 50 mA cm^{-2}, the $V_{2\text{-}4}$POMs cannot successfully generate this current density within the applied overpotential range. The data in Figure 4.24 and Figure 4.25,

suggest the V_1POM system has the highest exchange current density and this decreases in the order $V_1 > V_2 > V_3 > V_4$.

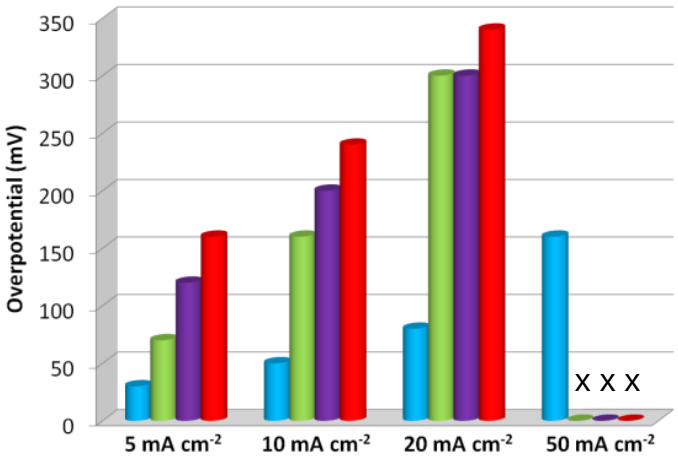

Figure 4.25: Normalisation of data in Figure 4.24 with respect to total vanadium concentration in the V_1POM system. Blue = V_1POM, Green = V_2POM, Purple = V_3POM and Red = V_4POM. The x at 50 mA cm^{-2} indicates that this current could not be achieved within the overpotential range observed.

4.2.2.9 In-situ Reduction of V_xPOM: Effects Upon Overpotential

The previous section considered the catalysts in their as synthesised form and the physical state of the catalyst when first pumped around the fuel cell system. In a working FlowCath® fuel cell the catalyst is never fully regenerated (oxidised) and always has a partial state of reduction. We now investigate the electrochemistry of partially reduced systems more akin to real fuel cell operating conditions. The incremental reduction of the V_xPOM systems was carried using a procedure provided by ACAL using stoichiometric quantities of hydrazine (Equation 4.11). Hydrazine was found to quantitatively reduce vanadium within the V_xPOM series in a ratio of 1:4 (Section 4.6.3).

$$N_2H_4 + 4\,V^{5+} \longrightarrow 4\,V^{4+} + 4\,H^{+} + N_2 \qquad (4.11)$$

By increasing the concentration of V^{4+} in solution we simultaneously decrease the concentration of V^{5+}. By doing this we decrease the open circuit potential of the system as predicted by the Nernst equation. Consider the following simple one electron reduction of an oxidised species:

$$Ox + e^- \longrightarrow Red \qquad (4.12)$$

where, D_o = 1 x10^{-5} cm^2 s^{-1} for both the oxidised an reduced species, k^o = 1 cm s^{-1}, α = 0.5, $E^{o'}$ = 0 V, electrode area = 1 cm^2 and [Ox] + [Red] = 0.1 M. The simulated CVs shown in Figure 4.26 represent the system described in Equation 4.12 where the start potential is set to equal the calculated OCP. Figure 4.26A is based upon the pre described conditions with the concentration of the oxidised species vastly outweighing the reduced species being 9.9 x10^{-1} and 1 x10^{-6} M respectively. Based on the Nernst equation the calculated open circuit potential (equilibrium potential) of the system is ~0.3 V. By adjusting the concentrations of the oxidised and reduced species to 0.098 and 0.002 respectively (Figure 4.26B) we see a shift in the open circuit potential to ~0.1 V. The shift in the open circuit potential results in a decrease in the overpotential required to reach the formal potential of the system and hence drive the reaction. By further increasing the concentration of the reduced species to 0.013 M (Figure 4.26C) we shift the open circuit potential (~0.05 V) closer to the formal potential, hence further reducing the overpotential required to reach ~20 mA.

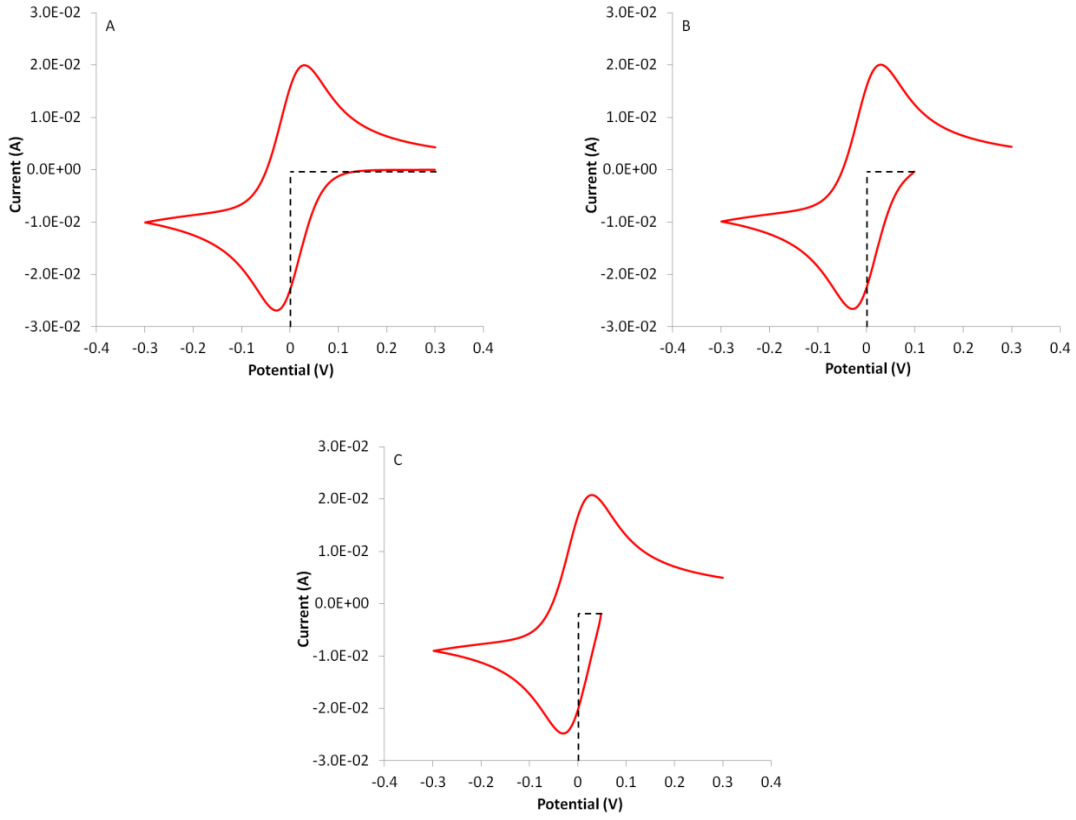

Figure 4.26: Simulated response for the change in OCP when changing the ratio of [Ox]:[Red]. A) [Ox] = 9.9 x10^{-1} M, [Red] = 1.0 x10^{-6} M. B) [Ox] = 0.098 M, [Red] = 0.002 M. C) [Ox] = 0.087 M, [Red] = 0.013 M. [Ox] + [Red] always equal to 0.1 M. See text for further parameters.

When comparing the data across the V_xPOM series we again normalised with respect to the total vanadium concentration of the V_1POM but it is also necessary to normalise with respect to the concentration of V^{5+} within each system under analysis. The data obtained for the four systems at the varying degrees of reduction are shown in Figure 4.27. If we first consider Figure 4.27A where 10% of the total vanadium in each system is in the V^{4+} oxidation state. It is clear that the same trend is observed by which a larger overpotential is required to drive the reaction in order to reach a higher current density. In each of the current densities observed we see that the increase in overpotential required follows the same order i.e. $V_1 < V_2 < V_3 < V_4$. However, at this 10 % reduced state the overpotential required to reach the desired current density is lower for each individual system when compared to the respective fully oxidised states. This same decrease in overpotential is also observed when the catalysts are in their 20 and 30 % reduced states (Figure 4.27B and C). As the percentage of V^{4+} is increased the open circuit potential (OCP) decreases in all four systems (Figure 4.27F).

However, although the OCP continues to decrease as we further increase the concentration of V^{4+} in solution the overpotential required to generate the current densities begins to increase in the $V_{2\text{-}4}$POMs but not V_1 up to a 30 % reduced state. When reducing the vanadium within the POM systems with hydrazine (Equation 4.11), we are not only reducing vanadium within the POM structure but also the VO_2^+ present in solution. If we consider equation 4.11 and assume all four vanadium's in the 5+ oxidation state are contained within the POM structure, then the four protons supplied by the in-situ decomposition of hydrazine are sufficient to balance the increase in charge upon the Keggin structure. The pH of the solution will only change if the pK_a of the reduced POM is different to the oxidised POM i.e. should only change slightly or not at all. If however, the VO_2^+ undergoes reduction then the four protons supplied by the hydrazine decompositions are not enough to protonate the four reduced species resulting in a mixture of VO^{2+} and VO_2^0 species being formed. We have previously observed the effect of the VO_2^0 species upon the electrode kinetics. The afore mentioned reduction process can happen individually, but more likely a mixture of the two is likely to occur resulting in the V^{4+} centre being present in the Keggin structure and in solution existing as the VO^{2+} cation as well as varying quantities of the VO_2^0 species. In this instance the pH of the POM

solution will go up as the dissociated protons from the Keggin as well as those from hydrazine decomposition will be involved in the protonation of the VO_2^0 species.

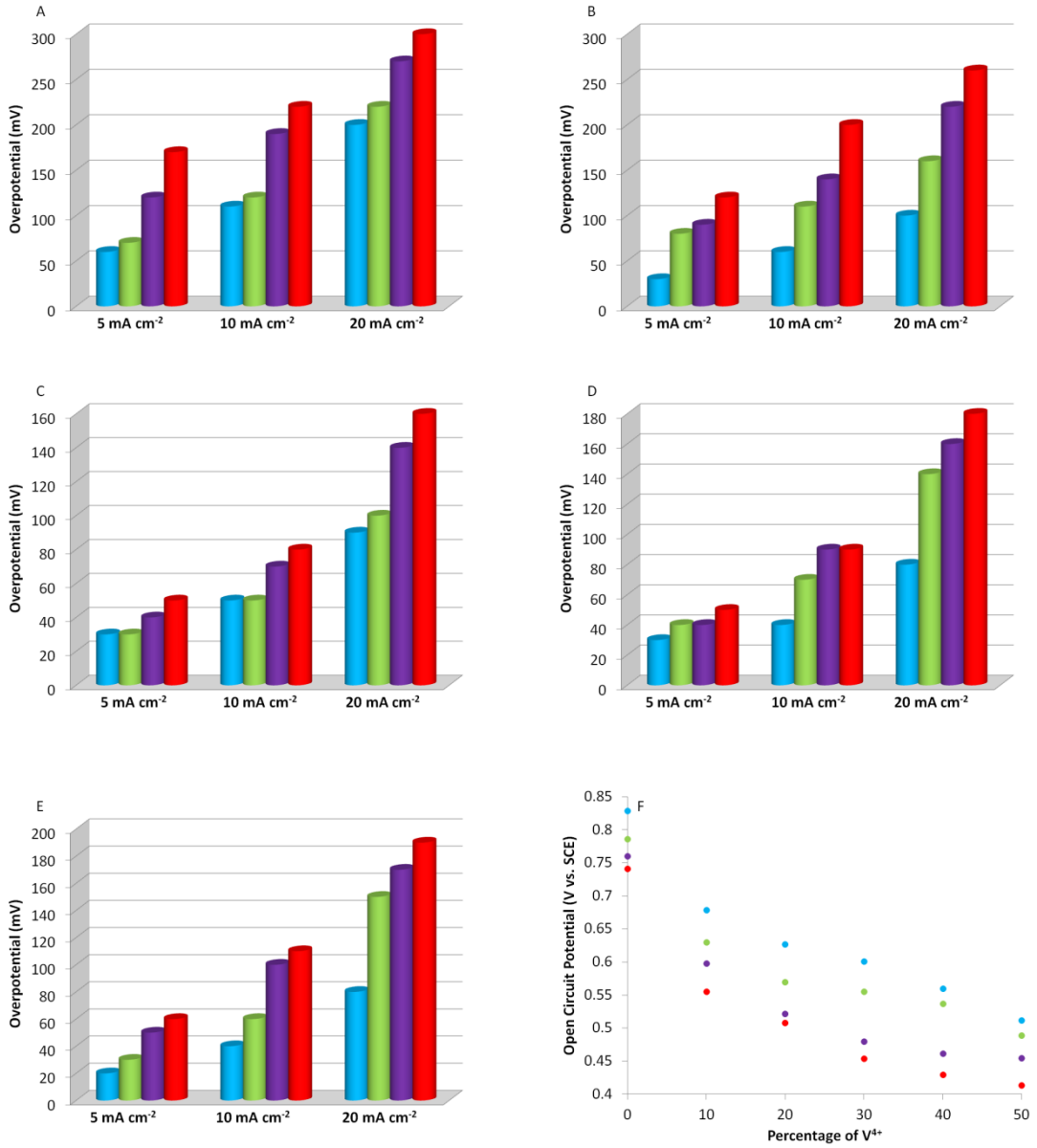

Figure 4.27: Comparison of (normalised) overpotential required by individual V_xPOMs to generate the desired current densities when at varying redox sates. Blue = V_1POM, Green = V_2POM, Purple = V_3POM and Red = V_4POM. A) Analysis carried out at 80 ^oC. Redox states refer to the percentage of the total vanadium in each individual V_xPOM system in the +4 oxidation state. A) 10 % of the total vanadium concentration in +4 oxidation state, B) 20 % of the total vanadium concentration in +4 oxidation sate, C) 30 % of the total vanadium concentration in +4 oxidation state, D) 40 % of the total vanadium concentration in +4 oxidation state and E) 50 % of the total vanadium concentration in +4 oxidation state. F) Showing the change in OCP with the increase in the V^{4+} percentage.

One explanation of the increase in overpotential when the $V_{2\text{-}4}$POM systems are in the 40 and 50 % reduced states is possibly due to a critical point in [VO_2^0]. Where now there could be sufficient quantities present in solution to form VO_2^0 driven

blocking effect at the electrode surface. This may simply due to the $V_{2\text{-}4}$POM voltammetry being limited 'more' by the proton concentration. The V_1POM is probably less likely to have this problem as there is no or minimal (free) VO_2^+ present in solution and any V^{4+} which has been reduced within the POM and dissociated leading to the VO_2^0 species, may not be at high enough concentrations to create a VO_2^0 driven blocking effect at the electrode surface. This is supported by the overpotential required in the V_1POM to continuously decrease even when the system is in the 40 and 50 % reduced states.

Upon completion of this analysis and re-oxidation of the catalysts it was noted that the OCP never returns to that of the fresh as synthesised POM, indicating the presence of V^{4+} in the system. This is also noted by ACAL when testing in the fuel cell. Before taking this forward a lead catalyst from the four V_xPOMs studied was selected to be the focal point of analysis and further development. The following discussion outlines the factors taken in to consideration when determining the lead system and is not just solely dependent upon the preceding electrochemical data but also takes into account the documented regeneration capabilities of the four V_xPOM systems.

Based on the results so far it is evident that the V_1POM demonstrates more favourable electrochemistry compared to the remaining three POMs. We observe that lower overpotentials are required to drive the reaction to reach a desired current density output. The overpotential required is as previously explained related to the fundamental fuel cell property, exchange current, which was the initial focus of the analysis. The lower overpotential values indicate that the V_1POM has the highest exchange current density across the fours systems and would indicate that this would be the lead catalyst to take forward. However under these conditions it is well documented that the one electron reduction of oxygen is thermodynamically unfavourable thus no oxidation of the reduced V_1POM species will occur. This would have detrimental effects on fuel cell performance and all though it shows the best performance with regards to overpotential and exchange current the V_1POM must be disregarded as the lead catalyst. To determine a lead catalyst from the remaining three systems one must consider not only the good and bad points but also the potential gain for improving the catalytic properties. Under typical fuel cell

operating conditions the POM system very rarely achieves 100 % reduction (with respect to vanadium) and under such conditions the rate of oxidation (regeneration) of the reduced V_xPOMs is in the order V_2POM < V_3POM > V_4POM.[30] The V_3 and V_4POM systems contain higher concentration of the V_2 and V_3 Keggins (believed to be the more active species in the oxidation process) as well as increased cathodic currents being achieved based on RDE analysis.[30] For these reasons the V_2POM is not believed to be the most suitable lead catalyst. The choice between the V_3 and V_4POM is difficult with both demonstrating very similar electrochemical behaviour as well as the proposed electrode blocking layer. However on the basis of Figure 4.11, the possible gains from improving the electrode kinetics of the V_4POM are far more than for the corresponding V_3POM system and thus the V_4POM is chosen as the lead catholyte to take forward.

4.2.2.10 Regenerated V_4POM System

It was stated previously that under fuel cell conditions the complete regeneration of the V_4POM i.e. all V^{4+} is oxidised back to V^{5+} is not achieved. For example after bubbling air through a solution of reduced V_4POM for 2 hours, a steady OCP of 0.659 V vs. SCE was obtained. Using the OCP data for the V_4POM at various redox states we can estimate the percentage of vanadium that has remained in the +4 oxidation state. Figure 4.28A shows the measured OCP for the V_4POM with a polynomial fit showing the general trend in OCP as the POM is reduced. After 2 hours of bubbling and results in a steady OCP is achieved we denote this the 'fully regenerated'. The measured OCP of the fully regenerated V_4POM was 0.659 V vs. SCE and using the equation of the fitted data we calculate that 3.3 % of the of the total vanadium concentration remains in the +4 oxidation state. Figure 4.28B shows the UV-Vis data obtained for the V_4POM at 4.6 mM for the various reduced states where we observe a linear dependence on the absorption at a wavelength of 776 nm. The linear fit allows for a second method to be used to determine the concentration of V^{4+} remaining in the system. The fully regenerated V_4POM shows an absorbance of 0.235 at 776 nm, which results in 4.6 % of the total vanadium remaining in the +4 oxidation state.

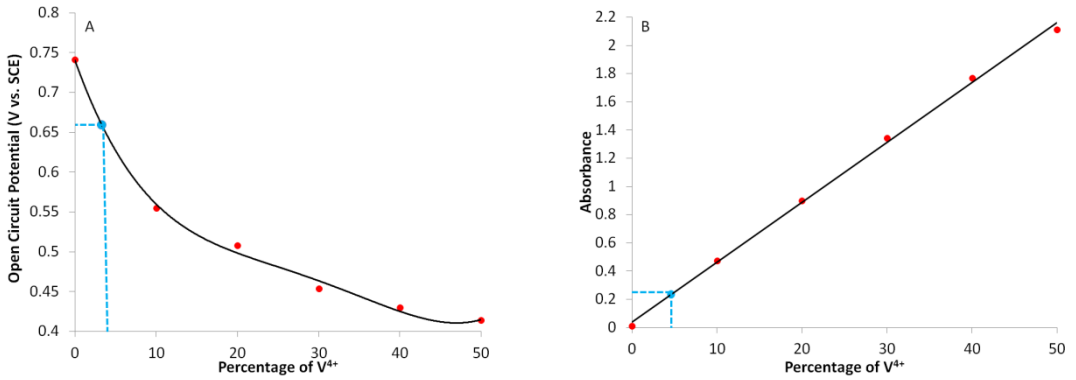

Figure 4.28: A) Change in OCP with increasing V^{4+} percentage showing a polynomial fit. Showing interpolation of residual V^{4+} percentage in the re-oxidised V_4POM system. B) UV-Vis absorption at 776 nm with increasing V^{4+} percentage. V_4POM concentration for 'on scale' measurement = 4.68 mM.

The two methods are in close agreement. Comparison of the V_4POM in its regenerated and fresh [(b)] states shows a distinct difference between the respective electrochemical properties.

Figure 4.29, which shows the comparison between the *iR* compensated CV's for the re-oxidised and fresh V_4POMs. The fully regenerated V_4POM shows the same anodic and cathodic peaks associated with the $V^{5+/4+}$ redox couple as seen in the fresh sample. However there is a significant increase in both the anodic and cathodic peak currents for the fully regenerated V_4POM compared to its fresh counterpart.. The small difference in peak separation could be assigned to the amount of *iR* compensation applied to each system all though the small change is not believed to be significant. A key point between the two CV's is the small pre-wave in the re-oxidised V_4POM (highlighted in yellow). It was initially thought that this could be due to an error in the reference electrode but upon testing the potential of the SCE against a new unused electrode this was ruled out. Alternatively the re-oxidised species could contain a species which has a formal potential more positive than the V_4POM hence would be reduced first.

[b] To clarify the 'fresh' state refers to the POM in its as synthesised oxidised form prior to being used in the fuel cell or reduced with hydrazine.

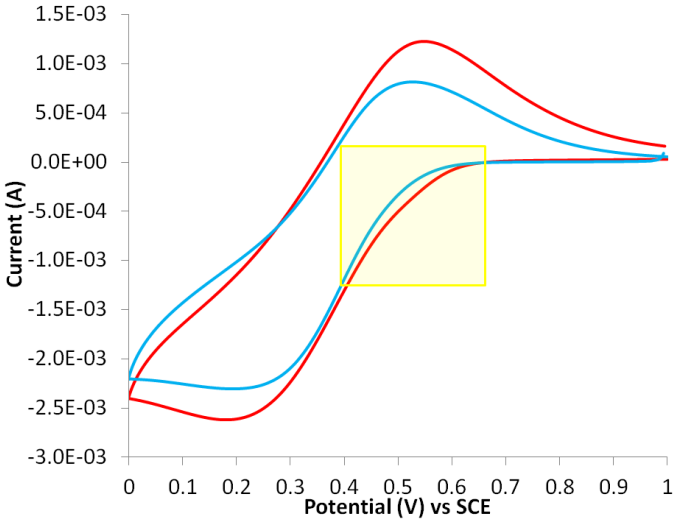

Figure 4.29: Overlay of CVs for fresh (blue) and re-oxidised (red) V4POM at a GC electrode. Scan rate = 0.04 V s^{-1}.

Figure 4.30 shows the overpotential required by the V_4POM to generate the desired current densities considered whilst in three different redox states, fresh, fully regenerated and 10 % reduced at the RDE. As we can see the fully regenerated POM (purple bar) does not require the same increased overpotential to generate the desired currents compared to the fresh oxidised V_4POM. The same argument of the OCP shifting in the re-oxidised V_4POM will still apply and contribute to the decrease in overpotential required to generate the desired currents observed.

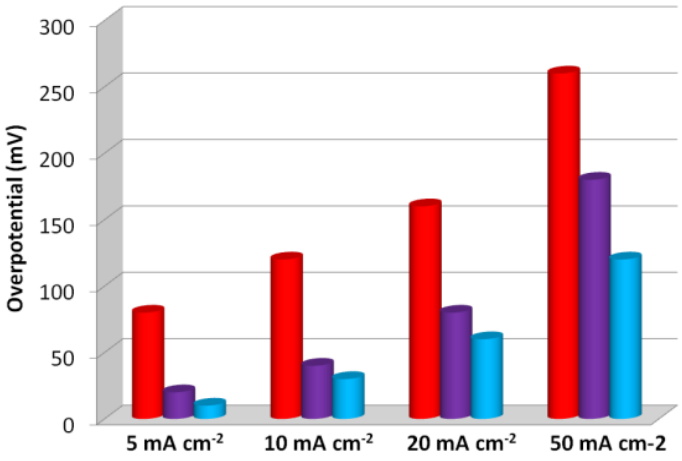

Figure 4.30: Comparison of overpotential required by the V_4POM in three different redox sates to generate desired current density. Red = fresh V_4POM, purple = re-oxidised V_4POM and blue = fresh V_4POM with 10 % of the total vanadium in +4 oxidation state.

However if one considers the magnitude of the decrease in overpotential in the re-oxidised V_4POM compared to that when in its 10% reduced state we observe almost the same decrease in overpotential. The decrease in overpotential when in the 10 % reduced state is substantial but almost the same decrease is observed in the re-oxidised state when only approximately 4 % of the vanadium is in the +4 oxidation state. This leads to the possibility of a change in the structure to a potentially more active state. The ^{31}P NMR of the V_4POM, as seen previously shows a multiple species system containing various positional and structural isomers. Work by Poblet et al studied the stability of the α and β isomers via density functional theory (DFT) calculations and showed that when the addenda atoms of a polyoxometalate structure have the d^0 configuration, the α isomer is favoured.[31-33] However, when the addenda atoms are no longer in the d^0 configuration and contain 1 or more electrons, the β isomer is more stable. [31-33] This potential change in the dominant isomeric form during reduction could lead to a more active species (towards reduction) upon re-oxidation. Identifying this change by NMR is difficult due to the V^{4+} centre being paramagnetic which distorts the peaks in the ^{31}P NMR.

Determination of the two structures via (single crystal) X-ray diffraction (see section 4.6.2 for details) reveals two very similar structures (Figure 4.31). The similarities are based around both structures adopting the Keggin like structure and having the same molecular formula. The major difference between the two structures is that the re-oxidised V_4POM displays a singularly vanadium capped Keggin structure (Figure 4.31B). Although the structure appears to be doubly capped this is not the case and the occupancies of the capped metal centres are 0.5 respectively indicating only one is present at any one time. The similarity between the two structures was determined via molecular similarity testing using Materials Studio 5.0 (Figure 4.31C) and showed a similarity of 88 %. Removing the capped metal centre increases the similarity to 96 % showing that there are no distinct differences in the basic structure of the compounds. The capped vanadium is not directly incorporated into the Keggin structure and is associated with the outer sphere of the structure. It has been reported previously by Matveev et al.[25] that these vanadium centres are reduced first which could result in the pre-wave observed in the re-oxidised V_4POM. The VO_2^+ ion is known to coordinate to the outer sphere of the fresh V_4POM species and this phenomenon is not solely assigned to the re-oxidised POM. However based on the

results obtained here the coordination of the free vanadium species appears to be more apparent in the re-oxidised species.

In the fresh V_4POM the specific location of the vanadium centres is difficult to determine due to the number of species and positional isomers. The vanadium atoms are statistically disordered across the entire structure and each metal centre has a partial occupancy for both molybdenum and vanadium. If we consider the same four metal centres which surround the capped vanadium (Figure 4.32) there is a distinct change in the vanadium partial occupancies. In the fresh V_4POM (Figure 4.32) the partial occupancies of the metal centres are 0.55, 0.66, 0.63 and 0.71 respectively, representative of the disorder with in structure with respect to vanadium. However in the re-oxidised V_4POM all four metal centres shown a partial occupancy of 0.65 indicating a more ordered structure and a preference for a specific configuration/isomer. This change could represent a more active state (towards reduction) resulting in the decrease in overpotential compared with the fresh V_4POM and comparable overpotentials with the V_4POM in its 10 % reduced state.

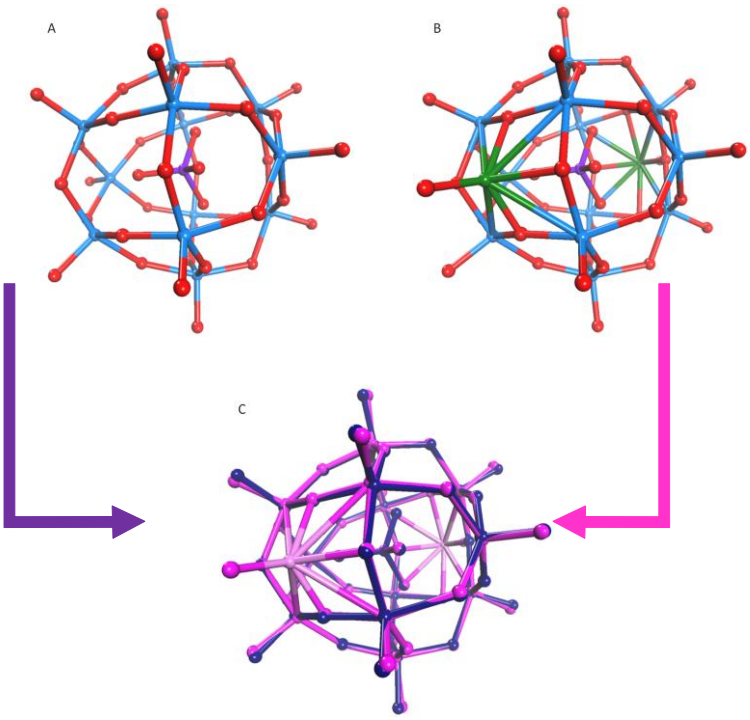

Figure 4.31: Single crystal structure of A) Fresh V_4POM and B) Regenerated V_4POM. Colour coding of balls is as follows, red = oxygen, purple = phosphorus and blue = molybdenum/vanadium and green = vanadium. C) Molecular similarity comparison of the two structures, dark purple represent the fresh V_4POM whilst pink represents the re-oxidised V_4POM.

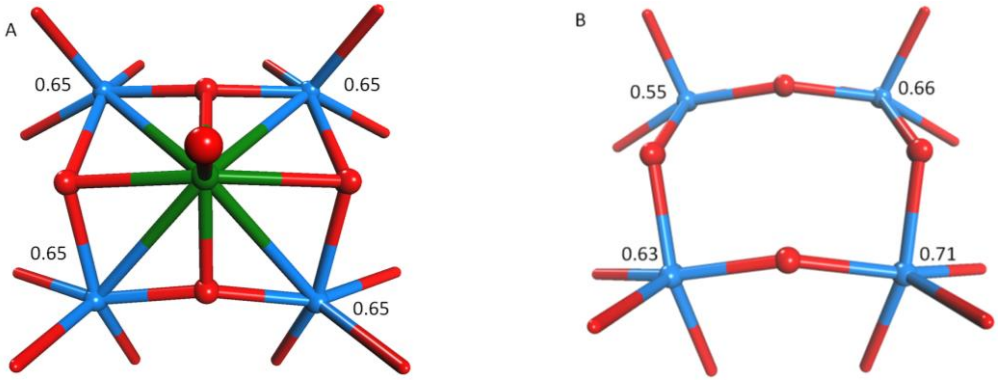

Figure 4.32: Comparison of the partial occupancies of the metal centres surrounding the capped vanadium entre. A) Re-oxidised V_4POM and B) fresh V_4POM

4.3 Conclusions

The aim of this chapter was to investigate the effects that current fuel cell conditions may have upon the electrode kinetics. Initially the $Fe(CN)_6^{3-/4-}$ redox system was selected as a suitable was compared to the V_xPOM systems. This system was selected due to its well documented electrochemical behaviour and high solubility in aqueous media. Under concentrated fuel cell conditions the reduction CV of $Fe(CN)_6^{3-}$ showed comparable results with that obtained under ideal conditions with an increase in peak separation to 158 mV (from 95 mV under ideal conditions). This led us to believe an apparent decrease in k^o and potentially slower electrode kinetics. Secondly it was noted that the apparent 300 times increase in peak current expected (due to the 300 time increase in concentration) did not occur as well as the anodic current (back sweep) approaching zero indicating that this is no longer solely diffusion controlled with respect to mass transport processes. This phenomenon was assigned to the effect of migration upon the ferri/ferrocyanide system with the reduced species acting as the ionic current carrier, effectively being 'swept' away from the electrode surface. This is supported by the high mobility of the ferri/ferrocyanide ions in aqueous media (Table 4.1).[14] The increased peak separation was assigned to an increase in the uncompensated resistance due to the lack of supporting electrolyte but more significantly the increased magnitude of the observed currents. The uncompensated resistance was measured using the current interrupt method resulting in a resistance of 51 ohms. Using *iR* compensation it was possible to successfully compensate for 85 % of this resistance which resulted in comparable

peak separations and k^o values under both ideal and fuel cell conditions. The small deviations that remain are likely a result of the 15 % uncompensated resistance.

Analysis of the V_xPOMs under fuel cell conditions showed similar problems to those encountered in the $Fe(CN)_6^{3-/4-}$ system i.e. increase in peak to peak separation. Although *iR* compensation was successful and reduced peak separation, the peak to peak separation still remained in excess of 200 mV for all four systems as well as a minimal increase in peak current. A comparison of the peak currents obtained under ideal and fuel cell conditions (Figure 4.11) shows clearly that under fuel cell conditions the voltammetry of the V_xPOM systems are severely affected. This is measured by the ratio between the peak currents obtained at ideal and fuel cell conditions (*iR* compensated) with values of 250, 213,173 and 149 for the V_1, V_2, V_3 and V_4 respectively, with the 0.3 M V_4POM solution effectively producing less than 50 % of the expected current.

The effect of the increase in concentration was simulated; specifically the effect of free VO_2^+ species has upon the POM system. Here it was evident that at increased concentrations ([V_xPOM] = 0.1 M) the VO_2^+ distorts the CV, i.e. the VO_2^+ species is oxidising the reduced POM via equation 3.7 in Chapter 3. The presence of this species at high concentrations (> 0.2 M in both V_3 and V_4POMs) can have detrimental effects upon electrode kinetics as reported by Gattrell.[3,4] The work by Gattrell provides a basis for the observed behaviour in the V_xPOM as at the concentrations used under fuel cell conditions there are a number of redox systems working simultaneously at the electrode surface. The first is the V_xPOM, which is the main redox system of interest, and secondly given the high concentrations of VO_2^+ we have a separate vanadium system analogous to that used in the vanadium redox flow battery. The effects of the VO_2^+ species and its reduced form VO_2^0 in conjunction with the adsorbed POM layer (Figure 4.14) upon electrode kinetics have been studied. These two systems effectively form a potential blocking layer upon the electrode surface and reduce the potential experienced by the POM species near the electrode surface producing voltammetry resembling slower kinetics. This is observed by the drastic increases in overpotential required to drive the redox reactions in the V_4POM when compared to V_1. The incremental reduction of the V_xPOM systems highlighted a decrease in the overpotential required by each

individual POM system to drive the reaction in order to generate a specific current (Figure 4.27). This is attributed to a shift in the open circuit potential or equilibrium potential to a value more representative of the formal potential of the redox system. As well as a possible proton limitation, this is not observed under ideal conditions.

The traditional Tafel analysis proved inadequate for the V_xPOM system due to the extreme curvature making extrapolation for J_o highly problematic. 'Simply striking a line through, or at a tangent, to a non-linear line is not the best option and understanding the reason for the non-linear behaviour may be more beneficial'.[26] This statement by Walsh is very apparent to this work carried out consequently an alternative method for comparing the four V_xPOM catalysts was developed.

The V_4POM system was selected as the lead catalyst to take forward for further development. Although the V_1POM displayed the best electrochemical properties it was disregarded due to the one electron reduction of oxygen being thermodynamically unfavourable i.e. regeneration was not possible. The V_2POM was considered to be less effective than the V_3 and V_4 due to reduced concentrations of the V_2 and V_3 Keggins compared with the V_3 and V_4POM. The V_3 and V_4POMs both displayed very similar electrochemical properties; with the V_4 system having the most promise for improvement is selected in favour of the V_3POM system (Figure 4.11).

Further analysis of the V_4POM revealed that upon regeneration approximately 4% of the vanadium remains in the +4 oxidation state. This regenerated V_4 species appears to be more active than the fresh V_4POM. The overpotential needed to drive the redox reaction is lower in the re-oxidised species as one would expect given the decrease in OCP. However when comparing with the V_4POM in its 10 % reduced state we observed very similar overpotentials required to drive the reaction hence the shift in OCP is not the sole reason for the improved performance. In reference to the work by Poblet and co workers[31-33] the POM oxidised species favours the α isomer whilst the reduced species favours the β isomer. Whilst it was difficult to ascertain the change in isomeric forms from ^{31}P NMR, the single crystal structure did show clear differences. The regenerated V_4POM showed a vanadium capped Keggin structure with the metal centres surrounding the capped unit showing a more ordered structure

based on the partial occupancies indicating a preference for a specific orientation/isomer.

4.4 Experimental

4.4.1 Synthesis of $N_xH_3PMo_{12-x}V_xO_{40}$ Series

The synthesis of the V_xPOM series was analogous to the method given in Chapter 3 with the method repeated here for reference. Example based upon the synthesis of 500 ml 0.3 M $Na_4H_3PMo_8V_4O_{40}$:

Vanadium pentaoxide (54.56 g, 0.3 mol) was suspended in 275 ml distilled water in a 500 ml round bottom flask equipped with a magnetic stirrer bar heated to 60 ^oC. To the slurry, sodium carbonate (31.80 g, 0.3 mol) was added slowly due to liberation of carbon dioxide. Upon complete addition the slurry was heated to 100 ^oC and refluxed for 60 minutes. The solution was cooled to room temperature and approximately 3 ml of 30% hydrogen peroxide was added drop wise with stirring to oxidise residual V^{IV}. The solution was refluxed for a further 60 minutes to ensure completion conversion to the sodium vanadate and decompose residual hydrogen peroxide. Impurities were removed by filtration. The clear red sodium vanadate solution was returned the 500 ml round bottom flask to which molybdenum oxide (172.73 g, 1.2 mol) was added with stirring. The mixture was heated to 60 ^oC and 85% phosphoric acid (17.29 g, 0.15 mol) was added. The mixture was heated to 100 ^oC and refluxed for 5 hours. The mixture was cooled to room temperature and volumetrically diluted to 500 ml with distilled water.[34] For analysis the salt was isolated by evaporating to dryness (using a rotary evaporator) and twice re-crystallised from hot H_2O.

4.4.2 Crystal Data

Fresh V_4POM: Formula $H_{77}Mo_8O_{76}PV_4$, M = 2295.87 g•mol^{-1}, tetragonal space group *P*4/*mnc*, orange crystal, a = 12.6666(4) Å, c = 17.8332(13) Å, V = 2861.2(2) Å^3, Z = 2, ρ = 2.567 g•cm^{-3}, μ = 2.491 mm^{-3}, F(000) = 2160, crystal size = 0.12 × 0.08 × 0.04 mm^3, T = 100(2) K. 42026 reflections measured (1.97 < Θ < 34.96°), 3238 unique (Rint = 0.0478), 2632 observed ($I > 2\sigma(I)$), R_1 = 0.0733 for the observed and R_1 = 0.0875 for all reflections, wR_2 = 0.1828 for all reflections, max/min residual

electron density = 1.348 and -1.166 e•Å^{-3}, data / restraints / parameters = 3238 / 0 / 131, GOF = 1.162.

Re-oxidised V_4POM: Formula $H_{36.5}Mo_8Na_{3.5}O_{40}PV_4$, M = 1759.51 g•mol^{-1}, monoclinic space group P21/m, brown crystal, a = 11.4306(2) Å, b = 15.1678(3) Å, c = 13.5841(10) Å, β = 106.955(7)°, V = 2252.93(18) Å3, Z = 2, ρ = 2.594 g•cm^{-3}, μ = 3.102 mm^{-3}, F(000) = 1676, crystal size = 0.10 × 0.10 × 0.05 mm3, T = 100(2) K. 96846 reflections measured (1.86° < Θ < 40.00°), 14263 unique (Rint = 0.0313), 12726 observed (I > 2σ(I)), R1 = 0.0326 for the observed and R1 = 0.0384 for all reflections, *wR2* = 0.0811 for all reflections, max/min residual electron density = 2.743 and -1.341 e•Å^{-3}, data / restraints / parameters = 14263 / 0 / 387, GOF = 1.119.

4.4.3 Reduction of V_xPOM Series

Hydrazine hydrate is able to quantitatively reduce the V_xPOM series in a ratio 1: 4. The quantity of hydrazine hydrate required was calculated based upon the total vanadium concentration used in the synthesis of the respective V_xPOM. Table 4.6 illustrates the quantities of 40 % hydrazine hydrate needed for the successful reduction of specific quantities of vanadium in each of the respective POM systems. Diluted (40 %) hydrazine was used due to concentrated (80 %) hydrazine being too harsh at reducing the POM species, causing decomposition into its individual metal components. This was observed as black precipitates forming upon reduction.

Table 4.6: Quantities of 40 % hydrazine hydrate used to reduce 70 ml of the individual V_xPOMs to the desired redox state.

Percentage of [V] reduced	V_1 POM	V_2 POM	V_3 POM	V_4 POM
10 %	0.06 ml	0.13 ml	0.19 ml	0.27 ml
20 %	0.13 ml	0.26 ml	0.39 ml	0.53ml
30 %	0.19 ml	0.39 ml	0.69 ml	0.82 ml
40 %	0.26 ml	0.53 ml	0.79 ml	1.09 ml
50 %	0.33 ml	0.66 ml	0.99 ml	1.36 ml

The general procedure involved 70 ml of the V_xPOM being added to the jacketed RDE cell and heated to 40 ^{0}C whilst purged with nitrogen. The solution was purged with nitrogen for at least 15 minutes. The cell was sealed and a reflux condenser

added to ensure no evaporation of the POM solution. With vigorous stirring the required amount of hydrazine was added (sub-surface) and left stirring for 40 minutes whilst under a positive nitrogen pressure to ensure complete reduction. Upon completion the cell was both sealed and used within 30 minutes (if using for UV-Vis measurements). The three electrodes required for the RDE analysis were inserted and the electrochemical measurement carried out whilst maintaining a positive nitrogen pressure.

4.4.4 Electrochemical Methods

For consistency throughout all measurements used the same procedure outlined chapter 3, highlighted here for convenience.

Cyclic voltammetry: Measurements were carried out using a standard three electrode system consisting of a glassy carbon working electrode, a saturated calomel reference electrode and a platinum wire counter electrode. The working electrode was prepared by polishing with 3 and 1 micron diamond paste with sonication in distilled water between and after each polish. The reference electrode was cleaned with distilled water whilst the platinum wire was cleaned with piranha solution and flamed annealed to remove impurities. For CV analysis of the V_xPOM under fuel cell conditions, 10 ml of 0.3 M V_xPOM was placed into the cell and the electrodes connected to the potentiostat. Cyclic voltammetry was carried out within the potential range of 0 – 1.0 V vs. SCE with each CV initiated at the OCP measured prior to the analysis. The Autolab *iR* compensation module was used with the solution resistance calculated via the current interrupt method. A maximum of 85 % compensation was used.

Rotating disc analysis: A three electrode system was used consisting of a glassy carbon RDE working electrode, a saturated calomel reference electrode and a platinum wire counter electrode. The working electrode was again polished using 3 and 1 micron diamond paste with sonication between and after polishing. 70 ml of 0.3 M V_xPOM was added to the RDE cell and the electrodes connected to the potentiostat. A series of linear voltammograms were recorded at varying rotation speeds ranging from 500 to 5000 rpm within the potential range of 0 to 1.0 V vs.

SCE. The Autolab *iR* compensation module was employed; again a maximum of 85 % *iR* compensation was applied.

4.5 References

(1) Gattrell, M.; Park, J.; MacDougall, B.; Apte, J.; McCarthy, S.; Wu, C. *Journal of The Electrochemical Society* **2004**, *151*, A123.

(2) Gattrell, M.; Qian, J.; Stewart, C.; Graham, P.; MacDougall, B. *Electrochimica Acta* **2005**, *51*, 395-407.

(3) McCreery, R. L. *Carbon Electrodes: Structural effects on electron transfer kinetics*; Electroanalytical Chemistry; Taylor & Francis, 1990; Vol. 17, pp. 221 - 375.

(4) Bard, A.; Faulkner, L. *Electrochemical Methods: Fundamentals and applications*; 2nd ed.; Wiley, New York, 2000.

(5) Pletcher, D. *Instrumental Methods in Electrochemistry*; Horwood Pub Limited, 2000.

(6) Compton, R.; Banks, C. *Understanding Voltammetry*; World Scientific Publishing, 2007.

(7) Dickinson, E.; Limon-Petersen, J.; Rees, N.; Compton, R. *Journal of Physical Chemistry* **2009**, *113*, 11157 - 11171.

(8) Priyantha, N. *Journal of the National Science Council of Sri Lanka* **1997**, *25*, 193-202.

(9) Atkins, P.; Paula, J. *Physical Chemistry*; 8 ed.; Oxford University Press, 2006.

(10) Soestbergen, M. *Russian journal of electrochemistry* **2012**, 1-10.

(11) Timmer, B.; Sluyters-Rehbach, M.; Sluyters, J. *Surface Science* **1969**, *18*, 44-61.

(12) Britz, D. *Chemistry and Interfacial Electrochemistry* **1978**, *88*, 309-352.

(13) Deakin, M.; Stutts, K.; Wightman, R. *Journal of Electroanalytical Chemistry and Interfacial Electrochemistry* **1985**, *182*, 113-122.

(14) Atkins, P.; Paula, J. *Physical Chemistry*; W H Freeman & Company, 2006.

(15) Nambu, J.; Ueda, T.; Guo, S.; Boas, J.; Bond, A. *Dalton Transactions* **2010**, *39*, 7364.

(16) Li, C.; Zhang, Y.; O'Halloran, K. P.; Zhang, J.; Ma, H. *Journal of Applied Electrochemistry* **2009**, *39*, 421-427.

(17) Pope, M.; Muller, A. *Angewandte Chemie International Edition* **1991**, *30*, 34-48.

(18) Parasuraman, A.; Lim, T.; Menictas, C.; Skyllas-Kazacos, M. *Electrochimica Acta* **2013**, *101*, 27-40.

(19) Kear, G.; Group, S.; Shah, A.; Walsh, F. *International Journal of Energy Research* **2012**, *36*, 1105-1120.

(20) Freund, M.; Lewis, N. *Inorganic Chemistry* **1994**, *33*, 1638 - 1643.

(21) Chen, P.; McCreery, R. *Analytical Chemistry* **1996**, *68*, 3958-3965.

(22) Choi, S.; Kim, J. *Bulletin of the Korean Chemical Society* **2009**, *30*, 810-816.

(23) Kovács, I. *Journal of Physics: Conference Series* **2007**, *61*, 623-627.

(24) Tang, Z.; Liu, S.; Wang, E.; Dong, S. *Langmuir* **2000**, *16*, 4946-4952.

(25) Zhizhina, E.; Odyakov, F.; Matveev, K. *European Journal of Inorganic Chemistry* **1999**, 1009-1014.

(26) Kear, G.; Walsh, F. *Corrosion Materials* **2005**, *30*, 51-55.

(27) Fletcher, S.; Varley, T. S. *Physical Chemistry Chemical Physics* **2011**, *13*, 5359.

(28) Yuan, X.; Zeng, X.; Zhang, H.; Ma, Z.; Wang, C. *Journal of the American Chemical Society* **2010**, *132*, 1754-1755.

(29) Bhatta, S.; Guptaa, B.; Sethib, V.; Pandeyb, M. *International Journal of Current Engineering and Technology* **2012**, 219-226.

(30) Kozhevnikov, I. *Chemical Reviews* **1998**, *98*, 171-198.

(31) López, X.; Maestre, J. M.; Bo, C.; Poblet, J. *Journal of the American Chemical Society* **2001**, *123*, 9571-9576.

(32) López, X.; Bo, C.; Poblet, J. M. *Journal of the American Chemical Society* **2002**, *124*, 12574-12582.

(33) Selling, U.; Ume; Selling, A.; Selling, A.; Andersson, I.; Grate, J. H.; Pettersson, L.; Ingeg; Chemistry, A.; Andersson, A.; John; Chemistry, N.; Chemistry, I.; Pettersson, A.; Andersson, U.; Chemistry, J.; Pettersson, U. *European Journal of Inorganic Chemistry 2000*, 1509-1521.

(34) Grate, J. *Journal of Molecular Catalysis A: Chemical* **1996**, *114*, 93-101.

(35) Faulkner, R.; He, P. *Analytical Chemistry*, **1986**, *58*, 517- 523.

Chapter 5

Formulation and Development of the Lead catalyst: $Na_4H_3PMo_8V_4O_{40}$

Table of Contents

5.1 Nomenclature

During this chapter a series of compounds will be explored all of which have a complex molecular formula. For ease of reading the corresponding molecular formula will be abbreviated using the nomenclature outlined below:

$Na_4H_3PMo_8V_4O_{40}$ = **V_4POM,** $H_7PMo_8V_4O_{40}$ = **HV_4POM,** $H_{12}P_3Mo_{18}V_7O_{40}$ = **$HV_4(P_3V_7)$,** $H_{10}P_2Mo_8V_4O_{44}$ = **$HV_4(PO_4)$**, $H_7PMo_8V_4O_{40}(HBF_4)$ = **$HV_4(BF_4)$** and $H_7PMo_8V_5O_{45}S$ = **HV_4(VOS)**

5.2 Introduction

In the previous chapter we focused upon the electrochemical analysis of the V_xPOM series under the conditions adopted when the catalyst is used in the fuel cell. The effects of these conditions upon the catalyst performance were highlighted and ultimately the V_4POM ($Na_4H_3PMo_8V_4O_{40}$) was selected as the lead catalyst system. This chapter aims to build upon the understanding of the catalyst behaviour developed in both Chapters 3 and 4 and use this to develop and improve the lead system. In the first instance there are some fairly simple changes that can be made to the system to improve fuel cell performance. These will be considered first. The effect that the sodium cations have upon the system will be considered as work by Goodwin and co-workers have reported the detrimental effects of sodium and other alkali metal cations upon membrane conductivity.[1]A poorly conducting membrane will affect both the anode and cathode processes and ultimately a breakdown of the fuel cell altogether.[2] Ultimately lowering the resistance in the fuel cells individual components should improve the overall performance.[2] The general formation of the polyoxometalate involves simple oxoanions in the presence of a suitable heteroatom via a self-assembly process when acidified with a common mineral acid.[3-7] There are also specific methods which focus upon the synthesis of substituted polyoxometalates with the aim of incorporating transition metals into the Keggin structure via a lacuanry derivative. [3-7] Specific cases include vanadium substituted polyoxometalates and increasing the concentration of vanadium incorporated into the Keggin.[8-11] Odyakov et al. proposed new methods for the eco friendly synthesis of heteropoly acids which posess no alkaline metals and are highly substituted.[8] This

synthesis combines the replacement of alkaline metal cations with protons and the required increase in vanadium incorporated into the Keggin structure. This is the first step for improving the lead catalyst; however, by increasing the proton concentration we ultimately change the pH of the system which could possibly affect the electrochemical and catalytic properties of the catalyst.

The aim of this chapter is to develop the lead V_4POM catalyst to improve fuel cell performance. The initial aim is firstly to replace the sodium cations in the V_4POM system to reduce membrane resistance and try and improve the electrode kinetics. We also aim to clarify the effect that the reduced pH and increase in free vanadium concentration has upon the system. The main aim of this chapter is the formulation development of the HV_4POM system by a) addition of coordinating groups to hinder/diminish the oxidative properties of the VO_2^+ species. Vanadium can readily form stable coordinated complexes through the addition of ligands or dimerization.[12-15] Ligand substitution is a relatively easy and effective way to alter a metal centre's electrochemical properties.[16] Or b) employing Le Chateliers principle to shift the dynamic equilibrium and favour of the incorporation of free vanadium into the Keggin structure. Observing the dynamic equilibrium that is in play in the vanadium POM systems, it may be possible to increase or decrease the concentration of substituents within the system to change the position of equilibrium. The formulations will then be tested via RDE analysis and subsequently undergo extensive fuel cell testing at ACAL Energy.

5.3 Results and Discussion

5.3.1 $Na_4H_3PMo_8V_4O_{40}$ vs. $H_7PMo_8V_4O_{40}$

5.3.1.1 Structure and Speciation Comparison

In Chapter 3 (section 3.2.3) we established the complex equilibrium that exists in vanadium substituted polyoxometalates and the corresponding effects of pH and concentration. For the $H_7PMo_8V_4O_{40}$ (HV_4POM) under fuel cell conditions we still maintain the same 0.3 M concentration used in the $Na_4H_3PMo_8V_4O_{40}$ (V_4POM) system, however the pH of the two systems differs with pH values of 1.2 and 0.41

obtained for the V_4POM and HV_4POM systems respectively. These pH values correspond to an increase in $[H^+]$ from 0.063 M to 0.39 M for the respective V_4 and HV_4POM systems. Figure 5.1 shows FT- IR and Raman spectra of the V_4 and HV_4POM systems in there fresh state in the solid phase. Solid samples used in FT-IR and Raman measurements were dried in a desiccator for 24 hours prior to analysis.

The FT-IR spectra of the two systems in question here show similar characteristic bands that are associated with the Keggin structure. Bands at approximately 1050, 950, 890 and 760 cm^{-1} in both spectra are assigned to the P – O, M – O (where M = Mo or V), inter-octahedral and intra octahedral M – O – M vibrations. The bands located at approximately 1600 and >3000 cm^{-1} are a result of water within the coordination sphere.[17] The Raman spectra of the two systems both show bands at ~ 980, ~ 850 and ~ 700 cm^{-1} which are assigned to M=O, M – O – M (asymmetric) and M – O – M (symmetric) stretching (where M = Mo or V) which are again typical of the Keggin motif.[18]

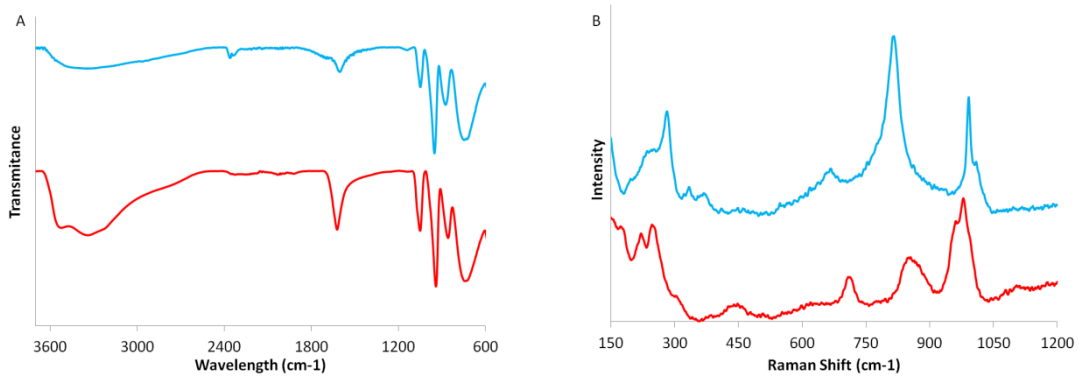

Figure 5.1: A) FT-IR spectrum of V_4POM (red) and HV_4POM (blue) B) Raman spectruma of V_4POM (red) and HV_4POM (blue).

The FT-IR and Raman spectra show that there is little difference between the physical structures of V_4 and HV_4POM. In addition X-ray analysis of the single crystal structure of HV_4POM (Figure 5.29) indicating that it is iso-structural to V_4POM. However, although the refined structure shows the same Keggin structure, its refined molecular formula is representative of the V_3POM ($Na_3H_3PMo_8V_3O_{40}$) as opposed to the V_4. The ^{31}P NMR of the HV_4POM (Figure 5.2, processed by Dr M. Herbet at ACAL Energy) demonstrates that the speciation of the HV_4POM (Table 5.1) shows an increase in the lower vanadium substituted Keggin species (V_1 and V_2,

-3.6 and *-3.4 – -3.1* ppm respectively) and a slight decrease in the higher substituted Keggin species (V_3 and V_4, *-2.9 – -2.3* and *-2.2 – -1.0* ppm respectively). This decrease in the concentration of highly substituted Keggin species results in an increase in the free vanadium (VO_2^+) present within solution.

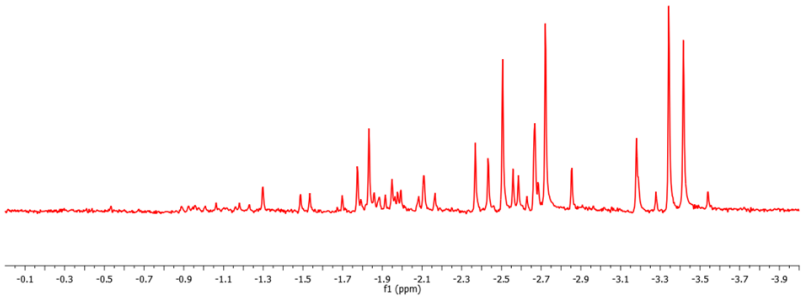

Figure 5.2: ^{31}P NMR of 0.3 M HV_4POM (aqueous) (pH = 0.42, 1 % H_3PO_4 as external reference).

Table 5.1: Speciation of the V_4 and HV_4POM 0.3 M systems based upon ^{31}P NMR. Speciation determined by Dr. M Herebt, ACAL Energy.

System	[V_1Keggin] M	[V_2Keggin] M	[V_3] M	[V_4] M	[Free V] M
V_4POM	1.1×10^{-3}	5.6×10^{-2}	1.2×10^{-1}	9.5×10^{-2}	3.5×10^{-1}
HV_4POM	3.9×10^{-3}	7.4×10^{-2}	1.1×10^{-1}	7.5×10^{-2}	4.1×10^{-1}

Based on the analysis above the two systems in question are similar in the respect that they both show complex equilibria of highly vanadium substituted polyoxometalates. The effect of decreasing pH upon the speciation of the HV_4PoM is evident with a decrease in the concentration of the V_3 and V_4 Keggin species, possibly the more reactive Keggin species towards oxygen reduction.[19] Secondly, and potentially most significantly, there is an increase in the concentration of free vanadium (VO_2^+) within the HV_4POM system. The increase in free vanadium indicates a shift in the equilibrium of the system resulting from a change in the preferential site of the vanadium when in the +5 oxidation state. Work by Lewis et al calculated equilibrium constants showing the preference of the free vanadium (VO_2^+) to be incorporated into the phosphomolybdic acid Keggin structure.[20] Using this same method (equation 5.1) we can observe the shifts in the equilibrium and ascertain in which system incorporation of the vanadium into the Keggin structure is preferred.

$$K = e^{\left(\frac{F}{RT}\right)\left(E_1^{o\prime} - E_2^{o\prime}\right)} \quad (5.1)$$

Where K is the equilibrium constant, $E_1^{o\prime}$ is the measured formal potential of the VO_2^+/VO^{2+} couple under these conditions and $E_2^{o\prime}$ is the measured formal potential of the V^{5+}/V^{4+} incorporated into the Keggin structure. For this method to be employed we first must ascertain the formal potential of the HV_4POM system under fuel cell conditions ($E^{o\prime}$).

5.3.1.2 Comparison of Cyclic Voltammetry Behaviour

When comparing the cyclic voltammetry behaviour of the V_4POM and HV_4POM system under both dilute and fuel cell conditions we observe very different results, especially under fuel cell conditions. First we will consider the question which arose with regards to the equilibrium constant of the VO_2^+ species in the two systems. Under dilute conditions (pH = 1), $E^{o\prime}$ = 0.389 vs. SCE for the vanadium redox couple when incorporated into the V_4POM Keggin structure and at pH 1, $E^{o\prime}$ = 0.636 vs. SCE for the VO_2^+/VO^{2+} redox couple when free in solution[a].

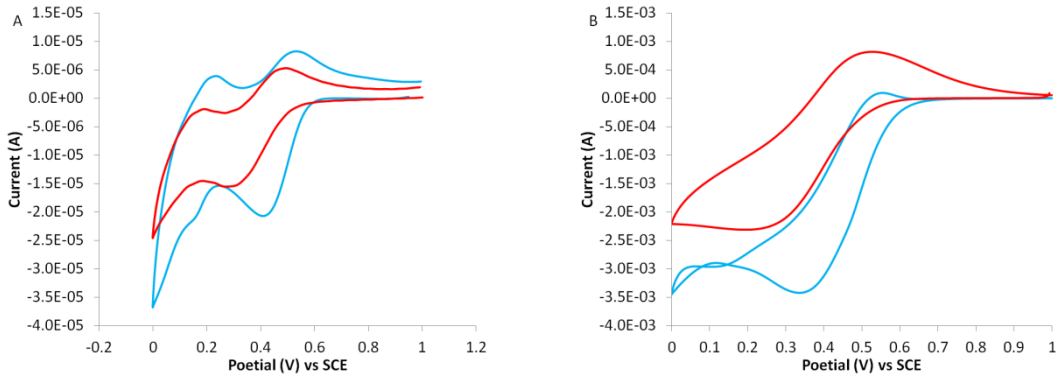

Figure 5.3: Cyclic voltammetry comparison of fresh V_4 and HV_4POM systems at GC electrode. A) V4POM (red): 0.001 M in 0.1 M $HClO_4$, pH = 1.12, ν = 0.04 V s^{-1}, HV_4POM (blue)L 0.001 M in 0.4 M $HClO_4$, pH = 0.42, ν = 0.04 V s^{-1}. B) V_4POM (red): 0.3 M no supporting electrolyte, pH = 1.1, ν = 0.04 V s^{-1}, HV_4POM (blue): 0.3 M no supporting electrolyte, pH = 0.4, ν = 0.04 V s^{-1}. CV's under fuel cell conditions have been run with 85 % IR compensation.

For the HV_4POM under dilute conditions (pH = 0.4) $E^{o\prime}$ = 0.48 and for the VO_2^+/VO^{2+} at pH 0.4 $E^{o\prime}$ = 0.706 V vs. SCE. The formal potentials for the V_4 and

[a] The change in formal potential was calculated using the Nernst equation under standard temperature conditions.

HV_4POM system were estimated from the CVs of the 0.001 M solutions assuming the mid potential in the CV is equal to the formal potential of the redox system. Under the respective dilute conditions we obtain equilibrium constants (*K*) of 1.50×10^4 and 6.61×10^3 M^{-1} for V_4 and HV_4POM respectively. This indicates an incorporation of the VO_2^+ into the Keggin is favoured in the V_4POM system more so than the HV_4POM which supports the speciation data in Table 5.1.[20] The same trend in *K* is observed under fuel cell conditions with values of 2.13×10^4 and 8.03×10^3 M^{-1} calculated for the V_4 and HV_4POMs respectively based upon the *iR* compensated CV data (Figure 5.3B)[b]. The larger negative shift in the formal potential of the VO_2^+/ VO^{2+} when incorporated into the V_4POM is a result of the shift in the equilibrium.[20]

Although the more positive formal potential of the vanadium redox couple in the HV_4POM does not favour incorporation of the vanadium metal centre (compared to the V_4POM), it does however, indicate the reduction is easier and occurs at a higher potential which is good for the fuel cell.[21] Consider Figure 5.3A which illustrates the CV behaviour of the V_4 and HV_4POM systems in the presence of supporting electrolyte. The reduction and oxidation peaks assigned to the vanadium redox couple incorporated into the Keggin occur at 0.28 and 0.49 V vs. SCE respectively for the V_4POM. The same corresponding peaks occur at 0.43 and 0.51 vs. SCE for HV_4POM system indicating a positive shift (by 150 mV) in the reduction potential. It was postulated in Chapter 3 that the negative shift in the formal potential of the V_4POM system compared to the other V_xPOMs was due an increase in the negative charge upon the Keggin. Here it is likely that we are observing a similar effect. A higher negative charge upon the Keggin results in much more difficult reduction, therefore the reduction potential is more negative.

The high negative charge is typical of the polyoxometalate compounds and results in an increase the negative charge density of the oxygen centres.[22,23] Previous work investigated the effects of the counter ion electronegatvitiy upon the reduction potentials of Keggin polyoxometalates.[24,25] These studies suggested that an increase

[b] The current interrupt method used in chapter 4 was employed again to calculate the uncompensated resistance in the HV_4POM. Applying a 1 mA cathodic current and observing the potential decay at the current interrupt an uncompensated resistance of 10.7 ohms was calculated.

in the counter ion electronegtivity leads to an decrease in the activation barrier for reduction of the polyoxometalate species, i.e. the reduction potential became less negative. The results from this work, shown in Figure 5.3A, are in agreement with previous results and show a more positive reduction potential when moving from the V_4 to HV_4POM due to the substitution of Na^+ counter ions with H^+. The electronegtivity of these two cations is 0.869 eV and 2.300 eV respectively. This same trend is also observed under fuel cell conditions (Figure 5.3B) however there is a distinct change in the CV for the HV_4POM. In the case of the V_4 and HV_4POM systems we can estimate based upon pH (0.44) that ~0.35 M of protons are dissociated in solution leaving 1.75 moles of protons to remain associated with Keggin structures. In the case of V_4POM the based upon pH (1.1) there is ~0.1 M of protons dissociated in solution leaving 0.5 M of protons to remain associated with the Keggin. Based on these values, the increased protons associated with the HV_4POM will reduce the overall negative charge leading to the positive shift in reduction potential.

For the HV_4POM, under fuel cell conditions, we observe a ~1 mA increase in cathodic current and a very low anodic current compared to V_4POM. Here the VO_2^+ concentration has a large impact on the observed electrode processes, as has been discussed in Chapter 4 (section 4.2.2.3, Figure 4.12). The pH of of the HV_4POM system shifts the E^o of the VO_2^+/VO^{2+} from 0.636 V vs. SCE observed in the V_4POM to 0.706 V vs. SCE in the HV_4POM. The combination of this positive shift in formal potential and the increase in $[VO_2^+]$ results in the oxidation of the reduced POM being dominated by the VO_2^+ species in solution (equation 5.2) as opposed to an electrochemical oxidation at the electrode surface (equation 5.3).

$$V_{POM}^{IV} + V_{Free}^{V} + 2H^+ \longrightarrow V_{Free}^{IV} V_{POM}^{V} \quad (5.2)$$

$$V_{POM}^{IV} \longrightarrow V_{POM}^{V} + e^- \quad (5.3)$$

The oxidation process outlined in equation 5.2 is hindered in the V_4POM due to the limitation of available protons shifting the equilibrium to favour the V_{POM}^{IV} based on Chatelier's principle.[26] It is also noted from Figure 5.3B that there is a decrease in

peak separation in the V_4 and HV_4POMs of 224 mV to 217 mV respectively. This indicates there may be an in electrode kinetics for the HV_4POM.

The effect of scan rate upon the HV_4POM system is minimal under both sets of conditions. Under ideal conditions at a scan rate of 0.04 V s^{-1} (Figure 5.3A) we observe a peak current (I_p) ratio of 0.3 and increasing the scan rate to 0.1 V s^{-1} results in a I_p ratio of 0.4. Under fuel cell conditions the observed I_p ratios for the two scan rates are 0.02 and 0.2 respectively. Under ideal conditions the peak current ratio for the HV_4POM system is comparable with that for the V_4POM system, however under fuel cell conditions the peak current ratio remains below 0.2. This suggests that the oxidation of the reduced HV_4POM is dominated by equation 5.2.

5.3.1.3 Comparison of Membrane Poisoning

The previous sections highlighted the changes in structure and speciation as well as changes in the basic electrochemistry of the V_4 systems. Here the effect on the membrane within the fuel cell will be investigated. It has been shown that the presence of not only sodium but other alkaline metals (Li^+, K^+ and Ca^{2+}) in trace amounts can have detrimental effects upon the proton conductivity of membranes, specifically in the liquid phase.[1,27-29] Okada et al. investigated the kinetics and transport properties of alkali metals as counter ions in various polyoxometalate structures and showed that conductivity decreases when protons are substituted for the afore mentioned metals. This is due to the alkali metal ions having a higher affinity for the sulfonic acid groups (SO_3^-) present in Nafion.[1,27-29] In the case of the V_4POM system when under fuel cell conditions (i.e. 0.3 M [POM]) there is also a high concentration of Na^+ present (approximately 1.5 M). When used inside the fuel cell the sodium becomes trapped inside the Nafion membrane, as illustrated in Figure 5.4.

The SEM images (Figure 5.4B and D) are taken of the cathode side which is not coated with Pt nanoparticles and show no signs of degradation even under the harsh conditions of the V_4 and HV_4POM catalysts. Energy dispersive X-ray spectroscopy (EDX) of the Nafion membrane samples shows an increase in the weight percentage

of sodium as the catalyst is pumped around the fuel cell for an initial 10 hours (Figure 5.4A) and secondly, for 3 consecutive days (Figure 5.4B).

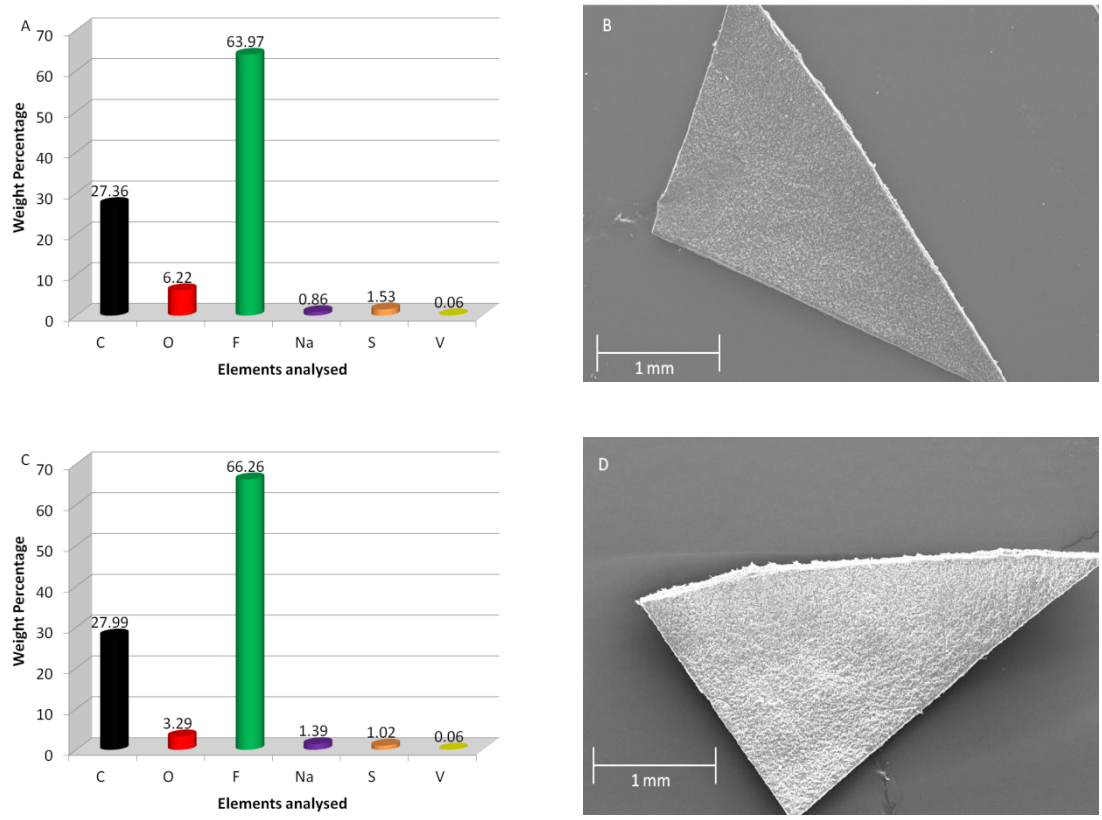

Figure 5.4: Analysis of Nafion membrane composition post fuel cell testing with V_4POM. A and C) Weight percentage of individual elements within the membrane composite after 10 hours and 3 days respectively. B and D) SEM image of membrane samples after 10 hours and 3 days respectively.

Substitution of the Na cations present in the V_4POM system with protons using the synthesis method proposed by Odyakov[8] results in a new V_4POM derivative, $H_7PMo_8V_4O_{40}$ (HV_4POM). Figure 5.5B shows the SEM image of the Nafion membrane after being used in the fuel cell and exposed to the HV_4POM. The small tear in the membrane is superficial damage likely caused during sample preparation. The EDX analysis (Figure 5.5A) shows that there is no sodium deposited within the membrane as expected. However, there is a significant increase the concentration of vanadium deposited in the membrane. The vanadium deposits are likely to be in the VO^{2+} state as multivalent cations have been shown to exchange more preferably with the polymer matrix and become 'trapped'.[27,29]

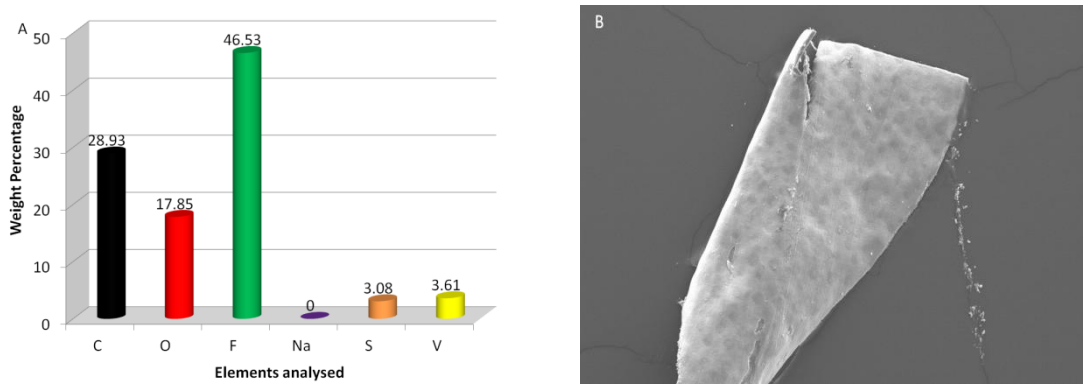

Figure 5.5: Analysis of Nafion membrane composition post fuel cell testing with HV_4POM. A) Weight percentage of individual elements within the membrane composite after 3 days. B) SEM image of membrane samples after 3 days.

We have seen from the results so far that substitution of the Na^+ ions with H^+ has overall had a positive effect resulting in a positive shift of the formal potential, increase in peak currents for the same potential and reduced solution resistance. The in-situ electrochemical impedance spectroscopy measured during fuel cell testing (see section 5.3.5) allows a comparison between the effects the systems have on membrane resistance. Although the HV_4POM system has successfully eliminated the Na^+ from the membrane there is a significant increase in the concentration of vanadium deposited within the membrane. The 'trapped' or 'blocking' vanadium could be in various states but likely to exist as the VO_2^+ species as mentioned previously which could have the same detrimental effects upon membrane resistance as the sodium cations.

Figure 5.6 shows the results obtained from electrochemical impedance measurements of the V_4 and HV_4POM system with a current of 0 amps being drawn from the fuel cell i.e. at a resting/standby state. Here an AC current signal (+/- 0.5 A) is applied to the system at a single frequency and the change in potential is measured, this measurement is then repeated for a series of frequencies ranging from 0.1 Hz to 20 kHz. It can be seen from the AC impedance plots (Figure 5.6) of the two POM systems that there is a loop situated at high frequencies with a slope of approximately 45^o in the lower frequency range. This indicates that the electrode process is controlled by both diffusion and the electrode kinetics.[21,30,31] Based on these plots the electrical equivalent circuit (Figure 5.7) for the system in question is based on the Randles circuit in the presence of a diffusion limitation.[21,30,31]

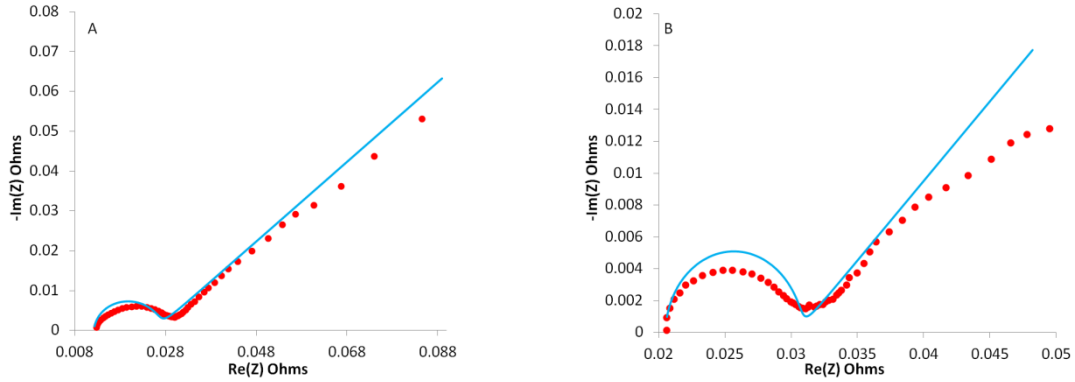

Figure 5.6: Electrochemical Impedance Spectroscopy (EIS) of A) 0.3 M V4POM (red: experimental, blue: fitted), B) 0.3 M HV_4POM (red: experimental, blue: fitted).

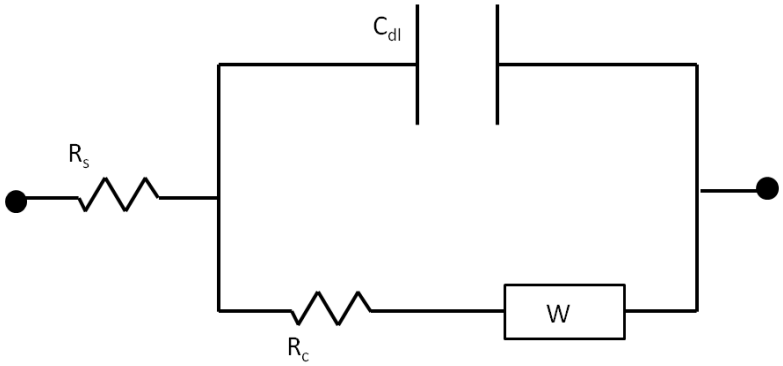

Figure 5.7: Equivalent circuit for the Ac impedance spectra of 0.3 M V_4POM and HV_4POM. R_s: solution resistance, R_c: charge transfer resistance, W: Warburg resistance and C_{dl}: capacitor.

Where R_s stands for the solution resistance in which the membrane resistance is incorporated, C_{dl} is the double layer capacitance connected in a parallel with the charge transfer resistance, R_c, which is represented by the semi-circle at lower frequency, W is the Warburg resistance which represents the resistance associated with the semi-infinite linear diffusion[21,30,31]. Simulation of the AC impedance based upon the proposed equivalent circuit allowed for data to be collected on the various components (Table 5.2).

Table 5.2 shows an increase in the value R_s for the HV_4POM compared to V_4POM. This is representative of an increase in membrane resistance caused by the incorporation of VO^{2+} cations. Interestingly, the results reveal a lower value of R_c for HV_4POM indicative of an improvement in electron transfer kinetics.

Table 5.2: Equivalent circuit parameters for the AC Impedance spectra of the 0.3 M V_4POM and HV_4POM systems.

System	R_s (ohms)	R_c (ohms)
V_4POM	0.012	0.013
HV_4POM	0.020	0.009

5.3.2 Fuel Cell Properties: Current vs. Overpotential

The alternative method developed in Chapter 4 ranked the performance of the individual catalysts using the overpotential required to generate the specific current densities. Figure 5.8A shows the comparison between the V_4 and HV_4POMs and clearly shows that at all measured currents the HV_4POM requires significantly less overpotential to drive the electrochemical reduction.

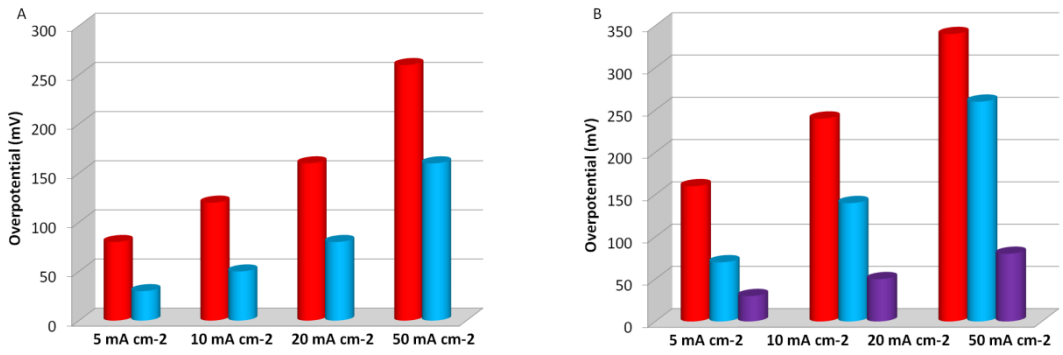

Figure 5.8: A) Comparison of overpotential required by the V_4 (red) and HV_4POMs (blue) to generate the desired current densities. B) Comparison of overpotential required by V_4 (red), HV_4 (blue) and V_1POM (purple) to generate desired current. Data here is normalised with respect to total vanadium concentration of V_1POM. Comparisons in both cases is based upon analysis carried out at 80 ^oC.

The overpotential required would have been expected to be comparable based on the theory of blocking layers postulated in Chapter 4. Furthermore, the HV_4POM would be expected to produce more blocking layers due to the increased concentration of free vanadium compared to V_4POM. However, this is not the case. A comparison between the V4, HV_4 and V_1POM systems shown in Figure 5.8B indicates that although there is a decrease in the required overpotential it is not significant enough to give comparable results with the V_1POM system indicating that a) the electrode kinetics in the HV_4POM are potentially slower compared to the V_1POM and b) a

blocking layer more substantial than that in the V_1POM may still be affecting the electron transfer process at the electrode surface.

If we consider the model proposed in chapter 4, Figure 4.14, it is apparent the free VO_2^+ species is not proving to be as significant to the blocking layer in the HV_4POM system. This is on the basis of the decrease in overpotential required to drive the reduction. The adsorbed POM layer on the electrode surface will remain and possibly increase in thickness and coverage under the increased acidic conditions,[32] which can hinder the electron transfer to solution based species.[33] Although this layer may increase, it does not block the electrode sufficiently enough to increase the overpotential to a magnitude comparable to the V_4POM and hence it is not the main contributor to the blocking effect. The final species to consider is the neutral intermediate formed during the reduction of VO_2^+ or dissociation of reduced vanadium from the Keggin structure prior to protonation (in both cases).[34] In the V_4POM analysis under fuel cell conditions there would be lack of protons available for step 2 in the reduction of VO_2^+ (equation 5.5)

$$[VO_2 \bullet 4H_2O]^+ + e^- \rightleftharpoons [VO_2 \bullet 4H_2O]^0 \quad (5.4)$$

$$[VO_2 \bullet 4H_2O]^0 + 2H^+ \rightleftharpoons [VO \bullet 5H_2O]^{2+} \quad (5.5)$$

However in the HV_4POM the lower pH, and hence increased $[H^+]$ results in the intermediate vanadyl species being readily protonated minimising the $[VO_2^0]$ at the electrode surface. This leads us to believe that the VO_2^0 is the main contributor to the blocking effect at the electrode surface. Figure 5.9 illustrates a schematic diagram of the proposed model. Here we see that a decrease in the $[VO_2^0]$ effectively makes the electrode surface more accessible to POM species (Figure 5.9A). As a result the redox molecules can experience a potential much closer to that applied at the electrode. Combining this model with the positive shift in the reduction potential results in an increase in electrode kinetics observed for the HV_4POM when compared to with the V_4POM system. Also, a higher $[H^+]$ means the voltammetry is less proton limited for the HV_4POM than V_4POM as well as the HV_4POM system consisting of species with higher D_o values will improve the apparent observed kinetics.

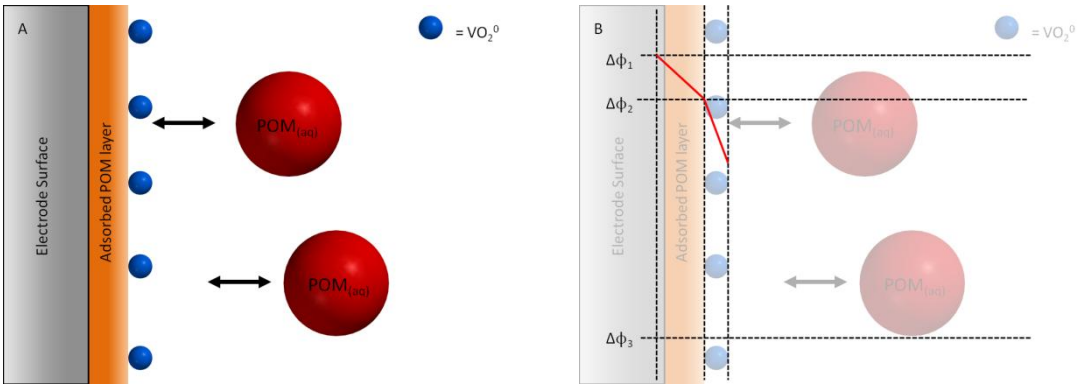

Figure 5.9: A) Model for the electrode solution interface for the HV_4POM systems. B) Overlay of proposed change in the applied potential at the electrode surface across the absorbed/ blocking layers

5.3.3 Regenerated HV_4POM

The V_4POM system showed that upon regeneration of the reduced POM system (by bubbling with air) the OCP never returned to that of the fresh POM indicating that a small quantity of vanadium remained in the +4 oxidation state. Based on the non-linear fit it was calculated that approximately 3.3 % of the vanadium was not regenerated (based on lab analysis)[c]. The same analysis carried out on the HV_4POM system showed a dramatic increase in the percentage of vanadium that remained in the +4 oxidation state (Figure 5.10). The OCP of the regenerated HV_4POM is 0.54 V vs. SCE which corresponds to approximately 28 % of the total vanadium remaining in the +4 oxidation state which is a dramatic increase compared to the V_4POM. It was believed that the method used for regeneration of the POM in the lab was insufficient to fully regenerate the POMs in question. The regeneration process within the actual fuel cell is optimised to increase the surface area of the POM | air interface (see section 5.3.5 for complete fuel cell testing details). The regeneration of the POM occurs at the liquid | air interface[7] and increasing the surface area of this interface effectively aids the regeneration process. Figure 5.11 shows the regeneration profiles of the HV_4POM (red) and V_4POM (blue) in the FlowCath®

[c] The lab based regeneration involved a 70 ml sample of the POM in question being placed in the RDE thermal jacket cell and reduced to a 50 % state, i.e. 50 % of the total vanadium concentration. was in the +4 oxidation state. This was carried out via the hydrazine method outlined in chapter 4. The POM sample was then bubbled vigorously with O_2 for 1 hour at 80 ^oC at which point the OCP was measured .

fuel cell system, i.e. the change in OCP with time whilst bubbling with air. The regular peaks observed in the regeneration profiles are due to the 'anode recovery purge' which needs to be performed regularly to remove water on the MEA. Previous experiments at ACAL have shown that false OCP readings can be obtained without regular purging during the regeneration profiles.

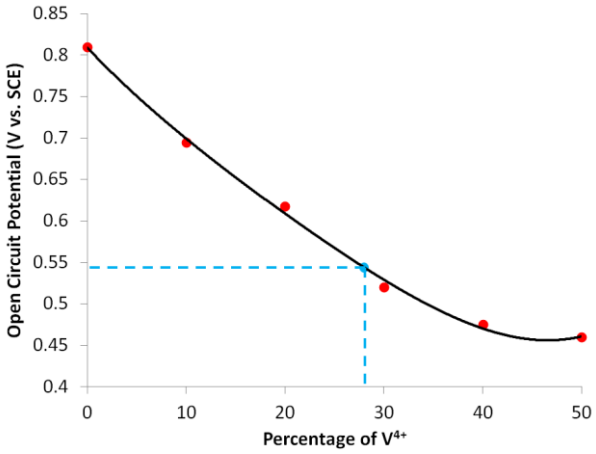

Figure 5.10: Change in OCP with increasing V^{4+} percentage for the HV_4POM showing a polynomial fit. Blue line shows extrapolation of residual V^{4+} percentage in the re-oxidised HV_4POM system based on measured OCP.

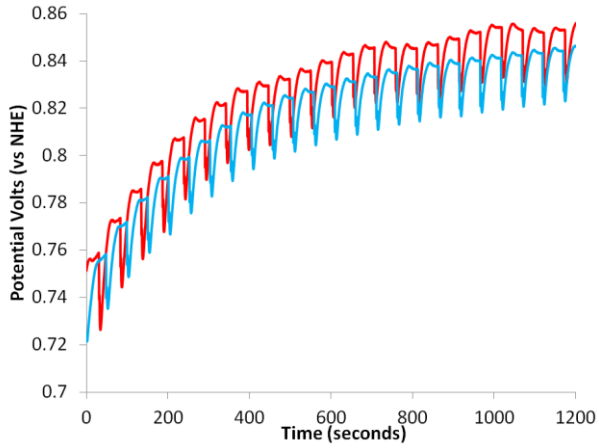

Figure 5.11: Regeneration profile of the HV_4POM red and V_4POM blue in the FlowCath® fuel cell system at 80°C, air flow 1.5 L min^{-1}, H_2 flow 1 L min^{-1}, POM flow 1.25 L min^{-1} with an air purge every 50 seconds.

After approximately 15 minutes (1000 seconds) we observe a plateau in the OCP indicating the POM has reached its maximum oxidation with OCP values of 0.84 and 0.85 V (~0.59 and ~0.60 V vs. SCE) for the V_4 and HV_4POM respectively. Given the

reaction at the anode is hydrogen oxidation on Pt, the potential of the anode is approximately 0 V vs. NHE. Based upon the polynomial fits for OCP this equates to approximately 4 % of the total vanadium remains in the +4 oxidation state in the V_4POM which is analogous to the result obtained for lab based regeneration. However for the HV_4POM the OCP after fuel cell re-oxidation equates to approximately 21.5 % of the total vanadium remaining in the +4 oxidation state. This shows that a) The HV_4POM does not regenerate as 'much' as the V_4POM and b) the lab based regeneration method is less optimised than the fuel cell regenerator. It is clear that the regeneration of the HV_4POM is poor, due to a fully regenerated sample remaining significantly reduced compared to the fresh (fully oxidised) sample. This is likely due to the stability of the free VO^{2+} ion in acidic media. Analysis of the POM in this state will likely yield results similar to that expected for incremental reduction, i.e. a decrease in the overpotential due to a shift in the OCP of the system. Ideally the system would need to be regenerated so that the percentage of vanadium in the +4 oxidation state is comparable with the regenerated V_4POM to prevent an unfair comparison between the two regenerated systems.

Further testing at ACAL Energy showed a development in the regeneration process. The ongoing development of a HTHP (High temperature and High Pressure) fuel cell proved beneficial for the HV4POM system. Here the regeneration process was vastly improved and efficiency increased resulting in improved overall performance. Figure 5.12 shows test data for the HV4POM using the HTHP test rig. It can be seen that when comparing the two regeneration profiles, although similar OCP values are achieved after regeneration, the time taken to reach this is drastically reduced.

Although the higher temperature and pressure are more favourable conditions for the HV_4POM this is a separate ongoing development project within ACAL Energy. All previous analysis under fuel cell conditions has been done at 80 ^{o}C and ambient pressure, the aim here is to develop and improve the HV_4POM system based upon these conditions rather than the elevated temperature and pressures.

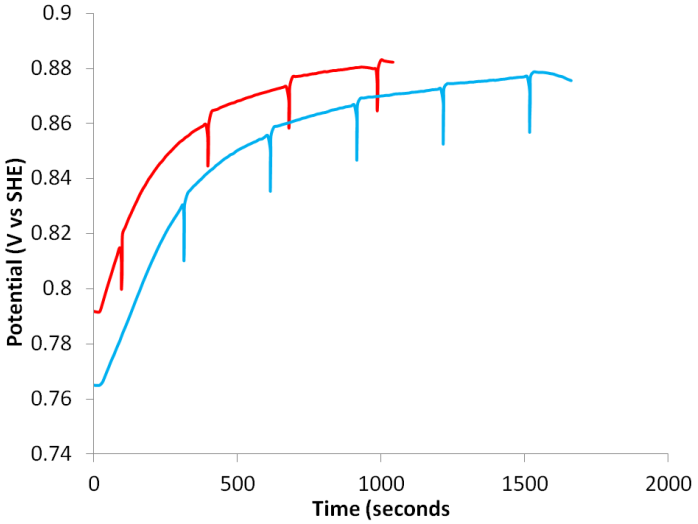

Figure 5.12: Regeneration profiles for the HV_4POM under fuel cell conditions (blue) and under HTTP conditions (red). For HTTP, temperature = 110 ^{o}C and pressure = 2 bar

5.3.4 Formulation Development

5.3.4.1 $HV_4(PO_4)$: Eliminating the Effect of the VO_2^+ Cation

Throughout this work there have been various issues/phenomena that have resulted in a hindrance upon the electron transfer. In nearly every case the root of the problem can be traced back to the presence of the free VO_2^+ species in solution. $VO_2^+{}_{(aq)}$ leads to the formation of blocking layers or oxidiation of the reduced V_xPOM species as well as limiting O_2 reduction during the regeneration. Successfully reducing the $[VO_2^+]$ or reducing its oxidative power could lead to improvements in the overall catalytic performance but would lower the OCP which is not ideal on the basis of fuel cell performance.

Work by Odyakov proposed a new method for the synthesis of high vanadium containing heteropoly acid composites that were stable up to 170 ^{o}C.[9] The presence of excess H_3PO_4 was used to stabilise the vanadium species in solution and during synthesis.[9] Synthesis of $H_{12}P_3Mo_{18}V_7O_{85}$ ($HV_4(P_3V_7)$) was carried out according to literature with, ^{31}P NMR and speciation analysis carried out by Dr M. Herbert at ACAL energy. The speciation of the $HV_4(P_3V_7)$ system (Table 5.2) was not as expected with a significant concentration of free vanadium still present in solution.

Table 5.3: Estimated concentrations of individual Keggin species in the $HV_4(P_3V_7)$ system. Sample measured at a POM system cocentration of 0.3 M

System	[V_1Keggin]	[V_2Keggin]	[V_3Keggin]	[V_4Keggin]	[Free V]
$H_{12}P_3Mo_{18}V_7O_{85}$	0.029 M	0.19 M	0.20 M	0.16 M	0.42 M

The increase in free vanadium accompanied with a decrease in pH (pH = 0.04) is the opposite of what was trying to be achieved. By decreasing the pH to ~0 we effectively shift $E^{o'}$ of the VO_2^+/VO^{2+} to 0.75 V vs. SCE further increasing the oxidising ability of the VO_2^+ species. Also if we assume the $HV_4(P_3V_7)$ adopts a similar formal potential to the HV_4POM system then we observe an increase in the equilibrium constant K (5.2×10^4) indicating a preference for the vanadium to be incorporated into the Keggin when in the +5 oxidation state. Although the work by Odyakov shows that the presence of excess phosphoric acid may stabilise the higher substituted Keggin species, there still remains large quantities of free vanadium.

Employing the ideas presented in Odyakov's work, we observed the effects of adding stoichiometric amounts of H_3PO_4 (post synthesis) to the HV_4POM system. The aim here being to either stabilise the present system by either a) increasing the concentration of the individual Keggin species or b) stabilise the free vanadium preventing oxidation of the reduced POM. Work by Kogerler has also shown that the PO_4^{3-} ion can mediate the assembly of polyoxometalates.[35] This is important as the reduced Keggin is the key species in the oxygen reduction reaction.[4] We have already observed the possibility of point (a) in the $HV_4(P_3V_7)$ system, but with vanadium phosphate complexes readily synthesised under the conditions employed,[13] the oxidative capabilities of the VO_2^+ species maybe hindered.

Figure 5.13 shows the effect of the addition of increasing molar ratios of H_3PO_4 to fresh 0.3 M HV_4POM. The solid black line indicates the peak anodic and cathodic currents obtained for the V_4POM system and is shown for comparison purposes. Figure 5.13A shows a decrease in the peak anodic current (measured at the potential of the V^{IV}/V^V redox couple when incorporated into the Keggin) with increasing phosphoric acid. This is can be due to a number of reasons a) the increased tendency for dissociation of the V^{IV} centre from the Keggin due to the increase in negative

charge of the Keggin,[23,36] b) increase in ionic radii[37] of the V^{4+} centre decreasing its stability within the Keggin and c) the stability of free VO^{2+} increases under the conditions employed.[38] Interestingly the cathodic current also decreases with increasing H_3PO_4 concentration (Figure 5.13B).

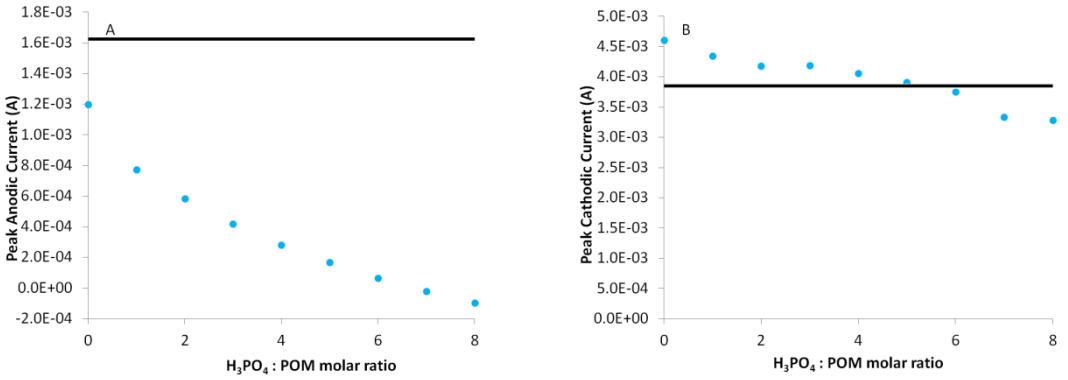

Figure 5.13: A) Peak anodic currents obtained from CV analysis of HV_4POM with increasing H_3PO_4 concentration. B) Peak cathodic currents obtained from CV analysis of HV_4POM with increasing H_3PO_4. CV analysis carried at a GC electrode with a constant [POM] = 0.3 M. Scan rate = 0.1 V s^{-1}.

The low I_p current ratio observed in the HV_4POM was due to the dramatic increase in I_p^c as a result of equation 5.2 (oxidation of reduced POM via free vanadium), the positive shift in $E^{o'}$ and the increase in D_o obtained via simulation analysis. If we consider the CV of 0.1 M $VOSO_4$ in 0.1 M H_2SO_4, pH = ~0.8 (Figure 5.14A), here we see the electrochemically irreversible oxidation of the VO^{2+} (E_p^a = 1.30 V vs. SCE) which is in agreement with results reported in literature.[39]

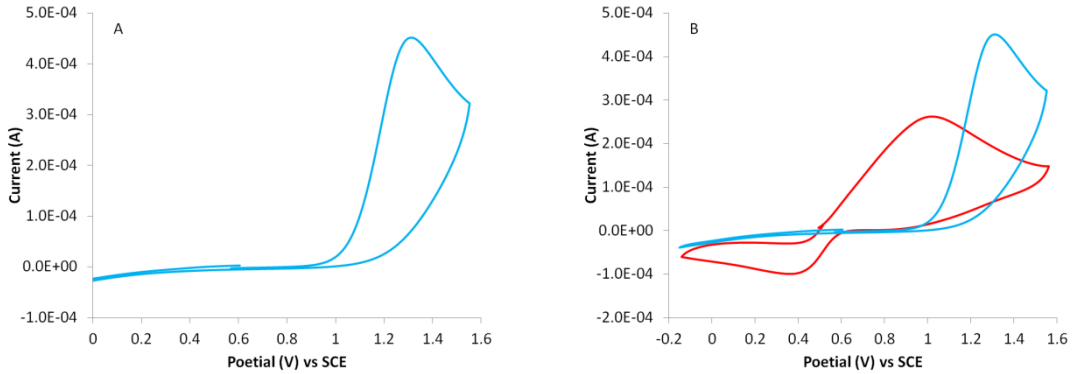

Figure 5.14: A) CV of 0.1 M $VOSO_4$ in 0.1 M H_2SO_4 at a GC electrode, pH = 1, v = 0.04 V s^{-1}. B) CV of 0.1 M $VOSO_4$ in 0.1 M H_3PO_4 at a GC electrode, pH = 1.61, v = 0.04 V s^{-1}. Both CVs run at standard pressure and temperature and degassed with N_2.

Under these conditions (relatively low concentrations of vanadium and sulphate species) there is little complexation between the VO^{2+} and SO_4^{2-} hence the redox process observed is solely based upon the VO^{2+} species. Figure 5.14B shows the comparison of the redox process shown in Figure 5.14A with 0.1 M $VOSO_4$ in 0.1 M H_3PO_4, pH = 1.6 (E_p^a = 1.01 V vs. SCE).

In the presence of H_3PO_4 the $VOSO_4$ system shows an improvement in its electrochemical reversibility with a peak observed at ~0.4 V vs. SCE, as well as a negative shift in E_p^a. Here we are possibly observing a complexation between vanadium and the phosphate ion ($H_2PO_4^-$) which are synthesised under the conditions and ratios used under fuel cell conditoins,[13] here the shift in oxidation potential indicates that the vanadium phosphate complex could be more stable when in the +5 oxidation state (vanadium). This shift in E_p^a also indicates a possible decrease in the oxidative capabilities of the VO_2^+ species, hence it is less likely to oxidise the reduced POM species. The presence of vanadium phosphate species is evident with precipitation of an insoluble green solid after being stagnant for 24 hours when more than 1 molar equivalent (0.3 M H_3PO_4) is added to the HV_4POM system. ICP analysis of the green precipitate shows the main constituents to be phosphorus, molybdenum and vanadium with weight percentages of 21.45, 25.2 and 39.1 % respectively with ^{31}P NMR of the solid not representative of any POM species. Due to the potential damage caused by precipitation of solid material whilst in the fuel cell, it is decided only 1 equimolar amount of H_3PO_4 should be used in HV_4POM. Interestingly, 1 equimolar amount introduces an extra 0.3 M H_3PO_4 which is slightly less than the concentration of free vanadium, above this concentration it is possible that the solution becomes saturated and induces precipitation. For clarification the 0.3 M HV_4POM with 1 equivalent of H_3PO_4 is the chosen formulation and labelled '$HV_4(PO_4)$'.

Comparison of the overpotentials required by the HV_4POM and $HV_4(PO_4)$ systems yields interesting results (Figure 5.15). At all currents used during the analysis the newly formulated $HV_4(PO_4)$ requires much larger overpotentials to drive the reaction (Figure 5.15A). This at first seems to demonstrate a decrease in the overall catalytic performance of the formulation, but a consideration of the systems equilibrium position must be taken. The CV analysis of the HV_4POM showed that there was a

drastic increase in the cathodic current accounted for by the assumption of equation 5.2, positive shift in $E^{o'}$ and an increase in D_o. By introducing excess phosphoric acid, hence formation of vanadium phosphate complexes, we are potentially hindering the homogenous oxidation of the reduced POM. However, we are hindering an electrode processes that is believed to contribute to the increased cathodic current observed in the HV_4POM. It is also a possibility that the formation of vanadium phosphates decrease the D_o for HV_4POM due to their decreased solubility.[40] This is observed in Figure 5.15B where the cathodic current of the $HV_4(PO_4)$ is less than the respective HV_4POM.

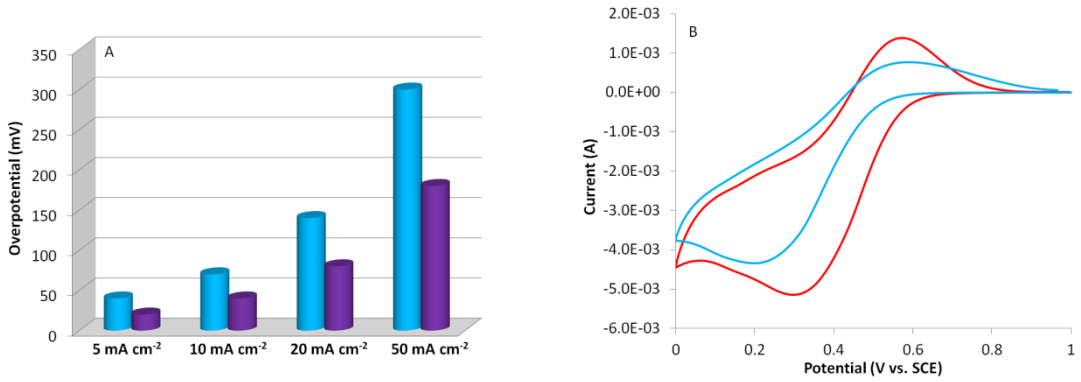

Figure 5.15: A) Comparison of overpotential required to generate a range of current densities used during analysis for HV_4POM (Purple) and $HV_4(PO_4)$ Blue. B) CV of 0.3 M HV_4POM pH = 0.45 (red) and CV of 0.3 M $HV_4(PO_4)$ pH = 0.4 (blue) at a GC electrode, v = 0.1 V s^{-1}. CVs measured and room temperature.

The decrease in the anodic current of the phosphoric acid formulation ($HV_4(PO_4)$) is a likely consequence of the reduced cathodic current and dissociation of V^{4+} from the Keggin. It is also apparent that there is an increase in peak separation from 273 mV (HV_4POM) to 336 mV ($HV_4(PO_4)$) which could represent slower electrode kinetics, or this increase could be due to the vanadium phosphate complexes adding to the blocking effect at the electrode surface. Commonly phosphates show a lower solubility in water.[40] It is unlikely that it is due to an increase in solution resistance (although solution conductivity does decrease from 218 mS cm^{-1} for HV_4POM to 207 mS cm^{-1} for $HV_4(PO_4)$) as this would be compensated by a decrease in the current generated. Based upon these results it is believed that the introduction of the phosphoric acid has shown the desired effect of hindering the oxidative capabilities of the VO_2^+ species. However there appears to be a decrease in electrochemical

performance based upon increases in overpotential to drive the electrochemical reduction and decreases in anodic current. The true extent of the potential benefit of this formulation can only be confirmed through fuel cell testing (section 5.3.5).

5.3.4.2 $HV_4(BF_4)$: Tetrafluoroborate vs. Phosphate

Vanadium phosphate complexes have been studied previously.[13,40] Section 5.3.4.1 demonstrated the effect of this complexation upon the oxidation potential of the vanadium +4/+5 redox couple and its potential benefits/stumbling blocks upon fuel cell performance. The complexation of VO_2^+ with dihydrogen phosphate showed a large shift in E_p^a with regards to the oxidation of the VO^{2+} species which favours the vanadium to be in the +5 oxidation, which consequently also favours incorporation into the Keggin structure. However this had unfavourable effects upon the overpotential required to drive the electrochemical reduction of the POM structure due to either:

1) The removal of the mediated reduction of free VO_2^+, one of the potential process relating to the increase in cathodic current in the HV_4POM
2) The presence of poorly soluble vanadium phosphate or other phosphate derivatives in solution adding to the blocking effect at the electrode surface.

Substitution of the phosphate ion with the weakly co-ordinating tetrafluoroborate ion[41] may result in a 'middle ground' between the HV_4POM and $HV_4(PO_4)$ systems. The aim here is to maintain the hindrance of the VO_2^+ oxidation of the reduced POM whilst limiting the increase in overpotential needed to drive the electrochemical reduction. Limiting the increase in overpotential is based upon tetrafluoroborate 'salts' having a greater solubility than the corresponding phosphates.

Figure 5.16 shows the effect of the addition of equimolar amounts of HBF_4 upon I_p^a and I_p^c, again the solid black line represent the peak currents associated with the V_4POM system. With increasing addition of HBF_4 to the HV_4POM system we observe an increase in anodic current with successive additions of HBF_4 up to three

molar equivalents, with respect to POM concentration, after which the peak current decreases with each further addition.

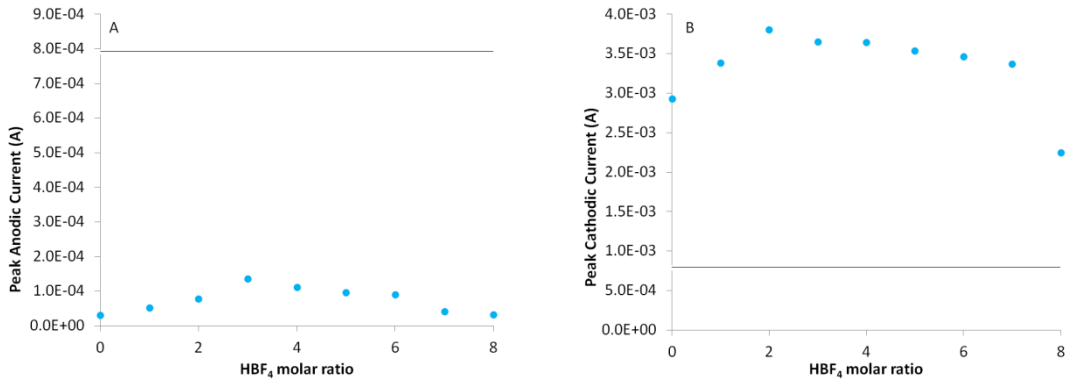

Figure 5.16: A) Dependence of I_p^a upon successive additions of equimolar amounts of HBF_4. B) Dependence of I_p^c upon successive additions of equimolar amounts of HBF_4. [POM] constant at 0.3 M. CV analysis run carried out at a GC electrode at room temperature, v = 0.04 V s^{-1}.

The same trend is observed in peak cathodic current with I_p^c reaching a maximum after two molar equivalents of HBF_4 have been added; however in both cases the peak currents do not match those obtained for the V_4POM system. The increased solubility of the tetrafluoroborate and its salts (compared to the phosphates) is evident here with no precipitation of solid in any of the formulations after remaining stagnant for a period of 24 hours. Insoluble solids were only detected when 12 ml of concentrated HBF_4 was added to a 10 ml aliquot of 0.3 M HV_4POM.

Figure 5.17A shows the cyclic voltammetry of the HV_4POM system with 0, 1, 2 and 3 equimolar amounts of HBF_4. We observed the effect on I_p in Figure 5.16, here we observe the effects upon E_p^a and E_p^c with a positive shift in both when 2 and 3 equivalents are added. The positive shift in potential is associated with increased $[H^+]$ and its association with the Keggin structure as discussed previously. This shift can also be caused by a change in thermodynamics with the increase in $[H^+]$.[24,25] Similar behaviour is observed for the $HV_4(PO_4)$ system although the shift was not of the same magnitude. This could be due to the strength of the respective acids with HBF_4 being deemed a strong acid and fully dissociates. There is a general decrease in peak separation from the 217 mV in the HV_4POM to 224, 188 and 187 mV for the addition of 1, 2 and 3 equivalents of HBF_4 respectively. Each addition also increases the solution conductivity to 273, 293 and 345 mS cm^{-1}

respectively. Although there will be an apparent decrease in the solution resistance, the magnitude of the currents generated remain high thus uncompensated solution resistance would still be a factor.

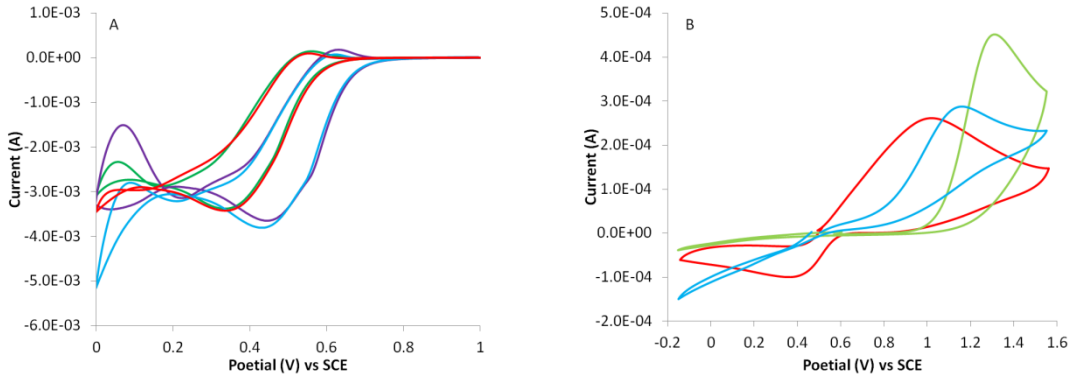

Figure 5.17: A) Change in the cyclic voltammetry behaviour of HV_4POM with successive addition of HBF_4 whilst maintaining a constant [POM] equal to 0.3 M. Red; 0.3 M HV_4POM pH = 0.45, Green; HV_4POM + 1 equivalence of HBF_4 pH = 0.4, Blue; 0.3 M HV_4POM + 2 equivalences of HBF_4 pH = 0.32 and Purple; HV_4POM + 3 equivalences of HBF_4 pH = 0.2. Analysis carried out at a GC electrode at room temperature. B) CV of 0.1 M $VOSO_4$ in 0.1 M H_2SO_4 pH =1 (green), 0.1 M H_3PO_4 pH = 1.61 (red) and 0.1 M HBF_4 pH = 1 (blue) at a GC electrode, v = 0.04 V s^{-1}. CVs measured and room temperature and under N_2.

The decrease in peak separation is more likely a consequence of a) increased solubility of the tetrafluoroborates[41] not contributing to the blocking layer at the electrode surface, b) voltammetry is less proton limited at higher $[H^+]$ and c) the speciation of the system may change upon addition of acid resulting in increases in the concentration of species with higher D_o.

On this basis the HV_4POM with 2 or 3 equivalents of HBF_4 would appear to be the ideal formulation. But a careful consideration of the possible effects when used in the fuel cell needs to be taken into account, as these formulation will taken forward for fuel cell testing. On this basis the HV_4POM with 1 equivalence of HBF_4 will be taken forward as the selected formulation and labelled $HV_4(BF_4)$. If this formulation shows improved performance then further additions can be considered.

Figure 5.17B shows the CV behaviour of 0.1 M $VOSO_4$ in 0.1 M H_2SO_4 ,pH 0.08 (green), H_3PO_4 pH 1.6 (red) and HBF4 pH 1 (blue). We discussed previously the difference in complexation of sulphate, and phosphate with vanadium at the given concentrations leading to the changes in CV behaviour. Tetrafluoroborates are

weakly coordinating ligands and are likely to have less an interaction with the vanadium compared to the phosphates. This is evident when comparing the CV behaviour with respect to E_p^a for the oxidation of VO^{2+} species. E_p^a shifs to 1.15 V vs. SCE when in HBF_4 compared to 1.30 V vs. SCE when in 0.1 M H_2SO_4 and 1.01V vs. SCE when in 0.1 M H_3PO_4. The fact the electrode kinetics for the VO_2^+ oxidation appear faster in HBF_4 than in H_2SO_4 suggest VO_2^+ is complexed in some way to HBF4, where we know from literature that sulphate does not interact with VO_2^+. Likewise, the fact that the VO^{2+} oxidation kinetics appear even faster in H_3PO_4 suggests that the level of complexation is higher in H_3PO_4 than HBF_4. It follows, the complexation may hinder the oxidative capacity of VO_2^+ effectively reducing the concentration of free VO_2^+

Figure 5.18 compares the overpotential required to generate the desired currents under analysis. The $HV_4(BF_4)$ system shows a relatively small improvement in comparison with the HV_4POM with comparable overpotentials of 20 and 40 mV required to generate current densities of 5 and 10 mA cm^{-2}, respectively. Only at higher current densities do we observe an improvement with the $HV_4(BF_4)$ requiring smaller overpotentials of 70 and 160 mV compared with 80 and 180 mV for the HV_4POM to generate 20 and 50 mA cm^{-2} respectively.

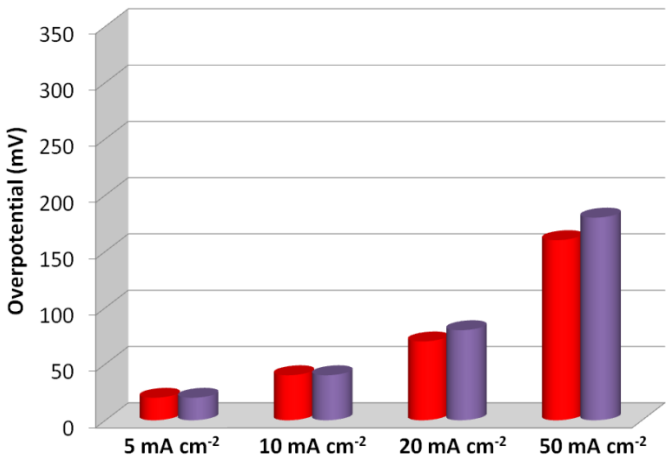

Figure 5.18: Comparison of overpotential required to generate the desired currents used during analysis for HV_4POM (Purple) and $HV_4(BF_4)$ red. Based on RDE data obtained at GC electrode at 80°C.

The general decrease in overpotential can be due to a number of reasons. These include the decrease in solution resistance and also a decrease in the surface blocking effect, resulting from the (weak) coordination of BF_4^- with VO_2^+.

5.3.4.3 HV_4(VOS): Shifting the Dynamic Equilibrium

So far the formulations have focused upon trying to manipulate the activity of the VO_2^+ with regards to its oxidative power through complexation with various ionic species (BF_4^- and $H_2PO_4^-$) or to remove it from the system completely. Here we adopt a very different (radical) method to shift the dynamic equilibrium and to force the incorporation of the 'free' vanadium into the Keggin, more specifically reduced solution based free vanadium (VO^{2+}). If we consider equation 5.6, which is a basic illustration of the dynamic equilibrium that is in place in any HV_xPOM system, we can see that there is a constant dissociation and re-association of the vanadium centres within the Keggin structure.[3,4,42] The dissociation of the vanadium could be due to the natural equilibrium in place for vanadium substituted polyoxometalates which is a result of the low stability of highly substituted POMs. [3,4,42] Or it could be due to the reduction of a vanadium centre incorporated in the Keggin which is unstable due to the increase in ionic radii. [37]

$$HV_xPOM \rightleftharpoons HV_{x-z}POM + Z\,V^{+\backslash 2+} \qquad (5.6)$$

If we now consider the equilibrium law, also known as Le Chatelier's principle, we can identify changes to the system that will shift the equilibrium to the left favouring incorporation of vanadium into the Keggin. Chatelier's principle states that:[26]

'When a chemical system is a at equilibrium and is subject to a change in temperature, partial pressure, volume or concentration the equilibrium of said system will shift to minimise the effect of the changed variable and establish a new equilibrium.'

Applying this principle, if we increase the concentration of the free vanadium within the system we should effectively shift the equilibrium to the left and favour vanadium incorporation into the Keggin. If we increase the concentration of free vanadium in solution by introducing excess VO_2^+ then we also may inadvertently

increase the concentration of VO_2^0 (adsorbed and in solution) at the electrode surface during electrochemical reduction. However, by introducing the VO^{2+} species by addition of vanadyl sulphate ($VOSO_4$) we should successfully increase the free vanadium within the system without the potential increase in concentration of the neutral VO_2^0 species.

Figure 5.19 shows the effect of $VOSO_4$ addition to the HV_4POM system. Figure 5.19A highlights the increase in peak anodic current when increasing the molar ratio of $VOSO_4$ present in the system. This continues to increases up until a molar equivalence of 3 after which point the peak current begins to decline, possibly due to a decrease in the diffusion coefficient of the POM species as the solution noticeably becomes increasingly viscous. Figure 5.19B shows a continuous decrease in peak cathodic current with increasing $VOSO_4$ concentration which initially will be a result of the shift of equilibrium reducing the amount of VO_2^+ for equation 5.2 to be effective. However, at higher concentrations of $VOSO_4$ a decrease in the diffusion coefficient of the POM species will also affect the peak currents obtained.

Analogous to the tetrafluoroborate formulations we see that addition of up to three molar equivalences of $VOSO_4$ can appear to have the desired effects upon the overall system as seen in Figure 5.20. Increasing the concentration of $VOSO_4$ does not result in a shift in potentials as seen in the HBF_4 formulations but there is an increase in peak separation with 244, 246 and 285 mV measured for 1, 2 and 3 equivalences of

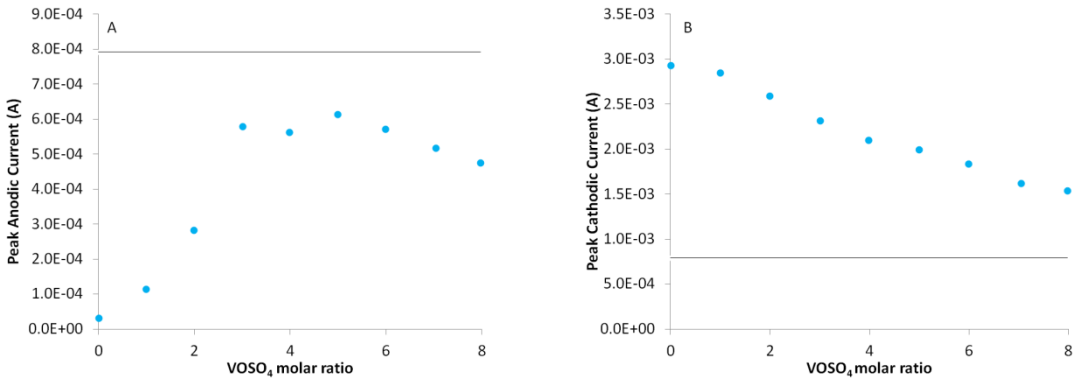

Figure 5.19: A) Dependence of I_p^a upon successive additions of equimolar amounts of $VOSO_4$. B) Dependence of I_p^c upon successive additions of equimolar amounts of $VOSO_4$. [POM] constant at 0.3 M. CV analysis run carried out at a GC electrode at room temperature, v = 0.04 V s^{-1}.

$VOSO_4$ respectively. As in the case of the previous formulations solution resistance is not believed to be the main contributor to the change in peak separation although solution resistance does increase compared with the HV_4POM. In this scenario the increased free vanadium present in solution is adding to the blocking layer at the electrode surface resulting in the increase in peak separation.

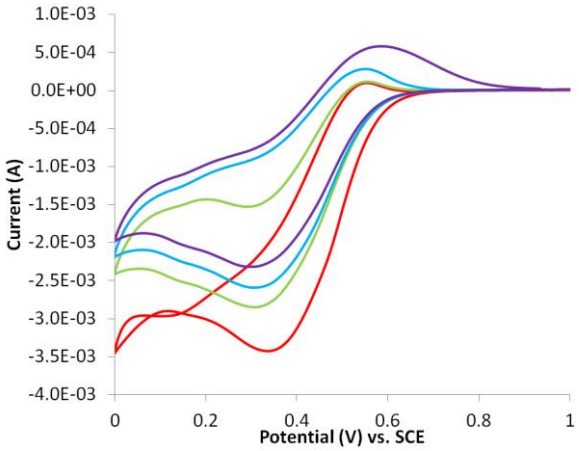

Figure 5.20: Change in the cyclic voltammetry behaviour of HV_4POM with successive addition of $VOSO_4$ whilst maintaining a constant [POM] equal to 0.3 M. Red; 0.3 M HV4POM pH = 0.45, Green; HV_4POM + 1 equivalence of $VOSO_4$ pH = 0.55, Blue; 0.3 M HV_4POM + 2 equivalences of $VOSO_4$pH = 0.6 and Purple; HV_4POM + 3 equivalences of $VOSO_4$ pH = 0.49. Analysis carried out at a GC electrode and at room temperature, v = 0.04 V s^{-1}

Although one could suggest that any one of the $VOSO_4$ formulations could be taken forward based on the observed results to maintain continuity the HV_4POM with one equivalence of $VOSO_4$ added, labelled HV_4(VOS) will be used. As in the HBF_4 formulations once fuel cell testing is complete and the stability of the compounds inside the fuel cell is known then further increases in $VOSO_4$ and HBF_4 concentration can be explored.

Figure 5.21 shows the analysis of overpotential vs. current density for HV_4POM vs. HV_4(VOS) and not surprisingly given the reduced cathodic currents, the HV_4(VOS) system requires larger overpotentials to drive the electrochemical reduction in order to reach the desired current densities compared to the HV_4POM. At the higher current density however (50 mA cm^{-2}) it is the opposite scenario with the HV_4POM requiring the larger overpotential to attain the higher current density. At the larger

current densities (50 mA cm^{-2}) the concentration of the VO_2^0 present is potentially at a concentration sufficient enough to begin to affect the electrode solution interface.

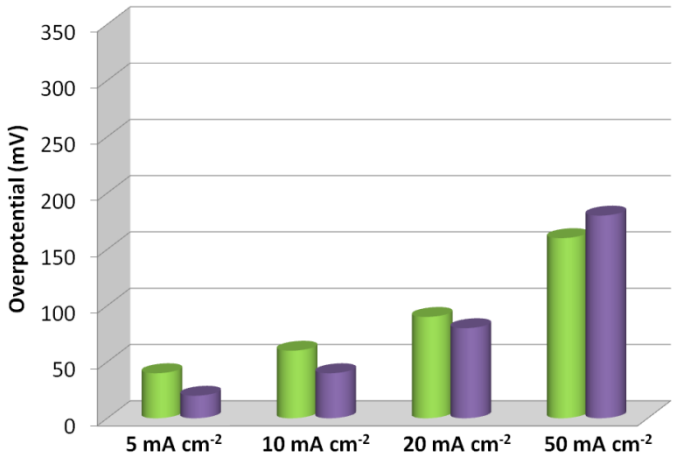

Figure 5.21: Comparison of overpotential required to generate the desired currents used during analysis for HV_4POM (Purple) and $HV_4(VOS)$ green. Based on RDE data obtained at GC electrode at 80°C.

5.3.5 Fuel Testing

5.3.5.1 Membrane Electrode Assembly for FlowCath® Technology

The fuel cell testing of the V_4POM, HV_4POM and subsequent formulations $HV_4(PO_4)$, $HV_4(BF_4)$ and $HV_4(VOS)$ where all carried out at ACAL Energy using there standard test rig which operated at atmospheric pressure and 80 °C. For the purpose of continuity the same materials for all test cells were used and are as follows:

Membrane/Anode: Ion Power Nafion (NR212) membrane with a typical Pt/C coating on the anode side. The cathode side has none.

Cathode: Carbon felt material (SGL Carbon GFD2.5), 2.5 mm thick which is compressed to approximately 1.1 mm when in the complete membrane electrode assembly.

Gas Diffusion layer: Microporous carbon fibre paper based material from SGL Carbon, product GDL 34BC

Each cell was constructed with the same membrane electrode assembly (MEA) as shown in Figure 5.22 which consists of:

- Heat plate: Steel end plate with holes for heater rods.
- Insulator: PTFE sheet
- Current Collector (Figure 5.22A)
- Electrode (cathode) (Figure 5.22B): Carbon plate with flow channel for the catholyte (plug flow design).
- 0.3 and 0.8 mm gaskets (Figure 5.22C): Gaskets used to seal the cathode compartment and define the depth of the cathode cell.
- Cathode: Carbon Felt (GFD) (Figure 5.22D)
- Membrane (Figure 5.22E): Used to seal the anode compartment and define the well for GDL.
- 0.3 mm gasket (Figure 5.22F)
- Gas Diffusion Layer (Figure 5.22G)
- Electrode (anode) (Figure 5.22H): Carbon plate with serpentine H_2 distribution channels
- Current collector
- Insulator (Figure 5.22I)
- Heat Plate (Figure 5.22J): Steel end plate with holes for heater rods.

The constructed cell was then subject to leak tests to ensure the cell was constructed correctly and safe for fuel cell testing with no hydrogen gas escaping from the cell assembly. The cell was also tested for short circuits. Once the cell ex-situ checks were complete, the cell was connected to the test rig and cell start up initiated. The POM solution was pumped around the system until solution temperature reached 80 ^{o}C at which point a manual flow rate test is carried out to ensure it is consistent at 150 ml min^{-1} by varying the pumping pressure (~1000 mbar was required for 150 ml min^{-1}). Prior to initiating any tests cut off procedures and values where checked as follows. Air pressure; 3000 mbar, Cell pressure; 2000 mbar, Hydrogen pressure; 2000 mbar, Min POM pressure -100 mbar, minimum cell voltage; 0 V and Tmax; 95^{o}C.

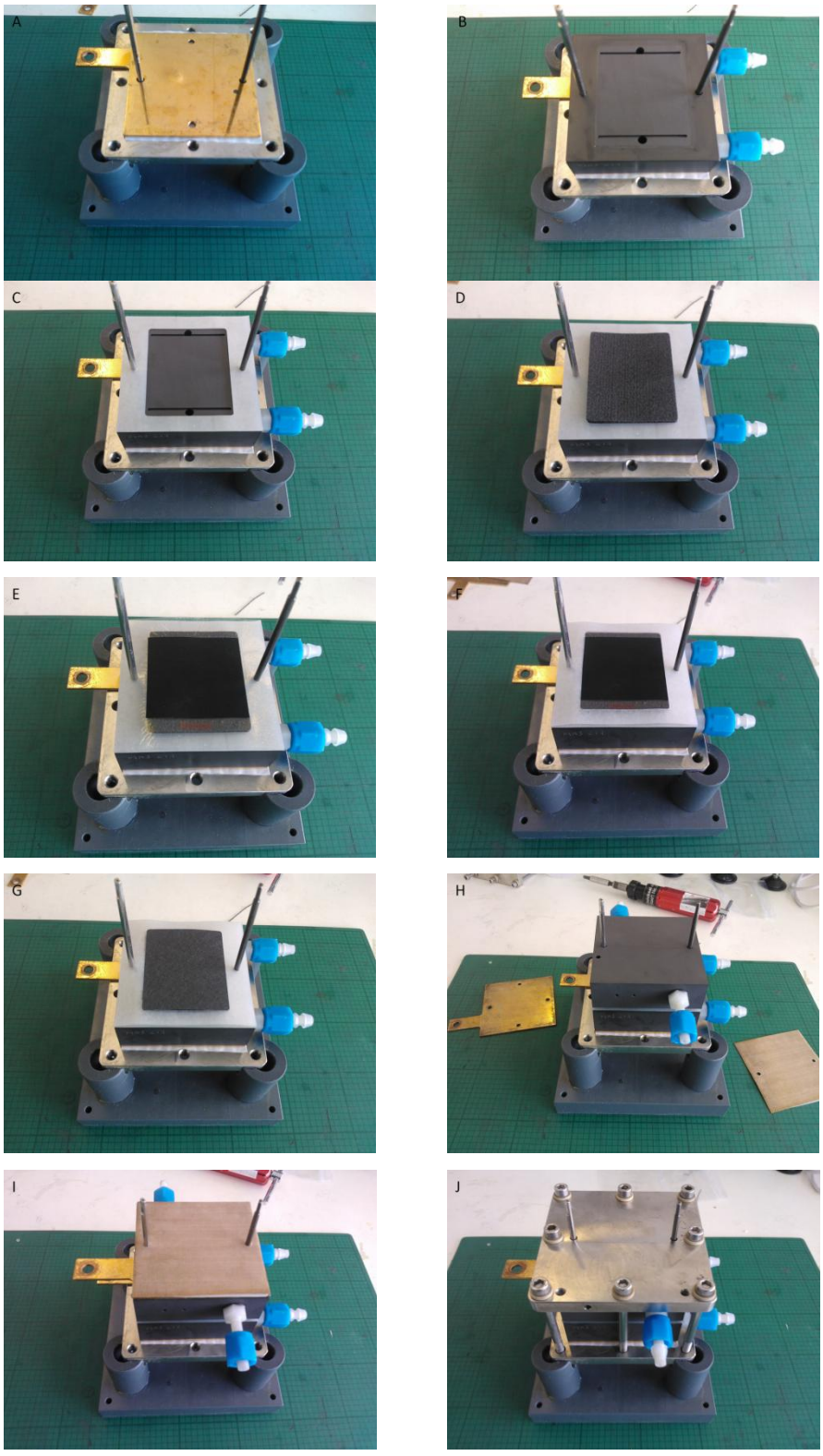

Figure 5.22: Stages involved in the construction of the membrane electrode. The addition of components added in each step is highlighted on the previous page.

The complete fuel cell test for each formulation consists of four individual tests:

Current Voltage Curve: The current voltage curves (IV curve) where measured from a pre-set OCP of 0.8 V and the current measured between 0.8 and 0.2 V. In each case a current of 5 Amps was drawn from the fuel cell in order to reduce the POM being tested until an OCP of 0.8 was attained. Prior to each I-V curve an anode recovery procedure was executed which involved 3 short burst of air being blown through the anode to remove excess water and any cross over material. This procedure also helps to 're-activate' the anode. When measuring the I-V curves the current is increased at a rate of 500 mA s^{-1} with the regeneration procedure not active. POM temperature was maintained at 80^{o}C throughout analysis. Each I-V curve was initiated at 0.8 V.

Steady State Measurement: The steady state measurement mimics the case of when the system is used in a real life situation under a constant load. Here a current of 15 Amps (approx. 600 mA cm^{-2}) is drawn from the cell for a period of 15 minutes and the cell potential and OCP monitored. During the measurement the following parameters are employed: Air flow (regeneration); 1.5 L min^{-1}, Hydrogen pressure; 1000 mbar, POM flow rate; 150 ml min^{-1}, Pumping pressure ~1000 mbar. As in the case of the I-V curves the OCP of the system is reduced to approximately 0.8 V prior to starting the measurement. The POM temperature was maintained at 80 ^{o}C throughout testing.

Impedance Measurement: The impedance measurements were carried out when the cell is under no load (0 Amps) at a frequency range from 2 x10^{4} to 0.1 Hz with an oscillating AC current of +/- 5 A. The measurements were carried out with the POM system in question adopting an OCP of ~0.8 V. The POM temperature maintained at 80^{o}C throughout analysis

Regeneration Profile: The regeneration profile is used to measure the regenerative capabilities of the POM system. This is achieved by reducing the POM OCP to ~0.75 V then running the cell at OCP with the regenerator now active. The POM is oxidised by the air and the OCP increases over time, producing a plot of OCP vs. time, a 'regeneration profile'. For the regeneration profile each POM system is

reduced to an OCP of 0.75 V. For the regeneration the following parameters are used: Air flow; 1.5 L min^{-1}, POM flow; 150 ml min^{-1}, Purge interval; 50 seconds, Purge duration; 2 seconds. POM temperature maintained at 80 ^{o}C throughout analysis

5.3.5.2 Results: I-V Curves

The first test conducted was the I-V curves with the overlay comparison for the V_4POM, HV_4POM and its three formulations shown in Figure 5.23. It is evident from the IV curves that the V_4POM shows a decrease in performance in comparison with the HV_4POM and its formulations with lower currents achieved at a given electrode potential. This is in agreement with RDE data shown previously. Interestingly, the HV_4POM, HV_4(VOS) and $HV_4(PO_4)$ systems show similar performance up to currents of ~12 A after which the $HV_4(PO_4)$ drops off with lower currents generated in comparison with HV_4POM. However the HV_4(VOS) shows the opposite trend with a minimal increase in current observed over the remaining potential range compared with HV_4POM.

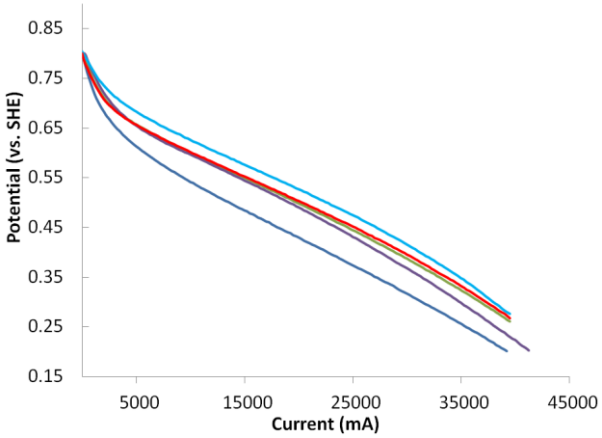

Figure 5.23: Comparison of IV curves obtained for 0.3 M V_4POM (dark blue), 0.3 M HV_4POM (green), 0.3 M $HV_4(BF_4)$ (light blue), 0.3 M $HV_4(PO_4)$ (purple), 0.3 M HV_4(VOS) (red) at 80^{o}C. Current step increase 500 mA s^{-1}, Hydrogen flow; 1000 mbar, POM flow 150 ml min^{-1} POM temperature; 80^{o}C

The HV_4(VOS) I-V curve again is in excellent agreement with the RDE results, which suggested that the $VOSO_4$ formulation would under perform at lower currents when compared with HV_4POM but showed a slight improvement at the higher

current range. The RDE results predicted that the phosphoric acid formulation, $HV_4(PO_4)$, would drastically under perform with much larger overpotentials required to generate the same current. However Figure 5.23 shows this was not observed in these fuel cell conditions with a relatively consistent performance observed especially in the lower current range. The $HV_4(BF_4)$ formulation as predicted is the clear winner, with increased currents observed across the entire potential range. The initial activation polarization is evident in each system with the HBF_4 formulation appearing to be the least affected but all five systems then show comparable loss due to ohmic resistance as expected considering the same membrane was used across all formulations. There is no significant voltage loss due mass transport effects either, with this being probably due to the current not being sufficiently large to induce concentration polarization.

5.3.5.3 Results: Steady State Measurements

The steady state measurements (Figure 5.24) should be consistent with the data obtained for the IV curves and show the $HV_4(BF_4)$ system to be operating at the highest potential, however this is not the case. Based upon the IV curve data taken at 15000 mA the five systems should be in the order of $HV_4(BF_4)$ > $HV_4(VOS)$ > HV_4POM > $HV_4(PO_4)$ > V_4POM with respect to cell potential. If we disregard the $HV_4(BF_4)$ system for the moment then the remaining four systems are in the correct order indicating apparently anomalous results for the tetrafluoroborate formulation.

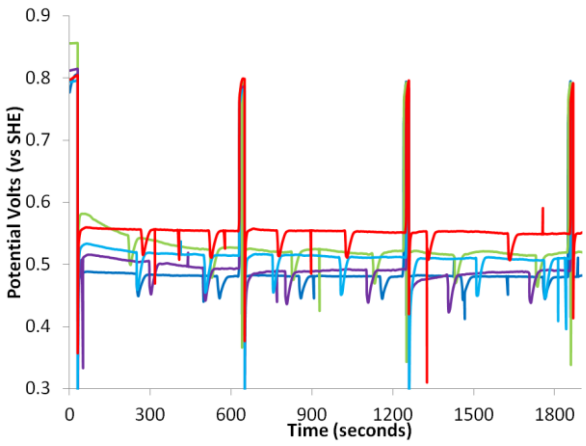

Figure 5.24: Steady state measurements for 0.3 M V_4POM (dark blue), 0.3 M HV_4POM (green), 0.3 M $HV_4(BF_4)$ (light blue), 0.3 M $HV_4(PO_4)$ (purple), 0.3 M $HV_4(VOS)$ (red) under a 15 A load. Air flow (regeneration); 1.5 L min^{-1}, Hydrogen pressure; 1000 mbar, POM flow rate; 150 ml min^{-1}, Cell Pressure ~1000 mbar, POM temperature; 80^{o}C

Comparing the IV curves obtained for the $HV_4(BF_4)$ system that have been run consecutively one after another (Figure 5.25), the potential reason for the drop in performance can be highlighted. Comparing the I-V curves measured first (blue) and second (red) it is clear that there is a drastic drop in performance between these two. This has been observed previously during fuel cell testing and is assigned to a deactivation of the anode. The reason for this is still under investigation. Running the anode recovery procedure (three short bursts of air blown directly into the anode) normally 're-activates' the anode. As shown in Figure 5.25 re-running the IV curve measurement after the anode recovery procedure drastically improves the cell performance and returns it to that of the original measurement. The effect of this electrode deactivation was only observed during the analysis of the data thus no subsequent steady state measurement after anode recovery was made.

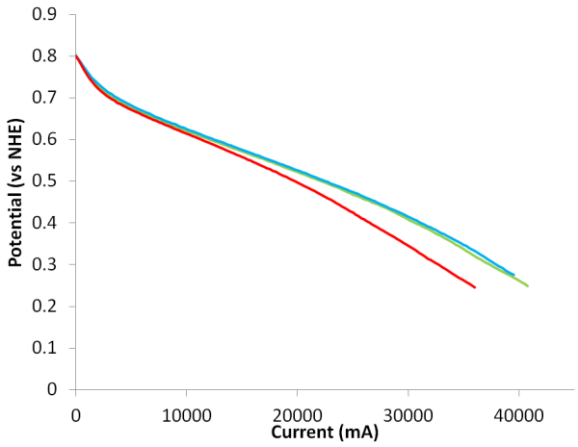

Figure 5.25: Comparison of IV curves obtained for 0.3 M $HV_4(BF_4)$ at 80°C. Blue is the first measurement, red is the second successive measurement and green is third successive measurement after the anode recovery procedure (see text). Current increase 500 mA s^{-1}, Hydrogen flow; 1000 mbar, POM flow 150 ml min^{-1}

5.3.5.3 Results: Electrical Impedance Measurements

The electrochemical impedance measurements of the five systems give a good insight into the effect each formulation has upon resistances within the cell. As observed when comparing the V_4 and HV_4POM systems in Figure 5.6 it can be seen from the AC impedance plots (Figure 5.26) that all five systems show similar characteristics with a polarization loop located at higher frequencies partnered with a slope of approximately 45° at lower frequencies. This indicates the process occurring

at the electrode surface is controlled by both the electrode kinetics and diffusion. [21,30,31] In this instance we can again use the equivalent circuit proposed in Figure 5.7 which is based upon the simple Randles circuit in the presence of diffusion limitation,[21,30,31]shown below for convenience:

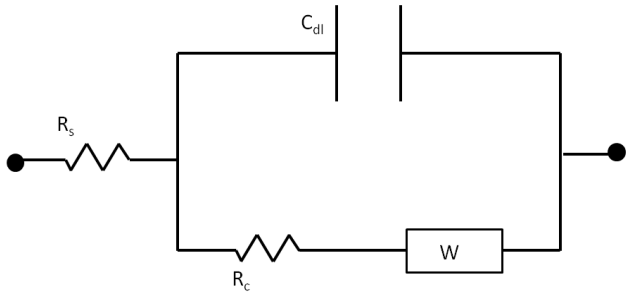

Where R_s stands for the solution resistance in which the membrane resistance is incorporated, C_{dl} is the double layer capacitance connected in a parallel with the charge transfer resistance, R_c, which gives rise to by the semi-circle at the higher frequency range, W is the Warburg resistance which represents the resistance associated with diffusion. [21,30,31]

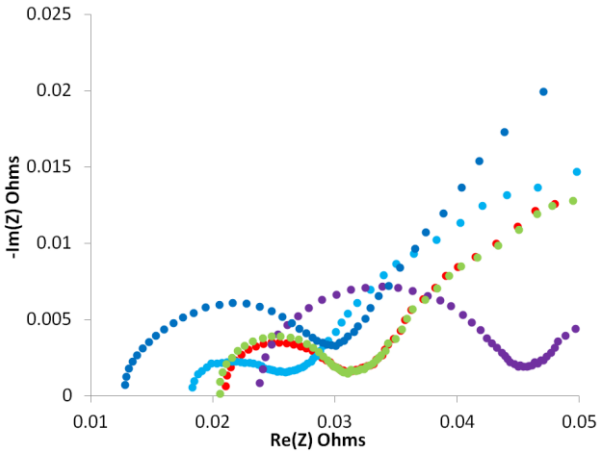

Figure 5.26: Electrochemical Impedance Spectroscopy (EIS) at 0 Amps with a frequency range from 2 x10^4 to 0.1 Hz with an amplitude of +/- 5 mV. 0.3 M V_4POM (dark blue), 0.3 M HV_4POM (green), 0.3 M $HV_4(BF_4)$ (light blue), 0.3 M $HV_4(PO_4)$ (purple) and HV_4(VOS) (red).

If we again simulate the AC impedance spectra based upon the equivalent circuit proposed in Figure 5.7 we can obtain data for the various components (Table 5.4) that make up the equivalent circuit. When comparing the solution resistance in each of the five systems, each ones shows a decrease when compared to the V_4POM (ex-

situ measurement). However in the fuel cell, each system demonstrates an increase in the resistance associated with R_s (compared with V_4POM) indicating that the membrane resistance is the dominating factor. The increase in resistance for the HV_4POM was correctly predicted as discussed previously and is associated with the increased deposition of vanadium (VO_2^+/VO^{2+}) confirmed by EDX. The increase in resistance in membrane resistance for the $HV_4(PO_4)$ was not expected since the complexation of free vanadium with the phosphate species was specifically done to reduce deposition in the membrane. However the relativly low solubility of vanadium phosphate complexes could be blocking the membrane resulting in the increase in membrane resistance. Comparing this with the vanadyl sulphate formulation where we specifically increase the concentration of free vanadium does not result in the same increased membrane resistance thus suggesting vanadium phosphate (and other phosphate species) as the species responsible for the significant increase in resistance in $HV_4(PO_4)$. The opposite effect however is observed with addition of the weakly coordinating yet highly soluble tetrafluoroborate salts (compared to the phosphate derivatives) which show a decrease in membrane resistance compared to the other HV_4 formulations possibly caused by the coordination between the tetrafluoroborate anions and vanadium cations being strong enough to prevent significant vanadium deposition onto the membrane.

Table 5.4: Simulated fit of resistance values for the components R_s and R_c based on the proposed equivalent circuit (Figure 5.7) for the AC impedance plots in Figure 5.26.

System	R_s (Ohms)	R_c (Ohms)
V_4POM	0.012	0.013
HV_4POM	0.020	0.009
$HV_4(PO_4)$	0.024	0.023
$HV_4(BF_4)$	0.018	0.007
$HV_4(VOS)$	0.021	0.009

The trends in the resistance associated with charge transfer $R_{c,}$ are in agreement with the proposed model for the electrode solution interface and electrochemical data obtained at both stationary and rating disc electrodes. The decrease in R_c is representative of more facile electrode kinetics in the HV_4POM system compared with V_4POM due to the substitution of the sodium cations with protons. The increase

in R_c for the $HV_4(PO_4)$ system is likely to be due to the low solubility of the phosphate complexes and although this may reduce the oxidising capability of the VO_2^+ species, overall this does not benefit the system with an increase in both membrane and charge transfer resistance. The opposite effect however is observed for the $HV_4(BF_4)$ system which shows a decrease in both membrane and charge transfer resistance possibly due to the tetrafluoroborate anion effectively coordinating with the VO_2^+ species. Thus reducing its oxidising capabilities but still maintaining a high level of solubility and not adding to the blocking effect observed at the electrode surface. The voltammetry of the HBF_4 formulation is not as proton limited as the other formulations. HV_4(VOS) shows signs of improvement with no significant increase in membrane and charge transfer resistance as well as electrochemical results comparable with the HV_4POM system. Importantly it shows a potential increase in the regenerative properties of the POM with increased anodic currents observed under CV analysis.

5.3.5.4 Results: Regeneration Profiles

The regeneration profiles of the five systems being tested are shown in Figure 5.27. This comparison shows that there is little difference between the perceived rate of regeneration of the different formulations with the change in OCP with time relatively consistent across all formulations.

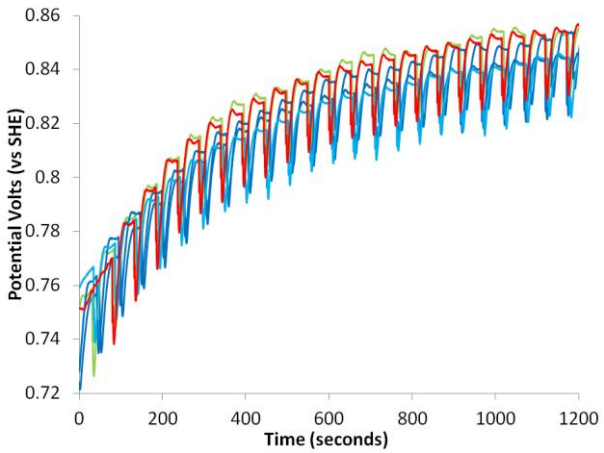

Figure 5.27: Regeneration profiles for the V_4POM (dark blue), HV_4POM (green), $HV_4(PO_4)$ (purple), $HV_4(BF_4)$ (light blue) and HV_4(VOS) (red). Air flow; 1.5 L min^{-1}, POM flow; 150 ml min^{-1}, Purge interval; 50 seconds, Purge duration; 2 seconds

However HV_4POM and $HV_4(VOS)$ do show slight differences compared to the remaining formulations with the final OCP values somewhat higher than their respective counter parts. The OCP values for each of the five systems in their fresh oxidised and regenerated states are shown in Table 5.5. The values vary by 105 mV across all systems when comparing the OCP of the fresh oxidised systems however. However, in their regenerated states there is only approximately 9 mV difference across all systems. Based on a crude analysis we have already estimated that there is approximately 20 % of the vanadium that remains in the +4 oxidation state in the HV_4POM. Using this value, we can estimate whether the percentage of V^{4+} is higher or lower than this under this condition based on the OCP values.

Table 5.5: Open circuit potentials measured at 80 ^{o}C for the V_4POM, HV_4POM, $HV_4(PO_4)$, $HV_4(BF_4)$ and $HV_4(VOS)$ systems both in the fresh and regenerated sates.

System	Fresh State OCP (V)	Regenerated State OCP (V)
V4POM	0.984	0.845
HV4POM	1.059	0.854
HV4(PO4)	1.074	0.853
HV4(BF4)	1.089	0.845
HV4(VOS)	1.008	0.855

The OCP of the $HV_4(PO_4)$ and $HV_4(BF_4)$ systems in the fresh oxidised state are higher than that of the HV_4POM but also the regenerated OCP values are lower indicating an increase in the percentage of vanadium remaining in the +4 oxidation state. This indicates that there is a decrease in the regenerative capabilities of these two systems. The $HV_4(VOS)$ system however has a lower OCP for the fresh system and an almost identical OCP for the regenerated system. However the fresh OCP is expected to be less than that of the other formulations due to the presence of 0.3 M VO^{2+}, although at this state no vanadium within the Keggin structure is in +4 oxidation state. Thus the OCP of the regenerated system whilst comparable to the HV_4POM could indicate a decrease in percentage of vanadium that remains in +4 oxidation state as a result from the electrochemical reduction. It should be noted that there is no significant difference between the OCP of the individual systems both in the fresh and regenerated states and the peculiar similarity in OCP for the

regenerated states could be a limitation of the regeneration process used within the fuel cell.

It was stated previously that the development of a high temperature and pressure (HTHP) fuel cell rig was under development which showed potential improvement in the regeneration performance of the HV_4POM. Testing the HTHP fuel cell with the $HV_4(PO_4)$ showed an interesting result with clear improvement in the cell potential when under constant load (Figure 5.28). Further development of the HTHP fuel cell could lead to further improvements in catalyst performance.

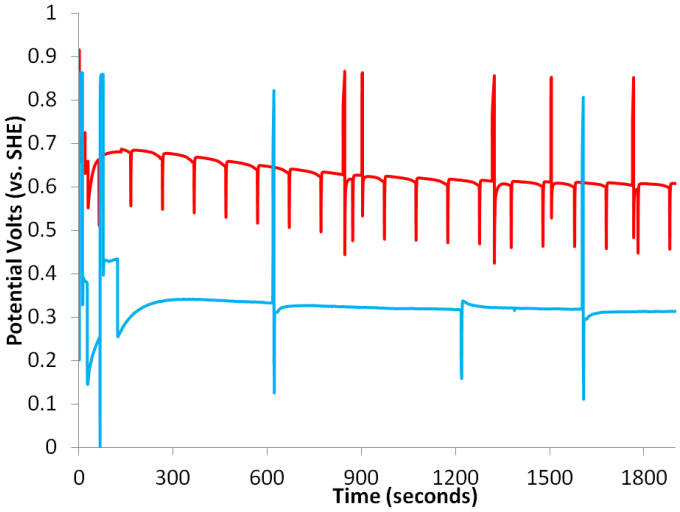

Figure 5.28: Steady state measurements for the HV4POM under fuel cell conditions (blue) and HTTP fuel cell conditions (red).

5.4 Conclusions

The key aim of this chapter was to use the knowledge developed in Chapters 3 and 4 to improve the electrode kinetics and overall catalytic performance of the lead system. We began the development process by first addressing the potential damaging effect the sodium cations present in the V_4POM where having upon the membrane conductivity. Employing the synthesis by Odyakov[8] we managed to successfully replace Na^+ with H^+ yielding the HV_4POM system. The structural comparison between the systems showed that the two compounds were isostrctural by IR, Raman, ^{31}P and single crystal X-Ray analysis with only slight variations in the individual Keggin speciation. HV_4POM showed that an increase in the concentration

of the lower substituted Keggin species containing one and two vanadium centres respectively. However there was a decrease in the concentration of the higher substituted Keggin species which contain three and four vanadium centres respectively, thus causing an increase in the solution free vanadium (VO_2^+) concentration. This at first appeared to be a set back as we aimed to reduce the free vanadium concentration. Upon further analysis and evaluation of the cyclic voltammetry data for the HV_4POM it became apparent that the substitution of Na^+ with H^+ has significantly benefited the system. The substitution resulted in a positive shift of $E^{o'}$ along with a decrease in the peak to peak separation as a result E_p^c shifting by 150 mV to a more positive potential. The shift in E_p^c and consequently $E^{o'}$ is thought to be due to the increased proton concentration successfully protonating the Keggin structure and reducing the overall negative charge on the Keggin. This is in agreement with previous work [24,25] which demonstrates that increasing the electronegativitiy of the Keggins counter ions shifts the reduction potentials to more positive value (decreases the activation barrier for polyoxometalate reduction). The increased proton concentration also affected the generated currents with a significant increase in cathodic current. This is a consequence of a number of possible processes effecting the CV, be it oxidation of reduced POM via free VO_2^+ (equation 5.4) now more readily available due to the increased proton concentration and a positive shift in the formal potential of the VO_2^+/VO^{2+} redox couple. The increased cathodic current can also be aided by an increase in the diffusion coefficient of the HV_4POM species on the basis of a reduced negative charge on the overall Keggin. The decrease in anodic current could represent a decrease in the regeneration capabilities of the HV_4POM system.

The EDX and EIS spectra of the V_4POM system shows that over time the Na^+ weight percentage of sodium deposited in to the membrane steadily increases in the V_4POM and this will contribute to the membrane resistance[1] calculated based on the simulation fit (0.12 Ohms). The same analysis of the HV_4POM did not yield the results we had hoped for. Indeed, there was a decrease in the Na^+ counterion in the membrane; however, there was a drastic increase in the deposited vanadium (VO_2^+ or VO^{2+} species) which affected the membrane resistance more than expected leading to a membrane resistance of 0.20 Ohms. A decrease in the charge transfer resistance

when comparing the V_4POM (0.013 Ohms) and the HV_4POM (0.009 ohms) supports the results from the earlier CV work. Here we saw a decrease in the peak to peak separation of the HV_4POM compared to the V_4POM which is indicative of better electrode kinetics.

The current vs. overpotential measurements supported the evidence obtained from the EIS measurements that there was a potential change in the electrode surface interface resulting in a much more facile electron transfer. This was believed to be due to the increased proton concentration (when compared to the V_4POM) allowing the neutral vanadyl species (VO_2^0) to be readily protonated. This minimises the blocking effect at the electrode surface. Combining this change in the electrode solution interface and the positive shift in the HV_4POM formal potential could contribute to the possible increase in electrode kinetics.

The HV_4POM showed poor regeneration capabilities compared to the V_4POM system with 28 % of the vanadium remaining in the +4 oxidation state (based upon lab regeneration) compared to 3.3 % for the V_4POM. This poor performance ultimately limits the fuel cell performance of this catalyst.

From the results obtained in this and previous chapters the formulation work focused on eliminating the effect the VO_2^+ by a) limiting its oxidative capabilities to allow reduced vanadium to remain within the Keggin and b) changing the dynamic equilibrium of the system to reduce the free vanadium concentration. The initial formulation used excess phosphoric acid in the system resulting in complexation of the free vanadium cations with the phosphate anions. This complexation could reduce the oxidative capabilities of the VO_2^+ and effectively hinder equation 5.2, which is evident in the corresponding CV comparison between the HV_4 and $HV_4(PO_4)$ systems. However the presence of vanadium phosphates which have a low solubility in aqueous media effectively replaces the role of the VO_2^0 species and could potentially add to the blocking effect at the electrode surface and cause the resulting larger overpotentials required to drive the reduction and increased peak separation in the cyclic voltammogram.

The tetrafluoroborate formulations were explored due to their high solubility and weakly coordinating nature. This was seen as a logical alternative to the phosphates. The tetrafluoroborate formulation ($HV_4(BF_4)$) gave the expected results, showing a weak coordination with the free vanadium based upon the negative shift in formal potential when in the presence of BF_4^- however the shift was not as significant as that observed with phosphate coordination (Figure 5.17B). The current overpotential measurements again showed promising results with low overpotentials required by the $HV_4(BF_4)$ system. This is believed to be due to the tetrafluoroborate coordinating with the free vanadium but also the tetrafluoroborate complexes are highly soluble compared to the phosphate derivative. In the HBF_4 and H_3PO_4 formulations it is noted that increase in $[H^+]$ will contribute to the shift in formal potential. But with different voltametric behaviour observed for the two systems with the same increase in $[H^+]$, the proposed complexation must play a role in the shift (of the formal potential).

The final formulation used Chateliers principle to shift the equilibrium in equation 5.6 and favour the incorporation of free vanadium in to the Keggin. This was done by introducing $VOSO_4$ into the system which is a source of VO^{2+}.

$$HV_xPOM \rightleftharpoons HV_{x-z}POM + Z\,V^{+\backslash 2+} \qquad (5.6)$$

By shifting the equilibrium we should increase the concentration of reduced Keggin, improving the regeneration reaction. This was again suggested by the observed decrease in cathodic current and an increase in anodic current. However the increased anodic current may be partly due to oxidation of coordinated VO^{2+} ions in the outer sphere of the Keggin structure. The current overpotential analysis showed the $HV_4(VOS)$ required larger overpotentials to reach the desired currents, although at larger currents the trend is reversed. It was postulated that at these large currents the concentration of the VO_2^0 species could be significant enough to begin to block the electrode surface. The $HV_4(VOS)$ system would not be subject to this as the already high free vanadium concentration would favour vanadium to remain within the Keggin structure.

Finally the V_4POM, HV_4POM and its formulations $HV_4(PO_4)$, $HV_4(BF_4)$ and $HV_4(VOS)$ were taken to ACAL Energy for fuel cell testing. The current voltage curves were in agreement with the data obtained at the RDE with the $HV_4(BF_4)$ system generating the highest currents with the smallest applied overpotential. Surprisingly the $HV_4(PO_4)$ showed comparable results with the HV_4POM and $HV_4(VOS)$ systems. Based on the RDE data this system should have performed a lot worse with much lower currents expected at specific overpotentials. The steady state measurements highlighted a key issue within the fuel cell system with anode deactivation significantly hindering the performance of the $HV_4(BF_4)$ system. The remaining systems appeared unaffected with the cell potentials when under a constant load in agreement with the IV curve data. Observing the IV curves for the $HV_4(BF_4)$ system it was noted that running two consecutive measurements resulted in a decrease in performance with lower currents generated at the same observed potentials. However, running the anode recovery procedure and re-measuring the I-V curve resulted in currents comparable with the original measurement.

The EIS measurements were particularly informative and complemented the analysis well by bringing together the notions behind each formulations performance. The $HV_4(PO_4)$ system which contains vanadium phosphates would most likely lead to an increase in membrane resistance due to their low solubility in aqueous media and also potentially increase the resistance associated with charge transfer. The impedance measurements show this trend with increases in both membrane resistance and charge transfer resistance. The $HV_4(VOS)$ system showed little change in membrane or charge transfer resistance when compared to the HV_4POM which is general in agreement with the RDE data. The main hope for this system was to improve the regeneration capabilities of the POM system however as discussed, under conditions tested here (80^oC and atmospheric pressure) the regeneration process does not lead to full regeneration of the system. Further development of the HTHP fuel cell needs to be achieved for this to be possible. The $HV_4(BF_4)$ system shows the biggest improvements overall when compared to the HV_4POM. This formulation is believed to reduce the blocking effect at the electrode surface resulting in facile electron transfer and also to limit the oxidising properties of the VO_2^+ species as well as reducing both the membrane and charge transfer resistance.

Presently at ACAL Energy employ the $HV_4(PO_4)$ system as their lead catalyst in conjunction with their improved HTHP fuel cell. Based on the results from this work careful consideration should be given to the possibility of utilising the $HV_4(BF_4)$ system in the HTHP fuel cell as it clearly has the potential for large improvements in performance over the $HV_4(PO_4)$ system.

5.5 Experimental

5.5.1 Synthesis of $H_7PMo_8V_4O_{40}$ (HV_4POM)

Stage 1, Preparation of $H_9PV_{14}O_{42}$ aqueous solution: vanadium pentaoxide (21.88 g, 0.12 moles) in 1000 ml of distilled water in a 2000 ml conical flask. The mixture was stirred and cooled in an ice bath until the temperature of the solution remained below 15 ^oC. To this suspension, hydrogen peroxide (180 ml, 30 % in H_2O) was added in portions to the cold solution and left to stir for 30 minutes. During this time the temperature of the solution was kept below 15 ^oC. The solution was then charged with phosphoric acid (4.64 ml 42 % in H_2O) and stirred for 2 hours during which time the ice bath was removed and the mixture was allowed to warm to room temperature. The final pH of the mixture was pH 0.45.

Stage 2, Preparation of $H_3PMo_{12}O_{40}$ aqueous solution: molybdenum trioxide (69.11 g, 0.48 moles) was suspended in 600 ml of distilled water in a 2000 ml conical flask. The slurry was then charged with phosphoric acid (3.70 ml 42 % in H_2O) and stirred. The mixture was then heated to boiling and stirred for 30 minutes or until a deep yellow colour was observed.

Stage 3, Combining the mixtures: The phosphomolybdic acid solution was cooled to approximately 60 ^oC. To the cooled solution, half of the $H_9PV_{14}O_{42}$ solution was added slowly and in small portions to the phosphomolybdic acid. After this addition the mixture was heated to boiling and evaporated to half its original volume before adding the second half of the $H_9PV_{14}O_{42}$ solution was added in the same manner as the first. The combined solution was heated further and evaporated to a volume of 200 ml giving a final solution of 0.3 M $H_7PMo_8V_4POM$ with a pH of 0.4 measured at

room temperature. $H_7PMo_8V_4O_{40}$ ICP analysis Calc.: P: 1.87, Mo: 46.54, V: 12.35 %. Found, P: 1.85, Mo:46.34, V:12.38 %.

5.5.2 Preparation of HV_4POM Formulations

Preparation of the HV_4POM formulations was carried out on the Chemspeed Accelerator SLT synthesis platform. The following example is based upon $HV_4(PO_4)$ series. Using a pre-synthesised stock solution of 0.3M HV_4POM, 10 ml aliquots were transferred to 27 ml double jacketed reactors. Phosphoric acid (85 % in H_2O) was then added slowly to each aliquot in varying stoichiometric amounts (Table 5.6) whilst under vigorous stirring. Upon complete addition the samples were evaporated to half the original volume and then diluted to 10 ml by hand, maintaining the original 0.3 M concentration of HV_4POM. Finally in each of the $HV_4(PO_4)$ samples 50 % of the total vanadium (expected within the Keggin) was reduced with hydrazine hydrate (1.33 ml 40 % in H_2O) and re-oxidised with O_2.

Table 5.6: Quantities required for stoichiometric addition of H_3PO_4, HBF_4 and $VOSO_4$ for the formulation development of the HV_4POM system

Aliquot	Stoichiometric ratio Additive: POM	Volume of 85 % H_3PO_4	Volume of 48 % HBF_4	Mass of $VOSO_4$
1	1 : 1	0.20 ml	0.40 ml	0.49 g
2	2 : 1	0.41 ml	0.80 ml	0.98 g
3	3 : 1	0.61 ml	1.20 ml	1.47 g
4	4 : 1	0.82 ml	1.60 ml	1.96 g
5	5 : 1	1.02 ml	2.00 ml	2.45 g
6	6 : 1	1.23 ml	2.40 ml	2.93 g
7	7 : 1	1.43 ml	2.80 ml	3.42 g
8	8 : 1	1.64 ml	3.20 ml	3.91 g

The same procedure outlined was used for the preparation of the HV_4(BF4) and HV_4(VOS) samples. The addition of $VOSO_4$ utilised the solid dispensing unit (SDU) incorporated into the SLT. The self teaching protocol was used to determine the dispensing parameters for the $VOSO_4$, Fine dispensing amount, 61.6 mg, fine dispensing speed, 4 %, dispense time 193.2 s g^{-1}, error +/- 0.3 mg.

5.5.3 Crystal Data

HV_4POM: Crystal data for BAV4RUS: Formula $H_{70}PMo_9V_3O_{72}$, M = 2269.81 g•mol-1, tetragonal space group P4/mnc, dark red crystal, a = 12.6871(3) Å, c = 17.9404(13) Å, V = 2887.7(2) Å3, Z = 2, ρ = 2.521 g•cm-3, μ = 2.610 mm-3, F(000) = 2216, crystal size = 0.06 × 0.06 × 0.03 mm3, T = 100(2) K. 27756 reflections measured (1.97° < Θ < 34.96°), 3274 unique (Rint = 0.0527), 2633 observed (I > 2σ(I)), R1 = 0.0668 for the observed and R1 = 0.0539 for all reflections, wR2 = 0.1509 for all reflections, max/min residual electron density = 1.397 and -1.644 e•Å-3, data / restraints / parameters = 3274 / 0 / 123, GOF = 1.089.

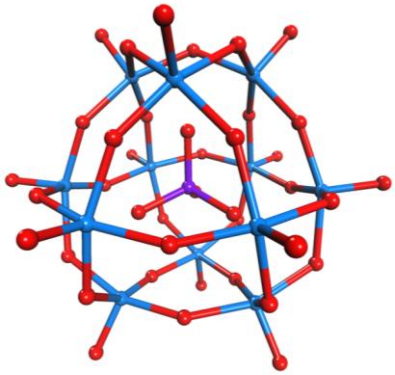

Figure 5.29: Single crystal structure of HV_4POM ($H_7PMo_8V_4O_{40}$). Iso-structural to the fresh V_4POM ($Na_4H_3PMo_8V_4O_{40}$)

5.5.4 Electrochemical Methods

For consistency throughout all measurements used the same procedure outlined in Chapter 3, which is shown again here for convenience.

Cyclic voltammetry: Measurements were carried out using a standard three electrode system consisting of a 3 mm diameter glassy carbon working electrode, a saturated calomel reference electrode and a platinum wire counter electrode. The working electrode was prepared by polishing with 3 and 1 micron diamond paste with sonication in distilled water between and after each polish. The reference electrode was cleaned with distilled water, whilst the platinum wire was cleaned with piranha solution and flamed annealed to remove impurities. CV analysis of the HV_4POM and corresponding formulations ($HV_4(PO_3)$, $HV_4(BF_4)$ and $HV_4(VOS)$)

under fuel cell conditions; 10 ml 0.3 M POM was placed into the cell and the electrodes connected to the potentiostat. Cyclic voltammetry analysis was carried out within the potential ranges of 0 – 1 or 0 - 1.5 V vs. SCE with each CV initiated at the OCP measured prior to the analysis. CV analysis that required potential sweeps beyond 1.0 V were degassed with N_2 for 15 minutes prior to analysis.

Rotating disc analysis: A three electrode system was used consisting of a glassy carbon 3 mm diameter RDE working electrode, a saturated calomel reference electrode and a platinum wire counter electrode. The working electrode was again polished using 3 and 1 micron diamond paste with sonication between and after polishing. 70 ml of 0.3 M HV_4POM (or corresponding formulation) was added to the RDE cell and the electrodes connected to the potentiostat. A series of linear voltammograms were recorded at varying rotation speeds ranging from 500 to 5000 rpm within the potential range of 0 to 1.0 V vs. SCE.

5.6 References

(1) Hongsirikarn, K.; Goodwin, J.; Greenway, S.; Creager, S. *Journal of Power Sources* **2010**, *195*, 7213-7220.

(2) Smitha, B.; Sridhar, S.; Khan, A. A. *Journal of Membrane Science* **2005**, *259*, 10-26.

(3) Souchay, P. *Polyanions et polycations*; Monographies de chimie mineerale; Gaithier-Villars, Paris, 1963.

(4) Kozhevnikov, I. *Catalysts For Fine Chemical Synthesis, Volume 2, Catalysis By Polyoxometalates*; Wiley, 2002.

(5) Pope, M. T. *Heteropoly and Isopoly Oxometaltes*; Inorganic Chemistry Concepts; Springer-Verlag, Berlin, 1983; Vol. 8, pp. 1-1.

(6) Maksimov, G. *Russian Chemical Reviews* **1995**, *64*, 445-461.

(7) Grate, J. *Journal of Molecular Catalysis A: Chemical* **1996**, *114*, 93-101.

(8) Odyakov, F. V.; Zhizhina, E. G. *Russian Journal of Inorganic Chemistry* **2009**, *54*, 361-367.

(9) Odyakov, V. F.; Zhizhina, E. G.; Maksimovskaya, R. I. *Applied Catalysis A: General* **2008**, *342*, 126-130.

(10) Arichi, J.; Eternot, M.; Louis, B. *Catalysis Today* **2008**, *138*, 117-122.

(11) Tsigdinos, G.; Hallada, C. *Inorganic Chemistry* **1968**, *7*, 437 - 441.

(12) Butler, A.; Clague, M.; Meister, G. *Chemical reviews* **1994**, *94*, 625-638.

(13) Bartley, J.; Kiely, C.; Wells, R.; Hutchings, G. *Catalysis letters* **2001**, *72*, 99-105.

(14) RAMASARMA, T. *Indian national Science Academy* **2003**, *4*, 649-672.

(15) Basuli, F.; Bailey, B. C.; Huffman, J. C.; Baik, M.; Mindiola, D. J. *Journal of the American Chemical Society* **2004**, *126*, 1924-1925.

(16) Yamigata, M.; Tachikawa, N.; Katayama, Y. -*ELECTROCHEMICAL* **2004**, 1-1.

(17) Arichi, J.; Pereira, M. M.; Esteves, P. M.; Louis, B. *Solid State Sciences* **2010**, *12*, 1866-1869.

(18) Cuentas-Gallegos, A. K.; Frausto, C.; Ortiz-Frade, L. A.; Orozco, G. *Vibrational Spectroscopy* **2011**, *57*, 49-54.

(19) Kozhevnikov, I. *Chemical Reviews* **1998**, *98*, 171-198.

(20) Freund, M.; Lewis, N. *Inorganic Chemistry* **1994**, *33*, 1638 - 1643.

(21) Bard, A.; Faulkner, L. *Electrochemical Methods: Fundamentals and applications*; 2nd ed.; Wiley, New York, 2000.

(22) Pope, M.; Mèuller, A. *Polyoxometalates: from platonic solids to anti-retroviral activity*; 1994.

(23) López, X.; Fernández, J.; Poblet, J. *Dalton Transactions* **2006**, 1162.

(24) Song, I. K.; Barteau, M. A. *Journal of Molecular Catalysis A: Chemical* **2004**, *212*, 229-236.

(25) AI, M. *Applied Catalysis* **1982**, *4*, 245-256.

(26) Fowles, G.; Brandou, J. R. *Jounral of Chemical Education* **1961**, *38*, A491.

(27) Kelly, M.; Fafilek, G.; Besenhard, J.; Kronberger, H. *Journal of Power* **2005**, 1-4.

(28) Okada, T.; Ayato, Y.; Yuasa; Sekine, I. *Journal of Physical Chemistry B* **1999**, *103*, 3315 - 3322.

(29) Okada, T.; Møller-Holst, S.; Gorseth, O. *Journal of Electroanalytical* **1998**, 1-9.

(30) Hunsom, M. *Spectroscopic Properties of Inorganic and Organometallic Compounds* **2012**, *42*, 196 -247.

(31) Pletcher, D. *Instrumental Methods in Electrochemistry*; Horwood Pub Limited, 2000.

(32) Kuhn, A.; Anson, F. *Langmuir* **1996**, *12*, 5481 - 5488.

(33) Choi, S.; Kim, J. *Bulletin of the Korean Chemical Society* **2009**, *30*, 810-816.

(34) Gattrell, M.; Qian, J.; Stewart, C.; Graham, P.; MacDougall, B. *Electrochimica Acta* **2005**, *51*, 395-407.

(35) Fang, X.; Kögerler, P. *Angewandte Chemie International Edition* **2008**, *47*, 8123-8126.

(36) Chaumont, A.; Wipff, G. *Comptes Rendus Chimie* **2012**, *15*, 107-117.

(37) Speight, J. *Lange's Handbook of Chemistry, 70th Anniversary Edition*; McGraw-Hill Professional, 2004.

(38) Earnshaw, A.; Greenwood, N. *Chemistry of the Elements*; Elsevier, 1997.

(39) Jie, X.; Shao, Z.; Hou, J.; Sun, G.; Yi, B. *Electrochimica Acta* **2010**, *55*, 4783-4788.

(40) Leusbrock, I.; Sybr; Metz, J.; Rexwinkel, G.; Versteeg, G. *The Journal of Supercritical Fluids* **2010**, *54*, 1-8.

(41) Honeychuck, R.; Hersh, W. *Inorganic Chemistry* **1989**, *28*, 2869 - 2886.

(42) Belai, N.; Pope, M. T. *Chemical Communications* **2005**, 5760.

Chapter 6

Conclusions

Table of Contents

6.1 Chapter 3

The applicability of the phosphomolybdovanadate polyoxometalate series of the general formula $H_xH_3PMo_{12-x}V_xO_{40}$ was investigated. Electrochemical and simulation was carried out under 'ideal' conditions to study the multi electron redox processes associated with V_xPOM systems (x = 1-4). It was determined that these systems showed electrochemically quasi-reversible behaviour, which was dissimilar to the $Ru(NH_3)_6^{3+/2+}$ redox system, considered to be a classical electrochemically reversible system. The V_xPOM systems showed an increase in peak separation and broadness which is not believed to be the result of reduced electrode kinetics, but a consequence of the multiple redox processes occurring simultaneously in solution. This idea was supported by electrochemical simulation which proposed the standard rate constant (k^o) would have to be equal to values representative of an irreversible electrochemical process. It was proposed that the various V_xKeggin species present in each V_xPOM system were subject to small changes in their respective formal potential resulting in the broader peaks and the indication of perceived 'slower' electrode kinetics.

Simulation models were developed based upon the V_xPOM systems, with model C being the most successful in simulating the behaviour of the multiple redox processes. This allowed for calculations of diffusion coefficients for the individual Keggin species and not the overall V_xPOM system. Model C successfully simulated the multiple redox processes as well the possible homogenous oxidation via VO_2^+. The change in diffusion coefficient for the V_xPOM was attributed to the increase in anion charge effectively increasing the hydration sphere of the Keggin. The diffusion coefficient decreased in the order V_1POM > V_2POM > V_3POM > V_4POM which is in agreement with literature.[1]

The rotating disc analysis of the V_xPOM systems showed two key points a) there is little change observed in k^o between the V_1 and V_4POM systems under 'ideal' conditions b) the free vanadium ion (VO_2^+) present in the system does not hinder the electrode kinetics in these conditions, instead it is believed to facilitate the observed electrode kinetics with coordination of the VO_2^+ in the outer sphere of the Keggin being more easily reduced.

6.2 Chapter 4

Chapter 4 demonstrated the effects of transition from a supported to a self supporting system upon the electrochemical behaviour of the V_xPOM systems. The $Fe(CN)_6^{3-/4-}$ system showed an increase in peak to peak separation from 95 mV in ideal conditions to 158 mV in fuel cell conditions. This lead to a perceived decrease in the electrode kinetics. It was also apparent that the 300 fold increase in concentration in fuel conditions did not transpire to a 300 fold increase in current and that the anodic current did not decrease in a manner consistent with a diffusion controlled process. The latter was a result of the $Fe(CN)_6^{4-}$ anion acting as the ionic current carrier, and effectively being swept away from the electrode surface. This was supported by the high ionic mobility of the ferri/ferrocyanide ions in aqueous media (Table 4.1, Chapter 4). The increased peak to peak separation is a result of increased resistance caused by a possible increase in solution resistance (self supported) but more significantly the drastic increase in current. *iR* compensated CVs resulted in peak to peak separations that are comparable with those obtained in ideal conditions.

The self supported V_xPOM showed the same increase in peak to peak separation observed in the self supported $Fe(CN)_6^{3-/4-}$. However *iR* compensation did not reduce the peak to peak separation to values comparable with those obtained in ideal conditions, indicating processes other than resistance were hindering the voltammetry. This is further supported by the V_xPOM system not showing the 300 fold increase in current expected under fuel cell conditions, with the 0.3 M V_4POM in particular, producing less than 50% of the expected current.

The free vanadium (VO_2^+) present in solution (V_xPOM where x >1) was shown to distort the CV by oxidising the reduced POM species via equation 3.7. Based upon the initial work by Gattrell, a model to describe the electrode solution interface and behaviour was proposed. This consisted of an adsorbed POM layer and adsorbed VO_2^+ and VO_2^0 species (Figure 4.14, Chapter 4). It is believed that these adsorbed layers reduced the actual potential experienced by the POM species near the electrode surface.

The Tafel analysis for the V_xPOM proved inadequate due to a curvature in the cathodic branch resulting in an inaccurate extrapolation of J_o. The alternative method

proposed involved the interpolation of the RDE data to obtain current densities for given overpotentials. The V_4POM was selected as the lead catalysts due to the increased currents observed during RDE analysis as well having the most 'promise' for improvement. The regenerated V_4POM was shown to not reach OCPs comparable to the fresh state with approximately 3 % of the total vanadium remaining in the 4+ oxidation state. The regenerated V_4POM displayed increased cathodic and anodic currents at the given overpotentials compared to the fresh V_4POM but comparable to the V_4POM in its 10 % redox state. This increase in current (or decrease in required overpotential) was believed to be due to a change in speciation with the reduced POM species favouring the β isomer. This was supported by comparing the single crystal data obtained for the fresh and regenerated V_4POMs with the vanadium atoms being statistically disordered over the entire structure (based on the partial occupancies of the metal centres). The regenerated V_4POM, however, showed a more ordered structure with the vanadiums more likely to be found in 'groups' surrounding the capped vanadium centre.

6.3 Chapter 5

The work in this chapter aimed to build upon the knowledge developed in Chapters 3 and 4 and improve the electrode solution interface and electrode kinetics. Firstly the HV_4POM formulation was introduced to prevent poisoning of the membrane with sodium ions which increased membrane resistance. The HV_4POM showed a speciation change with increases in V_1 and V_2Keggin species as well as an increase in free vanadium in solution (VO_2^+). This increase subsequently results in a decrease in the V_3 and V_4Keggin species, believed to be more active in the ORR. Analysis of membrane deposition after fuel cell testing with the HV_4POM showed a substantial increase in vanadium deposition resulting in a significant increase in membrane resistance based on EIS measurements.

The current vs. overpotential analysis of the HV_4POM showed a decrease in the overpotential required to generate the desired currents compared to the V_4POM. This was concordant with EIS data showing a decrease in the charge transfer resistance. This was believed to be due to an increase in proton concentration which resulted in the VO_2^0 species being readily protonated thus reducing its concentration at the

electrode surface. Hence, reducing the VO_2^0 driven blocking effect. This coincides with the poor regenerating capabilities of the HV_4POM with 28 % of the total vanadium remaining in the 4+ oxidation state upon regeneration.

Formulation of the HV_4POM aimed at limiting the oxidative capabilities of the free vanadium and changing the dynamic equilibrium of the V_xPOM systems. The phosphoric acid formulation ($HV_4(PO_4)$) was shown to potentially hinder oxidative capabilities of the VO_2^+ ion as a result of a possible complexation. However the $HV_4(PO_4)$ showed an apparent decrease in electrode kinetics with increases in CV peak separation and overpotential required to generate the desired currents. This was accounted for by the low solubility of the vanadium phosphate complex increasing the blocking effect at the electrode surface. The tetrafluoroboric acid formulations ($HV_4(BF_4)$) were analogous to the phosphoric acid in the sense that a complexation with the VO_2^+ is believed to hinder its oxidative capabilities, although not as effectively as the phosphoric acid. However the $HV_4(BF_4)$ system did not show an increase in peak to peak separation with lower overpotentials required to generate the desired currents. This was likely due to the high solubility of the vanadium tetrafluoroborate salt compared to the vanadium phosphate, thus not adding to the perceived blocking effect at the electrode surface. The HV_4(VOS) system showed an increase in peak separation and the overpotentials required to generate the desired currents. An increase in anodic current was observed in CV analysis but it is unclear if this was due to oxidation of the reduced Keggin (key aim of the formulation) or due to oxidation of coordinated of VO^{2+} in the outer sphere of the Keggin structure.

The fuel cell testing of the HV_4POM formulations were in agreement with the RDE data and showed that the HBF_4 formulation showed favourable improvement in fuel cell performance. Although the H_3PO_4 and $VOSO_4$ formulations did not show improved fuel cell performance at the current fuel cell conditions, it was demonstrated that the $HV_4(PO_4)$ formulation showed a significant improvement when used in ACAL's high temperature and pressure (HTP) fuel cell which is currently under development.

The work in this thesis has shown that the phosphomolybdovanadate polyoxometalate series are a diverse set of structures with unique electrochemical properties. Key achievements during this work include, successful simulation of the

multiple redox systems identifying individual Keggin diffusion coefficients, which was also key to determining the reason for the apparent slow electrode kinetics. The proposed electrode solution interface model was in good agreement with CV, RDE and EIS analysis as well fuel cell testing. Finally and most significant, was the formulations of the HV_4POM specifically the tetrafluoroboric acid formulation. This is now undergoing extensive testing at ACAL as a potential lead catalyst system for fuel cell and other developing technology.

6.4 References

(1) Chaumont, A.; Wipff, G. *European Journal of Inorganic Chemistry* **2013**, *2013*, 1835-1853.